JOINT TRANSPORTATION
RESEARCH PROGRAM
INDIANA DEPARTMENT OF TRANSPORTATION
AND PURDUE UNIVERSITY

Advancing INDOT's Friction Test Program for Seamless Coverage of System: Pavement Markings, Typical Aggregates, Color Surface Treatment, and Horizontal Curves

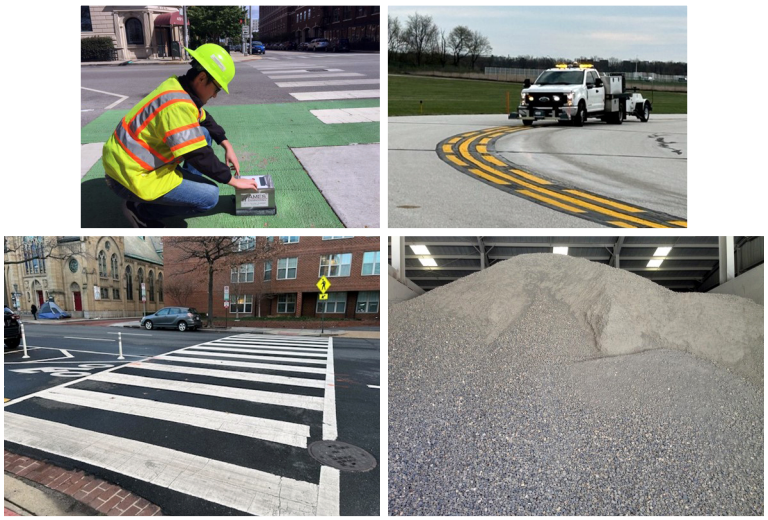

Jieyi Bao, Xiaoqiang Hu, Cheng Peng,
Junyi Duan, Yizhou Lin, Chengcheng Tao, Yi Jiang, Shuo Li

SPR-4646 • Report Number: FHWA/IN/JTRP-2024/09 • DOI: 10.5703/1288284317734

RECOMMENDED CITATION

Bao, J., Hu, X., Peng, C., Duan, J., Lin, Y., Tao, C., Jiang, Y., & Li, S. (2024). *Advancing INDOT's friction test program for seamless coverage of system: Pavement markings, typical aggregates, color surface treatment, and horizontal curves* (Joint Transportation Research Program Publication No. FHWA/IN/JTRP-2024/09). West Lafayette, IN: Purdue University. https://doi.org/10.5703/1288284317734

AUTHORS

Jieyi Bao
Xiaoqiang Hu
Cheng Peng
Junyi Duan
Yizhou Lin
Graduate Research Assistants
School of Construction Management Technology
Purdue University

Chengcheng Tao, PhD
Assistant Professor
School of Construction Management Technology
Purdue University

Yi Jiang, PhD, PE
Professor
School of Construction Management Technology
Purdue University
(765) 494-5602
jiang2@purdue.edu
Corresponding Author

Shuo Li, PhD, PE
Research Engineer
Division of Research and Development
Indiana Department of Transportation

JOINT TRANSPORTATION RESEARCH PROGRAM

The Joint Transportation Research Program serves as a vehicle for INDOT collaboration with higher education institutions and industry in Indiana to facilitate innovation that results in continuous improvement in the planning, design, construction, operation, management and economic efficiency of the Indiana transportation infrastructure. https://engineering.purdue.edu/JTRP/index_html

Published reports of the Joint Transportation Research Program are available at http://docs.lib.purdue.edu/jtrp/.

NOTICE

ACKNOWLEDGMENTS

This research project was sponsored by the Indiana Department of Transportation (INDOT) in collaboration with the Federal Highway Administration (FHWA) through the Joint Transportation Research Program (JTRP). The authors express gratitude to the diligent members of the study advisory committee (SAC), including Samy Noureldin, Tim Wells, Dave Boruff, Bart Williamson, Melissa Ehrhart, and Subhi Bazlamit of INDOT, as well as Kenneth Ferguson of 3M and Eryn Fletcher of FHWA Indiana Division. Special thanks are extended to Ayesha Shah of Purdue University, Mary Kay Salerno-Cahn of Potters Industries, Jon Sproul, Ling Tan, Jesse Salazar of SWARCO, Zhiming Tan of Tongji University, Matthew Duffy of IndyGo, Andrew DiPiazza of Surface Construction, and Adam Baxmeyer and Christopher Morris of Purdue University Airport. Their unwavering support, technical guidance, and the provision of valuable data and sample materials significantly contributed to the success of this research.

TECHNICAL REPORT DOCUMENTATION PAGE

1. Report No. FHWA/IN/JTRP-2024/09	2. Government Accession No.	3. Recipient's Catalog No.
4. Title and Subtitle Advancing INDOT's Friction Test Program for Seamless Coverage of System: Pavement Markings, Typical Aggregates, Color Surface Treatment, and Horizontal Curves		**5. Report Date** March 2024 **6. Performing Organization Code**
7. Author(s) Jieyi Bao, Xiaoqiang Hu, Cheng Peng, Shuo Li, Chengcheng Tao, Junyi Duan, Yizhou Lin, and Yi Jiang		**8. Performing Organization Report No.** FHWA/IN/JTRP-2024/09
9. Performing Organization Name and Address Joint Transportation Research Program Hall for Discovery and Learning Research (DLR), Suite 204 207 S. Martin Jischke Drive West Lafayette, IN 47907		**10. Work Unit No.** **11. Contract or Grant No.** SPR-4646
12. Sponsoring Agency Name and Address Indiana Department of Transportation (SPR) State Office Building 100 North Senate Avenue Indianapolis, IN 46204		**13. Type of Report and Period Covered** Final Report **14. Sponsoring Agency Code**

15. Supplementary Notes

Conducted in cooperation with the U.S. Department of Transportation, Federal Highway Administration.

16. Abstract

Various highway projects, roadway safety, and maintenance all hinge on pavement friction. INDOT's pavement friction test program has played a crucial role in addressing issues like wet pavement crash reduction, durable pavements surface friction, and sustainable aggregates. However, changes in the transportation sector, allied industries, societal needs, and economics present unique challenges that require proactive solutions. First, the existing field friction testing method, which uses a locked wheel skid tester (LWST) is limited to straight, flat pavement sections and excludes crash-prone areas like horizontal curves. Upgrading the program to cover horizontal curves on two-lane rural highways is vital for road safety. Second, the demand for friction testing on pavement markings at crash sites is rising. There's currently no widely accepted standard method for national-scale pavement marking friction testing. The shift to wider longitudinal pavement markings, from 4" to 6", driven by both human and autonomous vehicle safety, presents challenges for motorcyclists and pedestrians. The third challenge focuses on Color Surface Treatment (CST), which is increasingly used in Indiana bus and bike lanes for visibility, lane discipline, and friction performance, especially under frequent bus acceleration and braking. However, a lack of laboratory and field data necessitates investigating CST's metrics and requirements for adequate friction. Advancing INDOT's friction testing program to cover the entire highway system and address emerging friction challenges is imperative. The goals of this study included enhancing INDOT's friction testing, ensuring comprehensive highway network coverage and providing reliable friction data to help INDOT address safety concerns. The research encompassed a thorough evaluation of various aggregates and pavement marking materials commonly used in Indiana through laboratory experiments, field tests, and data analysis to unveil their influence on pavement friction. Field friction measurements on colored bus and bike lanes were also conducted and thoroughly analyzed. Moreover, the tire-pavement interaction on horizontal curves was assessed on airport runways and highway sections through mechanistic-empirical analysis, and a friction testing model for horizontal curves was devised using finite element analysis and machine learning methodologies.

17. Key Words	18. Distribution Statement
friction, pavement marking, aggregate, safety, color surface treatment, bus lane, bike lane, finite element analysis, machine learning	No restrictions. This document is available through the National Technical Information Service, Springfield, VA 22161.

19. Security Classif. (of this report)	20. Security Classif. (of this page)	21. No. of Pages	22. Price
Unclassified	Unclassified	133 including appendices	

EXECUTIVE SUMMARY

Introduction

Pavement friction directly aligns with not only the Indiana Department of Transportation's (INDOT) list of the key performance indicators (KPIs), especially roadway safety, but also the priority list of INDOT's operation activities, such as polish resistant aggregates, pavement resurfacing, pavement overlay, pavement and bridge preservation, and high friction surface treatment. Through the INDOT pavement friction test program, the INDOT Office of Research and Development (R&D) has collaborated with INDOT's Traffic Safety Office, Materials Management Office, Highway and Bridge Maintenance Office, and Districts Offices to address various issues, including wet pavement crash reduction, durable pavement and bridge deck surface friction, and sustainable aggregates. Nevertheless, recent changes in the transportation sector, related industries, societal needs, and economic considerations have created unique challenges that require more proactive and immediate solutions. There is a justified need to advance INDOT's current friction test program to provide seamless coverage of the highway system and to address the emerging issues pertaining to friction testing and performance in a timely manner. The primary research objective was to advance INDOT's current friction test program through an innovative mechanistic-empirical approach for seamless coverage of the agency's highway system. A secondary research objective was to provide reliable friction test data and performance metrics that will allow customers to address the safety issues and challenges of emerging traffic facilities, features, and technologies, which include pavement markings and color surface treatment.

Results and Findings

Pavement Markings

- *Wet and Dry Surface:* On average, the British Pendulum Number (BPN) in dry conditions is 44% higher than in wet conditions for new markings without polishing.
- *Waterborne and Non-Waterborne Markings:* For new markings without polishing, waterborne makings exhibit BPN values 27% greater on average than non-waterborne markings when the same type of beads, application rate, and thickness are applied. Most waterborne markings can withstand no more than 1,500 polishing cycles. However, waterborne markings with Type 1 beads and a thickness of 20 mils or more exhibit better durability, i.e., up to 5,000 polishing cycles.
- *Pavement Marking Thickness:* Increasing the thickness of pavement marking can significantly enhance durability but does not substantially increase friction.
- *Bead Size and Application Rate:* For glass beads, an increase in bead size contributes to initial mean profile depth (MPD) but doesn't necessarily result in higher initial friction. Larger beads, particularly Type 4, may lead to a decrease in durability. Nevertheless, smaller beads consistently exhibit higher durability and friction. A higher bead application rate also leads to an increase in MPD, particularly for waterborne markings.
- *Ceramic Particles:* Adding ceramic particles tends to increase both MPD and friction significantly, especially under wet conditions, but compromise the durability.
- *Friction Metrics:* In addition to macrotexture features, additional microtexture features should be considered to fully define the correlation between texture and friction. There also are discrepancies between BPN and DF40.
- *Friction Performance and Requirements:* Most new markings exhibit friction performance with BPN ranging from 30 to 65. A tentative minimum requirement of BPN = 40~45 is recommended. If a minimum BPN of 40 is required, only new thermoplastic (intermixed beads) markings, new epoxy markings, and waterborne markings in the later stage of their service life may not meet this requirement. However, this can be addressed by either adding ceramic particles or by combining the addition of ceramic particles with an increase in the marking thickness.

Aggregates

- *Physical Properties vs. Mechanical Properties:* Bulk specific gravity (BSG) has a more significant impact on the mechanical properties than water absorption (WA) and soundness. The correlation between LAA and PSV-10 is weak or very weak, regardless of the type of aggregate. MDA and PSV-10 exhibit mixed correlations, depending on the type of aggregate.
- *Chemical Compositions vs. Mechanical Properties:* The chemical contents of Al_2O_3 and TiO_2 have strong positive correlations with hardness and the contents of MgO and CaO have strong negative correlations with hardness. However, the chemical components, including Al_2O_3 and TiO_2, exhibit greater variabilities, regardless of aggregate types, including dolomite, limestone, and gravel. To ensure consistent aggregate quality (particularly aggregate mechanical properties), it is advisable to specify the chemical requirements for aggregates used in pavement construction (refer to Table 7.1).
- *Mg Content for Dolomite:* The current requirement for minimum Mg content in dolomite is 10.3%, which is lower than the Mg contents of most dolomite samples and some limestone samples. We recommend revising the current requirement to 12.0% to help ensure consistent engineering properties and performance characteristics of the dolomite aggregate.
- *Physical and Mechanical Properties:* Aligned with the recommended chemical requirements, the suggested criteria for aggregate physical and mechanical properties can be found in Table 7.2.
- When assessing the frictional performance of aggregates, including dolomite, limestone, gravel, steel slag, and calcined bauxite, they may be ranked in terms of abrasion resistance (LAA and MDA), resistance to polishing (PSV-10), and/or Mohs hardness in descending order as follows.

  Calcined bauxite → Steel slag → Gravel → Dolomite → Limestone

Color Surface Treatment

- *Green Bike Lane:* The current color surface treatment (CST) with bauxite aggregate of size 6×16 can maintain durable surface integrity and friction performance (BPN equal to or greater than 60, measured with a $6 \times 25 \times 76$ mm slider; and MPD not less than 1.00 mm) for over 3 years.
- *Red Bus Lane:* The current CST may perform satisfactorily for up to 3 years depending on the surface condition of underlying pavement. However, the current CST, featuring

bauxite aggregate of size 6×16, showed an MPD of 0.22 mm~0.23 mm after 3 years in service. Furthermore, it exhibited an MPD of 0.78 mm~0.85 mm and a friction number (FN) of 32~36 (measured with the standard smooth tire at 40 mph) after 6 months in service. Both the MPD and friction number are markedly lower than those of HFST. The two key takeaways are (1) the surface of the red bus lane undergoes severe polishing, necessitating the use of high polish-resistant aggregates (especially calcined bauxite), and (2) to enhance the surface frictional properties of the red bus lane, consideration can be given to appropriately increasing the size of the bauxite aggregate.

Locked Wheel Skid Trailer (LWST) Friction Testing on Horizontal Curves

- Tire cornering stiffness is dependent on numerous tire properties, including the material, size, vertical load, inflation pressure, and tread pattern, and can be estimated with the longitudinal friction force and the vertical force measured for a test tire in the case of pure side slip.
- The effect of the speed discrepancies between the vehicle and trailer on the friction coefficient measurement is negligible for locked wheel skid trailer (LWST) test on actual highway horizontal curves as long as a test failure due to trailer fishtailing is avoided.
- To limit the cornering impact on test tire vertical load (<100-lb), a radius of curvature greater than $0.3\ V^2$ is suggested for cornering tests in pure sideslip condition. If a selected superelevation rate of 4%, 6%, or 8% is added, a minimum curve radius of 445.92-ft, 432.576-ft, or 420.92-ft is suggested for realiable measurements at 40 mph, respectively.

Tire Friction Modeling with Finite Element Analysis and Machine Learning

- The adaptability of the Finite Element Analysis (FEA) model and the efficiency of machine learning techniques offer an effective avenue for comprehending the intricate dynamics between tires and varying roadway conditions.
- FEA simulations coupled with Gaussian process regression (GPR) predictions can derive true friction numbers on horizontal roadway curves from the testing results with locked wheel skid tester (LWST).
- A comprehensive reference table was developed to provide a practical tool for obtaining true friction numbers by directly referencing the measured friction values alongside the geometric characteristics of the roadway curves.

Implementation

This comprehensive study investigated multiple facets of pavement friction, including pavement markings, aggregates, color-treated bus and bike lanes, tire-pavement interactions on both straight and curved roadways, and the modeling of tire friction. The outcomes yield essential insights and offer essential requirements, specifications, and guidelines for appropriately selecting materials to enhance safety. The accompanying extensive reference table serves as a critical resource, facilitating the determination of accurate friction values on horizontal curves of roadways. The practical application of these research findings promises significant benefits to both highway agencies and motorists.

CONTENTS

1. CHAPTER 1. INTRODUCTION 1
1.1 Background 1
1.2 Literature Review 1
1.3 Main Tasks 4
2. CHAPTER 2. FRICTION PERFORMANCE OF COMMON PAVEMENT MARKINGS 5
2.1 Problem Statement 5
2.2 Laboratory Experiment 5
2.3 Testing 9
2.4 Results and Analysis 11
2.5 Expanded Data Interpretation 16
2.6 Field Assessment 21
3. CHAPTER 3. FRICTIONAL PROPERTIES OF TYPICAL AGGREGATES 25
3.1 Methodology 25
3.2 Laboratory Experiments and Analysis 25
3.3 Analysis of Parameters 27
3.4 Aggregate Hardness 29
3.5 Correlations Between Hardness and Chemical Elements 29
3.6 Range of Aggregate Property Values 30
4. CHAPTER 4. COLOR SURFACE TREATMENT 31
4.1 Problem Statement 31
4.2 Materials and Field Testing 31
4.3 Green Bike Lane 32
4.4 Red Bus Lane 33
5. CHAPTER 5. PRACTICABILITY OF FRICTION TESTING WITH A LOCKED WHEEL SKID TRAILER AT HORIZONTAL CURVES 35
5.1 Problem Statement 35
5.2 Mechanistic Analysis of Tire-Pavement Frictional Interaction at Horizontal Curves 36
5.3 Camera-Based Sideslip Angle and Articulation Angle Measuring 39
5.4 Field Validation Testing 42
5.5 Empirical Investigation of Tire-Pavement Frictional Interaction at Horizontal Curves 46
6. CHAPTER 6. MODELING OF TIRE-PAVEMENT FRICTIONAL INTERACTION WITH FINITE ELEMENT ANALYSIS AND MACHINE LEARNING 54
6.1 Tire Friction Model Setup 54
6.2 Tire Model Analysis 55
6.3 Validation of the 3D Tire-Pavement FEA Results with the Field Test Results 56
6.4 Friction Analysis on Straight and Curved Roads 58
7. CHAPTER 7. CONCLUSIONS 68
REFERENCES 70
APPENDICES
Appendix A. Pavement Markings Laboratory Test Results and Photos 75
Appendix B. Locked Wheel Skid Trailer In-Situ Test Results 75
Appendix C. Friction Simulation Results 75

LIST OF TABLES

Table 2.1 Recommended Pavement Marking Application 6

Table 2.2 Gradation of Glass Beads and Ceramic Particles 8

Table 2.3 Prepared Marking Specimens for Testing 11

Table 2.4 Pearson Correlation Coefficients 18

Table 2.5 Friction Levels for New Pavement Markings 19

Table 2.6 Classification of Friction Levels for All Marking Specimens 19

Table 2.7 Conversion Matrix Between MPD and DF Values 23

Table 2.8 Macrotexture MPD Values of Crosswalk Markings 24

Table 3.1 Aggregate Property Measurements Statistics 27

Table 3.2 Specified Limits for Aggregate Properties 27

Table 3.3 Statistics of Dolomite Properties 27

Table 3.4 Pearson Correlation Coefficients (R) of Dolomite Properties 28

Table 3.5 LR Models of Dolomite Aggregate Properties 28

Table 3.6 Statistics of Limestone Properties 28

Table 3.7 Pearson Correlation Coefficients (R) of Limestone Properties 28

Table 3.8 LR Models of Limestone Aggregate Properties 28

Table 3.9 Statistics of Gravel Properties 28

Table 3.10 Pearson Correlation Coefficients (R) of Gravel Properties 29

Table 3.11 LR Models of Gravel Aggregate Properties 29

Table 3.12 Statistics of Steel Slag Properties 29

Table 3.13 Pearson Correlation Coefficients (R) of Steel Slag Properties 29

Table 3.14 LR Models of Steel Slag Aggregate Properties 29

Table 3.15 Mohs Hardness and MDA Values 30

Table 3.16 Pearson Correlation Coefficients Between Hardness and Chemical Content 30

Table 3.17 Statistical Ranges of Main Aggregate Properties (95% Confidence Level) 31

Table 4.1 Measured Surface Textures on Green Bike Lane 33

Table 4.2 BPN Values on Green Bike Lane 33

Table 4.3 Measured Surface Textures on Red Bus Lane 34

Table 4.4 Measured Friction Values on New and Old Red Bus Lanes 35

Table 5.1 States of the LWST Bicycle Model 37

Table 5.2 Accuracy Assessment of Camera Measurements 45

Table 6.1 FEA Validation with Field Testing on INDOT Friction Test Track (05/2023) 58

Table 6.2 FEA Validation with Field Testing on Real-World SR-37 59

Table 6.3 FEA Validation with Field Testing on Curved Runways (04/2023) 61

Table 6.4 FEA Validation with Field Testing on Straight and Curved Runways (10/2023) 61

Table 7.1 Recommended Chemical Requirements 69

Table 7.2 Recommended Physical and Mechanical Requirements 69

LIST OF FIGURES

Figure 2.1 Glass beads and ceramic particles 8

Figure 2.2 Surfaces of preformed tape (left) and thermoplastic materials (right) 8

Figure 2.3 Texture measuring devices (left: LTS; right: CTM) 9

Figure 2.4 Friction measuring devices (left: BPT; right: DFT) 9

Figure 2.5 Three-wheel polishing device 9

Figure 2.6 Liquid pavement marking specimen preparation 10

Figure 2.7 Thermoplastic specimen preparation 10

Figure 2.8 BPN and MPD measurements of markings before polishing 12

Figure 2.9 Photos of a waterborne marking specimen surface before and after polishing 13

Figure 2.10 Numbers of terminal polishing cycles for waterborne marking specimens 13

Figure 2.11 MPD and DF40 values of waterborne paints during polishing 14

Figure 2.12 F60 values of waterborne paints 15

Figure 2.13 Polyurea specimen surface during polishing 15

Figure 2.14 Numbers of terminal polishing cycles for non-waterborne materials 15

Figure 2.15 MPD and DF40 values of non-waterborne paints during polishing 16

Figure 2.16 Closeups of pre-formed tape and thermoplastic specimen before and after polishing 17

Figure 2.17 F60 values of non-waterborne paints 17

Figure 2.18 Fuzzy C-means clustering results 18

Figure 2.19 Pearson correlation coefficients 20

Figure 2.20 Selection of optimal cluster numbers 21

Figure 2.21 Clustering results of each material types 22

Figure 2.22 Closeups of thermoplastics applied in laboratory and in field 23

Figure 2.23 Closeups of a crosswalk marking 23

Figure 2.24 Closeups of roundabout crosswalk markings in different conditions 24

Figure 2.25 Truck tires traveling right edge line marking 24

Figure 3.1 Laboratory experiment plan 26

Figure 3.2 LAA, MDA, and PSV test machines 26

Figure 4.1 Bus and bike CST lanes in Indianapolis 32

Figure 4.2 Visual inspection on green bike lane 32

Figure 4.3 Photos of red bus lanes (left and middle: old; right: new) 33

Figure 4.4 Variations of MPD over time 34

Figure 5.1 Bicycle model for articulated vehicle 37

Figure 5.2 KLT tracking performance on images of pavement marking 40

Figure 5.3 Motion tracking of good corner features and outlier (red) rejection 41

Figure 5.4 Performance of the algorithms over asphalt road surface 41

Figure 5.5 Calibrated video frame at zero articulation angle 42

Figure 5.6 Sensers installed on LWST 42

Figure 5.7 LWST testing on airport runway 43

Figure 5.8 Footprints of friction tests on airport runway 43

Figure 5.9 Time series of friction testing on a right turn runway 44
Figure 5.10 Two horizontal curves on a two-lane state highway 45
Figure 5.11 Time series of friction testing on a straight section of SR-26 45
Figure 5.12 Time series of friction testing at a right turn followed by a left turn on SR-26 46
Figure 5.13 Time series of friction testing within 1-second friction test time window 47
Figure 5.14 Tire lateral force estimation with sideslip angle 48
Figure 5.15 Tire lateral force estimation with sideslip angle and lateral inclination 48
Figure 5.16 Tire cornering stiffness estimation with vertical loads 48
Figure 5.17 Test tire sideslip angle with vehicle articulation angle in field tests 49
Figure 5.18 Pavement MPD variations at different directions 49
Figure 5.19 Friction coefficient variation with test speed 50
Figure 5.20 Minimum radius required for various design speed at 8% superelevation 50
Figure 5.21 LWST speed transducer performance for friction tests on horizontal curves 51
Figure 5.22 Measured tire speed vs. estimated tire speed 51
Figure 5.23 Absolute value of test tire sideslip angles 52
Figure 5.24 Test tire vertical force measurements on straight roadway 52
Figure 5.25 Regression models of additional tire vertical forces 53
Figure 5.26 Additional tire vertical forces $\left(\frac{h}{w}\frac{mV^2}{R}\right)$ 53
Figure 5.27 Test tire vertical forces 54
Figure 6.1 Workflow of the tire-pavement frictional interaction simulation 54
Figure 6.2 2D model of tire: (a) radial structure of tire, (b) 2D tire components, and (c) tire-pavement friction area 55
Figure 6.3 Map 2D to 3D tire model for (a) rib tire, and (b) smooth tire 55
Figure 6.4 Footprint analysis results. 56
Figure 6.5 Cornering analysis angles 57
Figure 6.6 Force analysis 57
Figure 6.7 Tire lateral inclination 58
Figure 6.8 Straight road FEA results on INDOT friction test track and SR-37 59
Figure 6.9 3D tire with slip angle 60
Figure 6.10 FEA results on curved runways 60
Figure 6.11 Correlation map from field-testing data 62
Figure 6.12 Top view of the tire under pure sideslip cornering conditions 63
Figure 6.13 Estimated friction numbers under pure sideslip cornering conditions 63
Figure 6.14 Estimated friction numbers on curved and straight roads 64
Figure 6.15 GPR predicted vs. actual measured friction numbers 64
Figure 6.16 Estimated friction numbers on curved road at various speeds 65
Figure 6.17 Locked wheel smooth tire vertical forces 65
Figure 6.18 Locked wheel smooth tire friction numbers 65
Figure 6.19 Locked wheel smooth tire longitudinal friction forces 66
Figure 6.20 GPR predicted vs. measured friction (04/2023) 66
Figure 6.21 GPR predicted vs. measured friction (04/2023 and 10/2023) 66

Figure 6.22 Plot of 500 runs of FEA inputs 67

Figure 6.23 Differences between GPR and FEA calculated Fx values 68

Figure 6.24 The box plot of differences of GPR and FEA results 68

1. CHAPTER 1. INTRODUCTION

1.1 Background

Pavement friction is a crucial aspect that directly relates to the key performance indicators (KPIs) of the Indiana Department of Transportation (INDOT) and is vital in ensuring roadway safety. INDOT's operational activities, which encompass the use of polish-resistant aggregates ITM 214, pavement resurfacing, overlay, pavement and bridge preservation, and high friction surface treatment (HFST), all rely on adequate pavement friction. The INDOT Research and Development (R&D) Division has been actively engaged in addressing various issues, including mitigating wet pavement crashes, ensuring durable surface friction on pavements and bridge decks, and promoting the sustainability of aggregates. However, recent developments in the transportation sector, allied industries, societal demands, and economic factors have brought forth unique challenges that necessitate proactive solutions.

Firstly, INDOT's R&D Division has observed an increasing demand for friction testing on pavement markings at crash sites, especially on two-lane rural highways and intersections. Although it is stated that consideration should be given to selecting pavement marking materials that will minimize tripping or loss of traction for road users, including pedestrians, bicyclists, and motorcyclists (FHWA, 2023), there is currently no widely accepted standard method for testing and assessing the friction performance of pavement markings at a national level. Furthermore, the significance of pavement markings has surged due to the safety concerns of autonomous vehicles (AVs). There is a nationwide trend to widen 4″ longitudinal pavement markings to 6″ or wider, aimed not only at improving human driving safety but also aiding AVs in detecting lane markings for determining their lateral positions (NCUTCD, 2019; Pike et al., 2019). While the use of 6″ lines on high-speed roadways is not mandated (FHWA, 2020), many state highway agencies are adopting the 6″-line width in recognizing the crash reductions.

However, wider markings may pose challenges, especially for motorcyclists and pedestrians at crosswalks, intersections, and locations where markings dominate the road surface (Figueroa & Colucci, 2007). Skid resistance or friction is a crucial aspect of pavement markings in addition to factors like reflection, retroreflection, and color, particularly for markings occupying significant trafficked areas such as zebra crossings, arrows, transverse markings, and symbols (BSI, 2018). Though the use of glass beads may improve marking surface friction, information on this is limited. Evaluating standardized test methods and assessing the friction performance of commonly used pavement markings is essential to enhance road safety, especially considering the coexistence of conventional and autonomous vehicles.

Secondly, color surface treatment (CST), which involves colored pavements, is increasingly utilized in bus and bike lanes to enhance their visibility, and deter unauthorized lane usage (FHWA, 2011; NACTO, 2020). CST is also expected to improve safety by providing durable friction performance for bicyclists and buses during frequent braking and acceleration. This practice is becoming more common in Indiana cities, notably in Indianapolis. However, despite the frequent consultation with INDOT's R&D Division on CST friction performance, there is a lack of laboratory and field data to meet these emerging needs. It is a pressing need to investigate the metrics and requirements for CST to better serve INDOT's customers and the public.

Thirdly, INDOT's current friction testing program employs a locked wheel skid trailer (or locked wheel skid tester) (LWST) following the ASTM E274 standard method for field friction testing (ASTM, 2020a). This method is designed for testing straight, flat pavement sections and does not encompass crash-prone areas like horizontal curves. Alarmingly, horizontal curves have reported an average crash rate three times higher than other highway segments, with three-quarters of curve-related fatal crashes involving single vehicles leaving the road and colliding with roadside objects (Albin et al., 2016). To enhance road safety, there is a growing need to upgrade the existing friction testing program to include areas susceptible to polish, such as horizontal curves and steep grades on two-lane rural highways.

Undoubtedly, there is a legitimate requirement to enhance INDOT's current friction testing program to ensure comprehensive coverage of the highway system and address emerging friction testing and performance challenges promptly. The primary objective of this study is to advance INDOT's current friction testing program through an innovative mechanistic-empirical approach, ensuring seamless coverage of the agency's extensive highway network. The secondary objective aims to provide reliable friction test data and performance metrics, empowering INDOT to address the safety issues and challenges associated with emerging traffic facilities, features, and technologies, with a specific focus on pavement markings and CST.

1.2 Literature Review

Pavement markings can be divided into two primary categories based on their durability: durable marking materials and non-durable marking materials. Several studies have evaluated the frictional performances of diverse pavement marking materials. Richard (1975) noted that thermoplastics surpassed cold plastics in friction performance, while fast-dry paint typically exceeded the performance of both. Conversely, Rodin et al. (2018) reported that preformed tape had superior anti-skid properties compared to neat concrete surfaces, yet both waterborne paint and thermoplastic lagged behind neat concrete in this regard. Kassem et al. (2021) discovered that the anti-skid capability of thermoplastic is inferior to that of waterborne paint and methacrylate (MMA) paint.

Several instruments, including British pendulum tester (BPT) (AASHTO, 2021), dynamic friction tester (DFT) (ASTM, 2015b), and LWST, have been utilized to directly evaluate surface anti-skid properties. Notably, both BPT and DFT are versatile for laboratory or field testing, whereas LWST is exclusively designed for field testing. However, the friction properties measured by distinct devices are not directly interchangeable. Additionally, it is imperative to devise a distinct evaluation criterion for each device. Based on ASTM E1960-07, the friction coefficient measured by the DFT at 20 km/h should not be less than 0.3 (ASTM, 2015b). Recent research regarding the friction number measured by LWST with the standard smooth tire at 40 mph suggests that values between 35 and 50 are deemed within the acceptable range (Bao et al., 2023). For values obtained using the BPT, often referred to as the British Pendulum Number (BPN), previous studies have employed a tripartite threshold system. They set a minimum acceptable BPN value at 45, with subsequent levels at 55 and 65, tailored especially for heavily trafficked roads (Asi, 2007; Giles et al., 1965; Harlow, 2005). Contrastingly, the European Standard EN 1436 delineates five BPN thresholds, ranging from 45 to 65, with 5-unit intervals (BSI, 2018).

Retro-reflective beads are commonly integrated into pavement marking to enhance visibility. Through comparative testing of skid resistance values between waterborne paint with and without glass beads, it was observed that markings containing glass beads significantly enhanced in skid resistance (Anderson et al., 1982; Bagot, 1996; Harlow, 2005). Additionally, the inclusion of angular particles in pavement marking has been shown to effectively reduce slipperiness within marked areas (Bagot, 1996; Coves-Campos, 2018; Harlow, 2005; Siyahi et al., 2015). For instance, waterborne paint coated with silica demonstrated enhanced anti-skid performance compared to that coated with retro-reflective glass beads (Bagot, 1996). Besides silica, quartz has also been demonstrated as an excellent additive to enhance the friction properties of pavement markings (Harlow, 2005). Siyahi et al. (2015) found that multi-component paint specimens enhanced with sharp-cornered silica granules, waste glass powders, and expanded clay additives showed marked improvements in skid-resistance. Among these, waste glass powder exhibited the most superior skid-resistance performance. Coves-Campos et al. (2018) blended glass beads with white marble sand and irregularly shaped sodium-calcium glass particles characterized by sharp edges and observed that the incorporation of white marble sand into the paint yielded excellent anti-skid properties. Nevertheless, the usage of sharp-edge additives is not extensively prevalent in practical applications as it leads to diminished reflectivity of markings. This outcome is attributed to the shadows generated by angular particles situated above the surface of applied glass beads (Harlow, 2005).

The fundamental basis for enhancing skid resistance in pavement markings through the incorporation of additives lies in the intentional modification of the surface texture attributes of these markings. Surface texture characteristics, categorized into macrotexture and microtexture, constitute essential metrics for evaluating surface friction. Macrotexture and microtexture can be discerned based on their distinct wavelength ranges (PIARC, 1987). Specifically, macrotexture wavelength spans from 0.5 mm to 50 mm (0.2 in. to 2 in.), whereas microtexture wavelength falls within the range of 0.001 mm to 0.5 mm (0.0004 in. to 0.02 in.) (Henry, 2000; Li et al., 2010). These texture variations play a critical role in the modulation of skid resistance by influencing the adhesion and hysteresis forces at the interface between the tire and pavement (Alhasan et al., 2018; Kassem et al., 2013; Kogbara et al., 2016; Kummer, 1966; Li et al., 2010; Li et al., 2016; Lorenz et al., 2015). Under dry conditions and at lower speeds, it is the microtexture that primarily dictates pavement friction performance. In contrast, under wet conditions and at higher velocities, the role of macrotexture becomes preeminent (Alhasan et al., 2018; Kassem et al., 2013; Kogbara et al., 2016; Li et al., 2010; Li et al., 2016; Lorenz et al., 2015). Texture information can be acquired using the circular track meter (CTM) for macrotexture (ASTM, 2019b), and using LTS for both macrotexture and partial microtexture characteristics. Previous research posits that friction data gathered via BPT can act as a microtexture surrogate, due to low slip speed of BPT (Henry, 2000). Currently, research primarily emphasizes the relationship between texture and friction of aggregates and pavement surface (Alhasan et al., 2018; Fowler & Rached, 2012; Heitzman & Erukulla, 2011; Kassem et al., 2013; Kogbara et al., 2016; Komaragiri et al., 2020; Li et al., 2010, 2016; Lorenz et al., 2015; Saghafi et al., 2022; Xiong et al., 2021). Even though existing research indicated that the alterations in pavement marking texture and skid resistance exhibit a similar trend (Anderson et al., 1982; Pasetto & Barbati, 2011), studies into the link between pavement marking surface texture and friction performance remain scarce.

Three-wheel polishing device (TWPD) is commonly employed in laboratory environments to accelerate the polishing process of pavement materials and aggregates (Fowler & Rached, 2012; Hajj et al., 2019; Heitzman & Erukulla, 2011; Komaragiri et al., 2020; Saghafi et al., 2022; Xiong et al., 2021; Zong et al., 2021). It can be synergistically used with CTM and DFT to assess macrotexture and dynamic friction of polished surfaces. Lately, TWPD has been employed to emulate pavement marking abrasion in the field (Kassem et al., 2021; Mohamed et al., 2019, 2020). This offers a viable alternative to the historically time-intensive and labor-demanding field test-deck procedures, which frequently necessitated road closures (Asdrubali et al., 2013; Bagot, 1996; Coves-Campos et al., 2018; Johnson et al., 2009; Pasetto & Barbati, 2011; Richard, 1975; Rodin et al., 2018; Scalici et al., 2014; Su et al., 2022). The academic discourse extensively covers the reflective and durability aspects of pavement markings

(Babić et al., 2015; Bektas et al., 2016; Donnell et al., 2009; Jiang, 2008; Mohamed et al., 2019; Mohamed et al., 2020). However, given the traditionally subdued emphasis on skid resistance (Pasetto & Barbati, 2011), there remains a paucity of in-depth research into anti-skid attributes of pavement markings, particularly during their wear phase (Pasetto & Barbati, 2011; Su et al., 2022).

Pavements, crucial for smooth and secure driving, heavily rely on aggregates in their mix design, construction, and operational phases. Constituting a substantial portion of both hot mix asphalt (HMA) and Portland cement concrete (PCC), aggregates are fundamental to pavement structural integrity (Papagiannakis & Masad, 2008). The safety, longevity, and overall quality of pavement surfaces are significantly impacted by aggregate properties. For example, the utilization of polish-resistant aggregates like calcined bauxite enhances durable skid resistance, effectively reducing road crashes (Li et al., 2017). However, certain chemical components in aggregates may trigger concrete cracking and spalling, potentially compromising pavement quality (Hanna, 2003).

The Federal Highway Administration (FHWA) is actively investigating aggregate properties to enhance pavement sustainability while balancing economic, environmental, and social impacts (Xu et al., 2022). Recycled concrete aggregate (RCA) has been proposed as an environmentally friendly alternative to virgin aggregate (VA) for asphalt pavements, considering moisture and temperature effects on pavement structure (Aytekin & Mardani-Aghabaglou, 2022). Additionally, fiber-reinforced recycled aggregate concrete (FRRAC) has shown promise in promoting sustainable rigid pavements based on its strength properties (Chan et al., 2019).

Natural and industrially manufactured aggregates both play a vital role in pavement structure. Natural aggregates are obtained and crushed from various rocks, while manufactured aggregates often comprise industrial by-products like steel slag and air-cooled blast furnace slag. Even crushed asphalt or concrete pavement can be repurposed as aggregate materials. Commonly used aggregates by the Indiana Department of Transportation (INDOT) include dolomite, limestone, gravel, and steel slag, with aggregate properties directly influencing pavement performance (INDOT, 2022). INDOT specifically mandates that the dolomite utilized should contain a minimum elemental magnesium content of 10.3%. However, the influence of magnesium concentration on the frictional characteristics of aggregate materials requires further investigation.

Aggregates possess physical, chemical, and mechanical properties with various key parameters. Physical properties include bulk specific gravity (BSG), water absorption (WA), and soundness, while chemical properties encompass elements such as aluminum oxide (Al_2O_3), silicon dioxide (SiO_2), iron oxide (Fe_2O_3), titanium dioxide (TiO_2), calcium oxide (CaO), and magnesium oxide (MgO). Mechanical properties, vital in assessing aggregate quality within the pavement structure, are typically evaluated through the Los Angeles abrasion (LAA) test, micro-Deval abrasion (MDA) test, and polished stone value (PSV) test. Studies by Yu et al. (2019) and Zhan et al. (2021) have emphasized the profound impact of mechanical properties on pavement surface friction, where lower LAA or MDA values, or higher PSV values, correlate with superior friction performance of the aggregate.

The LAA, MDA, and PSV tests are pivotal indicators for evaluating pavement friction performance, garnering substantial research attention. Ajalloeian and Kamani (2019) delved into the intricate interplay between LAA loss and rock aggregate textural intricacies, constructing regression models to predict LAA loss in real-world applications. Teymen (2019) conducted comprehensive trials involving a diverse array of rock aggregates, elucidating the nexus between LAA values and tangible physical properties through regression analysis. Mahmoud and Masad (2007) contributed a methodology to quantitatively gauge aggregate resistance to abrasion and fragmentation, hinging on MDA tests, demonstrating its utility in aggregate selection and evaluation.

Heitzman et al. (2015) explored the performance landscape of various aggregates concerning surface friction, establishing a significant linkage between surface friction and MDA loss. Liu et al. (2020) presented a mathematical framework capturing PSV attenuation within coarse aggregates, aiding predictions regarding skid resistance and durability. Zong et al. (2021) advanced the discourse by deriving equations capturing PSV evolution with successive polishing cycles and highlighting the robust correlation between PSV attenuation and the friction coefficient. In a comprehensive study, Li et al. (2017) conducted LAA, MDA, and PSV tests on calcined bauxite and steel slag, specifying precise requirements for optimal surface friction performance.

However, the existing literature lacks a thorough analysis of aggregate property correlations covering physical, chemical, and mechanical aspects. Additionally, inferring aggregate friction performance based on specific associated physical, chemical, or mechanical indices remains a significant challenge. The present study endeavors to address these gaps by comprehensively analyzing the interconnections between aggregate properties and their influence on pavement friction performance.

Tire-road friction, a critical factor in road safety and vehicle control, is influenced by various parameters. One key factor is the alteration in vehicle operating conditions, determined by the geometric properties of the pavement structure (Kogbara et al., 2016). While pavement friction testing can be conducted on various road sections at different speeds, it is important to note that the LWST field friction test method is specifically designed for straight and level pavement segments (Hall et al., 2009). Horizontal curves pose unique

challenges for the LWST method due to several reasons. These include issues related to biased tire speed and force measurements, a lack of information about vehicle side friction, and the risk of trailer fishtailing. Highway engineers have emphasized the need for timely friction measurements on various parts of the mainline pavement network, irrespective of geometric properties like the curvature radius and superelevation rate (Albin et al., 2016). Given that most highways include horizontal curves, avoiding these sections during routine LWST friction monitoring is not a viable solution. Furthermore, the crash rate for horizontal curves is approximately three times higher than that of tangent segments with a flat surface on the entire INDOT highway system (Li et al., 2017). However, a suitable method for assessing the LWST friction results on horizontal curves is currently unavailable.

A key component is the sideslip angle, which represents the angle between the tire's orientation and its actual direction of travel. The magnitude of the sideslip angle significantly affects the lateral friction force on the tire-pavement contact patch (Gillespie, 2021). Previous methods for direct sideslip angle measurement have been expensive and cumbersome. As a result, estimation algorithms using vehicle models with simplifications are often proposed, but these can limit real-time field applications (Jeong et al., 2022). GPS-aided algorithms have been explored, but their precision is limited due to low sampling rates and noisy GPS signals (Park et al., 2018). Commercial sensors like the Corrsys Datron Correvit sensor can measure the slip angle but are costly and limited in field friction tests (Caroux et al., 2007). Camera-based solutions with advanced image processing algorithms have recently been introduced for measuring sideslip angles in vehicle dynamics tasks, offering cost and time efficiency (Botha & Els, 2014; Fuchs et al., 2015). However, to date, no system has proven compatible with a LWST in field applications, where both the vehicle articulation angle and the test wheel sideslip angle need to be simultaneously measured and assessed to correct tire-road friction measurements.

1.3 Main Tasks

The following tasks were accomplished in this study.

1. *Synthesis of Literature:* A comprehensive review of existing literature was conducted, encompassing research related to pavement friction. This included investigations into the frictional properties of aggregates, pavement marking materials, vehicle dynamics, friction testing methodologies and equipment, colored pavements, and friction measurement techniques on roadway horizontal curves.
2. *Laboratory Evaluation of the Friction Performance of Pavement Markings:* The frictional characteristics of four specific pavement marking materials—waterborne paint, liquid epoxy, liquid polyurea, and preformed tape—were systematically examined through rigorous laboratory experiments and subsequent data analysis. Various proportions of glass beads and ceramic particles were introduced into these materials to assess their impact on skid resistance. Multiple devices, including the BPT, laser texture scanner (LTS) (Ames Engineering, n.d.), CTM, and DFT, were employed to measure surface texture features and friction coefficients. Additionally, a TWPD was used to estimate possible wear and tear caused by traffic (INDOT, 2018).
3. *Field Evaluation of the Friction Performance of Pavement Markings:* To understand the effect of traffic on pavement markings, a section of an interstate highway was recorded via video. This footage was used to evaluate the frequency of vehicle tires crossing over and traveling on longitudinal pavement markings. The texture features of recently installed pavement markings on a street section were assessed by measuring friction and texture with BPT. LTS was used to measure macrotexture Mean Profile Depth (MPD) values of an aged sidewalk marking. The data collected through both laboratory and field assessments were analyzed to gauge the frictional impact of pavement marking materials.
4. *Laboratory Evaluation of Aggregate Frictional Properties:* The study encompassed an extensive evaluation of aggregates commonly used in Indiana. This evaluation covered various physical, chemical, and mechanical properties of these aggregates. Physical properties include BSG, WA, and soundness, while chemical properties encompass elements Al_2O_3, SiO_2, Fe_2O_3, TiO_2, CaO, and MgO. The mechanical properties of these aggregates were assessed using tests including LAA, MDA, and PSV. Mohs hardness values of the aggregates were also determined. All these laboratory measurements were analyzed in the context of their impact on pavement friction.
5. *Field Evaluation of Color Surface Treatment (CST) Friction:* The study emphasized the crucial role of CST in enhancing road safety, particularly for buses and bicycles. The frictional characteristics of CST pavements were evaluated through tests including LTS, BPT, and LWST on selected red bus lanes and green bike lanes in the Indianapolis area. Measures were taken to assess CST conditions based on the obtained measurements and observations.
6. *Mechanistic Investigation of Tire-Pavement Interaction at Horizontal Curves:* The research involved a deep dive into the mechanistic relationships between vehicle operating parameters and force properties at the tire-road interface, with a focus on articulated vehicles and tire cornering scenarios on horizontal curves. An innovative setup, employing dual cameras, was proposed to measure slip angles and articulation angles for a LWST during friction tests. This approach utilized image processing algorithms for real-time measurement of tire speed, tire sideslip angle, and vehicle articulation angle with high accuracy. These measurements allowed for monitoring the directional behavior of the LWST on straight pavements and horizontal curves during friction tests. The data collected was analyzed in terms of test speed levels and pavement geometric properties to examine the variation in variable measurements. Relationships and equations derived from the mechanistic investigation were validated and analyzed. The upgraded tester operated not only as a vehicle side friction sensor but also as an oversteering alert system. The study also assessed the impact of pavement horizontal alignment on LWST friction measurements.

7. *Tire Friction Modeling with Finite Element Analysis (FEA) and Machine Learning:* The study delved into tire friction modeling using both FEA and machine learning techniques. The FEA model was employed to investigate friction forces on tires under various scenarios, considering factors such as road type, vehicle speed, coefficient of friction, slip angle, and road inclination. Machine learning algorithms, in conjunction with theoretical equations of vehicle dynamics, were applied to analyze friction and guide the determination of appropriate friction values under different conditions.

2. CHAPTER 2. FRICTION PERFORMANCE OF COMMON PAVEMENT MARKINGS

2.1 Problem Statement

Pavement markings are required and extensively used for certain roadways for organizing traffic flow (FHWA, 2023). They enhance traffic safety by conveying messages, regulating traffic flow, and improving nighttime visibility, resulting in a 20% reduction in crashes for both drivers and pedestrians (Miller, 1993). However, these markings may cause concerns due to insufficient friction or skid-resistance under wet conditions, particularly affecting vulnerable road users such as motorcyclists, bicyclists, and pedestrians. The challenge has been intensified in recent years with the use of larger signage, wider 6″ to 8″ longitudinal lines, and the adoption of fully painted bicycle and bus lanes, which might further reduce the roadway's frictional properties (Anderson et al., 1982; Harlow, 2005). Consequently, assessing the friction performance of commonly used pavement markings is imperative to enhance safety for vulnerable road users.

Skidding-related crashes commonly manifest lower distributions of skid resistance values (Giles et al., 1965). Also, the differential skid resistance between pavement and pavement marking surfaces may also precipitate slippery events (Anderson et al., 1982; Anderson & Henry, 1980; Harlow, 2005; Pasetto & Barbati, 2011; Richard, 1975; Su et al., 2022), potentially compromising a driver's vehicular control and leading to severe outcomes. Currently, only the European standard EN 1436 (BSI, 2018) addresses the requirement of skid resistance for pavement markings. There is no standard procedure or practice in the United States for assessing and evaluating the friction properties of pavement markings. This lack of standards is particularly evident when focusing on vulnerable road users such as motorcyclists, bicyclists, and pedestrians, who are significantly affected by inadequate pavement marking friction.

Moreover, the existing methods for directly measuring friction performance are not optimal for in-situ pavement marking measurements. Predominantly, most on-site pavement markings are characteristically narrow, especially the longitudinal ones, posing challenges for rapid measurements using devices like DFT or LWST. While the BPT allows for in-field assessments, its need for pre-test calibration can cause traffic disruptions. Moreover, BPT is ill-suited for measuring the friction properties of polished specimens in a laboratory setting, primarily due to discrepancies between the polishing trajectory and the tester's measurement criteria.

The following are the objectives of the pavement marking evaluation.

- To evaluate the friction properties of various pavement marking materials commonly used by INDOT in laboratory and/or in-situ conditions, considering different thicknesses and the inclusion of diverse additives.
- To assess the practical testing methods for evaluating the friction performance of pavement markings based on their application scenarios and geometric features.
- To pioneer friction level rating for pavement markings to enhance the safety of all road users, including motorcyclists, bicyclists, and pedestrians.
- To establish conversion matrix for evaluating dynamic friction values of pavement markings using the macrotexture metric.

Specifically, various test devices, including BPT, DFT, LTS, and CTM, were employed to characterize the skid resistance properties of six types of pavement marking materials, namely waterborne paint, preformed tape, epoxy paint, polyurea paint, methyl methacrylate (MMA) paint, and thermoplastic. A three-wheel polishing device (TWPD) (INDOT, 2012) was also utilized to replicate the wear and tear of traffic experienced by marking materials on pavement surfaces. Table 2.1 illustrates the pavement marking applications utilized by INDOT. Pavement markings can be divided into two primary categories based on their durability, including durable marking materials such as thermoplastic, multi-component, and preformed plastic tape, and non-durable marking materials such as waterborne paint. Moreover, these different materials may manifest distinct anti-skid characteristics.

2.2 Laboratory Experiment

2.2.1 Materials

2.2.1.1 Waterborne paint. Waterborne paint, characterized by its low volatile organic compound (VOC) content, is a single component marking material, and widely used in the United States due to its low cost (Babić et al., 2015), suitability for both asphalt and concrete surfaces (Jiang, 2008), ease of use, and environmentally friendly properties. However, waterborne paint has been frequently cited for its compromised durability, particularly under conditions of elevated traffic intensity and rigorous winter maintenance practices. Typically, waterborne paints exhibit a lifespan of 9 to 36 months before showing symptoms of color degradation or attrition (Rodin et al., 2018). Consequently, their application may not be ideal for roadways subjected to intense vehicular traffic (Gates et al., 2003; Jiang, 2008). According to the

TABLE 2.1
Recommended Pavement Marking Application (INDOT, 2013/2022)

Application	Material Type			
	Paint	Thermoplastic	Multi-Component	Preformed Plastic
AADT and Pavement Surface Life	**<3,000 or <4 Years**	**≥3,000 and ≥4 Years**	**≥3,000 and ≥4 Years**	**≥18,000 and ≥8 Years**
Edge Lines	×	×	×	×
Center Lines	×	×	×	×
Lane Lines	×	×	×	×
Transverse Markings	×	×	–	–
Concrete Pavement	×	–	×	×
Asphalt Pavement	×	×	×	×
Pedestrian Crossings	–	×	–	–
Bike Lanes	–	×	–	–

standard specification of INDOT (2022), either Type 1 or Type 2 (i.e., modified standard glass beads) (AASHTO, 2018) is required when using waterborne paint to improve the retro-reflectivity, and the minimum thickness shall be 15 mils (0.381 mm) and is being proposed to be 20 mils for in-house restriping work.

2.2.1.2 Epoxy. Epoxy is a two-component pavement marking material that includes a pigmented resin base consisting of resin, pigment, extenders, and fillers, and a catalyst that accelerates the setting time (Jiang, 2008). During the application process, the pigmented resin base and the catalyst are typically mixed in either a 1:1 or 2:1 ratio by volume. This combination commonly initiates an "exothermic reaction," where heat is emitted during the curing process. Epoxy can be applied to concrete as well as asphalt surfaces and produces a more resilient and durable pavement marking. Notably, epoxy pavement markings have been observed to last over 4 years on roads with low to medium traffic volumes (Rodin et al., 2018), a durability that owes much to the robust bond between epoxy and glass beads (Babić et al., 2015). Nonetheless, epoxy pavement markings are susceptible to yellowing or fading when subjected to extended ultraviolet radiation exposure. As per the INDOT standard specification, the requisite minimum wet film thickness for epoxy pavement marking is set at 20 mils (0.508 mm) (INDOT, 2022). Furthermore, the inclusion of specific glass beads is essential to augment the retro-reflectivity of pavement marking surfaces according to the application scenarios.

2.2.1.3 Polyurea. Polyurea is also a two-component pavement material. The first component is a resin mixture containing pigments and fillers, and the second is a catalyst (Jiang, 2008). Polyurea results from a chemical reaction between its two components, typically mixed at a 2:1 ratio by volume. During the reaction, the "polyaddition reaction" forms a high cross-linked polymer network by breaking existing chemical bonds and creating new ones. Contrary to exothermic reactions, this process is endothermic, necessitating energy input. The reaction is rapid, solidifying in mere seconds, resulting in a material highly resistant to abrasion, chemicals, and ultraviolet radiation. Polyurea typically has a service life extending up to 5 years, surpassing the longevity of epoxies (Robin et al., 2018). Notably, it demonstrates resilience to moisture and retains applicability even in sub-freezing temperatures. INDOT stipulates that projects completed between November 15 and March 15 of the following year may use polyurea pavement marking materials (INDOT, 2022). The major drawback of the material was the requirement for special striping apparatus for its application (Gates et al., 2003; Rodin et al., 2018). The minimum wet film thickness of polyurea pavement marking should be 20 mils (0.508 mm) (INDOT, 2022). Also, glass beads must be applied immediately after the installation of polyurea.

2.2.1.4 Preformed tape. Preformed tapes come in continuous rolls, embedding glass beads or other particles to enhance both reflectivity. The initial retro-reflectivity values of these particles are estimated to be four to six times higher than those of waterborne paints (Jiang, 2008). Typically, these tapes are produced in a variety of thicknesses, widths, and lengths, allowing for selection based on specific application scenarios. According to the standard specification of INDOT (2022), preformed tapes should have an embossed surface area ranging from 35% to 65% with a minimum thickness of 60 mils (1.524 mm) for the elevated sections, and 20 mils (0.508 mm) for the interstitial spaces between the elevated areas. Preformed tapes, especially permanent preformed tapes, are suitable for application on both asphalt and concrete pavements without the need for additional equipment. It is advisable to reopen roadways promptly after installing permanent preformed tapes. As traffic passes over the tapes, the impact from the vehicles enhances the adhesion between the tape and the pavement surface (Rodin et al., 2018). When properly installed, the service life of preformed tapes can extend from 4 to 8 years, surpassing the durability of other pavement marking materials (Babić et al., 2015; Jiang, 2008).

2.2.1.5 Methyl methacrylate. Methyl methacrylate (MMA) is utilized in a two-component pavement marking system, comprising an MMA resin and an associated catalyst, which can be either liquid or powder form (Jiang, 2008). Various mix ratios exist for these components, typically 4:1 or 1:1 by volume, and 98:2 by weight. To enhance its skid-resistant capabilities, aggregates may be integrated into the mixture. Recent research indicates MMA's anti-skid performance surpasses that of both thermoplastic and waterborne paint (Kassem, 2021). When MMA interacts with pavement surfaces, it forms a bond through exothermic reactions. The resultant heat from these reactions aids in the curing process, ensuring a robust bond with the pavement. Therefore, MMA is recognized for its durability as a pavement marking material, frequently lasting beyond 3 years (Rodin et al., 2018), and finds utility in a variety of applications, including extended segments of bicycle lanes and dedicated bus corridors. To achieve the best outcomes, the application of MMA should be conducted solely in environmental conditions marked by the absence of moisture, specifically under arid weather conditions on pavements devoid of moisture (Gates et al., 2003; Jiang, 2008). MMA materials are typically applied at thicknesses of 20–40 mils (sprayed) or over 60 mils (extruded) (Jesse Salazar, personal communication, August 17, 2022).

2.2.1.6 Thermoplastic. Thermoplastic pavement marking materials, comprising a blend of resin, fillers, pigments, and glass beads (Jiang, 2008), are engineered to provide essential retro-reflectivity vital for road applications. Capable of enduring temperatures up to 200 degrees Celsius (Babić et al., 2015), these materials demonstrate adaptability to various weather conditions, although requiring dry application settings. Uniquely, they can be superimposed over existing thermoplastic markings, providing cost efficiency by obviating the need for removal of old markings (Jiang, 2008). Regarding longevity, thermoplastic markings typically last between 3 and 6 years and exhibit resistance to damage from snowplows due to their integration into the pavement via melting (Rodin et al., 2018). However, their application is restricted to asphalt pavement surfaces. The minimum thickness of each 36-inch segment of thermoplastic pavement marking should range from 90 mils (2.286 mm) to 125 mils (3.175 mm) (INDOT, 2022). To augment their retro-reflectivity, the incorporation of glass beads is imperative. This study utilizes preformed thermoplastics with thicknesses adhering to the specified standards.

2.2.1.7 Glass beads and ceramic particles. Particle additives are instrumental in improving primarily the retro-reflectivity of pavement marking surfaces. Typically, these small spherical glass beads are applied by dropping or spraying onto liquid pavement marking materials. The AASHTO M247 specification categorizes glass beads into six types based on varying gradations (AASHTO, 2018). The ceramic particles, available in both yellow and white, consist of microcrystalline ceramic beads partially embedded in composite cores. Ceramic particles are commonly applied to markings with a minimum thickness of 25 mils (0.635 mm) and before applying the glass beads (3M, n.d., 2020).

This study evaluated Types 1, 2 and 4 beads, and ceramic particles for liquid pavement marking materials. For preformed tape, the manufacturers embed microcrystalline ceramic beads (3M, 2022), while in thermoplastics, Types 1 and 3 glass beads, and microcrystalline ceramic beads are all dropped during production (3M, 2020). Figure 2.1 depicts the three types of glass beads and yellow ceramic particles. Figure 2.2 illustrates the surfaces of preformed tape and thermoplastics with additives. Table 2.2 presents the gradations of glass beads and ceramic particles, with the sizes arranged in ascending order: Types 1, 2, 3 and 4 glass beads, ceramic particles, and microcrystalline ceramic beads. Note that the Type 3 glass beads are typically manufactured using virgin glass for higher index of refraction. Therefore, they are more expensive and commonly used for airport runways for enhanced night visibility. Note that INDOT is moving towards the use of Type 3 beads exclusively for our in-house restriping program and may make the same change to construction projects. Both Type 4 beads and ceramic particles have the same maximum size, but the latter are gap-graded. Similarly, Types 1 and 2, as well as microcrystalline ceramic beads, share the same maximum size. In addition, microcrystalline ceramic beads are more gap-graded.

2.2.2 Experiment Devices

2.2.2.1 Devices for measuring surface texture. Figure 2.3 shows photos of two devices, including laser texture scanner (LTS) and circular track meter (CTM), for measuring surface texture depth in this study. This LTS has a sampling frequency of 1 kHz, providing a low scanning speed of approximately 15 mm/sec. It meets the requirements specified in ASTM E1845 (2015a), with a laser spot size, vertical resolution, and sampling spacing of 0.05 mm, 0.015 mm, and 0.015 mm, respectively (Li et al., 2010). The scanner has a wavelength range of 0.03 mm to 50 mm, allowing it to capture the information of macrotexture and part of microtexture with a scanning area of 76.2 mm × 101.6 mm.

The CTM is equipped with a charge couple device (CCD) laser-displacement sensor which measures vertical macrotexture depth without considering the concave recesses in the pavement surface (ASTM, 2019b). The sensor is installed on an arm that rotates at a tangential velocity of 6 m/min in a counterclockwise direction with a diameter of 284 mm at 80 mm above the measuring surface. In addition, a CTM is commonly used in conjunction with a TWPD to measure macrotexture profiles.

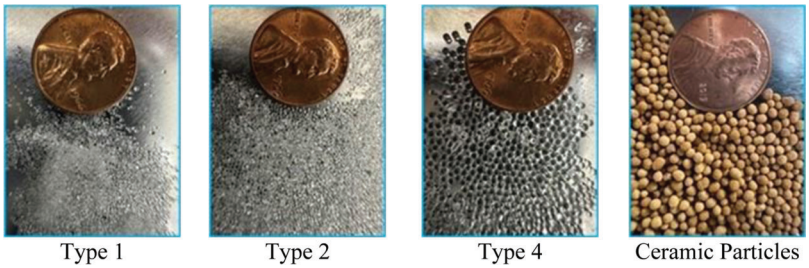

Figure 2.1 Glass beads and ceramic particles.

Figure 2.2 Surfaces of preformed tape (left) and thermoplastic materials (right).

TABLE 2.2
Gradation of Glass Beads and Ceramic Particles

Sieve Size		Mass Percent Passing					
Standard (mm)	**Sieve No.**	**Type 1**	**Type 2**	**Type 3**	**Type 4**	**Ceramic Particles**	**Microcrystalline Ceramic Beads**
2.00	10	–	–	–	100	95–100	–
1.70	12	–	–	100	95–100	–	–
1.40	14	–	–	95–100	80–95	0–40	–
1.18	16	100	100	80–95	10–40	–	–
1.00	18	–	–	10–40	0–5	–	65–80
0.850	20	95–100	90–100	0–5	0–2	0–5	–
0.600	30	75–95	50–75	0–2	–	–	0–30
0.425	40	–	15–45	–	–	–	–
0.300	50	15–35	0–15	–	–	–	0–5
0.180	80	–	0–5	–	–	–	–
0.150	100	0–5	–	–	–	–	–

2.2.2.2 Devices for measuring surface friction. Figure 2.4 shows the photos of two devices, including British pendulum tester (BPT) (AASHTO, 2021) and dynamic friction tester (DFT) (ASTM, 2015b), for measuring pavement surface friction inn this study. The BPT is a dynamic, pendulum impact-type tester, consisting of a free-swinging pendulum arm with a rubber slider attached at the bottom. Rubber sliders are available in two sizes: large–dimensions of $3.0 \times 1.0 \times 0.24$ in. ($76 \times 25.4 \times 6.35$ mm) for field testing; and small–dimensions of $1.25 \times 1.0 \times 0.24$ in. ($31.75 \times 25.4 \times 6.35$ mm) for laboratory testing. The BPT quantified friction by assessing the energy loss when the rubber slider edge moves across the tested surface. The typical slip speed for the BPT is usually assumed to be about 6 mph (10 km/h) (Henry, 2000). The BPT measurements are denoted as British Pendulum Number (BPN). Some studies acknowledge that the BPN values are essentially equivalent to the friction coefficient multiplied by 100, while others suggest slight variations between the two values (Giles et al., 1965; Richard, 1975).

The Dynamic Friction Tester (DFT) is specifically designed to measure the coefficient of dynamic friction (DF). It is equipped with a horizontal spinning disk featuring three spring-loaded rubber sliders that are in contact with the measuring surface. During testing, water is supplied through a water supply unit, and the rotating disk makes the three spring-loaded rubber sliders contact the surface, with each rubber slider applying a load of 1.2 kg (2.65 lbs). In this study, the friction coefficients were measured and recorded at speeds of 0, 12, 19, 25 and 37 mph (0, 20, 30, 40 and 60 km/h).

2.2.2.3 Three-wheel polishing device. Figure 2.5 shows the photo of a three-wheel polishing device (TWPD) employed in this study. The TWPD was used to condition the surface of test specimen by rotating three

Figure 2.3 Texture measuring devices (left: LTS; right: CTM).

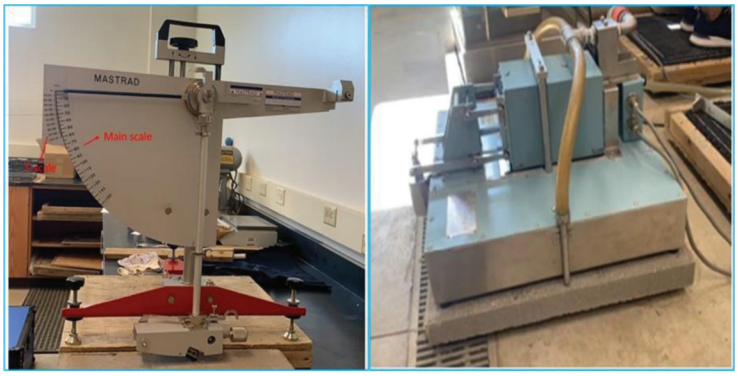

Figure 2.4 Friction measuring devices (left: BPT; right: DFT).

Figure 2.5 Three-wheel polishing device.

polishing wheels to simulate the tear and wear of vehicular traffic. This TWPD comprises a rotating plate with three rubber tires in contact with the polishing surface, exerting a total load of 217 lbm. (approximately 98.5 kg) and rotating at a rate of 47 revolutions per minute (INDOT, 2018). Water is sprayed on the surface of the slab during the polishing process to remove debris. The polishing intervals vary depending on the material being tested. In this study, the endpoint of a polishing process was reached when the surface materials were worn away and peeled off or attained 100,000 polishing cycles.

2.3 Testing

2.3.1 Specimen Preparation

The concrete and asphalt slabs of $20 \times 20 \times 2$ in. ($50.8 \times 50.8 \times 8.89$ cm) were used as substrates for the test specimens. Asphalt slabs served exclusively as the application surface for thermoplastic. In the preparation of specimens, excluding thermoplastics, the surfaces of these slabs were scrubbed clean of dust and debris before applying marking materials. For liquid paint, a controlled volume of paint was applied to the concrete slabs using a paint roller to make it as close as possible to the desired thickness. Ceramic particles and glass beads were dropped onto the wet paint immediately following the liquid paint application. Figure 2.6 illustrates the preparation process of the specimens of liquid marking materials.

In the preparation of thermoplastic marking specimens, asphalt slabs were initially compacted to attain a

Figure 2.6 Liquid pavement marking specimen preparation.

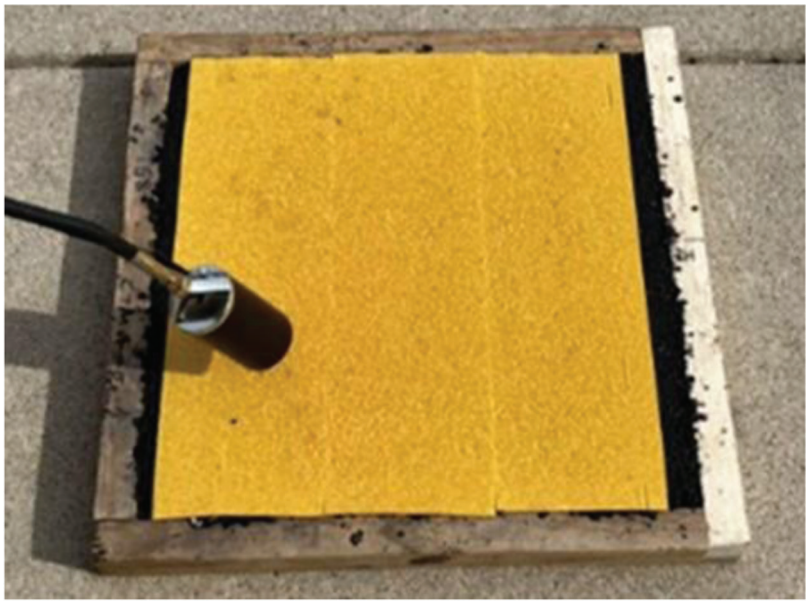

Figure 2.7 Thermoplastic specimen preparation.

void rate of 7.5%. Prior to thermoplastic application, the slabs underwent a heating process using a propane torch to eradicate any surface moisture. Thereafter, thermoplastic materials were placed on the slabs and subjected to additional heating with the propane torch, a methodology depicted in Figure 2.7.

As presented in Table 2.3, eighteen sets of specimens were prepared. Each set is comprised of two specimens, except for Group 1 and Group 10. These two groups contain four specimens each, owing to the use of both white and yellow pavement marking materials. The liquid paint thicknesses and application rates of beads and particles for the specimens were determined based on the INDOT standard specifications (INDOT, 2022), the 3M product manual (3M, 2022), and the Federal Highway Administration (FHWA) report (Carlson et al., 2013). Note that the thickness of each marking specimen was decided based on either the INDOT's specification or the vendor's recommendation.

2.3.2 Measurements

Three experiments were used to evaluate the surface friction and texture characteristics of the markings in both controlled laboratory settings and real-world field scenarios as follows.

- *Experiment 1:* The BPN values of the prepared specimens under both dry (Mastrad, 2001) and wet conditions (AASHTO, 2021) were measured before conducting the polishing tests. The LTS was performed to determine the initial macrotexture and the microtexture in the wavelength range of 0.03 mm~50 mm (Li et al., 2016) characteristics of the various pavement marking materials in detail. The macrotexture MPD and dynamic friction of the prepared specimens were also obtained using the CTM and DFT devices, respectively.
- *Experiment 2:* The prepared pavement marking specimens were subjected to polishing using the TWPD. The polishing process was deemed complete when the pavement marking materials exhibited noticeable wear. After each polishing interval, the macrotexture, characterized by the MPD and dynamic friction (DF) were determined using the CTM and DFT, respectively.
- *Experiment 3:* A 1-hour video was captured on I-65 southbound in West Lafayette to identify the frequency at which vehicles crossed and/or drove directly over the longitudinal pavement markings. In addition, the surface texture characteristics of both newly installed and aged pavement markings were measured on a street in West

TABLE 2.3
Prepared Marking Specimens for Testing

Product Group ID	Marking Material	Type of Bead/Particle	Bead and Particle Application Rate	Desired Thickness	No. of Specimens
1	Waterborne	Type 1	6 lbs./gal	15 mils	4
2	Waterborne	Type 2	6 lbs./gal	15 mils	2
3	Waterborne	Type 1	6 lbs./gal	20 mils	2
4	Waterborne	Type 1	6 lbs./gal	25 mils	2
5	Waterborne	Type 1	20 lbs./gal	20 mils	2
6	Waterborne	Type 1 and Ceramic Particle	12 lbs./100 ft^2 (Type 1) and 5 lbs./100 ft^2 (Ceramic Particle)	25 mils	2
7	Waterborne	Type 2 and Ceramic Particle	12 lbs./100 ft^2 (Type 2) and 5 lbs./100 ft^2 (Ceramic Particle)	25 mils	2
8	Waterborne	Type 4	6 lbs./gal	25 mils	2
9	Waterborne	Type 4 and Ceramic Particle	12 lbs./100 ft^2 (Type 4) and 5 lbs./100 ft^2 (Ceramic Particle)	25 mils	2
10	Preformed Tape	Microcrystalline Ceramic	–	120 mils	4
11	Epoxy	Type 1	20 lbs./gal	20 mils	2
12	Epoxy	Type 1 and Type 4	6 lbs./100 ft^2 (Type 1) and 10 lbs./100 ft^2 (Type 4)	20 mils	2
13	Polyurea	Type 1 and Type 4	6 lbs./100 ft^2 (Type 1) and 10 lbs./100 ft^2 (Type 4)	20 mils	2
14	Polyurea	Type 1 and Ceramic Particle	10 lbs./100 ft^2 (Type 1) and 8 lbs./100 ft^2 (Ceramic Particle)	25 mils	2
15	Polyurea	Type 1	20 lbs./gal	20 mils	2
16	MMA	Type 1 and Corundum	8 lbs./100 ft^2 (Type 1) and 5 lbs./gal (Corundum Aggregate)	95 mils	2
17	125 mils Thermoplastic	Type 1, Type 3 and Microcrystalline Ceramic	–	125 mils	2
18	90 mils Thermoplastic	Type 1, Type 3 and Microcrystalline Ceramic	–	90 mils	2

Lafayette, Indiana. The BPN values of newly applied markings, as well as those exposed to traffic applications for 4 and 8 weeks, were systematically documented. This was done to assess the correlation among the surface friction metrics such as MPD, BPN, and DF in the real world.

2.3.2.1 International friction index. The International Friction Index (IFI) offers a harmonized approach to articulating friction measurements by integrating the effects of MPD on friction. This methodology necessitates the amalgamation of MPD and DF to derive the IFI. Central to the IFI are two pivotal parameters: the standardized wet friction measured at 60 km/h (F_{60}) and the speed constant pertinent to wet pavement friction (S_p), as delineated by ASTM (2019a). In alignment with ASTM E1960 (2015b), the computations for S_p and F_{60} are prescribed as follows.

$$S_p = 14.2 + 89.7\,MPD \qquad \text{(Eq. 2.1)}$$

$$F_{60} = 0.081 + 0.732DF\,\exp\left(-\frac{DF40}{S_p}\right) \qquad \text{(Eq. 2.2)}$$

where DF40 denotes the DF measured at 40 km/h, and other variables are as defined earlier.

2.3.2.2 Texture characteristics. Texture characteristics usually have been conventionally defined by parameters MPD and the corresponding root mean square (RMS) and/or slope variance (SV) (Li et al., 2010). The SV quantifies the sharpness of pavement surface asperities (Li et al., 2010; Schmidt, 2000). The calculation of slope variance for each 100 mm segment is as follows.

$$SV_k = \frac{z_{j+1} - z_j}{y_{j+1} - y_j} = \frac{\Delta z_j}{\Delta y_j} \qquad \text{(Eq. 2.3)}$$

where k = 0, 1, 2, …, N-1; y_j = the j-th spaced points that divide the 100-mm segment into n equal parts; z_j = corresponding macrotexture profile values associated with y_j. The final SV can be generated by calculating the root mean square of all SV_k values as follows.

$$SV = \sqrt{\frac{\sum {SV_k}^2}{k}} \qquad \text{(Eq. 2.4)}$$

2.4 Results and Analysis

2.4.1 Surface Friction Characteristics Before Polishing

Surface friction metrics, including BPN, MPD, and DF40, were first measured for the specimens listed in

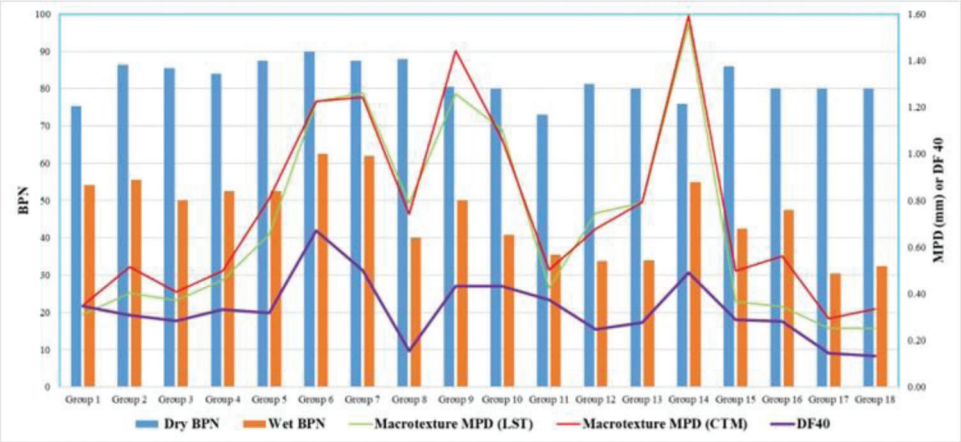

Figure 2.8 BPN and MPD measurements of markings before polishing.

Table 2.3 before the polishing (i.e., new markings) took place. These metrics were measured under dry and wet conditions, respectively, as shown in Figure 2.8. The macrotexture MPDs were measured by both LTS and CTM, and the results were very close. Careful inspection of both Figure 2.8 and Table 2.3 yielded the following observations.

- BPN values under dry conditions are notably higher than those under wet conditions, with an increase ranging from 28% to 62%. On average, the BPN values under dry conditions are 44% higher than those under wet conditions.
- Waterborne markings (except for Group 8) show higher wet BPN values compared to other non-waterborne markings when the same types of beads, application rates, and thicknesses were applied. On average, the wet BPN for waterborne markings is 27% greater than for other markings.
- The larger the bead size, the higher the MPD, regardless of the type of bead material. However, a larger bead size does not necessarily increase friction, such as BPN or DF (see Groups 1 and 2, Groups 4 and 8, Groups 6 and 7, Groups 7 and 9, Groups 11 and 12, and Groups 13 and 15), particularly for waterborne markings and in wet conditions. When larger beads are used, the surfaces of the exposed large glass beads may come into contact with the rubber sliders. This may involve the possible effect of the microtexture of the glass bead surface, which cannot be readily measured at present.
- A higher bead application rate leads to increased MPD. In the case of waterborne markings (refer to Groups 3 and 5), a higher bead application rate may also result in higher friction. However, this correlation is not conclusive for non-waterborne markings (possibly referring to Groups 13 and 14).
- For identical marking materials and a consistent bead application rate, the MPD increases with the thickness of the marking. However, increasing marking thickness yields mixed results of BPN and DF40 (see Groups 1, 3 and 4, and Groups 17 and 18).
- Adding ceramic particles tends to increase both MPD and friction significantly, especially under wet conditions (see Groups 6, 7, 9, and 14).

2.4.2 Surface Friction Characteristics After Polishing

2.4.2.1 Waterborne paints. The marking specimens were polished using the TWPD in accordance with the test method of ITM No. 221 (INDOT, 2018). The polishing conditioning was terminated after applying 100,000 cycles as specified in the above test method or when the surface of specimen exhibited visible distresses such as tearing and/or wearing, whichever occurred first. Figure 2.9 shows the closeups of the waterborne (Groups 3, 4, and 8) specimen surfaces before and after (at termination polishing conditioning. It is demonstrated that the polishing conditioning may induce wear, tear, loss of beads, and removal of binder. Ultimately, this process may lead to a change in the surface friction characteristics of the marking specimen.

Figure 2.10 presents the numbers of polishing cycles at termination, indicating durability for all waterborne marking specimens. The following observations can be made through careful inspection of Figure 2.10 and Table 2.3.

- Most waterborne markings can withstand no more than 1,500 polishing cycles. Groups 4 and 5, featuring Type 1 beads and a thickness of 20 mils or more, exhibit better durability, i.e., up to 5,000 polishing cycles.
- Increasing the thickness of the waterborne markings may increase the number of terminal polishing cycles (i.e., durability), possibly referring to Groups 1 and 4.
- A higher bead application rate may yield a larger number of terminal polishing cycles (refer to Groups 3 and 5).
- The larger the size of the beads, the fewer the number of terminal polishing cycles (refer to Groups 4 and 8). One possible reason is that the polishing action may more easily dislodge and wear away individual larger glass beads than smaller beads. As shown by Group 8 specimens with Type 4 beads in Figure 2.9, although they are 25 mils (0.635 mm) thick, excessive loss of beads arises after 500 polishing cycles.
- Adding ceramic particles yields larger initial MPD and DF40 but may compromise the durability (refer to Groups 6, 7, and 9).

MPD and DF40 values were measured after different polishing cycles and at the termination of polishing, and

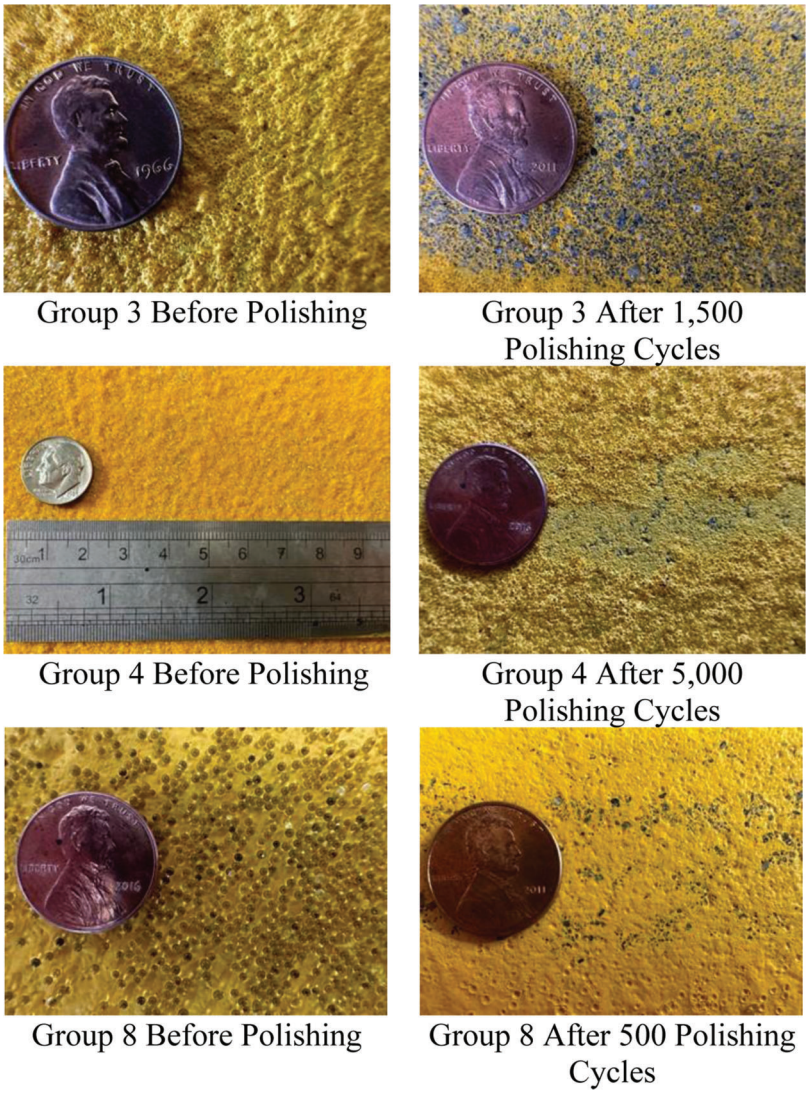

Figure 2.9 Photos of a waterborne marking specimen surface before and after polishing.

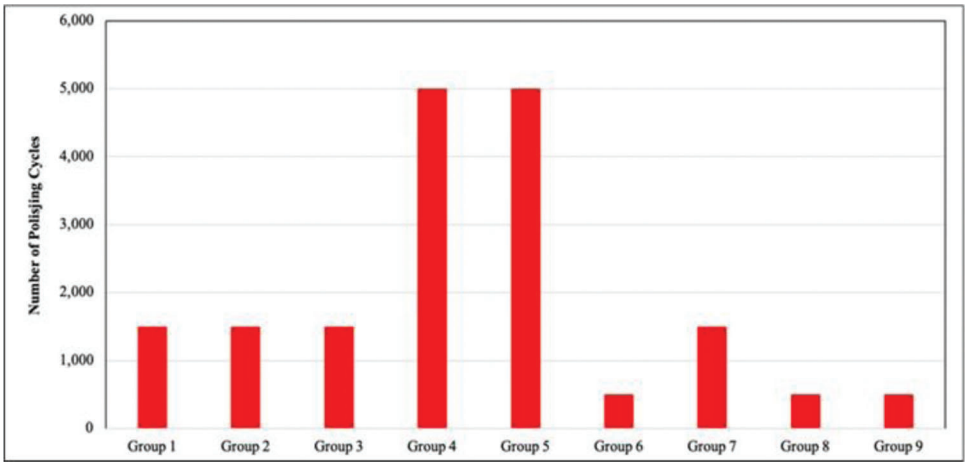

Figure 2.10 Numbers of terminal polishing cycles for waterborne marking specimens.

the results are presented in Figures 2.11. The following observations can be made in combination with Table 2.3.

- All curves exhibit a similar variation trend. During the initial 500 polishing cycles, both MPD and DF40 decrease dramatically. Subsequently, the decrease in both

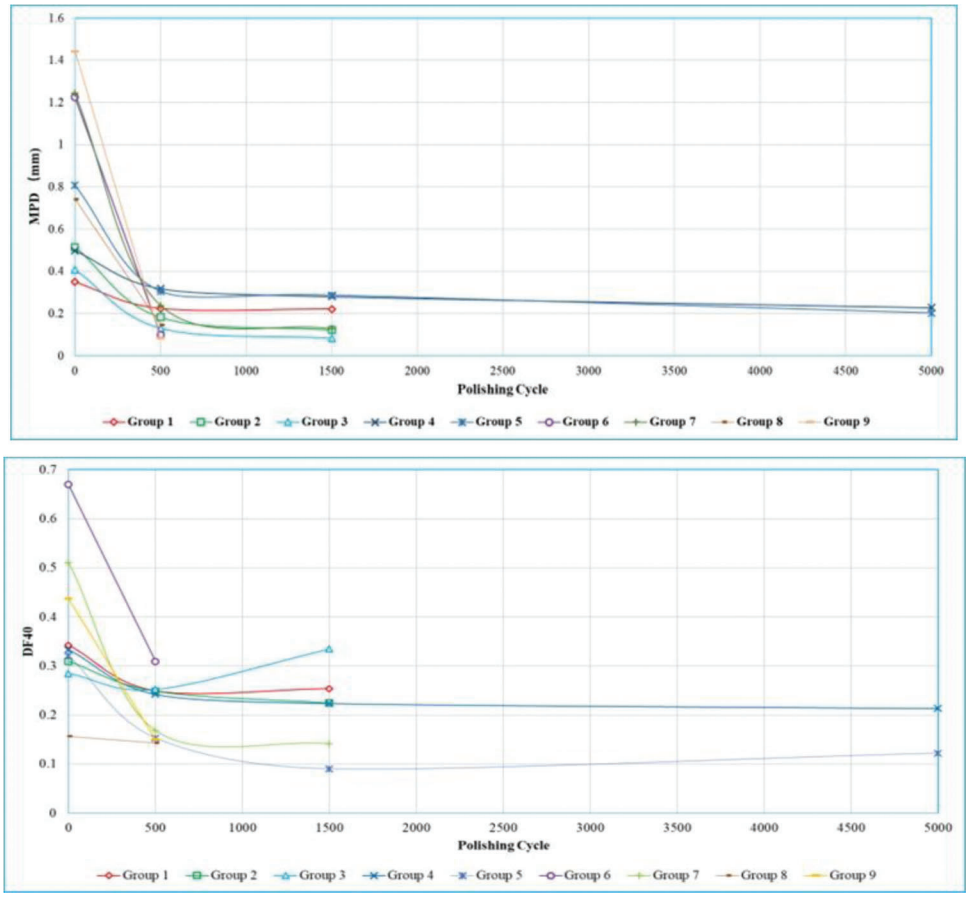

Figure 2.11 MPD and DF40 values of waterborne paints during polishing.

MPD and DF40 slows down significantly. This suggests that the waterborne markings may be completely worn away due to traffic applications.

- While specimens with larger beads tend to produce higher initial MPD values, their MPDs may decline faster than those of with smaller beads after polishing conditioning (refer to Groups 6, 7, and 9). Right after 500 polishing cycles, for example, the average MPD for specimens with small beads (Types 1 and 2) decreases from 0.52 mm to 0.23 mm, a 55% reduction, whereas from 1.16 mm to 0.15 mm for larger beads (Type 4 and ceramic particles), marking an 88% decrease. This aligns well with the visual appearance of the Group 8 specimen in Figure 2.9.
- Larger beads also tend to exhibit lower long-term friction compared to smaller beads (refer to Groups 4 and 8). After 500 polishing cycles, for example, Group 4 exhibits an MPD value of 0.32 mm and a DF40 value of 0.33, but Group 8 exhibits an MPD value of 0.15 mm and a DF40 value of 0.14. Again, the main reason is the potential effect of the loss of larger beads.
- Adding ceramic particles yields larger initial MPD and DF40 but may compromise the long-term friction (refer to Groups 4 and 6, and Groups 8 and 9).

The International Friction Index (IFI) allows for the harmonizing of friction measurements with different equipment to a common calibrated index (ASTM 2019a). Therefore, the International Friction Indices in terms of F60 were computed with MPD and DF40 values using Equations 2.1 and 2.2. The F60 values at different polishing cycles are shown in Figure 2.12. F60 values associated with larger beads decrease more rapidly than smaller beads. Markings with smaller beads demonstrate higher post-polishing F60 values. Increasing the thickness of marking leads to mixed results with F60 values. Increasing the application rate of bead yields greater initial F60 values, but there is no significant difference observed after 500 cycles of polishing.

2.4.2.2 Durability and friction performance of non-waterborne materials. As shown in Table 2.3, the non-waterborne materials evaluated in this study include preformed tape (Group 10), epoxy (Groups 11 and 12), polyurea (Groups 13, 14, and 15), MMA (Group 16), and thermoplastic (Groups 17 and 18). Figure 2.13 shows the surfaces of a 20-mil thick polyurea specimen with combined Type 1 and Type 4 glass beads (Group 13) before polishing, after 10,000 polishing cycles, and after 50,000 polishing cycles. It is evident that the characteristics of surface texture vary with polishing cycles, indicating the progressive loss of glass beads in the polishing process.

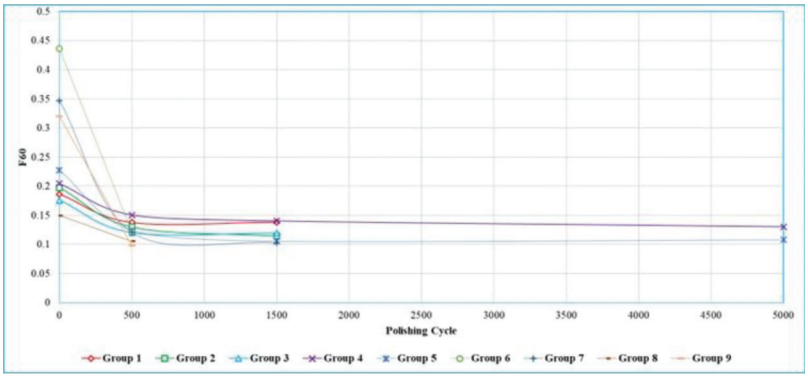

Figure 2.12 F60 values of waterborne paints.

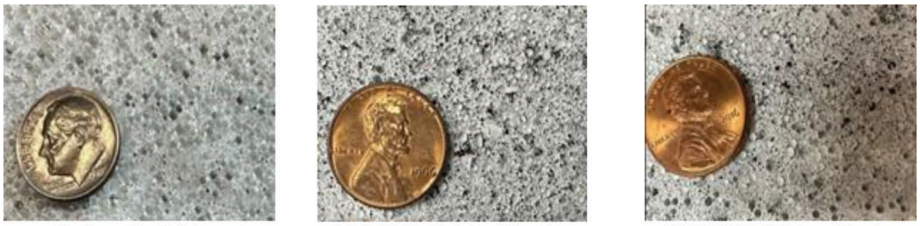

Figure 2.13 Polyurea specimen surface during polishing.

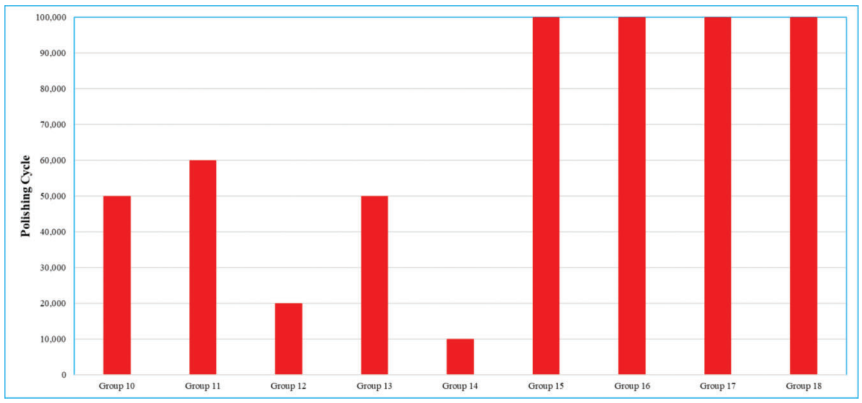

Figure 2.14 Numbers of terminal polishing cycles for non-waterborne materials.

Figure 2.14 presents the numbers of polishing cycles at termination (i.e., durability) of the non-waterborne materials. Careful inspection of Figure 2.14 yields the following observations.

- Non-waterborne markings can withstand 20,000 to 100,000 polishing cycles; a range much higher than the waterborne counterparts (see Figure 2.10). In particular, MMA and thermoplastic markings, which commonly come with greater thicknesses, exhibit the greatest durability. Polyurea markings exhibit greater durability than epoxy markings.
- Non-waterborne markings containing smaller beads exhibit much higher durability compared to those composed of the same binders and containing larger beads (refer to Groups 11 and 12, and Groups 13, 14 and 15). This agrees with the finding associated with waterborne markings, i.e., larger beads may more easily become lost from the specimen surface due to the tear and wear caused by polishing.
- Adding ceramic particles may result in lower durability, as seen in Group 14. This may be because the ceramic particles have a maximum size the same as Type 4.

Like the waterborne markings, MPD and DF40 values were also measured at different polishing cycles during the polishing process, and the results are plotted in Figure 2.15. The following observation are made through careful inspection of Figure 2.15.

- For all non-waterborne markings, the MPD values decrease with the number of polishing cycles, particularly in the initial polishing phase. Larger beads may contribute to a faster rate of decrease, as observed in Groups

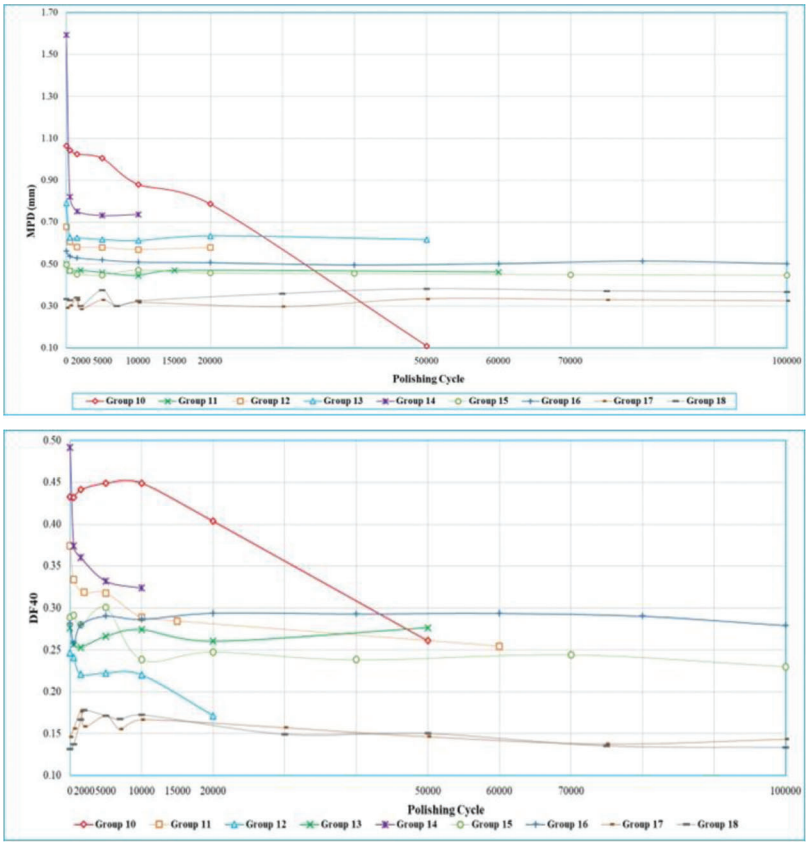

Figure 2.15 MPD and DF40 values of non-waterborne paints during polishing.

12, 13, and 14, which agrees with the trends seen in waterborne markings.

- The DF40 values demonstrate different variation trends, depending on the type of binder. For epoxy markings, DF40 values generally decrease with polishing. For other non-waterborne markings, except for the preformed tape, DF40 values may fluctuate during polishing, likely due to the bead loss process.
- For the preformed tape (refer to Group 10), both its MPD and DF40 decrease continuously and rapidly until the termination of polishing conditioning, i.e., the occurrence of marking failure. Meanwhile, the DF40 increases in the initial polishing phase. As shown in Figure 2.2, the preformed tape specimens have a profiled surface that can wear out rapidly under the action of polishing (see Figure 2.16).
- Polyurea, MMA, and thermoplastic markings demonstrate greater resistance to polishing than epoxy markings. For polyurea markings, however, the addition of large beads or ceramic particles tends to compromise the resistance to polishing.
- The thermoplastic markings exhibit the lowest friction, including both surface texture and friction (particularly DF40) before and after polishing (refer to Groups 17 and 18). This is because glass beads were intermixed into the binder material for the thermoplastic marking specimens, allowing the beads to be completely coated by the binder (see Figure 2.2). As polishing action progresses, the beads become exposed but not lost as the binder material is worn down by polishing (see Figure 2.17). Therefore, the surface of thermoplastic markings can maintain stable friction as the polishing action progresses.

Figure 2.17 presents the International Friction Indices in terms of F60 for the non-waterborne marking specimens. Overall, F60 values exhibit variation trends similar to the DF40 values (see Figure 2.15). Polyurea with Type 4 and ceramic beads (Group 14) exhibits the highest initial F60 followed by the preformed tape (Group 10); however, it decreases at a relatively greater pace compared to other materials. Except for Group 14, which consists of polyurea integrated with Type 4 and ceramic beads, the F60 values for the three multi-component pavement markings—epoxy, polyurea, and MMA—without ceramic beads exhibited similar frictional performance during the polishing process. The thermoplastic specimens (Group 17 and Group 18) demonstrated the lowest friction performance in terms of both initial F60 values both before and after polishing.

2.5 Expanded Data Interpretation

2.5.1 Statistical Correlations Between Texture and Friction Metrics

Challenges exist related to measuring the surface friction metrics of markings in both laboratory and

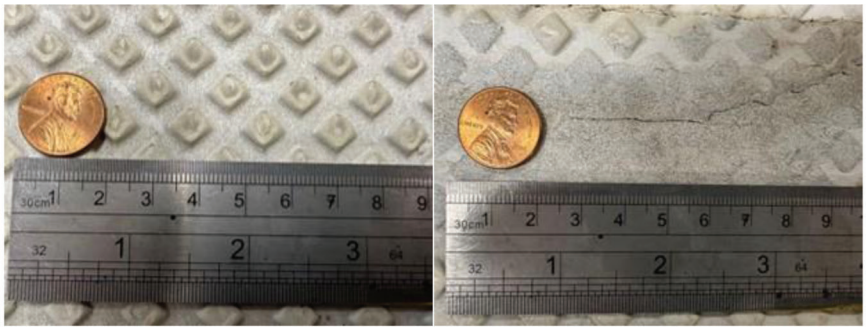

Group 10-preformed tape (left: before polishing; right: after 50,000 polishing cycles).

Group 16-Thermoplastic (left: before polishing; right: after 100,000 polishing cycles)

Figure 2.16 Closeups of pre-formed tape and thermoplastic specimen before and after polishing.

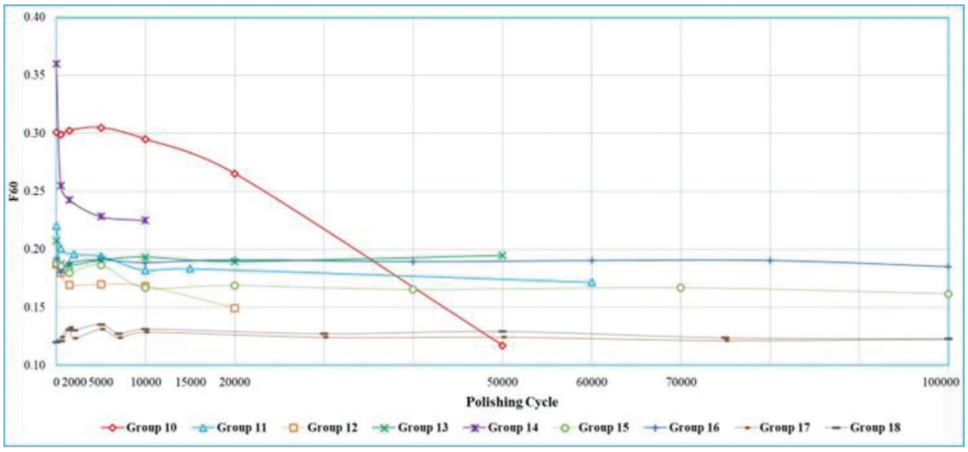

Figure 2.17 F60 values of non-waterborne paints.

field settings, especially when implementing the laboratory test results in field applications. In the laboratory setting, all experimental devices such as the British pendulum tester (BPT), laser texture scanner (LTS), circular track meter (CTM), and dynamic friction tester (DFT) are suitable for measuring texture or friction before polishing. After polishing, only CTM and DFT are suitable because the three-wheel polishing device (TWPD) is designed to complement these two experimental devices. In the field setting, however, the surface texture and friction of a marking may only be measured by BPT and LTS due to the dimensions of the marking. Hence, exploring the connections, patterns, and correlations between pairs of surface friction metrics, like BPN and DF40, MPD, and DF40, and others, and offering a more comprehensive interpretation of the test data through advanced analytical techniques and additional factors, are of immense importance. This is crucial for ensuring coherence between laboratory test results and real-world applications and for formulating practical specifications and requirements.

The Pearson correlation coefficients (Kutner et al., 2013) were utilized to assess the significance of a linear relationship between surface texture and friction metrics. The features of macrotexture profile used in the analysis, including MPD, slope variance (SV), and root mean square (RMS), were calculated based on the

data captured from the specimens using LTS before polishing, and are presented in Table 2.4. As a rule of thumb, the absolute values falling within the ranges (0, 0.2), (0.2, 0.4), (0.4, 0.6), (0.6, 0.8), and (0.8, 1.0) correspond to the correlation levels of very weak, weak, moderate, strong, and very strong, respectively.

The Pearson correlation coefficients in Table 2.4 reveal the degrees of correlations between various surface texture features and friction measurements as follows.

- MPD exhibits a moderate correlation with BPN (dry) or DF40, and a weak correlation with BPN (wet). This observation resonates with findings about the macrotexture on friction performance under wet and high-speed conditions (Alhasan et al., 2018; Kogbara et al., 2016; Li et al., 2010, 2016).
- RMS also exhibits a moderate correlation with DF40, and very weak correlation with BPN (dry) or BPN (wet). SV exhibits a weak correlation with BPN (dry) or DF40, and a weak correlation with BP (wet).
- In addition to macrotexture features, additional factors should be considered to fully define the correlation between texture and friction.

TABLE 2.4
Pearson Correlation Coefficients

Macrotexture Characteristics	BPN (Dry)	BPN (Wet)	DF40
MPD of Macrotexture	0.44	0.25	0.60
SV of Macrotexture	0.07	-0.27	0.14
RMS of Macrotexture	-0.02	0.06	0.48

2.5.2 Pavement Marking Friction Performance

2.5.2.1 Assessment of friction levels. The fuzzy C-means algorithm (Tan et al., 2006) was used to delineate friction thresholds predicted on BPN and DF40 metrics. By fine-tuning the model using the Silhouette score, the optimum cluster number was identified as three with a weight of 1.5, including (30, 40.0), (40, 55), and (55, 65) (see Figure 2.18). Due to the limited number of data points, the bootstrap sampling method (Johnson, 2001) was employed to generate 1,000 replications for each of the three clusters based on the actual data points within each cluster. Consequently, the three clusters above were adjusted to (32.3, 36.9), (46.3, 52.4), and (55.0, 62.5) with 95% confidence intervals.

Note that there are gaps between the three adjusted clusters. Also, in the real world, the BPN of markings may be less than 32.3 or greater than 62.5. Furthermore, inherent variations in the BPN measurements arise from system errors and the influence of surface attributes. As shown in Appendix A, the standard deviation ranges from 0 to 7.1, depending on the type of marking materials. Dravitzki et al. (1997) also confirmed wide margins of repeatability and reproducibility in measurements when using BPT on road pavement surfaces, with standard deviations ranging from 2.0 to 5.0. Therefore, the research team recommends the five friction levels for pavement markings in terms of BPN, as shown in Table 2.5. The boundaries are rounded to the nearest 5, representing the possible greatest standard deviation.

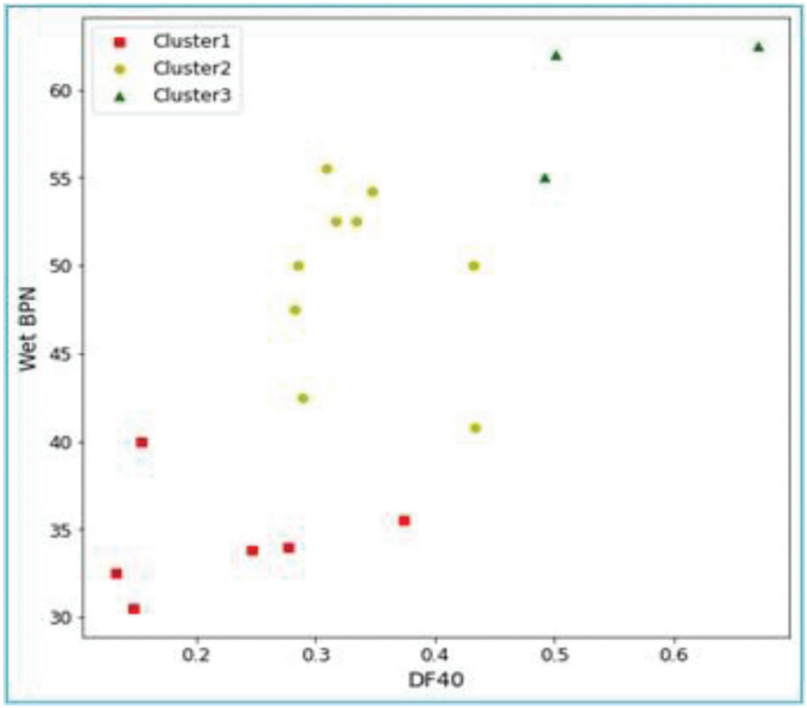

Figure 2.18 Fuzzy C-means clustering results.

Presented in Table 2.6 are the friction levels classified according to Table 2.5, BPN (wet) before polishing, and DF40 at 0, 500, and terminal polishing cycles for all marking specimens. All marking specimens exhibit friction performance at Level 4 or lower. Further interpretation of Table 2.6 can yield the following insights.

- There are discrepancies between the friction levels defined according to BPN (wet) before polishing and DF40 before polishing, respectively.
- Waterborne markings with smaller beads, including Type 1 or Type 2, exhibit friction performance of Level 3 or 4 in terms of BPN (wet).
- The friction performance of preformed tapes falls in Level 2.
- Epoxy markings typically provide friction performance at Levels 1 and 2, depending on the type of beads. When only Type 1 beads are used, the friction performance is at Level 2, and it decreases to Level 1 when Type 4 beads are added.
- Polyurea markings normally provide friction performance at Levels 1, 2, and 3, depending on the type of beads. When only Type 1 beads are used, the friction performance is at Level 3. It decreases to Level 1 when Type 4 beads are added but increases to Level 3 when ceramic particles are introduced.
- MMA markings normally exhibit friction performance at Level 3.
- The friction performance of thermoplastic markings (intermixed beads) falls to Level 1.
- Adding ceramic particles enhances their friction performance, and Type 4 beads should not be used alone, regardless of the type of marking material.
- The friction performance falls to Level 3 or below at the termination of polishing.

TABLE 2.5
Friction Levels for New Pavement Markings

Level	Wet BPN Before Polishing	DF40 Before Polishing
1	(0, 35)	(0, 0.25)
2	(35, 45)	(0.25, 0.3)
3	(45, 55)	(0.3, 0.49)
4	(55, 65)	(0.49, 0.67)
5	(65, ∞)	(0.67, ∞)

The DF40 values at different friction levels in Table 2.5 are determined using interpolation or extrapolation based on the association between BPN and DF40. To illustrate the systematic association between BPN and DF values, a correlation analysis was performed, and the results are presented in Figure 2.19. The significant correlation coefficients between BPN and DF at different speeds indicate a robust association. Due to the substantial correlation coefficients observed between DF40 and other DF variables, including DF0, DF20, and DF60, Table 2.5 can be readily extended to include DF0, DF20, and DF60. For example, ASTM E1960 (2015b) indicates that the friction coefficient measured using the DFT at 20 km/h should not be lower than 0.3. In this case, DF20 and DF40 at BPN (wet) = 45 are equal to each other, i.e., 0.30.

2.5.2.2 Safety-oriented minimum requirement. Europe and New Zealand specify a minimum BPN of 45 for pavement markings (BSI, 2018; Harlow, 2005).

TABLE 2.6
Classification of Friction Levels for All Marking Specimens

Level	Group No.	Type of Material	Type of Beads[1]	Wet BPN (Before)	DF40 After Different Polishing Cycles		
					0	500	@Termination
1	Group 12	Epoxy	1 and 4	33.8	0.25	0.24	0.17@20,000
	Group 13	Polyurea	1 and 4	34.0	0.28	0.26	0.28@50,000
	Group 17	Thermoplastic	1, 3, and MC Ceramic	30.5	0.15	0.16	0.14@100,000
	Group 18	Thermoplastic	1, 3, and MC Ceramic	32.5	0.13	0.14	0.13@100,000
2	Group 8	Waterborne	4	40.0	0.15	0.14	0.14@500
	Group 10	Preformed Tape	MC Ceramic	40.8	0.43	0.43	0.26@50,000
	Group 11	Epoxy	1	35.5	0.37	0.33	0.25@60,000
	Group 15	Polyurea	1	42.5	0.29	0.29	0.23@100,000
3	Group 1	Waterborne	1	54.2	0.35	0.25	0.25@1,500
	Group 3	Waterborne	1	50.0	0.29	0.25	0.33@1,500
	Group 4	Waterborne	1	52.5	0.33	0.24	0.21@5,000
	Group 5	Waterborne	1	52.5	0.32	0.15	0.13@5,000
	Group 9	Waterborne	4 and Ceramic	50.0	0.43	0.15	0.15@500
	Group 14	Polyurea	1 and Ceramic	55.0	0.49	0.37	0.32@10,000
	Group 16	MMA	1 and Corundum	47.5	0.28	0.26	0.28@100,000
4	Group 2	Waterborne	2	55.5	0.31	0.25	0.22@1,500
	Group 6	Waterborne	1 and Ceramic	62.5	0.67	0.31	0.31@500
	Group 7	Waterborne	2 and Ceramic	62.0	0.50	0.17	0.14@1,500
5	There are no specimens in this level.						

[1]MC denotes microcrystalline.

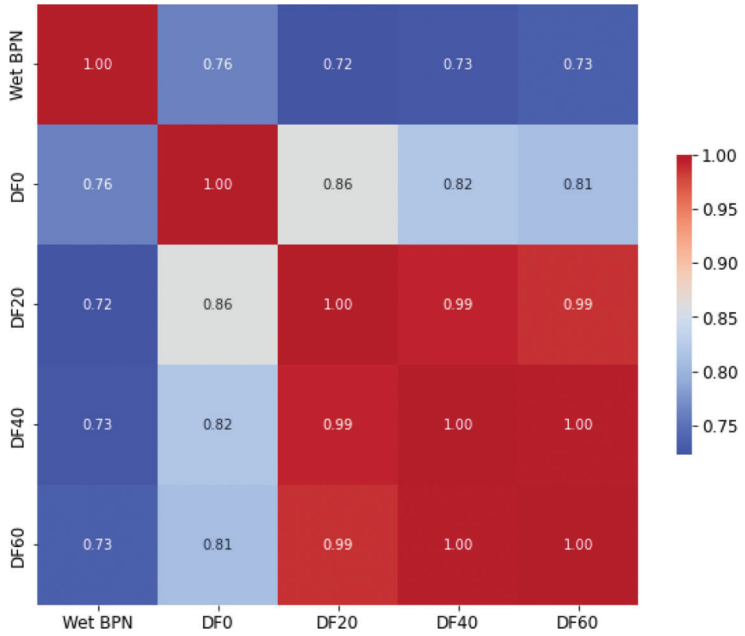

Figure 2.19 Pearson correlation coefficients.

Rodin et al. (2018) conducted an evaluative study on the suitability of pavement marking surfaces for bicyclists under diverse conditions. They recommended a wet BPN of 48 for bicyclists traveling on a straight road without the necessity to brake. For optimal safety in more complex manoeuvres requiring turning and braking, a wet BPN of 65 is deemed acceptable for mountain bikes and 70 for ordinary bikes. The current practice of INDOT suggests a minimum friction number of 20 mph at 40 mph with the standard smooth tire for highway pavements, and the ribbed tire commonly yields a friction number 12 to 17 points greater than the smooth tire (Li et al., 2005). The friction number with the standard ribbed tire at 40 mph is about 77% of the BPN value (Ahammed & Tighe, 2012). Therefore, a minimum friction number of 20 with the smooth tire equals to 34.5 with the ribbed tire or a BPN of 44.8 on average.

Like INDOT, the friction requirements by most State DOTs (Henry, 2000) are determined for high-speed roads without considering vulnerable road users such as motorcyclist and bicyclists. However, the posted speeds are commonly around 30 mph on urban collector and local streets, particularly intersections (FHWA, n.d.; NACTO, 2013). A BPN (wet) of 45 at 40 mph is equivalent to 39.5 at 30 mph based on the INDOT test data. Therefore, a tentative friction requirement of BPN = 40~45 is recommended for crosswalks, symbols, and letters. If a BPN of 40 is required, all new markings may meet this requirement, except for epoxy (Groups 11 and 12) and thermoplastic (Groups 17 and 18). However, adding ceramic particles to epoxy and thermoplastics can easily enhance their BPN values. Most importantly, all non-waterborne markings may also meet this requirement at the end of their service life (refer to Appendix A).

2.5.3 Texture and Friction Conversion Matrix

It was indicated earlier that, in addition to macrotexture features, additional factors should be considered to fully define the correlation between texture and friction. To address this challenge, the K-means algorithm was employed to further explore the relationships between macrotexture MPD and DF40 values, which were measured before and during polishing. Recognizing the unique frictional properties of different marking materials, this study conducted individual clustering analysis for each of the six types of materials, including waterborne paint, preformed tape, epoxy, polyurea, MMA, and thermoplastics. The Sum of Squared Errors (SSE) was utilized to ascertain the optimal clustering numbers, as shown in Figure 2.20 and Figure 2.21.

By consolidating the MPD and DF40 ranges for each cluster and considering the high correlation between DF40 and MPD (Pearson correlation coefficients = 0.774), a conversion matrix relating MPD to DF values was further developed, as outlined in Table 2.7. This matrix offers a methodological approach for estimating the DF40 values based solely on the MPD ranges, which is particularly useful in scenarios where DFT measurements are unavailable. In addition, this matrix may be used to help practitioners potentially develop friction requirements in terms of MPD.

Again, it is critical to highlight the significance of the varied beads and particles contributing to the surface texture of pavement markings, necessitating a subtle understanding of the additives utilized in these markings when consulting this table for reference. For instance, the preformed tapes examined in this study exclusively incorporate microcrystalline ceramic beads. Consequently, preformed tapes comprising other bead

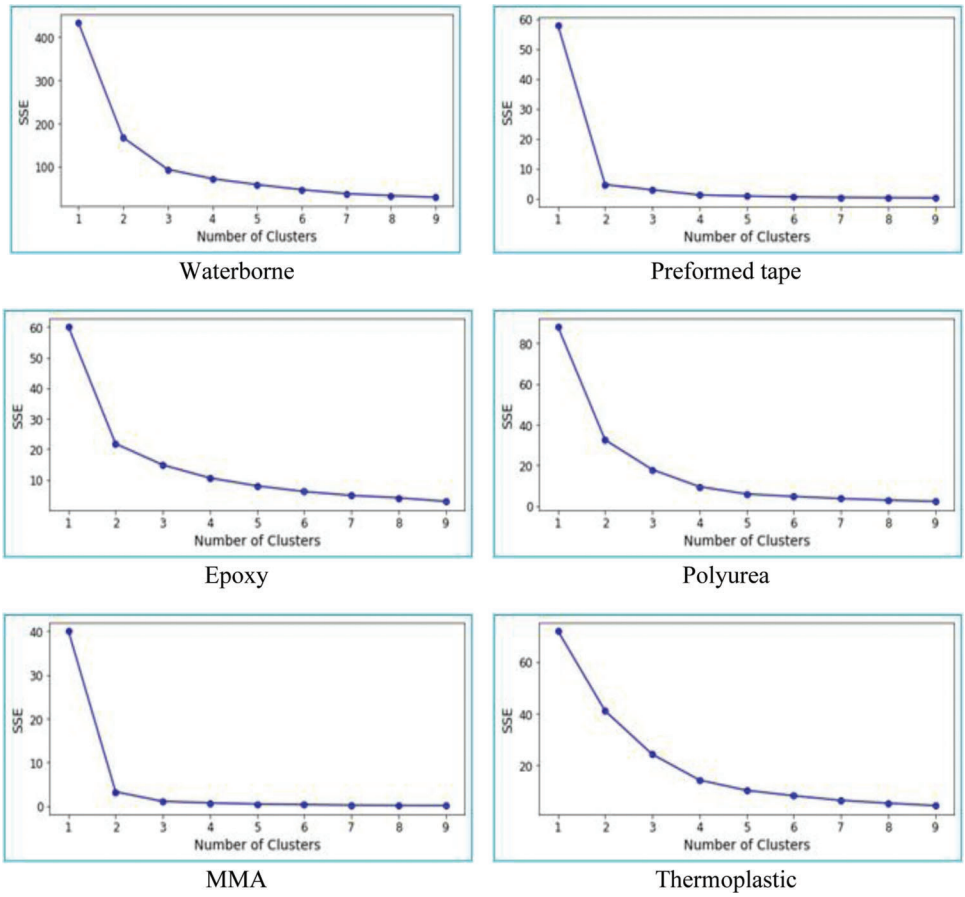

Figure 2.20 Selection of optimal cluster numbers.

and particle types fall outside the applicability of the DF40 value conversion matrix derived here.

2.6 Field Assessment

2.6.1 Surface Friction

A field assessment was conducted on recently installed pavement markings on a street in West Lafayette, Indiana, to enhance understanding their friction and macrotexture under real-world conditions. This field assessment consisted of three distinct evaluations. The first evaluation involved utilizing BPT and LST to systematically measure the BPN and MPD of newly applied longitudinal pavement markings. This was accomplished under ambient conditions of an outdoor temperature of 30.5°C and a water temperature of 26°C. The longitudinal pavement marking tested was composed of thermoplastics, integrated with a combination of large- and small-sized glass beads (Types 1 and 4). Figure 2.22 illustrates the surface texture of thermoplastic materials applied in the laboratory and field settings, respectively.

The average MPD value at three different test locations was 0.12 mm. Based on Table 2.5 and Table 2.7, the corresponding DF40 falls within the range of (0, 0.1), and the corresponding wet BPN value is anticipated to be less than 35. This projection is substantiated by empirical measurements obtained on-site, where the recorded wet BPN value in the field was observed to be 27. This average wet BPN of 27 is significantly below 45. This significant deviation may highlight the necessity of treating longitudinal pavement markings differently from transverse markings such as crosswalks, symbols, and letters.

The second evaluation focused on analyzing the MPD of freshly established crosswalk markings based on both the BPN and MPD measured after 4 weeks and 8 weeks in service, respectively. The pavement markings were composed of thermoplastics with drop-on Type 1 beads. Figure 2.23 depicts the visual changes of the crosswalk marking surfaces following 4 and 8 weeks of traffic exposure. Initially, the MPD stood at 0.18 mm. It increased to 0.21 mm after 4 weeks in service and 0.28 mm after 8 weeks in service, because of wear and tear from traffic. Concurrently, the wet BPN was recorded at 45 and 55 after 4 and 8 weeks, respectively, in service. Moreover, the volume of traffic traversing the pavement marking was estimated using a 15-minute traffic flow analysis, revealing that the monthly traffic volume passing over the pavement marking amounted to 21,504 passenger cars.

The third evaluation pertained to the texture analysis of aged crosswalk markings at a roundabout to

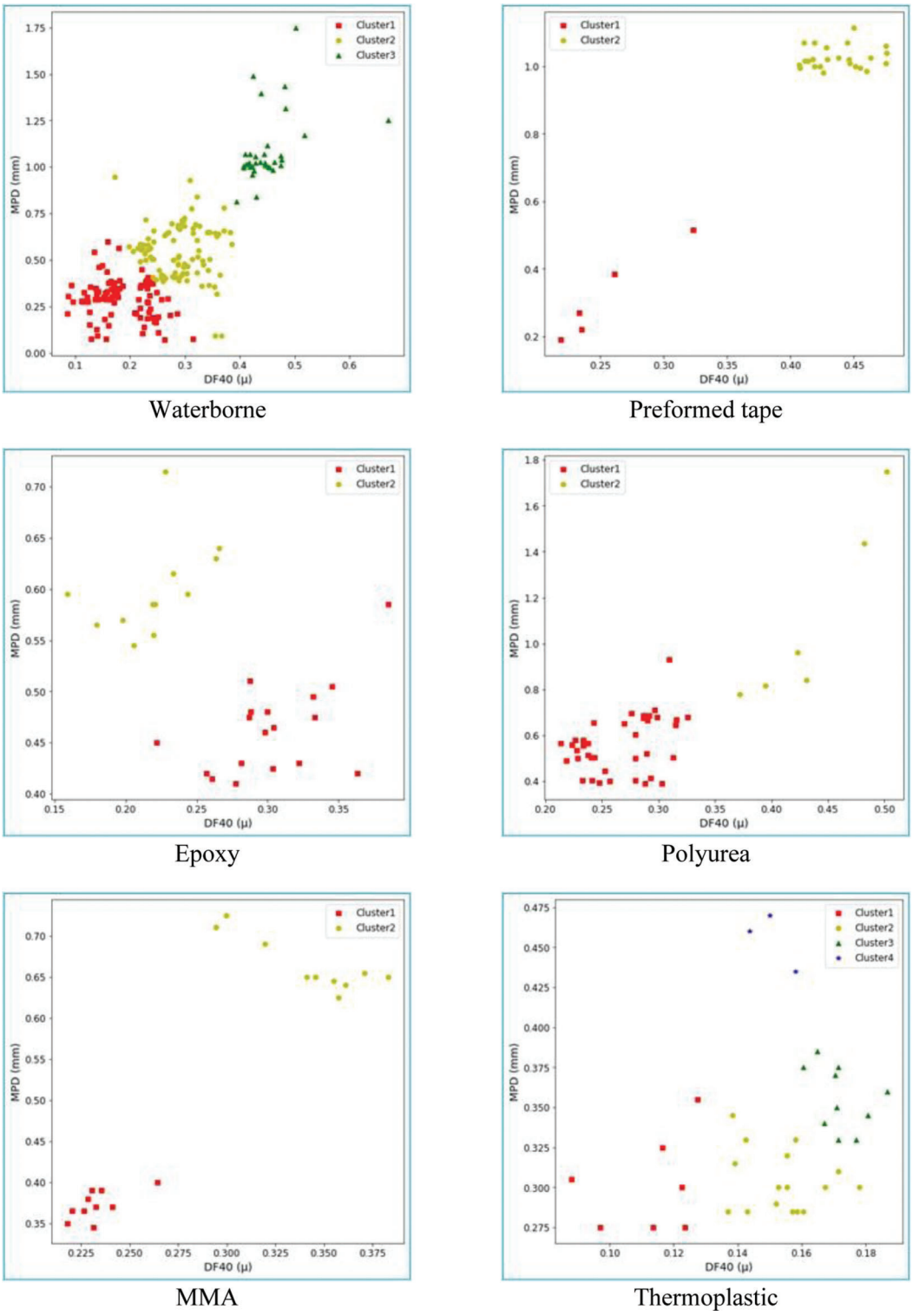

Figure 2.21 Clustering results of each material type.

understand the long-term effects of environmental and traffic factors on pavement markings (see Figure 2.24). The macrotexture MPD values were measured at five distinct locations as shown in Table 2.8, Sites 1 and 2 exhibit relatively good conditions, while Sites 3, 4, and 5 showed signs of wear, tear, and cracking. The texture measurements revealed that the markings in good condition exhibited a smoother surface, resulting in lower MPD values. Conversely, as the markings deteriorated, the texture became rougher, leading to increased MPD values, approximating the pavement surface MPD of 0.45. This pattern underscores

TABLE 2.7
Conversion Matrix Between MPD and DF Values

Marking Material	MPD Range (mm)	DF40 Range
Waterborne Paint	(0, 0.3)	(0, 0.2)
	(0.3, 0.5)	(0.2, 0.28)
	(0.5, 0.57)	(0.28, 0.3)
	(0.57, 1)	(0.3, 0.44)
	(1, 1.15)	(0.44, 0.47)
	(1.15, ∞)	(0.47, ∞)
Preformed Tape	(0, 0.24)	(0, 0.23)
	(0.24, 0.45)	(0.23, 0.3)
	(0.45, 1)	(0.3, 0.43)
	(1, ∞)	(0.43, ∞)
Epoxy	(0, 0.44)	(0, 0.28)
	(0.44, 0.63)	(0.28,0.32)
	(0.63, ∞)	(0.32, ∞)
Polyurea	(0, 0.5)	(0, 0.25)
	(0.5, 0.6)	(0.25, 0.3)
	(0.6, 0.84)	(0.3, 0.4)
	(0.84, 1.5)	(0.4, 0.47)
	(1.5, ∞)	(0.47, ∞)
MMA	(0, 0.38)	(0, 0.24)
	(0.38, 0.65)	(0.24, 0.32)
	(0.65, 0.68)	(0.32, 0.36)
	(0.68, ∞)	(0.36, ∞)
Thermoplastics	(0, 0.28)	(0, 0.1)
	(0.28, 0.32)	(0.1, 0.16)
	(0.32, 0.47)	(0.16, 0.18)
	(0.47, ∞)	(0.18, ∞)

Figure 2.22 Closeups of thermoplastics applied in laboratory and in field.

Figure 2.23 Closeups of a crosswalk marking.

TABLE 2.8
Macrotexture MPD Values of Crosswalk Markings

Age	Condition	Date	MPD (mm)[1]
New	New	10/12/2023	0.18 (0.350)
	New	11/9/2023	0.21 (0.500)
	New	12/7/2023	0.28 (0.500)
Aged	Fair	8/16/2023	0.170
	Wear-and-Tear	8/16/2023	0.307

[1]The values in parentheses are measured on adjacent pavement surfaces.

Figure 2.24 Closeups of roundabout crosswalk markings in different conditions.

Figure 2.25 Truck tires traveling over right edge line marking.

the potential of regular MPD value monitoring as an effective indicator of pavement marking health and longevity. It also implies that the friction of pavement markings would increase as their condition deteriorates.

2.6.2 Traffic Application

To assess the possible applications of traffic on pavement markings, a video was recorded on the right lane of southbound I-65 near West Lafayette for a duration of 1 hour. The video was used to examine vehicular behavior in relation to longitudinal pavement markings. Out of the 714 observed vehicles, 419 were identified as trucks. Overall, it was observed that 12.61% of vehicles traversed over the right edge line markings, while 1.68% crossed the dashed white center line markings during lane changes. Notably, 20.29% of the trucks were seen driving on pavement markings, and 1.43% crossed them while changing lanes. Noteworthy is the fact that nearly 90% of the trucks driving on the furthest right longitudinal marking were semitrucks, as depicted in Figure 2.25.

Clearly, only a small number of vehicles may travel over the longitudinal markings. Also, the tire widths typically range from 165 mm to 325 mm for passenger cars and from 280 mm to 445 mm for trucks (Goodyear, n.d., 2018). Consequently, the tire-road contact area of the vehicle should encompass both road markings and the road surface simultaneously. This further implies that the friction requirements for longitudinal pavement markings should be treated differently from transverse markings such as crosswalks, symbols, and letters. Even if a minimum BPN of 40 is required, the BPN values of all waterborne (or longitudinal) markings are above it in the early stage of their service life but become slightly lower than it at the end of their service life.

3. CHAPTER 3. FRICTIONAL PROPERTIES OF TYPICAL AGGREGATES

3.1 Methodology

Aggregates play a significant role in pavement structure, whether they are naturally sourced or produced through industrial processes. Natural aggregates are obtained by extracting and crushing various rock types, while manufactured aggregates often consist of industrial by-products such as steel slag and air-cooled blast furnace slag. Even recycled materials such as crushed old asphalt pavement or concrete slabs can be transformed into valuable aggregates. INDOT commonly employs aggregates such as dolomite, limestone, gravel, and steel slag in pavement construction. To ensure quality, aggregates must undergo the friction test as outlined in the ITM 214 procedures (INDOT, 2016). The inherent characteristics of these aggregates profoundly influence their performance when integrated into pavement structures (INDOT, 2022). Federal Highway Administration (FHWA) studies underscore the potential of aggregates such as calcined bauxites to significantly enhance pavement surface friction, leading to a reduction in crash rates (Atkinson et al., 2016; Merritt et al., 2021). This study focuses on the aggregates commonly employed by INDOT.

Aggregates showcase a wide range of physical, chemical, and mechanical properties, each defined by key parameters. Pertaining to physical attributes, critical factors include bulk specific gravity (BSG), water absorption (WA), and soundness. Chemical attributes encompass vital elements such as aluminum oxide (Al_2O_3), silicon dioxide (SiO_2), iron (III) oxide (Fe_2O_3), titanium dioxide (TiO_2), calcium oxide (CaO), and magnesium oxide (MgO). Mechanical properties, which hold great significance in assessing aggregate frictional performance, are commonly evaluated through tests such as the Los Angeles abrasion (LAA), micro-Deval abrasion (MDA) and polished stone value (PSV) tests. Lower values of LAA or MDA, or higher values of PSV, correlate with superior frictional performance of the aggregate.

The long-term surface friction performance is directly influenced by the LAA, MDA, and PSV values of aggregates, necessitating a thorough examination of these key indicators. A comprehensive analysis of the distribution and interplay between these indicators was conducted. Additionally, an expanded array of laboratory tests was undertaken to broaden the spectrum of parameters under consideration. The intricate relationships between the LAA, MDA, PSV values, and factors such as specific gravity and water absorption were also examined. To establish predictive frameworks, encompassing LAA, MDA, and PSV values, regression models were formulated. In the field, the evaluation of surface frictional properties involved the employment of instruments such as the British pendulum tester (BPT), laser texture scanner (LTS), and locked-wheel skid tester (LWST).

Samples of dolomite (from 27 sources), limestone (from 12 sources), gravel (from 5 sources), and steel slag (from 7 sources) aggregates were obtained from INDOT to conduct an exhaustive analysis. These samples underwent laboratory tests to determine key parameters such as BSG, WA, soundness, and chemical element composition (including Al_2O_3, SiO_2, Fe_2O_3, TiO_2, CaO, and MgO). Additional tests were performed to assess LAA, MDA, and PSV. Moreover, Mohs scratch hardness tests were executed to assess the hardness of the aggregate, which not only established a relationship between its chemical composition and hardness but also provided insights into its friction performance. By analyzing specific physical, chemical, or mechanical attributes linked to the typical aggregates, their friction performance was able to be evaluated and estimated. A representation of the laboratory experiment plan is shown in Figure 3.1.

3.2 Laboratory Experiments and Analysis

3.2.1 Aggregates and Laboratory Tests

The common aggregate types utilized by INDOT for pavement construction include dolomite, limestone, gravel, and steel slag. All assessments were conducted in compliance with the standards established by either AASHTO or ASTM. The BSG and WA were evaluated according to the *AASHTO T 85 Standard Method. Aggregate* (AASHTO, 2022c) soundness was determined by subjecting samples to freezing and thawing, following the AASHTO T 103. For the LAA test, aggregate samples (Grading C of 9.5 mm-19.0 mm) were prepared following the *AASHTO T96 Standard Method* (AASHTO, 2022d). Similarly, the MDA test involved preparing samples (Grading of 4.75 mm-12.5 mm except for calcined bauxite with Grading of 4.75 mm-9.5 mm) according to the AASHTO T 327 (AASHTO, 2022a). The PSV test required aggregate samples (grading of 6.3 mm-9.5 mm) and followed the protocols outlined in AASHTO T 278 (2021) and AASHTO T 279 (2022b). To determine the chemical compositions of aggregates, the X-ray fluorescence (XRF) method, guided by the ASTM C25 (2019b), was utilized. Figure 3.2 illustrates the equipment used by the Indiana Department of Transportation (INDOT) for conducting LAA, MDA, and PSV tests.

Table 3.1 provides a comprehensive overview of the distribution of characteristics related to key parameters for the four distinct aggregates. This table includes sample size (SS), mean values, and standard deviations (SD). PSV-10 indicates the polished stone value of aggregates following a 10-hour polishing process. For the steel slag aggregate, chemical composition analysis was only feasible for a single sample, leading to the exclusion of SD values. In addition to the four aggregate types, Table 3.1 also incorporates parameter values for calcined bauxite from a prior study (Li et al., 2017) as a reference. The chemical components, including Al_2O_3 and TiO_2, exhibit greater variabilities, regardless of aggregate type, with limestone showing

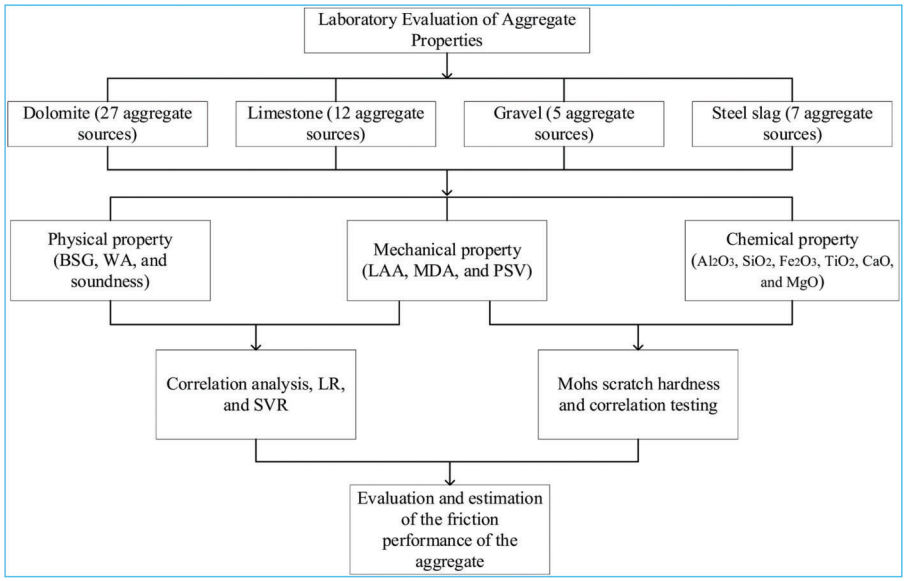

Figure 3.1 Laboratory experiment plan.

Figure 3.2 LAA, MDA, and PSV test machines.

the least variability in all chemical components except for MgO and CaO.

INDOT has set specific guidelines for coarse aggregates. These guidelines specify a maximum LAA value of 30% and an upper limit of 18% for MDA (INDOT, 2022). Regarding PSV-10, INDOT recommends a minimum value of 28 for aggregates that resist polishing (INDOT, 2016). Moreover, a previous study by Li et al. (2017) suggests an average PSV-10 value of 27.8 for one steel slag source. Furthermore, INDOT specifies that dolomite aggregates should contain a minimum magnesium content of 10.3%. To facilitate easy reference, the MgO content can be converted to magnesium (Mg) content using the relationship:

$$(\text{Mg Content}) = (\text{MgO Content}) \times 0.60317$$

Thus, the stipulated minimum Mg content of 10.3% is equivalent to a minimum MgO content of 17.1%. These specified values are summarized in Table 3.2. The average LAA and MDA values, as detailed in Table 3.1, all fall within the limits set by INDOT, indicating conformity to abrasion resistance standards. While the average PSV-10 value for dolomite aggregate slightly falls below 28, the corresponding values for the other three aggregates consistently meet the prescribed PSV-10 benchmark.

3.2.2 Analytical Methods

To thoroughly explore the intricate interactions among mechanical parameters and the connections between physical and mechanical properties, correlation analysis and linear regression (LR) were applied. To uncover strong correlations between variables, the Pearson correlation coefficients (R) were calculated. Subsequently, LR models were utilized to establish meaningful relationships between these variables. LR operates as a regression analysis tool, utilizing the least squares approach to elucidate the relationship between independent and dependent variables. In this study, a dependable LR model needed to meet two fundamental criteria: (1) all coefficients must demonstrate statistical significance at a 0.05 threshold; (2) the F-test should indicate significance at the 0.05 level.

TABLE 3.1
Aggregate Property Measurements Statistics

	Dolomite			Limestone			Gravel			Steel Slag			Calcined Bauxite[1]		
Parameter	**SS**	**Mean**	**SD**	**SS**	**Mean**	**SD**	**SS**	**Mean**	**SD**	**SS**	**Mean**	**SD**	**SS**	**Mean**	**SD**
BSG	91	2.62	0.08	79	2.61	0.11	49	2.63	0.03	44	3.49	0.18	–	–	–
WA, %	91	2.07	0.84	79	1.91	1.61	49	1.61	0.33	44	1.37	0.52	–	–	–
Soundness, %	92	2.07	2.19	78	4.23	4.58	12	2.02	1.05	38	1.59	1.36	–	–	–
LAA, %	92	28.75	4.33	76	25.48	3.01	47	22.20	4.32	40	14.28	2.60	4	9.3	0.28
MDA, %	47	11.54	2.68	28	15.28	2.77	13	8.82	4.47	38	6.26	1.34	3	5.23[2]	0.06
PSV-10[3]	14	27.78	2.47	59	30.48	2.21	19	28.88	2.67	2	29.90	2.97	9	35.4	0.89
MgO, %	4	20.54	0.67	4	15.96	1.95	4	5.73	2.18	1	10.22	–	1	0.09	–
Al_2O_3, %	4	0.50	0.48	4	0.85	0.24	4	4.36	1.49	1	5.71	–	1	86.93	–
SiO_2, %	4	2.10	2.14	4	4.40	0.63	4	40.62	13.97	1	12.52	–	1	6.82	–
CaO, %	4	30.21	0.81	4	35.35	1.64	4	22.64	11.06	1	38.49	–	1	0.36	–
Fe_2O_3, %	4	0.35	0.24	4	0.74	0.20	4	2.59	1.11	1	29.53	–	1	1.63	–
TiO_2, %	4	0.03	0.02	4	0.06	0.01	4	0.26	0.15	1	0.33	–	1	3.45	–

[1]The testing results of calcined bauxite are from a published study by Li et al. (2017).
[2]MDA of 5.23% for calcined bauxite was determined using grading of 4.75-9.5mm.
[3]PSV-10 was measured in terms of the main scale.

TABLE 3.2
Specified Limits for Aggregate Properties

Property	**Limit**	**Note**
LAA	<30%	
MDA	<18%	
PSV-10	>28	
Magnesium (Mg) Content	>10.3%[1]	For Dolomite

[1](Magnesium)>10.3% is equal to (Magnesium Oxide)/0.60317 >17.1%

TABLE 3.3
Statistics of Dolomite Properties

Variable	**Sample Size**	**Mean**	**SD**	**95% Confidence Interval**
BSG	91	2.62	0.08	(2.60, 2.63)
WA	91	2.07	0.84	(1.90, 2.25)
Soundness	92	2.07	2.19	(1.63, 2.52)
LAA	92	28.75	4.33	(27.87, 29.64)
MDA	47	11.54	2.68	(10.77, 12.30)
PSV-10	14	27.78	2.47	(26.49, 29.07)
MgO	4	20.54	0.67	(19.88, 21.20)
Al_2O_3	4	0.50	0.48	(0.03, 0.98)
SiO_2	4	2.10	2.14	(0.00, 4.20)
CaO	4	30.21	0.81	(29.41, 31.01)
Fe_2O_3	4	0.35	0.24	(0.12, 0.58)
TiO_2	4	0.03	0.02	(0.01, 0.04)

3.3 Analysis of Parameters

3.3.1 Dolomite

Table 3.3 offers a comprehensive view of the statistics of dolomite parameters, including sample size, mean value, standard deviation (SD), and 95% confidence interval (CI) for each parameter. To explore the intricate relationships between mechanical and physical parameters, the Pearson correlation coefficients (R) were computed, as depicted in Table 3.4. The Pearson coefficient is a mathematical correlation coefficient that signifies the relationship between two variables. Its values span from -1 to +1: +1 denotes a positive correlation, -1 indicates a negative correlation, and 0 signifies no relationship. This table is instrumental in discerning the correlation patterns among the LAA, MDA, and PSV-10 variables. Specifically, LAA has moderate correlation with BSG and weak to very weak correlations with other parameters. MDA has very strong correlations with BSG and WA and moderate correlation with soundness. PSV-10 has strong correlations with BSG and moderate correlation with WA. The correlations are strong between PSV-10 and MDA and very weak between PSV-10 and LAA.

The linear regression (LR) models were constructed to establish relationships among different variables. LR is a form of regression analysis that uses the least squares method to express the relationship between independent and dependent variables. For a LR model to be valid in this study, two primary criteria need to be satisfied: (1) all coefficients should be statistically significant at a 0.05 significance level; and (2) the F-test must reveal significance at the 0.05 level. The Root-Mean-Square Error (RMSE) is a widely employed measure to gauge the disparity between a model's predictions and the actual observed values. As such, the RMSE offers an effective means to evaluate and contrast the performance of the LR models. A lower RMSE value signifies superior model performance, indicating a more accurate fit and estimation. The corresponding models are detailed in Table 3.5 for dolomite aggregate.

3.3.2 Limestone

The statistics, Pearson correlation coefficients and the LR models for limestone parameters are detailed in

TABLE 3.4
Pearson Correlation Coefficients (R) of Dolomite Properties

	Pearson Correlation Coefficient (R)		
	LAA	**MDA**	**PSV-10**
LAA	1.00	0.26	0.08
MDA	0.26	1.00	0.71
PSV-10	0.08	0.71	1.00
BSG	-0.54	-0.85	-0.65
WA	0.40	0.87	0.47
Soundness	-0.11	0.53	0.05

TABLE 3.5
LR Models of Dolomite Aggregate Properties

LR Model	R^2	F-test ($\alpha = 0.05$)	RMSE
$LAA = -30.56 * BSG + 108.70$	0.29	Significant	3.49
$MDA = 2.69 * WA + 6.34$	0.76	Significant	1.31
$PSV - 10 = 0.83 * MDA + 18.73$	0.50	Significant	1.87

Tables 3.6, 3.7, and 3.8, respectively. Table 3.6 provides sample sizes, mean values, standard deviations, and 95% confidence intervals for the limestone parameters. In Table 3.7, Pearson correlation coefficients display the degrees of correlation among physical and mechanical variables of the limestone aggregate. Both LAA and MDA exhibit weak correlations with GSB, WA and soundness. PSV-10 exhibits relatively strong correlations with BSG and WA and moderate correlation with soundness. Nevertheless, the correlations among LAA, MDA, and PSV-10 are all weak.

3.3.3 Gravel

Tables 3.9, 3.10 and 3.11 present the statistics, Pearson correlation coefficients and the LR models for gravel parameters. Table 3.10 outlines sample sizes, mean values, standard deviations, and 95% confidence intervals for the gravel parameters. As shown in Table 3.10, LAA exhibits weak to very weak correlations with BSG, WA and soundness, respectively. MDA has very weak correlations with BSG and WA, and moderate correlation with soundness. PSV-10 has very strong correlation with BSG, strong correlation with soundness, and moderate correlation with WA. LAA and MDA demonstrate a very strong correlation. However, PSV-10 exhibits weak and very weak correlations with LAA and MDA, respectively.

The LR models for gravel are listed in Table 3.11. The R^2 values agree well with the results of the Pearson correlation analysis as shown in Table 3.10.

3.3.4 Steel Slag

Tables 3.12, 3.13, and 3.14 contain detailed information regarding steel slag. In Table 3.12, sample sizes,

TABLE 3.6
Statistics of Limestone Properties

Variable	Sample Size	Mean	SD	95% Confidence Interval
BSG	79	2.61	0.11	(2.59, 2.63)
WA, %	79	1.91	1.61	(1.55, 2.27)
Soundness, %	78	4.23	4.58	(3.22, 5.25)
LAA, %	76	25.48	3.01	(24.80, 26.15)
MDA, %	28	15.28	2.77	(14.25, 16.30)
PSV-10	59	30.48	2.21	(29.91, 31.04)
MgO, %	4	15.96	1.95	(14.05, 17.88)
Al_2O_3, %	4	0.85	0.24	(0.61, 1.08)
SiO_2, %	4	4.40	0.63	(3.78, 5.01)
CaO, %	4	35.35	1.64	(33.74, 36.95)
Fe_2O_3, %	4	0.74	0.20	(0.54, 0.93)
TiO_2, %	4	0.06	0.01	(0.04, 0.07)

TABLE 3.7
Pearson Correlation Coefficients (R) of Limestone Properties

	Pearson Correlation Coefficient (R)		
	LAA	**MDA**	**PSV-10**
LAA	1.00	-0.20	0.28
MDA	-0.20	1.00	-0.26
PSV-10	0.28	-0.26	1.00
BSG	-0.32	0.40	-0.71
WA	0.33	-0.41	0.69
Soundness	0.31	-0.04	0.57

TABLE 3.8
LR Models of Limestone Aggregate Properties

LR Model	R^2	F-test ($\alpha = 0.05$)	RMSE
$LAA = 0.60 * WA + 24.24$	0.11	Significant	2.82
$MDA = -1.67 * WA + 18.67$	0.17	Significant	2.52
$PSV - 10 = -19.17 * BSG + 80.80$	0.50	Significant	1.01

TABLE 3.9
Statistics of Gravel Properties

Variable	Sample Size	Mean	SD	95% Confidence Interval
BSG	49c	2.63	0.03	(2.62, 2.64)
WA, %	49	1.61	0.33	(1.52, 1.70)
Soundness, %	12	2.02	1.05	(1.42, 2.61)
LAA, %	47	22.20	4.32	(20.97, 23.43)
MDA, %	13	8.82	4.47	(6.39, 11.24)
PSV-10	19	28.88	2.67	(27.68, 30.08)
MgO, %	4	5.73	2.18	(3.59, 7.87)
Al_2O_3, %	4	4.36	1.49	(2.89, 5.82)
SiO_2, %	4	40.62	13.97	(26.93, 54.31)
CaO, %	4	22.64	11.06	(11.80, 33.48)
Fe_2O_3, %	4	2.59	1.11	(1.50, 3.68)
TiO_2, %	4	0.26	0.15	(0.11, 0.40)

TABLE 3.10
Pearson Correlation Coefficients (R) of Gravel Properties

	Pearson Correlation Coefficient (R)		
	LAA	**MDA**	**PSV-10**
LAA	1.00	0.91	-0.35
MDA	0.91	1.00	-0.16
PSV-10	-0.35	-0.16	1.00
BSG	-0.28	-0.13	0.97
WA	0.39	-0.13	-0.59
Soundness	0.05	-0.56	0.64

TABLE 3.11
LR Models of Gravel Aggregate Properties

LR Model	R^2	F-test (α = 0.05)	RMSE
$LAA = 0.94 * MDA + 12.33$	0.83	Significant	1.92
$MDA = 0.87 * LAA - 9.23$	0.83	Significant	1.85
$PSV\text{-}10 = 35.51 * BSG - 64.90$	0.92	Significant	0.24

TABLE 3.12
Statistics of Steel Slag Properties

Variable	Sample Size	Mean	SD	95% Confidence Interval
BSG	44	3.49	0.18	(3.44, 3.55)
WA, %	44	1.37	0.52	(1.22, 1.53)
Soundness, %	38	1.59	1.36	(1.16, 2.02)
LAA, %	40	14.28	2.60	(13.47, 15.08)
MDA, %	38	6.26	1.34	(5.84, 6.69)
PSV-10	2	29.90	2.97	(25.78, 34.02)
MgO, %	1	10.22	–	–
Al_2O_3, %	1	5.71	–	–
SiO_2, %	1	12.52	–	–
CaO, %	1	38.49	–	–
Fe_2O_3, %	1	29.53	–	–
TiO_2, %	1	0.33	–	–

mean values, standard deviations, and 95% confidence intervals for gravel parameters are presented. However, it is important to note that due to a limited sample size for PSV and chemical content tests, some data distributions, correlation attributes, and regression equations are not available. The Pearson correlation coefficients in Table 3.13 display the relationships between various physical and mechanical variables of the gravel aggregate. Specifically, LAA shows very weak correlations with BSG, WA, and soundness. MDA exhibits a very strong correlation with WA and strong correlations with BSG and soundness. However, not enough PSV-10 data is currently available for steel slag.

Table 3.15 highlights LR models for both LAA and MDA variables. Although the F-tests indicate there is a significant linear relationship between LAA and MDA and between MDA and WA, the R^2, especially for the

TABLE 3.13
Pearson Correlation Coefficients (R) of Steel Slag Properties

	Pearson Correlation Coefficient (R)		
	LAA	**MDA**	**PSV-10**
LAA	1.00	0.48	–
MDA	0.48	1.00	–
PSV-10	–	–	1.00
BSG	-0.14	-0.68	–
WA	0.21	0.81	–
Soundness	-0.09	0.61	–

TABLE 3.14
LR Models of Steel Slag Aggregate Properties

LR Model	R^2	F-test (α=0.05)	RMSE
$LAA = 0.96 * MDA + 8.28$	0.23	Significant	2.30
$MDA = 1.96 * WA + 3.54$	0.66	Significant	0.77

LAA linear model, is very small, which indicates that the model may not explain a large proportion of the variability in LAA.

3.4 Aggregate Hardness

Aggregate hardness is a crucial property that assesses a material's ability to withstand localized deformation, providing insights into its strength and resistance to abrasion. In general, higher aggregate hardness is indicative of superior frictional performance. This characteristic is conveniently quantified through mineral hardness, typically assessed qualitatively using the Mohs scale, which spans from 1 (softest) to 10 (hardest). In adherence to the ASTM C1895 (2020b) standard method, the hardness tests were conducted on the four aggregates as well as on calcined bauxite aggregate, which is often used for High Friction Surface Treatments (HFST). Since micro-Deval abrasion (MDA) is an indicator of aggregate durability, the MDA values (in % aggregate volume loss due to abrasion) are listed along with the Mohs hardness values of the aggregates in Table 3.15. Calcined bauxite exhibits an impressive Mohs rating of 9.0, while limestone has the lowest hardness with a score of 3.5. As anticipated, the order of Mohs hardness aligns with MDA values for the four common pavement aggregates, where higher Mohs hardness corresponds to lower MDA values.

3.5 Correlations Between Hardness and Chemical Elements

A Pearson correlation analysis was conducted to explore the relationship between aggregate hardness and chemical element content across a variety of aggregates, including dolomite, limestone, gravel, steel slag, and calcined bauxite. The outcomes of this analysis are summarized in Table 3.16. Significantly

positive correlations were evident between aggregate hardness and the levels of Al_2O_3 and TiO_2. Conversely, negative correlations were observed between aggregate hardness and MgO and CaO levels. The statistical analysis was performed with the t-test at a 0.05 significance level. This underscores the substantial influence of Al_2O_3, TiO_2, and MgO content on aggregate hardness and consequently on its frictional properties.

It is noteworthy that INDOT specifies a minimum magnesium content of 10.3% for dolomite aggregate in pavement construction. Interestingly, the Pearson correlation test revealed a significant negative relationship between magnesium oxide content and aggregate hardness. Essentially, higher magnesium content leads to reduced aggregate hardness and consequently diminished resistance to abrasion or polishing. This finding may prompt a reevaluation of the INDOT's current practice associated with the use of dolomite aggregate in pavement construction, considering its potential negative impact on friction. A previous study by Li et al. (2007) also indicated that dolomite did not show superior polishing resistance. Moreover, the positive correlations between aggregate hardness and levels of Al_2O_3 and TiO_2 advocate for the establishment of minimum Al_2O_3 and TiO_2 contents for aggregates to ensure adequate pavement friction.

TABLE 3.15
Mohs Hardness and MDA Values

Aggregate	Mohs Hardness	MDA[1]
Calcined Bauxite	9.0	5.23
Steel Slag	6.0	6.26
Gravel	5.5	8.82
Dolomite	4.0	11.54
Limestone	3.5	15.28

[1]Grading of 4.75 mm-12.5 mm except for calcined bauxite with Grading of 4.75 mm-9.5 mm.

3.6 Range of Aggregate Property Values

The study involved extensive laboratory testing and detailed data analysis to establish the distributions of physical, chemical, and mechanical characteristics inherent in the four commonly used types of aggregates for pavement construction in Indiana. The findings are succinctly presented in Table 3.17, providing statistical ranges at a 95% confidence level for various attributes. This comprehensive table serves as a valuable reference, illustrating the variability in attributes such as Los Angeles abrasion (LAA), micro-Deval abrasion (MDA), polished stone value after 10-hour polishing (PSV-10), bulk specific gravity (BSG), water absorption (WA), soundness, hardness, and the chemical composition including Al_2O_3, TiO_2, SiO_2, Fe_2O_3, MgO, and CaO. In recognition of INDOT's specifications being in terms of Mg content, Mg ranges are also provided along with MgO ranges in Table 3.17. The information in the table is instrumental for understanding the diverse characteristics of different aggregates. The variations outlined in the table facilitate informed decision-making in selecting materials tailored to specific needs related to pavement friction.

It should be high source and the Mg content of limestone may be up to 10.78%, depending on the aggregate source, and is higher than the minimum requirement of Mg for dolomite. The dolomite aggregates exhibit an Mg content of 11.99% to 12.77%. For a practical and consistent definition, the requirement for minimum Mg content in dolomite should be revised from 10.3% to 12.0%. This may also help ensure the engineering properties and performance characteristics of dolomite in pavement construction, particularly durability and freeze-thaw resistance.

TABLE 3.16
Pearson Correlation Coefficients Between Hardness and Chemical Content

Parameter	Al_2O_3	TiO_2	SiO_2	Fe_2O_3	MgO	CaO
Pearson Correlation Coefficient	0.91	0.92	0.08	0.14	-0.89	-0.82
p-value	0.03	0.03	0.89	0.83	0.04	0.09

TABLE 3.17
Statistical Ranges of Main Aggregate Properties (95% Confidence Level)

Attribute	Method	Grading	Dolomite	Limestone	Gravel	Steel Slag	Bauxite[1]
LAA	AASHTO T96	9.5~19.0 mm	(27.9%, 29.6%)	(24.8%, 26.2%)	(21.0%, 23.4%)	(13.5%, 15.1%)	9.3%
MDA	AASHTO T327	4.75~12.5 mm	(10.8%, 12.3%)	(14.3%, 16.3%)	(6.4%, 11.2%)	(5.8%, 6.7%)	5.23%[2]
PSV-10	AASHTO T278/ T279	6.3~9.5 mm	(26.5, 29.1)	(29.9, 31.0)	(27.7, 30.1)	(25.8, 34.0)	35.4
BSG	AASHTO T85	–	(2.60, 2.63)	(2.59, 2.63)	(2.62, 2.64)	(3.44, 3.55)	3.38[b]
WA	AASHTO T85	–	(1.9%, 2.3%)	(1.6%, 2.3%)	(1.5%, 1.7%)	(1.2%, 1.5%)	0.81%
Soundness	AASHTO T103	–	(1.6%, 2.5%)	(3.2%, 5.3%)	(1.4%, 2.6%)	(1.2%, 2.0%)	–
Hardness	ASTM C1895	–	3.5	4.0	5.5	6.0	9.0
Al_2O_3	ASTM C25	–	(0.03%, 0.98%)	(0.61%, 1.08%)	(2.89%, 5.82%)	5.71%	86.93%
TiO_2	ASTM C25	–	(0.01%, 0.04%)	(0.04%, 0.07%)	(0.11%, 0.40%)	0.33%	3.45%
SiO_2	ASTM C25	–	(0.004%, 4.20%)	(3.78%, 5.01%)	(26.93%, 54.31%)	12.52%	6.82%
Fe_2O_3	ASTM C25	–	(0.12%, 0.58%)	(0.54%, 0.93%)	(1.50%, 3.68%)	29.53%	1.63%
MgO	ASTM C25	–	(19.88%, 21.20%)	(14.05%, 17.88%)	(3.59%, 7.87%)	10.22%	0.09%
Mg			(11.99%, 12.79%)	(8.47%, 10.78%)	(2.16%, 4.75%)		
CaO	ASTM C25	–	(29.41%, 31.01%)	(33.74%, 36.95%)	(11.80%, 33.48%)	38.49%	0.36%

[1]Refer to Li et al. (2017).
[2]Grading of 4.75~9.5 mm, and [c]3.38 is the apparent specific gravity.

4. CHAPTER 4. COLOR SURFACE TREATMENT

4.1 Problem Statement

Color surface treatment (CST) on roadway or street pavements has gained popularity, especially for bus and bike lanes in urban areas. These CST lanes not only serve as a clear identifier but also act as a deterrent against unauthorized lane usage. Figure 4.1 provides a visual representation, showing a red bus lane and a green bike lane in Downtown Indianapolis, Indiana. The frictional characteristics of CST are vital for enhancing the safety of CST, especially for buses and bicycles. Buses, due to their frequent stops and significant wheel loads, create a pronounced polishing effect on the pavement's surface. Also, ensuring robust friction is crucial for CST to mitigate the risk of cyclists slipping on the road, especially in wet weather conditions. There is a variety of color surface treatments, including street paints, cement- or asphalt-based surfacing, and anti-skidding coatings. However, this study specifically focused on the latter—anti-skidding coatings—which are currently used for the red bus and green bike lanes in Indianapolis.

Anti-skidding CST composition primarily involves an engineered binder system and high-quality, polish-resistant aggregate. Employing aggregates resistant to polishing effects is crucial for achieving great and durable skid resistance. Despite the widespread use of CST, comprehensive laboratory and field test data regarding its frictional performance and the associated aggregates are still limited. The design and application of CST mainly rely on the expertise of CSTs' manufacturers due to the proprietary nature of the products involved. It is important to note that even although both the CST and high friction surface treatment (HFST) may contain similar materials, their friction characteristics and performance may differ significantly due possibly to binder application processes.

Taking these factors into account, conducting a thorough examination of the frictional properties of the CSTs of both the red bus and green bike lanes and their aggregates holds considerable practical significance. These efforts are crucial for elevating safety standards in dedicated bus and bike lanes. By bridging existing knowledge gaps and attaining a comprehensive understanding of CST's frictional performance, informed decisions can be made to optimize its design and application. This, in turn, contributes to the creation of safer and more secure dedicated bus and bike lanes.

4.2 Materials and Field Testing

Both the CST red bus and green bike lanes in Indianapolis were installed in August 2019 (Andrew DiPiazza, personal communication, November 15, 2022). Some of the red bus lanes had been renovated again in October 2022. Both the red bus and green bike lanes utilized commercial products that commonly employ a methyl methacrylate (MMA) resin system for pavement area markings and anti-skid surfacing. Such a system typically consists of three components: pigmented resin, catalyst, and aggregate. The aggregate material chosen for the red bus and green bike lanes in Indianapolis was calcined bauxite aggregate 6×16 (1.18 mm~3.35 mm), a durable and high-friction material suitable for pavement surfaces. The properties of both the MMA binder and calcined bauxite aggregate, as well as the complete application process of CST, can be found elsewhere (Transpo Industries, n.d.).

To comprehensively evaluate the frictional performance of CST, a series of tests were conducted in September 2022 on Capitol Avenue in Indianapolis.

Figure 4.1 Bus and bike CST lanes in Indianapolis.

Outside Wheel Path Inside Wheel Path

Figure 4.2 Visual inspection on green bike lane.

The tests measured surface frictional properties, including surface texture MPD by laser texture scanner (LTS) and British Pendulum Numbers (BPN) by the British pendulum tester (BPT), on both the red bus lanes and green bike lanes. Specifically, LTS and BPT tests were conducted on the 3-year-old green bike lanes, whereas they were performed on both new and 3-year-old red bus lanes. After the renovation of the red bus lane on Capitol Avenue, field tests were conducted again in May 2023 to measure the surface friction number (FN) using the locked wheel skid trailer (LWST), which is interchangeably used with the locked wheel skid tester. In addition, surface texture MPD was measured using a texture measuring system reported elsewhere (Zhao et al., 2018) on both the resurfaced and old red bus lanes. The testing protocols strictly followed the ASTM or AASHTO standards, including ASTM E1845 (2015a), E274 (2020a) and E524 (2020c), and AASHTO T 278 (2021).

4.3 Green Bike Lane

Before conducting the LTS assessments for the green bike lanes, an on-site initial visual inspection was carried out. This visual inspection covered both the wheel path and adjacent areas, as shown in Figure 4.2. After approximately 3 years in service, there is no visible deterioration, such as chipping, peeling, cracking, or fading, on both the surfaces inside and outside the wheel path. This suggests satisfactory surface integrity and durability after around 3 years in service.

In the subsequent phase, a total of 15 test points were selected randomly for LTS texture measurements. The measured surface textures in terms of MPD are presented in Table 4.1. The average MPD values were 1.10 mm with a standard deviation of 0.16 mm outside the wheel path and 1.05 mm with a standard deviation of 0.14 mm inside the wheel path. The Technical Working Group of the FHWA recommends an average MPD value not falling below 0.75 mm, with an individual result threshold of 0.38 mm, to ensure satisfactory performance (Cairney & Styles, 2005; Hibbs & Larson, 1996). Both the observed texture depths inside and outside the wheel path met FHWA's stipulated requirements for the green bike lane. Also, the MPD measurements varied from point to point both inside and outside the wheel paths. The MPD values outside the wheel path do not consistently exceed their corresponding values inside the wheel path. However, the discrepancies between the average MPD values outside and inside the wheel paths are less than 5%. Evidently, wear from bicycle traffic will not lead to a significant reduction in the surface frictional properties of the green bike lanes after 3 years in service.

A series of BPT tests were also conducted with a $6 \times 25 \times 76$ mm slider at six randomly selected locations,

TABLE 4.1
Measured Surface Textures on Green Bike Lane

	MPD (mm)	
Location	**Outside Wheel Path**	**Inside Wheel Path**
1	1.10	1.02
2	0.86	0.77
3	1.05	1.17
4	1.17	1.00
5	1.34	1.12
6	1.02	1.15
7	1.05	1.25
8	1.05	1.19
9	0.79	1.06
10	1.18	1.10
11	1.29	0.92
12	1.02	0.82
13	1.28	1.09
14	0.99	1.15
15	1.30	0.89
Average	1.10	1.05
Standard Deviation	0.16	0.14

TABLE 4.2
BPN Values on Green Bike Lane

	BPN	
Location	**Outside Wheel Path**	**Inside Wheel Path**
1	60	60
2	62	61
3	62	60
4	65	64
5	65	64
6	65	64
Average	63.2	62.2
Standard Deviation	2.1	2.0

and the results are presented in Table 4.2. These BPT values reveal a very similar average BPN value of 63.2 (with a standard deviation of 2.1) outside the wheel path and 62.2 (with a standard deviation of 2.0) inside the wheel path. This again indicates that wear from bicycle traffic will not lead to a significant reduction in the surface frictional properties of the green bike lanes. It is worth mentioning that the New York City Department of Transportation specifies a minimum skid resistance BPN value of 60 for colored lanes (NYC DOT, 2017). As shown clearly in Table 4.2, both the induvial BPT measurements and the average BPT values are either equal to or greater than 60, both inside and outside the wheel paths.

4.4 Red Bus Lane

An on-site visual inspection was likewise carried out on the old and newly resurfaced red bus lanes. The results of this visual inspection, for areas both inside and outside the wheel path, are visually illustrated in Figure 4.3. While the new red bus lane exhibits almost no deterioration in the surface, the 3-year-old red bus lanes exhibit cracking, chipping, and staining. As reported elsewhere (Wei et al., 2021), the coefficient of thermal expansion of the CST material mix is significantly higher than that of HMA or PCC. This simply implies that thermal incompatibilities will arise between CST and the underlying HMA or PCC pavement. Therefore, any defects, especially cracks, pits, and repair patches in the surface of the underlying pavement, will reflect through the CST.

Moreover, a total of 15 randomly selected test points underwent LTS texture testing before the CST was resurfaced. The results are presented in Table 4.3, which shows an average MPD value of 0.23 mm for areas outside the wheel path and 0.22 mm for areas inside the wheel path. Correspondingly, the standard deviations were 0.05 mm and 0.04 mm, respectively. Carry et al. (2012) reported MPD values of 1.51 mm and 0.99 mm, respectively, measured in a red MMA with aggregate (anti-skid) bus lane in New York City two weeks after installation and after 6 months in service. Because there are no field MPD test values reported for a CST red bus lane of 3 years old so far, this study reviewed the MPD values measured over an 18-month period for HFSTs made up of epoxy resin and calcined bauxite aggregate of similar size as reported by Zhao et al. (2021).

As shown in Figure 4.4, the MDP value of HFST is around 1.91 mm immediately after installation,

Figure 4.3 Photos of red bus lanes (left and middle: old; right: new).

TABLE 4.3
Measured Surface Textures on Red Bus Lane

	MPD (mm)	
Location	**Outside Wheel Path**	**Inside Wheel Path**
1	0.34	0.26
2	0.25	0.18
3	0.21	0.23
4	0.19	0.19
5	0.25	0.24
6	0.19	0.25
7	0.20	0.22
8	0.28	0.22
9	0.26	0.18
10	0.20	0.22
11	0.20	0.17
12	0.18	0.15
13	0.28	0.27
14	0.16	0.29
15	0.21	0.22
Average	0.23	0.22
Standard Deviation	0.05	0.04

decreases significantly within two months, and then decreases very slowly and consistently afterwards. The total decreasing rate is around 34.8% within the first 2 months and slightly less than 5% over the remaining 16 months. If a hypothesis that the MPD of HFST will decrease at a consistent rate after the first two months is valid, the average MPD of HFSTs will be around 1.12 mm after 3 years (36 months) in services. As mentioned earlier, Carry et al. (2012) reported an MPD value of 1.51 mm for a new CST red bus lane, 20% less than the MPD of new HFST. The above can be extended to suggest that the surface MPD value of CST may be much lower than that of HFST, especially as time increases.

Although the MPD of CST may decrease more rapidly due to factors such as bus traffic wear and frequent starts and stops, one possible reason is that the installation process of HFST is entirely different from that of CST. The installation of HFST involves first applying a consistent layer of resin binder and then broadcasting of a uniform layer of bauxite aggregate. The installation of CST, however, involves first mixing the three components (pigmented resin, catalyst, and aggregate) thoroughly, and then pouring and spreading the mixed material evenly onto the pavement surface. Therefore, voids between aggregate particles are filled completely with the binder, and the surfaces of aggregate particles are entirely coated by the binder. Consequently, the MPD of CST will be lower than that of HFST. It is doubtful that an MPD value of around 0.20 mm (see Table 4.3) is sufficient for an anti-skidding CST, especially in rainy seasons. The above may warrant use of larger bauxite aggregates in CST, instead of the bauxite aggregate size of 6×16 commonly used in HFST.

The red bus lanes on Capitol Avenue, except for certain sections between West New York Street and West Ohio Street, were resurfaced in October/November 2022 (Matthew Duffy, personal communication, May 12, 2023). Field tests were further conducted to measure surface MPD and friction on the resurfaced red bus lanes in May 2023, approximately 6 months after installation, and the results are presented in Table 4.4. The average friction number lies between 32 and 36, and the MPD values lie between 0.78 mm and 0.85 mm for the newly resurfaced red bus lanes. Carry et al. (2012) also reported a friction of 0.34 (friction number = 34) of for a red bus lane of 2 weeks old and 0.35 (friction number = 0.35) after 6 months in service. These friction numbers were measured at 30 mph (the type of test tire was not reported). Wei et al. (2021) reported friction numbers of 83.4, 87.8, 80.9, and 82.8 (smooth tire and 40 mph) for HFSTs after 0, 6, 12, and 18 months in service, respectively. Evidently, the bauxite aggregate can provide durable friction performance. However, the friction performance of CST is significantly lower than that of HFST. Again, this may also warrant use of bauxite aggregate larger than size of 6×16 in CST.

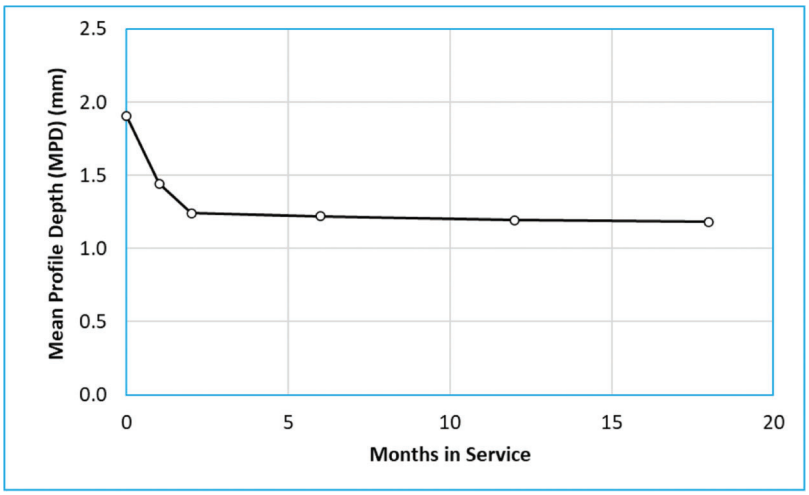

Figure 4.4 Variations of MPD over time (replotted from Zhao et al., 2021).

TABLE 4.4
Measured Friction Values on New and Old Red Bus Lanes

Section	No. of Tests	Average Friction Number (FN)[1]	MPD(mm)	Note
10th Street ~ St Clair Street	12	35.9	0.854	Resurfaced
West New York Street ~ West Ohio Street	7[2]	30.2[2]	0.844[2]	Resurfaced and Old
West Ohio Street ~ West Market Street	5	32.5	0.788	Resurfaced

[1]Friction tests were conducted with a standard smooth tire at 40 mph.
[2]Combined data for both resurfaced and old red bus lanes because they could not be divided precisely.

5. CHAPTER 5. PRACTICABILITY OF FRICTION TESTING WITH A LOCKED WHEEL SKID TRAILER AT HORIZONTAL CURVES

5.1 Problem Statement

Locked wheel skid trailer (LWST) is widely employed by various Departments of Transportation (DOTs) to test the pavement skid resistance at the network level as per ASTM E274 (ASTM, 2015). This method calculates the tire-pavement friction coefficient or friction coefficient number by considering the friction force at the interface of a locked wheel and the pavement surface, relative to the vertical load on the wheel. Tire-road friction is affected by numerous factors, one of which is the change in vehicle operating parameters developed from the geometric properties of a pavement structure (Kogbara et al., 2016).

However, the applicability of the LWST friction test on horizontal curves, despite the prevalence of such roadway configurations, poses challenges. The method, designed for straight and level pavement segments, may encounter reliability issues during cornering due to biased tire speed and force measurements, lack of information on vehicle side friction, and the potential for risky trailer fishtailing (NCHRP et al., 2009). Despite the fact that a considerable portion of highways feature horizontal curves, crucial for network-wide friction assessment, the routine LWST friction monitoring program often neglects these areas. This oversight is significant, considering that horizontal curves exhibit approximately three times the crash rate compared to tangent segments in the entire highway system of the Indiana Department of Transportation (INDOT) (Li et al., 2017). Although pavement friction tests can be performed on any roadway sections at various driving speed, the LWST field friction test method is designated for straight and level pavement segments only (NCHRP et al., 2009). Possible reasons that the LWST test may fail to provide reliable friction data during vehicle cornering are biased tire speed and force measurements, missing information of vehicle side friction, and risky tailer fishtailing. Highway engineers have stressed the importance of timely friction measurements on surface spots of mainline pavement covered in the network regardless of the roadway geometric properties such as radius of curvature and superelevation rate (Albin et al., 2016). Most of the highway in-service are designed full of horizontal curves and such sections should not be avoided on purpose during the routine LWST friction monitoring program. Moreover, the average crash rate for highway horizontal curves is reported about three times that of tangent segments with a flat surface on the INDOT's entire highway system (Li et al., 2017). However, a viable method assessing the LWST friction result of test spots on horizontal curves is lacking, contributing to the unavailability of a significant portion of the collected raw friction data measurements. Therefore, it is essential to investigate the standard LWST friction test program's practicability on crash-prone areas such as horizontal curves. Qualitative and quantitative performance of the collected LWST friction data under such conditions requires further assessment. The standard friction test program using such an articulated vehicle with relatively lightweight trailer needs a practical data correction method that allows for reliable LWST friction measurements on horizontal curves.

As the lateral motion of a LWST is governed by the lateral force the horizontal curved road generated to the tires. Knowledge of the lateral force plays a key role in understanding handling performance and lateral stability control of any articulated vehicle on horizontal curves. Sideslip angle, the angle between the tire orientation and its actual direction of travel, is a critical vehicle state to be measured for vehicle cornering analyses. When the centrifugal lateral acceleration is small, the rear wheels on trailer develop small slip angles and track the inboard side of vehicle body. For small side slips, the resulted lateral friction force on tire-pavement contact patch increases approximately linearly with the increasing value of sideslip angle (Dugoff et al., 1970). Both hysteresis and adhesion, the two primary mechanisms of the tire-road surface friction, depend on the developed small slip (Gillespie, 2021). If the sideslip angle is large and the lateral acceleration increased on a tight curve at high speed, the test trailer of a LWST could lose stability and drift outboard, resulting in a failure of friction measurement. Sensing the magnitude and direction of test wheel sideslip angle is significant to ensure LWST stability during friction test on horizontal curves. In conventional studies, direct sideslip angle measurement has been an expensive and arduous task. Hence, estimation algorithms using transient or dynamic based vehicle models with

simplifications are typically proposed, often limiting the scalability for real-time field applications (Jeong et al., 2022). GPS aided algorithms have also been studied for vehicle sideslip angle estimation (Yoon & Peng, 2014). However, the achieved precision level is limited due to the low sampling rate and noisy natural of GPS signals (Park et al., 2018). A commercial Corrsys Datron Correvit sensor (Caroux et al., 2007) can measure the slip angle within $\pm 15^{\circ}$ at speeds higher than 10 km/h (6 mph). The sensor is at high cost, heavy, and has limitations to field friction tests. Camera-based solutions with advanced computer-vision image processing algorithms have been recently introduced to employ measurements in vehicle dynamic tasks with cost and time efficiency (Botha & Els, 2014; Fuchs et al., 2015). Botha and Els (2015) introduced a camera-based tire-road interface parameter measurement method for vehicle traveling at a low-speed level and off-road conditions. De Saxe et al. (2019) validate the accuracy of camera-based slip angle measurements by comparing the measured results with measurements from a commercial sensor during sample field tests.

Besides, a LWST used in field friction tests consists of a relatively light weight test trailer towed by a pick-up tractor. For such an articulated vehicle, the articulation angle between the headings of trailer and tractor body units is another critical component for vehicle lateral maneuverability and stability control. A small articulation angle during cornering is desired for articulated vehicles to avoid extreme oversteer that causes instability such as trailer fishtailing and jackknifing. Previous safety-oriented studies measure the articulation angle with combined modeling analysis to develop stability enhancement or alert systems for articulated vehicles (Chu et al., 2010). State observers, which make use of both sensing information and models, require knowledge of vehicle parameters and produce limited accuracy in full-scaled field tests (Ehlgen et al., 2008). Recent camera-based works have been demonstrated in literatures addressing remote articulation angle sensing in the field but are limited to certain types or shapes of trailers (De Saxe & Cebon, 2021). Caup et al. (2013) shows reliability in articulation angle measurement using a single rear-facing camera. A single digit level of measurement error is obtained for camera-based methods compared to ground truths from mechanical sensor measurements.

Although the aforementioned computer vision-based techniques have been proved to provide measurements for vehicle operating parameters with minimal effort, no existing sensing system has shown compatibility with a LWST in field implements, in which the vehicle articulation angle and the test wheel sideslip angle must be measured simultaneously and assessed for correcting the tire-road friction measurements. In this study, the performance of a LWST operating on horizontal curves was evaluated in a mechanistic-empirical manner. The investigation was realized by completing three main tasks.

1. The mechanistic relationships among vehicle operating parameters and the equilibrium of force properties exerted on the tire-road interface were theoretically investigated in particular for articulated vehicles and tire cornering scenarios on horizontal curves.
2. A dual-camera-based slip angle and articulation angle measurement setup for a LWST during in-situ friction field tests was proposed. Captured video frames were utilized in image processing algorithms for real-time test tire speed, tire sideslip angle, and vehicle articulation angle measurements with high accuracies. The camera-upgraded system can monitor instant directional behaviors of a LWST traversing on both straight pavements and horizontal curves during friction tests without interruption. Based on the time series of measured variables recorded from individual test time intervals, the data mean value was obtained for empirical investigation.
3. The variation of the averaged variable measurements in terms of test speed level and pavement geometric properties was examined through several configurations of field testing. Relationships and equations from the mechanistic investigation were validated and analyzed to allow upgradation of the current INDOT's friction test program. Along with data from the standard LWST speed sensor and force transducer, the upgraded tester operated as a vehicle side friction sensor and an oversteering alert system. The impact of pavement horizontal alignment design on LWST friction measurements and the test performance were assessed. The investigation extended LWST practicability on highway horizontal curves with evaluated restrictions.

5.2 Mechanistic Analysis of Tire-Pavement Frictional Interaction at Horizontal Curves

5.2.1 Vehicle Dynamics and Physical Constraints

In cornering maneuvers of an articulated vehicle such as LWST, the changes in speed and direction of two vehicle body units lead to the development of side friction forces at the tire-road interfaces. Tire lateral force (i.e., cornering force) is paramount to vehicle safety control. Lateral force can be resulted by lateral deformation of the tire-pavement contact patch, by lateral inclination of the road, or a combination of both (Pauwelussen, 2015). Camber angle, the lateral inclination angle between the wheels plane normal direction and the road surface, can be easily obtained by measuring the highway superelevation rate using a leveling tool. First consider the articulated vehicle as a 2DOF linear rigid model under steady state motion in the plane parallel to the road's surface, neglecting the vehicle width, camber, and aerodynamics (Figure 5.1).

For a LWST testing on horizontal curves, the speed difference between the inner and outer wheels is negligible since the pavement radius of curvature is extremely greater than the vehicle width. The bicycle model shown in Figure 5.1 displays the physical constraints of the LWST in terms of tire lateral forces and velocities with simplicity (Rajamani, 2012). In such model, like in LWST, the vehicle is front steered only. As a result, the heading direction of the trailer wheels is the same as the

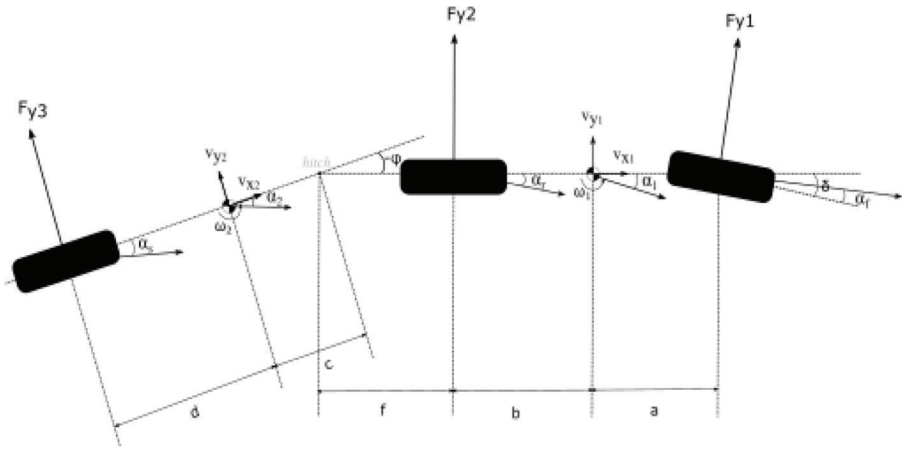

Figure 5.1 Bicycle model for articulated vehicle.

TABLE 5.1
States of the LWST Bicycle Model

Symbol	Parameter	Unit
δ	Front wheel steering angle	rad
α_i	Sideslip angle of the i^{th} unit	rad
α_f, α_r, α_s	Sideslip angle of the front, rear, and trailer axle, respectively	rad
ω_i	Angular velocity (yaw rate) of the i^{th} unit	rad/s
φ	Vehicle articulation angle	rad
v_{xi}	Longitudinal velocity of the i^{th} unit	mph
v_{yi}	Lateral velocity of the i^{th} unit	mph
F_{yi}	Lateral friction force of the i^{th} axle	lbs

heading of the trailer body. The longitudinal forces can be neglected assuming constant traveling speed during a friction test. Therefore, the centrifugal accelerations are balanced with the summation of tire lateral forces (Ma, 2020). The states of the model are listed in Table 5.1.

When the vehicle is driving straight forward ($\varphi = 0$), slip angle is zero for all the tires and the speed is identical among different axles. However, for vehicles turning on horizontal curves, both the vehicle articulation angle and the tire sideslip angles arise. In this particular case, the speed of the trailer test wheels becomes different from the tractor speed which is provided by instrumentation of the vehicle. Calibration of tire testing speed for a LWST friction test performed on horizontal curves is needed to reconstruct the actual relationship between test speed and tire-road friction coefficient.

The hitch joint is a kinematic point connection between the two vehicle body units. By utilizing rigid body principles, the velocity of the hitch joint can be calculated with respect to the velocity of both the tractor center of gravity (CG) and the trailer wheel axle, as shown in Equation 5.1. The middle part and right part of the equation represents the vector of hitch velocity calculated through the tractor CG and the third axle, respectively.

$$\begin{bmatrix} v_{xh} \\ v_{yh} \end{bmatrix} = \begin{bmatrix} \cos\varphi & -\sin\varphi \\ \sin\varphi & \cos\varphi \end{bmatrix} \begin{bmatrix} v_{x1} \\ v_{y1} - (b+e)\omega_1 \end{bmatrix} = \begin{bmatrix} v_{xs} \\ v_{ys} \end{bmatrix} + \begin{bmatrix} 0 \\ (c+d)\omega_2 \end{bmatrix} \quad \text{(Eq. 5.1)}$$

where $V_h = [\, v_{xh} \quad v_{yh} \,]^T$ is the velocity at the hitch joint, expressed in the trailer-body local coordinates. $(b + e)$ is the longitudinal distance between the tractor CG and the hitch joint, and $(c + d)$ is the length of the trailer. In the linear case of slip angles, the longitudinal and lateral components of the test wheel velocity V_s can be defined as a function of ($cos\ \alpha_s$, $sin\ \alpha_s$).

It is realistically assumed the articulation angle is small ($cos\ \varphi = 1$ and $sin\ \varphi = \varphi$) and longitudinal velocities are constant. The longitudinal and lateral velocities can be expressed as:

$$\begin{aligned} v_{xh} &= v_{x1} = v_{xs} = v_x \\ v_{yh} &= \varphi v_x = v_{y1} - (b+f)\omega_1 = v_{ys} + (c+d)\omega_2 \end{aligned} \quad \text{(Eq. 5.2)}$$

The above equation can also be expressed as in Equation 5.3, which calculates the locked wheel slip

angle in terms of the slip angle of the tractor unit, indicating that the two variables are dependent.

$$\alpha_s = \varphi + \alpha_1 - \frac{(b+f)\omega_1 + (c+d)\omega_2}{\upsilon_x} \qquad \text{(Eq. 5.3)}$$

where the value of angular velocity can be approximately calculated as the ratio of the tangential velocity and the radius of curvature. The kinematic constraint for the articulation angle can be calculated as:

$$\dot{\varphi} = \omega_2 - \omega_1 \qquad \text{(Eq. 5.4)}$$

Therefore, the assumption of consistent angular velocity ($\omega_1 = \omega_2 = \omega$) is valid only when $\dot{\varphi} \approx 0$, indicating the requirement for vehicle lateral stability and neutral steering. The radiuses of curvature among vehicle body units are assumed identical based on relatively large radius of curvature in most highway horizontal curves. Lateral stability is required for reliable friction test as the measured friction coefficient is calculated from the averaged value of wheel force measurements observed during a test time interval (ASTM, 2015). Instability may happen for high-speed testing on a horizontal curve with limited radius of curvature as the trailer equipped with a locked wheel will show excessive oversteer and cause trailer fish-tailing. In this case of test failure, the absolute value of articulation angle could decrease as much as 10 deg/sec during the short 1-sec data-averaging time interval of a LWST friction test.

Substituting the linear (*cos* α, *sin* α) function for velocity components in Equation 5.2 with assumption of small angles, the relationship between the tractor speed V_1 and the test wheel speed V_s upon an empirical constant value C can be approximately expressed as in Equation 5.5.

$$V_s = \frac{V_1}{\sqrt{1 + (\alpha_s - \varphi + C/R)^2}} \qquad \text{(Eq. 5.5)}$$

where C/R is a dimensionless value that depends on length of the vehicle body units and the pavement radius of curvature. The C value for a LWST vehicle can be empirically estimated using the measurements of tractor and locked wheel speeds, test wheel slip angle, and articulation angle properties from multiple field friction tests on horizontal curves.

5.2.2 Tire Model Without Camber

The lateral force of a pneumatic tire varies with both the slip angle and the cornering stiffness. Cornering stiffness, the slope of the lateral force versus tire slip angle curve near the origin, is asserted the determining variable that governs the cornering properties and stability performance of vehicles in a normal driving region (Bergman & Beauregard, 1974). Tire cornering stiffness is dependent on numerous tire properties, including the material, size, vertical load, inflation pressure, and tread pattern. The influence of the above factors on tire stiffness is nonlinear and extremely complex. The slip angle, on the other hand, is a function of the lateral and longitudinal tire velocities and is feasible to be measured from captured images of real-time wheel paths.

The locked tire slip ratio is negligible as the LWST only measures the tire-pavement skid resistance at a 100% slip ratio (NCHRP et al., 2009). For the locked test tire during a LWST friction test at a horizontal curve without camber (or superelevation), the tire cornering stiffness is at its minimum. A linear tire model (Equation 5.6) can be applied with pure slip condition and small sideslip angles ($\alpha_s \ll 1$), independent to the linearity of the locked wheel tire slip model in Equation 5.7 (Jeong et al., 2022). The tire model indicates that the relationship between lateral force and slip angle remains in linear region when the lateral force is smaller than half of the total friction force (van Ginkel, 2014).

$$F_y \approx -\frac{\partial F_{y3}}{\partial \alpha_s} | \alpha_s = 0 \quad \alpha_s = -K_s \alpha_s \qquad \text{(Eq. 5.6)}$$

$$F_y = F_x \ tan \ \alpha_s \approx F_x \alpha_s \qquad \text{(Eq. 5.7)}$$

where K_s is the test tire cornering stiffness at a 100% slip ratio. F_x is the tire longitudinal force taking place on the tire-pavement interface in the plane parallel to roadway surface.

The LWST is equipped with a dual axis force transducer on the test wheel, which can provide the averaged data of two test tire force properties within a 2,000-lbs range during a friction test: a vertical force F_z that is normal to the road surface and a longitudinal friction force F_x that is parallel to the handing direction of the trailer body. According to a modified Dugoff model (Doumiati et al., 2011), tire cornering stiffness K_s is not a constant value with respect to the normal load transfer and can be represented using a 2nd order polynomial model in terms of the normal force F_z. In the case of pure side slip, the longitudinal friction force F_f and the vertical force F_z measured for a test tire can be used to estimate the cornering stiffness absolute value of a standard test tire using $K_s = F_x / \alpha_s \approx F_x \alpha_s / \alpha_s = F_x$. The cornering stiffness polynomial regression coefficients can be empirically estimated through a data fitting between field measurements of F_x and F_z.

5.2.3 Impact of Lateral Inclination

Highway horizontal curves are commonly constructed with a superelevation rate, denoted as e, indicating lateral inclination. In such cases, an additional force known as "camber trust" contributes to the total lateral force, replacing Equation 5.6 with the following.

$$F_y = K_s \alpha_s + F_z \tan \gamma = K_s \alpha_s + F_z e \qquad \text{(Eq. 5.8)}$$

where $F_z e$ is the additional lateral force and γ is the road camber angle (or superelevation rate). The frictional

force measured by LWST wheel force transducer includes only the longitudinal friction force, which decreases as the lateral force increases. The additive camber trust is much less than the side slip for a same level of camber and sideslip angle (Gillespie, 2021).

When vertical load increases, the measured friction coefficient will reduce as the increases in friction force and vertical force are not proportional to one another (Gillespie, 2021). In a standard LWST test employed on straight pavement, the vertical load is assumed a constant value with negligible impact from test water delivery and texture roughness of pavements. However, the added superelevation and the radius of curvature of a cornering maneuver will influence the tire vertical force measured from friction test on horizontal curves. Field friction test scenarios with vertical force that is measured far away from the standard value on straight pavement tests can result in unreliable test results for pavement friction coefficient.

Due to the inertial lateral acceleration of the vehicle units at their CGs, unevenness additional to the lateral inclination are applied to vertical loads on the left and right trailer wheels available in a LWST test when making turns on a horizontal curve. The total cornering impact on a test tire vertical force can be estimated from force equilibriums in the plane normal to the tires' handing direction (Equation 5.9), in which the positive sign applies to an outboard test tire. The superelevation rate $e = \tan\gamma$ is assumed small ($\cos\gamma = 1$ and $\sin\gamma = \gamma$) for most highway horizontal curves. This mechanistic relationship will be empirically examined using experimental test results of vertical force on test tire.

$$F_z \cong F_Z{}' + \left(\frac{c}{c+d}\right)\frac{mV_s{}^2}{2R}e \pm \frac{h}{w}\left(\frac{mV_s{}^2}{R} - mge\right) + \epsilon \qquad \text{(Eq. 5.9)}$$

where $F_Z{}'$ is an estimated standard test tire vertical force collected from straight pavement tests; m is the trailer lumped mass and the weight is assumed symmetrically distributed among the left and right tires; h is the height of the trailer's CG; g is the gravity acceleration quantity; and ϵ contains measurement errors in a field test.

5.3 Camera-Based Sideslip Angle and Articulation Angle Measuring

The second task involves a vision-based method for simultaneous test tire slip angle and vehicle articulation angle measurements. The method is composed of three main steps: (1) camera setup and calibration, (2) the dual-camera-based time series monitoring of measured variables through field tests, and (3) friction test time data-averaging.

5.3.1 Calibration

Consumer-grade cameras, especially the ones with wide lens, are affected by optical distortion that cause measurement error in their captured video frames. Therefore, the distortion effects are removed using camera intrinsic matrix estimated through a calibration procedure (Zhang, 2000) before applying the cameras to field tests for angle measurements. Once the distortion removal step is done, a camera's intrinsic parameters remain constant during the tracking mode. Time series of test wheel longitudinal and lateral velocity as well as rotational behavior of vehicle hitch joint can then be measured simultaneously by analyzing camera pose changes in video recordings frame by frame.

The tracking mode of any vision-based monitoring method requires precise pose estimation of the target object in camera's region of interest (ROI). The Cartesian coordinates of an arbitrary point in the 3D world can be written as $[\,X_\omega \quad Y_\omega \quad Z_\omega \quad 1\,]^T$. Using a pinhole camera model, vector $[\,u_i \quad v_i \quad 1\,]^T$ represent the of the 2D pixel coordinates of the same point on the image plane. The perspective projection relationship between two vectors is:

$$s\begin{bmatrix} u_i \\ v_i \\ 1 \end{bmatrix} = [C] \times [R|t] \times \begin{bmatrix} X_\omega \\ Y_\omega \\ Z_\omega \\ 1 \end{bmatrix} \qquad \text{(Eq. 5.10)}$$

where s is a scale factor donating the pixel distance between the image plane and the camera's projection center. C is the camera intrinsic matrix containing parameters obtained in the calibration procedure with removed optical distortion. The extrinsic matrix $[R|t]$ includes three orthogonal rotational vectors r_x, r_y, and r_z and one translational vector t.

Moreover, the vertical vibration of both the trailer body unit and the hitch joint is negligible due to the high stiffnesses. Therefore, object tracking algorithms employed in both cameras are assumed as planar motion tracking. Any point on the image plane can be considered has identical height in 3D world coordinates ($Z_\omega = 0$) after perspective correction. Hence, we can dense out r_z and the projection between the target motion plane and the image plane becomes a homography mapping.

$$[C] \times [\,r_X \quad r_Y|t\,] = \lambda[\,h_1 \quad h_2 \quad h_3\,]$$

where $H = [\,h_1 \quad h_2 \quad h_3\,]$ the 8 DOF homography matrix, which is unique up to a nonzero scale factor λ. The classical approach of homography decomposition (Zhang, 2000) is followed to estimate parameters in camera extrinsic matrix using world coordinates of at least four target points.

5.3.2 Locked Wheel Slip Angle Measuring Algorithms

The speed and sideslip angle of a test wheel during LSWT friction tests are trackable by recording the instant longitudinal and lateral velocity of the wheel motion with time. Since LSWT is a front steered only vehicle, the orientation of test wheels aligned with the

orientation of the trailer body. Instead of directly measuring the invisible motion of the tire carcass underneath, the relative motion between the trailer body and the pavement surface near the tire is the tracking objective of the sensor camera. This slip angle measurement setup comprises a camera that is rigidly mounted on the side of trailer body and facing down to capture the road surface in front of the test wheel. The tracked longitudinal and lateral pavement motion relative to the camera over the road surface can be considered the apparent planar motion of test tire. By tracking multiple texture feature points detected from the pavement surface in the camera's ROI over a sequence of calibrated video frames, we can estimate the target motion as averaged pixel longitudinal and lateral displacements frame by frame. In the end, the amplitude and direction of the detected planar motion in scale represent the test wheel's speed and sideslip angle. As discussed in the previous section, the scaling value is obtained using pose estimation of a calibration board attached to the ground before the start of motion ($\alpha_s = 0$).

Instead of tracking the motion of a fixed object, the slip angle measurement algorithm requires an additional detection step of trackable feature points located from pavement textures in each video frame during the vehicle movements. Shi-Tomasi corner detection is used to identify easy-to-track feature points (Shi & Tomasi, 1994) and Lucas-Kanade sparse optical flow technique is used as the motion tracker for the purpose of computational efficiency (Lucas & Kanade, 1981). The overall accuracy of the Kanade–Lucas–Tomasi (KLT) motion tracker depends on performance of both the corner detection and the optical flow tracking.

Consider two consecutive video frames I_t (x, y) and I_{t+1} (x, y) in grayscale values, where x and y are the pixel coordinates. The feature tracking algorithm aims to find an image velocity $[u, v]^T$ such that I_t (x, y) and I_{t+1} $(x + u, y + v)$ are "similar." The similarity measured within multiple pixels in a neighborhood of size $(2w_x + 1, 2w_y + 1)$ is needed for the aperture problem. The target velocity $[u, v]^T$ of an image feature point $[x_0, y_0]^T$ is the least square solution that minimizes the residual function as follows:

$$\sum_{x_i = x_0 - w_x}^{x_i = x_0 + w_x} \sum_{y_i = y_0 - w_y}^{y_i = y_0 + w_y} (I_t(x_i, y_i) - I_{t+1}(x_i + u, y_i + v))^2 \qquad \text{(Eq. 5.11)}$$

Efficient corner detection of feature points requires large variation of pixel intensity in camera's ROI. Most paved road surfaces as a mixture of aggregates exhibit enough texture, except for areas that are fully covered with pavement markings with consistent brightness. Figure 5.2 represents limited tracking performance of the proposed method when large area of three different colors of pavement marking is captured in camera ROI. As shown in the pictures, large pavement markings in camera ROI could provide insufficient easy-to track feature points specially for higher speeds.

Figure 5.3 depicts a good example of the motion tracking obtained from two calibrated consecutive video frames over an asphalt road surface. The green line traces showing the good measures of the target instant motion displacement of the test tire. The red line traces are incorrect tracking measurements that are removed using an outlier rejection based on a combination of the RANSAC algorithm (Fischler & Bolles, 1981) and the spatiotemporal relationship between consecutive displacement measurements. The outlier filter uses an iterative procedure to make sure that each remaining feature point travels with a pixel displacement that is similar to both the other good features and the motion of the previous pair of frames. In Figure 5.3, the corner detector provides enough feature points and the majority of them were travelling in the same direction with same speed.

Accuracy and robustness are the two critical components of any feature tracker. Naturally there is a tradeoff between the accuracy and robustness components. The local accuracy of sub-pixels for this pavement motion tracking application is not very sensitive to the choice of integration window size as all the scene points in camera's ROI theoretically move with the same target velocity. On the other hand, the robustness component relates to the sensitivity of the changing in pavement texture as well as the size of apparent motion. Pyramid levels of image resolution were employed to handle large motion. In most cases, motion in an image going beyond a max pyramid level of 4 has extreme computational cost and make less improvement in accuracy. The spatiotemporal relationship between consecutive video frames can estimate the reasonable motion size according to the previous tracking result. Therefore, an iterative implementation of the optical flow algorithm with various window sizes to allow tracking at various speed levels. A fixed

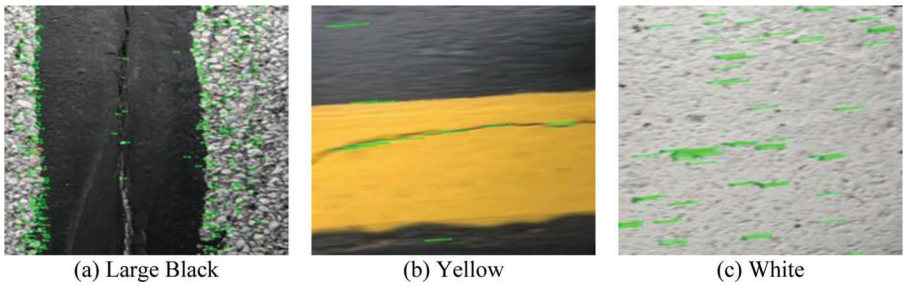

(a) Large Black (b) Yellow (c) White

Figure 5.2 KLT tracking performance on images of pavement marking.

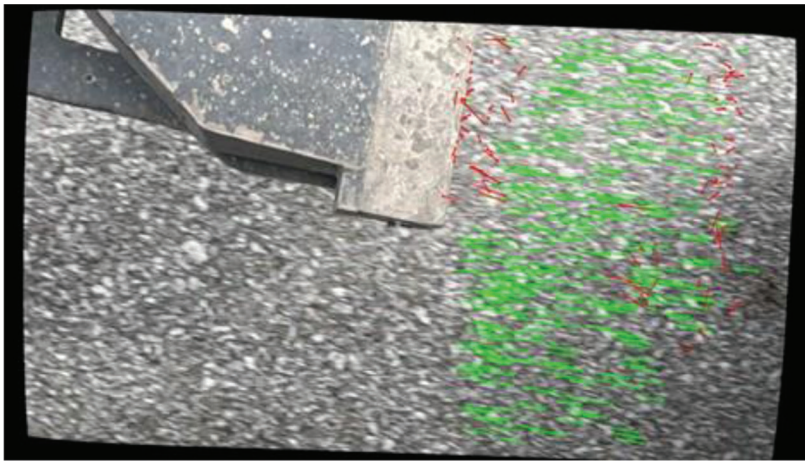

Figure 5.3 Motion tracking of good corner features and outlier (red) rejection.

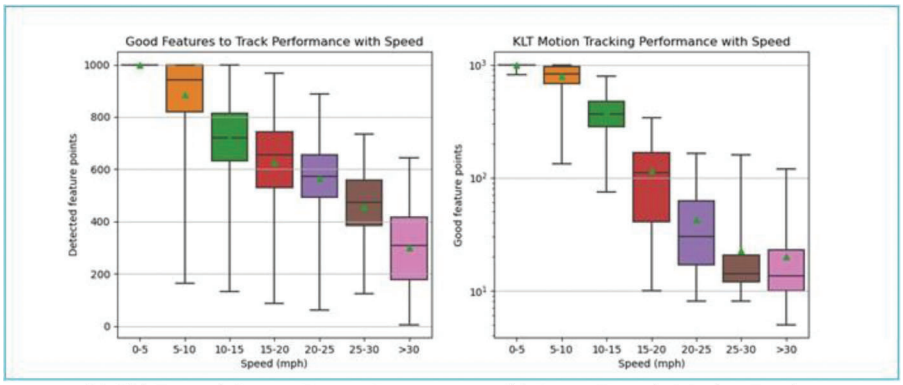

(a) Shi-Tomasi Corner Feature Detector (b) Lucas-Kanade Motion Tracker

Figure 5.4 Performance of the algorithms over asphalt road surface.

maximum pyramid level of 4 is selected to provide sufficient local tracking accuracy. Figure 5.4 shows the performance of two algorithms conducted in the proposed method over a typical asphalt road surface. Images blur when the vehicle (camera) moves at high speed. Thus, the accuracy of both the Shi-Tomasi corner feature detector and the Lucas-Kanade motion tracker declines as speed increases. The performance of Lucas-Kanade motion tracker (KLT) declines more rapidly as it compares feature points from two video frames. Other factors such pavement surface texture consistency and pavement marking obstacle in the image ROI can also influence the method performance. Horizontal curves have smaller speed limits compared to straight segment with same structural design. As shown in Figure 5.4, multiple good measures remain available when vehicles move at high speed (>30 mph), which is enough to obtain robust measurements of tire speed and slip angle. The mean measurement values of motion magnitude and direction among all the good feature points are the final results of the detected instant tire speed and sideslip angle with time.

5.3.3 Target-Based Articulation Angle Measuring Algorithm

Another camera is equipped for vehicle articulation angle tracking. Vison-based techniques for articulation angle measurement can be classified into either target-free or target-based categories. Target-free methods rely on natural tracking features and require no defined pattern pre-installed on the trailer at the camera's ROI. However, the measurement errors in the order of 1° for target-free approaches are not sufficient for small angles (Harris, 2013). This study implements a target-based articulation angle monitoring approach using a ArUco fiducial marker for improved robustness and precision of tracking (Ababsa & Mallem, 2004). The marker provides precise and robust detection of its four corner points and the detected image coordinates can be used for unique estimation of object pose estimation. In this approach, the fiducial marker is horizontally attached to the hitch joint on the trailer and is captured by a camera rigidly mounted on the back of the tractor as a passive target. This tracking algorithm takes the advantage to assume that the fiducial marker only

Figure 5.5 Calibrated video frame at zero articulation angle.

(a) For sideslip angle (b) For articulation angle (c) For tire forces

Figure 5.6 Sensers installed on LWST.

performs rotation (yaw) about the vertical axis normal to the vehicle plane. For pure 1D rotational tracking such as this articulation angle measurement, the error in scale factor estimation is not as sensitive as displacement tracking algorithms. Thus, λ can be simply estimated as the average of $1/\|C^{-1}h_1\|$ and $1/\|C^{-1}h_2\|$ for homography decomposition.

After pose estimation, the yaw rate of the marker in terms of time is obtained by subtracting its reference pose at the start of monitoring (zero articulation angle). Pose estimation of each video frame is compared against the start frame and thus minimized the accumulated draft-related error. Figure 5.5 depicts a sample image captured from the articulation tracking camera after an appropriate calibration process.

5.3.4 Experimental Setup

Two GoPro cameras are mounted as shown in Figure 5.6 to measure the real-time vehicle articulation angle and test tire sideslip angle when a standard LWST carries out full scale field friction tests at various scenarios. LWST is also equipped with a test tire force transducer to provide longitudinal and vertical forces of the left test tire during each friction test (Figure 5.6). Images in both cameras were captured at 1920 × 1080 resolution. The maximum frame sampling rate of 240 FPS is selected for tire motion detection camera. A lower sampling rate of 60 FPS is selected to save computational cost for articulation angle measurement which is a single object (the hitch joint) tracking.

5.4 Field Validation Testing

5.4.1 Testing on Airport Runways

Asphalt runways at Purdue Airport were selected as the test field of extreme cornering scenarios for their sharp curves and zero lateral inclination (Figure 5.7).

Three sharp horizontal curves with radius of curvature between 136-ft to 165-ft are used to investigate the LWST maneuverability and its friction test results under extreme cornering conditions. One straight road in the same field is also tested for comparison.

(a) Straight road (b) Left turn (c) Right turn

Figure 5.7 LWST testing on airport runway.

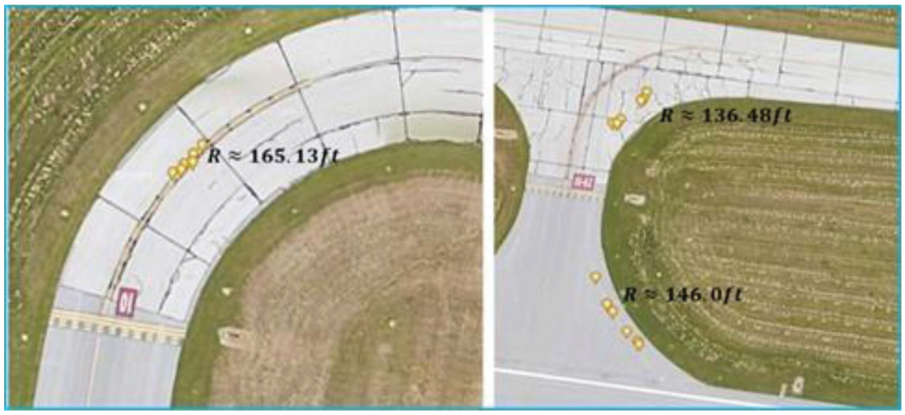

Figure 5.8 Footprints of friction tests on airport runway.

Figure 5.8 shows the map locations of all friction tests on curves at the time of wheel locking performed on airport runways. The vehicle turns left when traversing the left curve in Figure 5.8 and turns right on two curves on the right.

Significant declines in the absolute value of both the test tire sideslip angle and the articulation angle are observed in multiple airport friction tests, especially for tests performed at the 40-mph speed level. Figure 5.9 presents a sample measurement time series when the vehicle is making a right turn on the curve with 136.48-ft radius of curvature. The LWST force transducer measures forces by averaging data recorded in a fixed 1-sec test time window. Therefore, the monitoring data of camera measured variables also needs data-averaging. During each of the friction tests, this experimental vehicle tester delivers water in front of the test tire at first. Approximately 0.5-sec later, the test wheel will be fully locked. After a 0.4-sec wait stable testing, 1-sec of test time interval is used as the duration of data-averaging for force measurements. In final speed and angle measurements of field tests, 1-sec length of time intervals that are the same as the ones used in force measurements are located to provide the averaged tire sideslip angle and articulation angle as the results for data analysis.

The friction test involved in Figure 5.9 was performed at time equal 1,328–1,329 sec. The articulation angle is rapidly changing when the test smooth tire is locked, indicating that the trailer lost stability and drifted to the outboard direction (fishtailing) in a very short test time interval. The tire side slip angle also decreases more than expected because of the instability. As a result, the data time series of the two angle measurements are unstable during the 1-sec time interval. The resulted 3.92° of slip angle and -0.35° of articulation angle averaged from this data are much smaller (in absolute value) than expected under stable assumptions. The friction test was unreliable even if the tire force transducer provided a friction coefficient result 771-lbs/1,271-lbs = 0.607.

Three test speed levels: 15-mph, 25-mph, and 40-mph were selected. In total of nine combinations of speed level and test curve radius were tested at the airport field. The test trailer lost its stability during tests at 40-mph, low speeds are preferable for sharp curve tests. Additionally, three speed levels (15-mph, 20-mph, and 25-mph) were tested for both left turn and right turn on the curve with R = 165.13-ft radius so that the unevenness in test tire vertical load can be analyzed. Each test scenario is repeated at least two times. Detailed measurement results of test tire sideslip angle and vehicle articulation angle for different configuration of friction test in the airport field are listed in Appendix B.1.

5.4.2 Testing on Two-Lane Road

Superelevation works together with side friction to offset the centrifugal outward pull of vehicle body units and allows a vehicle to traverse horizontal curves at higher speeds (INDOT, 2013/2022). An 8% maximum rate of superelevation for urban and rural facilities with a large design speed (V > 45 mph) is typically used in

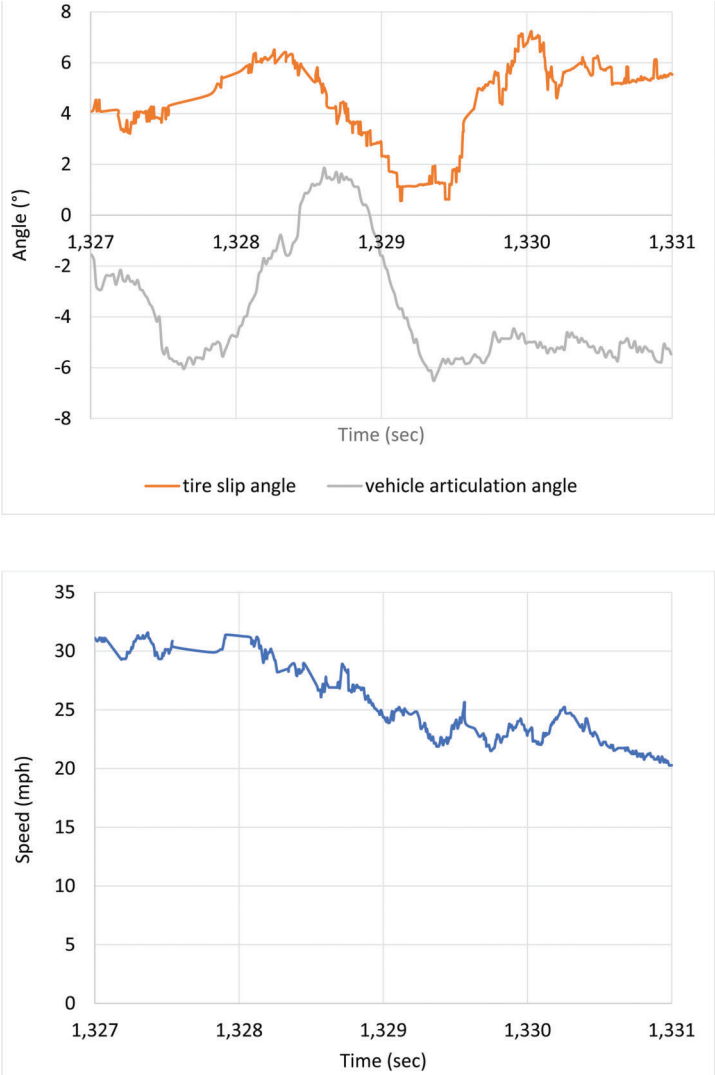

Figure 5.9 Time series of friction testing on a right turn runway.

highway pavement design. Two two-lane asphalt pavement curves on SR-26 are selected to further investigate the impact of lateral inclination on LWST test performance (Figure 5.10). The two curves have the same radius of curvature R = 1,438-ft, similar superelevation rates (7.71% and 8.33%) and comparable pavement macrotexture (Mean Profile Depth or MPD) in both driving directions. Furthermore, straight pavement sections with an averaged MPD = 1.366 mm near these two curves were also tested as a reference.

The accuracy of the proposed camera-based measurement method is validated using friction tests performed on straight pavements on SR-26 at various speed. Although noises in data measurements are inevitable, both the test tire sideslip angle and the vehicle articulation angle are theoretically equal to zero on a straight road test regardless of the senser setup and vehicle operational characteristics. Furthermore, the radius of curvature R is considered infinity on straight pavement tests. The magnitude of the camera measured tire velocity should be identical to the tractor speed ($V_1 = V_s$).

Three speed levels (15 mph, 30 mph, 40 mph) were performed and repeated multiple times for camera-aided straight pavement friction tests on SR-26. Figure 5.11 displays time series of the three measured variables on straight pavements, in which seven LWST friction tests are performed at all the three different speed levels. As shown in the plots, both measurements of angle variables keep a null result with neglectable noises due to vehicle vibration. Furthermore, the tire speed measurement performance was less robust when the vehicle is driving at higher traveling speeds.

Table 5.2 summarizes the performance of the dual-camera-based system comparing camera measurements on straight pavement tests with the true values. The measurements of tractor speed V_1 provided by the original LWST speed transducer are presumed accurate. All null hypotheses are not rejected at a significant level of 0.05, indicating that the proposed solution can

Figure 5.10 Two horizontal curves on a two-lane state highway.

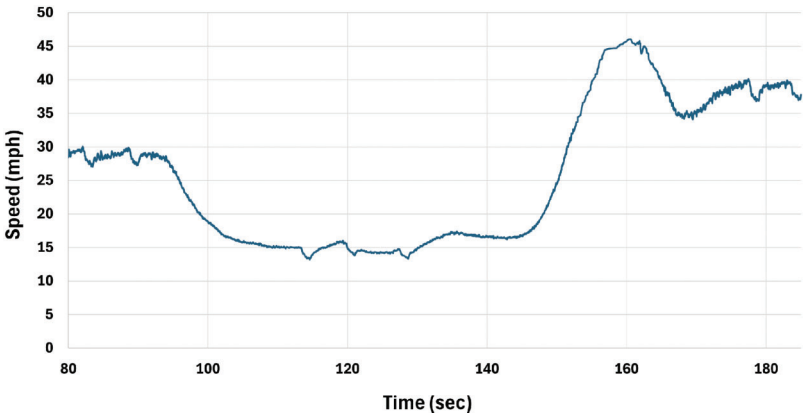

Figure 5.11 Time series of friction testing on a straight section of SR-26.

provide reliable measurements of the three target variables during a LWST friction test at various speeds. Compared to measurements of test tire speed and sideslip, some error sensitivity among the articulation angle measurements was observed due to vibration of the target hitch joint plane when the vehicle traverses at high speed on rough ground.

Figure 5.12 presents a sample monitored time series of test tire speed, test tire sideslip angle, and vehicle articulation angle under a typical vehicle maneuver of a right turn followed by a left turn on two SR-26 curves. The angle measurements were set clockwise positive. As can be seen in Figure 5.12, in stable cornering conditions, the trailer wheels always track the inboard side with small sideslip angles. On the other hand, the trailer sideslip angle α_s and vehicle articulation angle φ have opposite signs during the maneuver regardless of the turning direction. The maximum tire sideslip angle was observed larger than the maximum articulation angle during each turn.

In total of five friction tests were performed in the sample dataset shown above. Figure 5.13 shows an example of the three camera measured variables within a 1-second test time window. Figure 5.13 is the same data time series cut from Figure 5.12 at time 439.33–440.33 sec. It represents a friction test performed when the vehicle is making a right turn on a highway horizontal curve with 2,438-ft radius and a 7.71% superelevation. In this sample friction test, the averaged tire speed was 13.58 mph, and the averaged slip angle and articulation angle were 2.00° and -0.68°,

TABLE 5.2
Accuracy Assessment of Camera Measurements

Hypotheses	p-value	RMSE
$V_1 = V_s$	0.3331	0.6614 mph
Tire sideslip angle $\alpha_s = 0°$	0.6175	0.2535°
Articulation angle $\varphi = 0°$	0.9076	0.5814°

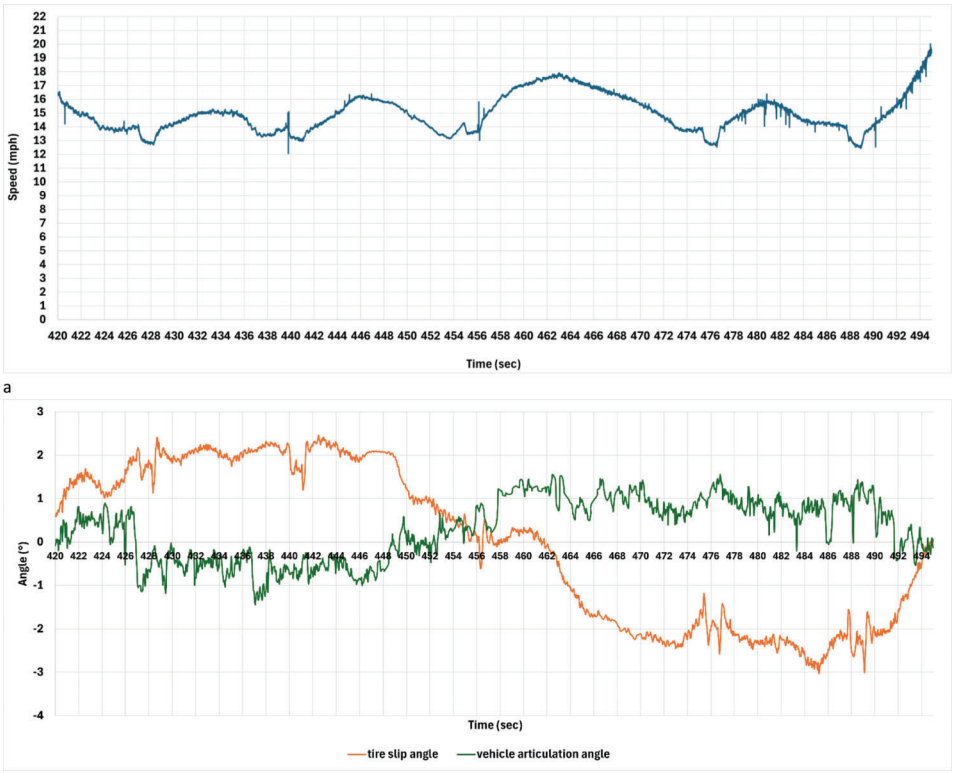

Figure 5.12 Time series of friction testing at a right turn followed by a left turn on SR-26.

respectively. The corresponding tractor speed was measured 14.77 mph. The measured test tire vertical tire force was 958-lbs, and the longitudinal friction force was 557-lbs, resulting in a friction coefficient measurement of 0.581.

In both driving directions, the LWST vehicle on SR-26 always traveled with repeated maneuvers under a right turn followed by a left turn at various test speed levels. Three test speed levels, including 15 mph, 30 mph, and 40 mph, were selected to perform standard friction tests on a nearby SR-26 straight pavement, while only 15 mph and 30 mph tests were performed on the two horizontal curves for lateral safety. Tests performed at each speed level was repeated at least three times for error minimization. Detailed angle measurement results for different friction tests performed on both straight pavements and the two horizontal curves in the two-lane state highway field are listed in Appendix B.2.

5.5 Empirical Investigation of Tire-Pavement Frictional Interaction at Horizontal Curves

In addition to the three camera measurement variables, the original LWST friction test program provides averaged measurements of tractor speed, test tire longitudinal friction force, and test tire vertical load. Several equations discussed in the mechanistic investigation task indicate potential impact of different variables on the measuring performance of the LWST pavement skid-resistance results. Using variation of field test results among the total six variables with respect to multiple combinations of test speed level and pavement geometric properties, the final task was empirically examining the factor impacts in both qualitative and quantitative way.

5.5.1 Tire Lateral Force and Cornering Stiffness

Tire lateral force is the most critical component required to understand tire side friction performance in cornering analysis. As discussed in previous sections, the test tire lateral force generated from pure sideslip has a linear relationship with the measured sideslip angle when the slip angle is small (Equation 5.6 and Equation 5.8). The camera measured real-time sideslip angle together with the force transducer measured tire longitudinal friction force can provide measurements of tire lateral force using $F_y = F_x \tan \alpha_s$. The linearity was validated in regression line of data measurements in both fields. Figure 5.14 depicts linear regression of the pure sideslip tests performed on airport runways with zero superelevation. The small offset observed in the plot with respect to the origin may be caused by the unavoidable occurrence of the tire-pull phenomenon.

Figure 5.15 represents similar linear relationship between the test tire lateral force and the slip angle α_s

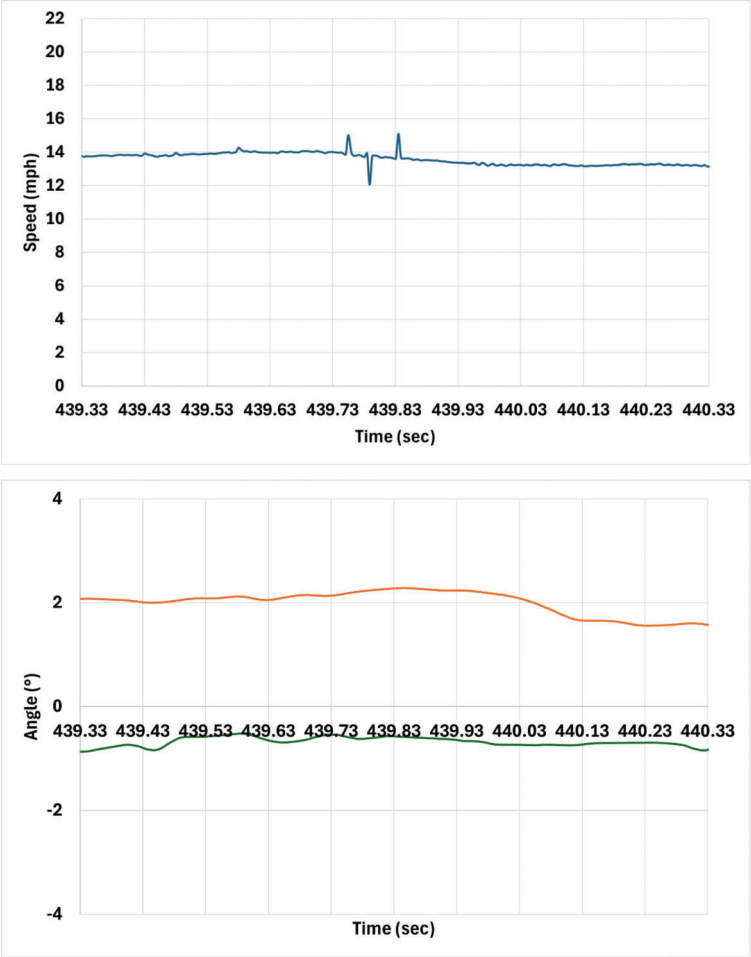

Figure 5.13 Time series of friction testing within 1-second friction test time window.

observed in SR-26 friction tests, in which the effects of the additive camber trust is included. The lateral forces calculated from SR-26 measurements is smaller than lateral forces generated in airport tests, which make sense as horizontal curves on SR-26 highway has a radius of curvature more than ten times greater than the airport curves. A greater radius means smaller lateral acceleration and smaller side friction. Moreover, a different intercept is observed because of the added component of lateral force generated by the approximately 8% of superelevation.

With the absence of lateral inclination in airport test results, the longitudinal friction force F_x and the vertical force F_Z measured for the left test tire in airport field tests can be used to estimate the cornering stiffness value of a standard test tire at 100% slip ratio. A second order polynomial regression model between F_x and F_Z is applied to the airport force measurements using $K_s = F_y/\alpha_s = F_x\alpha_s/\alpha_s \approx F_x$ (Figure 5.16). The regression validates the second order polynomial relationship between the tire cornering stiffness and the tire vertical force. According to the model, the tire cornering stiffness K_s is estimated 772.96-lbs/rad under standard 1,085-lbs of tire vertical load.

5.5.2 Angle-Based Test Failure Alert

Taking advantage of the camber trust and low traveling speed, all friction tests performed on the two SR-26 highway horizontal curves were measured under stable conditions. As previously shown in speed time series from different friction test configurations, instant reduction in the absolute value of tire sideslip angle were observed before the start of each friction test because of the tire locking and water delivery. However, the state of the slip angle became stable shortly after the end of test preparation. The measurement of both angles remained stable in the duration of each data-averaging time interval (Figure 5.12).

Figure 5.17 illustrates the relationship between the test tire sideslip angle and the vehicle articulation angle in the friction tests measured from two fields. For stable tests with neutral steering behaviors collected from the tests on SR-26, the magnitude of tire sideslip angle was observed increasing proportionally with increased vehicle articulation angle. On the other hand, the angle measurements from airport tests were more unstable and the two variables were not high linearly correlated as trailer fishtailing occurred on numerous of these

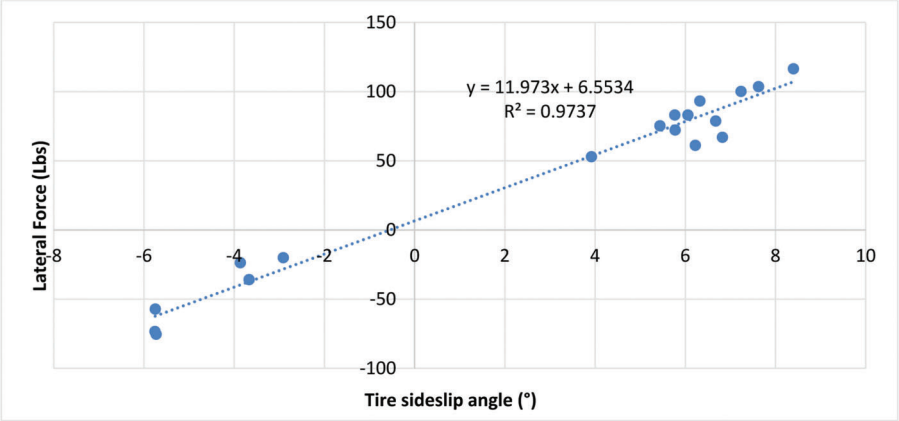

Figure 5.14 Tire lateral force estimation with sideslip angle.

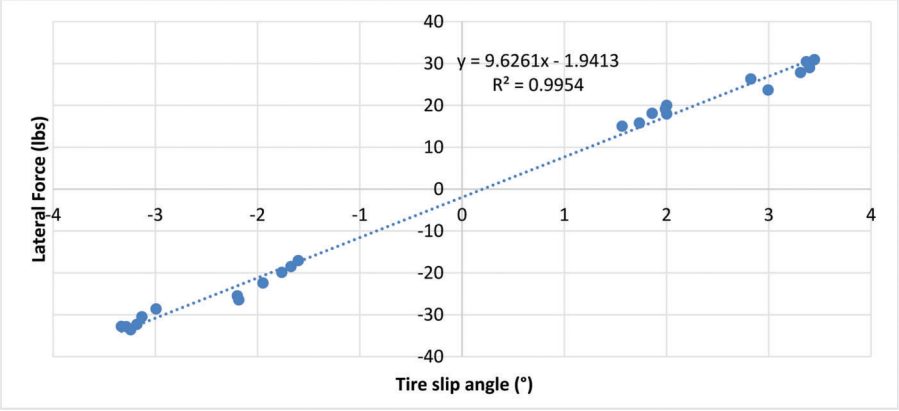

Figure 5.15 Tire lateral force estimation with sideslip angle and lateral inclination.

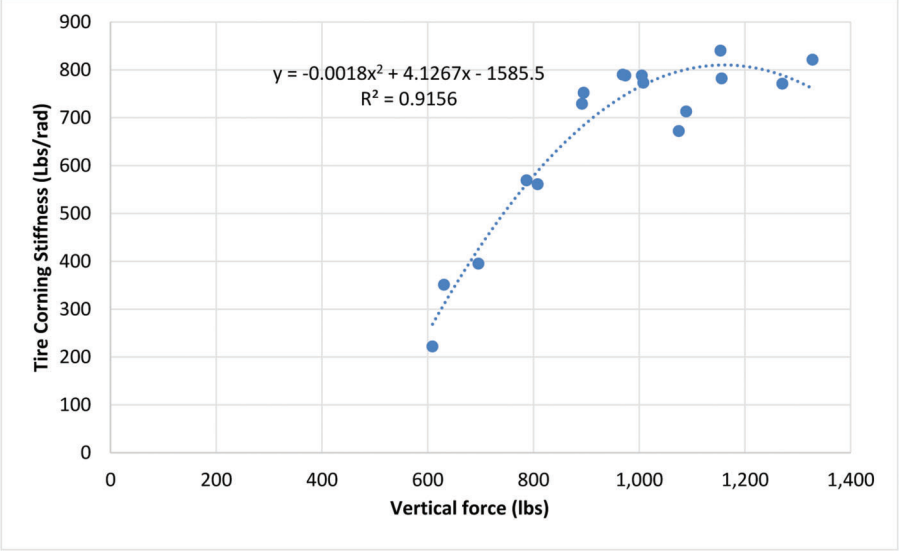

Figure 5.16 Tire cornering stiffness estimation with vertical loads.

friction tests at high-speed levels. Both angles during the SR-26 LWST friction test were smaller than angles in the airport test at the same speed level because of both the larger radius and the effect of lateral inclination.

5.5.3 Pavement Macrotexture and Speed Variation

Pavement MPD variation with texture scanning direction was first analyzed from macrotexture data collected on three different types of pavements at the INDOT friction test tracks using a laser texture scanner. Figure 5.18 shows boxplots of MPD measured from a slick concrete pavement, a hot mix asphalt (HMA) pavement, and a tined concrete pavement at three scanning directions, longitudinal, lateral, and 45-degrees. Although different types of pavement materials provide different MPD values and data variances, no significant difference with texture scanning direction was found among all three types of pavements. The observation indicates that the varied moving direction for vehicles traveling at horizontal curves did not affect the tire-pavement skid resistance with respect to pavement macrotexture properties.

As expected, the friction coefficient measured from a LSWT is negatively correlated to its test speed (Saito et al., 1996). A friction-conversion method developed by Flintsch et al. (2010) proved that a linear correlation between the two variables is valid and the smoothed tire friction loss with speed depends on pavement macrotexture. The MPD values of the test pavements on SR-26 have a mean value of 1.28 mm and a standard deviation of 0.09 mm. According to the speed adjustment factor from the texture method (Flintsch et al., 2010), the friction coefficient with speed diagram yields an estimated slope value of -0.55 (%) at MPD of 1.28 mm. This level of friction conversion with speed was observed in SR-26 test results on both straight pavements and horizontal curves (Figure 5.19), indicating a speed measurement error of 1.82 mph can result in 1% error in the final result of friction coefficient.

Figure 5.20 shows the minimum design values of the radius of curvature with speed required for typical highways in the state of Indiana (INDOT, 2013/2022).

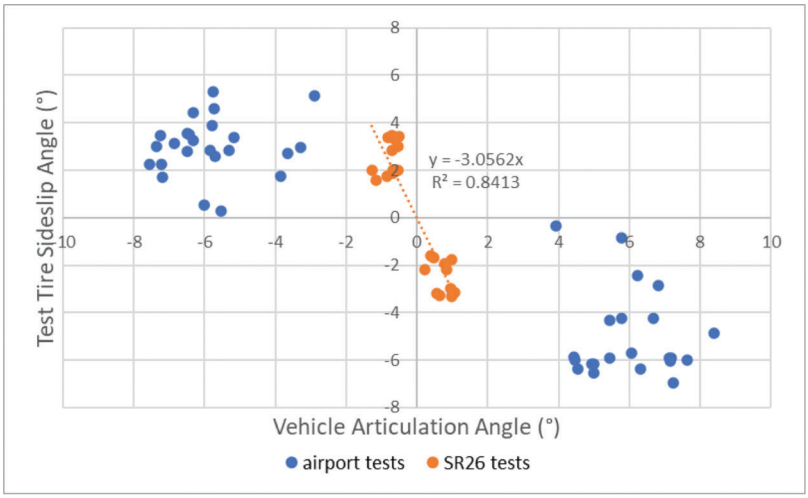

Figure 5.17 Test tire sideslip angle with vehicle articulation angle in field tests.

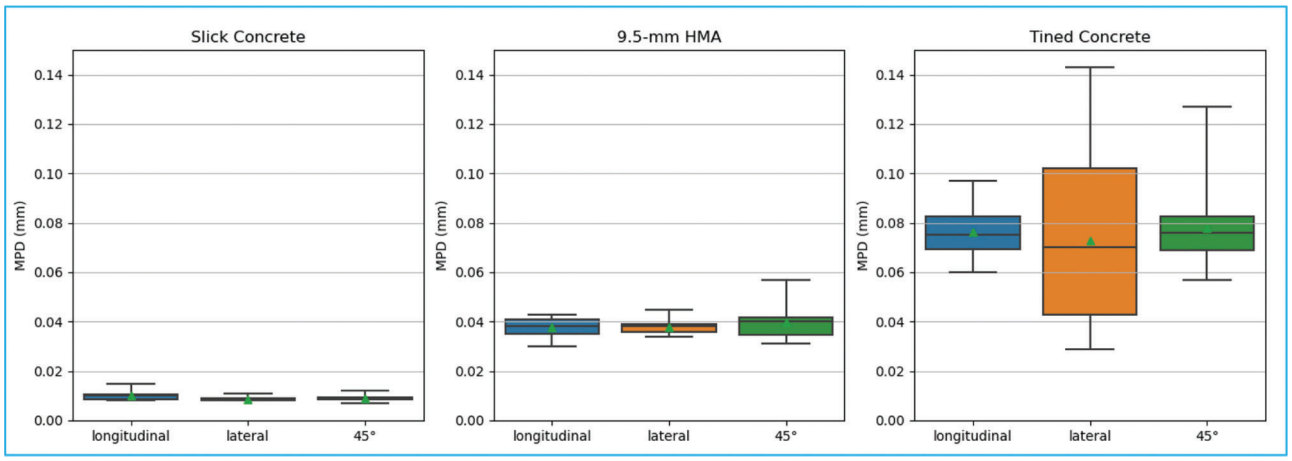

Figure 5.18 Pavement MPD variations at different directions.

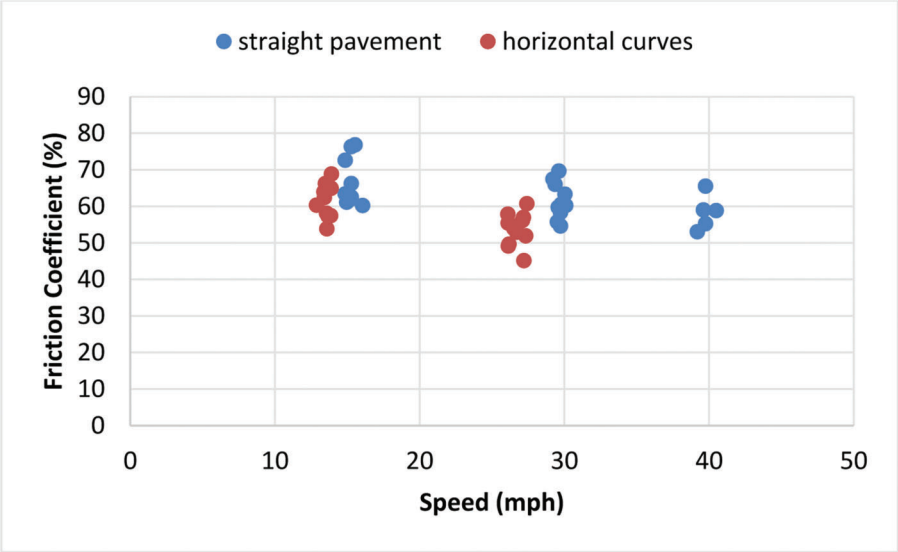

Figure 5.19 Friction coefficient variation with test speed.

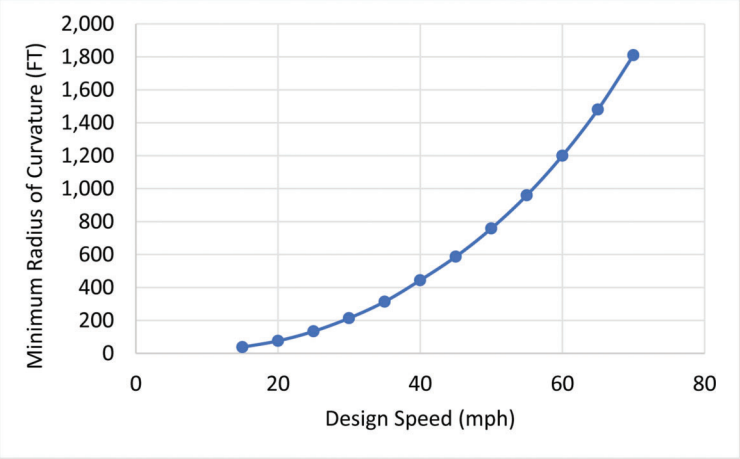

Figure 5.20 Minimum radius required for various design speed at 8% superelevation.

This figure indicates that a horizontal curve allows for friction test at the standard 40 mph among Indiana highways should have a radius much greater than the minimum 444-ft. Slower testing speed of a LWST is required not only for vertical force impact control but also for vehicle safety.

Unlike straight pavements tests, the vehicle tractor speed V_1 and test tire speed V_s on cornering tests are not identical with non-zero side slip angle and articulation angle measurements. The simplified theoretical relationship between the two speed variables is introduced in Equation 5.5. Increase in absolute value of both the tire sideslip angle and vehicle articulation angle result in larger difference between the two speed measurements ($\Delta V = V_1 - V_s$). Figure 5.21 shows the measurement difference ΔV observations among tests from two fields. The airport runways have sharper curves and zero superelevation. Therefore, large measurements of both angles were observed. Unstable oversteer behaviors witnessed among airport tests at high-speed increase the variance of angle measurements. As can be seen in the ΔV data calculated from the SR-26 tests, the speed differences are small (<5 mph) and thus the friction coefficient error with speed is negligible ($<2.31\%$). Speed initially measured by the LWST speed transducer can be used as an approximation of the actual tire speed if camera measured tire speed is unavailable for tests on highway curves constructed with a typical superelevation rate and a large radius of curvature.

Linear regression analysis on variables measured from field tests in stable conditions is used to provide empirical values of C/R in Equation 5.5. Figure 5.22 displays the estimated and camera measured tire speeds from all friction tests performed at horizontal curves. The precision of tire speed empirical estimation was stable at various speed levels regardless of test fields. A small root-mean-square error (RMSE = 1.80 mph) in tire speed estimation resulted among experimental tests compared to the ground truths in camera

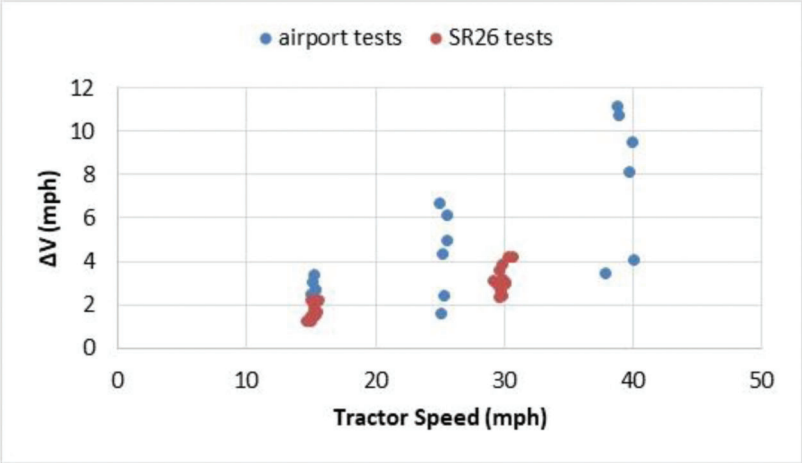

Figure 5.21 LWST speed transducer performance for friction tests on horizontal curves.

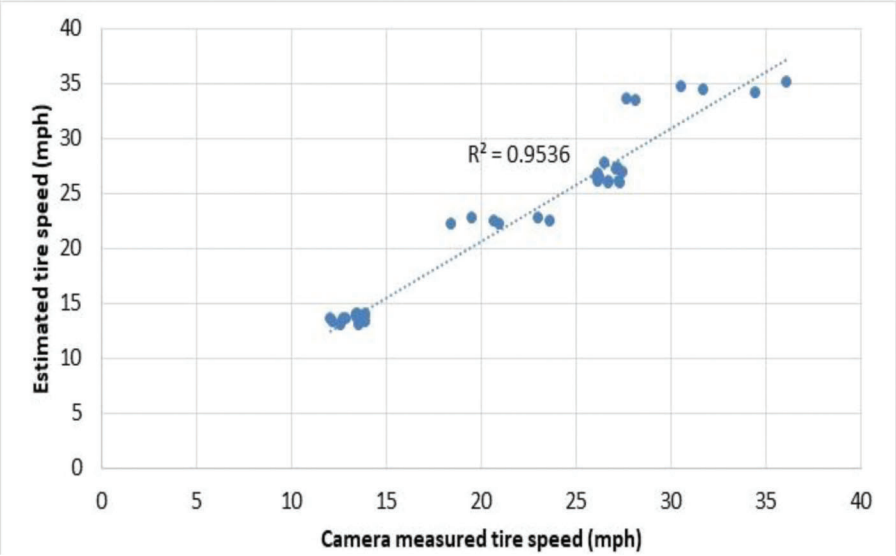

Figure 5.22 Measured tire speed vs. estimated tire speed.

measurements. This estimator provides an alternative speed calibration solution for LWST tests when tire speed measurement is unavailable during future friction tests. However, the empirically estimated value C is valid only for the specific LWST vehicle employed in the experiments. Adjustment is needed if another vehicle tester with a different size and design is selected.

Equation 5.12 shows a simplified relationship of trailer side friction, speed, and the superelevation rate of a horizontal curve. The single tire lateral force F_y and vertical force F_Z obtained in our field tests is not the trailer axle's total lateral force F_{y3} and total vertical force F_{Z3}. However, the left and right tires share the same sideslip angle. A tire lateral force is linearly proportional to the tire sideslip angle, indicating that increasing speed should increase the sideslip angle categorically if the vehicle is traveling under stable conditions.

$$\frac{F_{y3}}{F_{Z3}} \cong \frac{\left(\frac{mV^2}{R} - mge\right)}{mg + \frac{mV^2}{R}e} \approx \frac{V^2}{Rg} - e \qquad \text{(Eq. 5.12)}$$

Sideslip angle measurements from SR26 highway curves are collected using the same radius of curvature and similar superelevation rate (about 8%). Similar tendency described in Equation 5.12 can be found in Figure 5.23, although second order regression analysis is invalid using only two speed levels.

5.5.4 Impact of Pavement Geometric Design

As discussed in the mechanistic task, the geometric design of a pavement horizontal curve makes significant impact on friction coefficient result of LWST tests by influencing the test tire vertical force F_Z (Equation 5.9). Test tire vertical force tested from straight

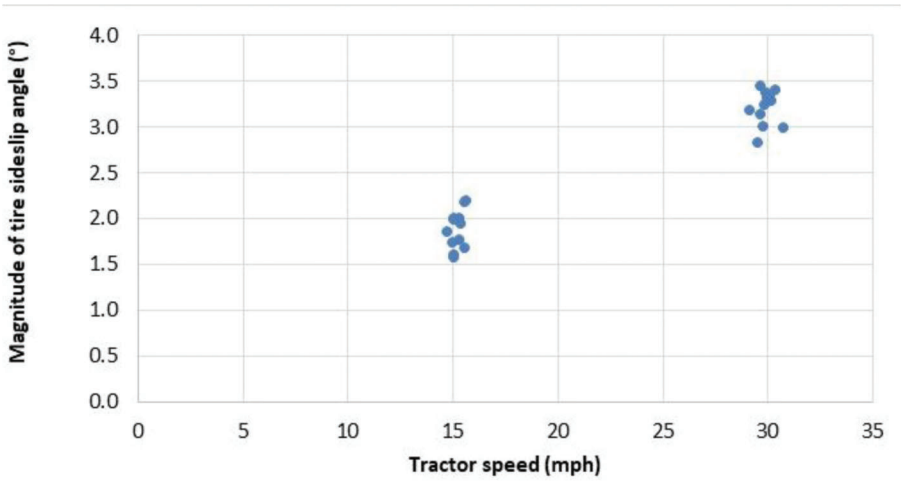

Figure 5.23 Absolute value of test tire sideslip angles.

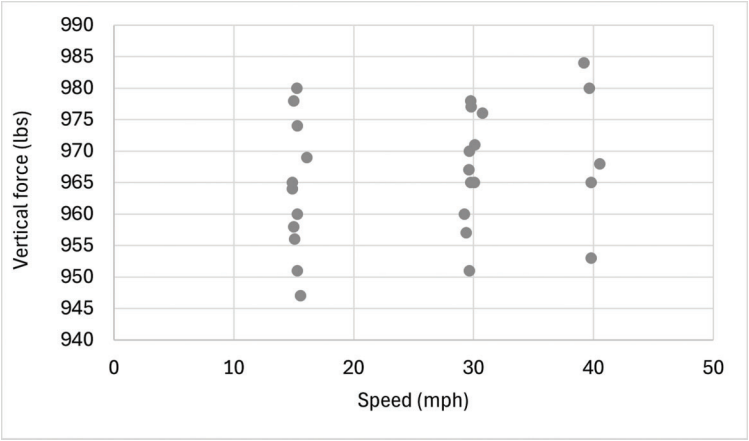

Figure 5.24 Test tire vertical force measurements on straight roadway.

pavements was measured 967 ± 17 lbs (Figure 5.24). Compared to friction tests on straight road under the same condition of test pavement texture, the measured vertical force F_z from an outboard test tire can be significantly larger in a test scenario with high speed, limited radius of curvature, and small superelevation rate. Therefore, the resulting friction coefficient will be smaller than expected. This study investigates the LWST vertical force measurements under various testing scenarios with or without curvature and lateral inclination. The unknown terms that depend on vehicle mass and dimension in Equation 5.9 can be estimated using regression analyses among the test data on curves. The quantitative impact of the pavement geometric design variables on tire vertical force is then measurable and can be used in evaluation for LWST practicability on any highway horizontal curve.

5.5.5 Radius of Curvature

Without the additional impact of superelevation, Equation 5.9 can be simplified as $F_z = F_Z' \pm \frac{h}{w}\frac{mV^2}{R} + \in$ in pure sideslip cornering scenarios. The impact of horizontal curvature on test tire vertical force has a second order polynomial relationship with the test speed variation. Test measurements collected from the three different airport runway curves provide an estimated value for term $\frac{mh}{w} \approx 30$ (Figure 5.25).

The empirical estimation value of the vehicle dimension properties $\frac{mh}{w} \approx 30\,\text{lbs} \times \text{ft/mph}^2$ restricts the influence level of a curvature without superelevation on test tire vertical force. Figure 5.26 represents the quantitative impact in terms of speed level and the radius of curvature. To perform the LWST friction test at the standard 40 mph on a horizontal curve, the radius of curvature should be greater than 400-ft so that the impact term is limited to a small value less than 100-lb. Most horizontal curves designed in Indiana highways meet this requirement as discussed in previous section.

5.5.6 Superelevation Rate

A limited value of superelevation rate can provide additional impact on the measured tire vertical force.

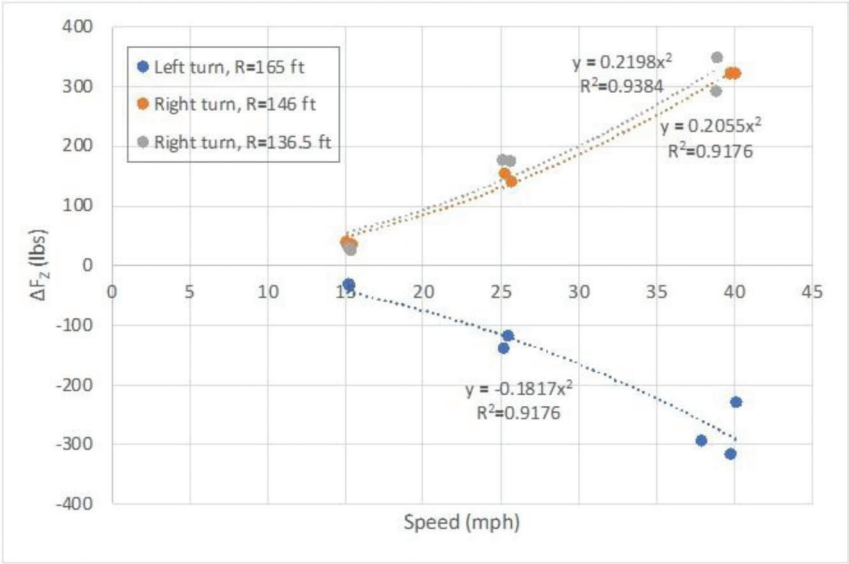

Figure 5.25 Regression models of additional tire vertical forces.

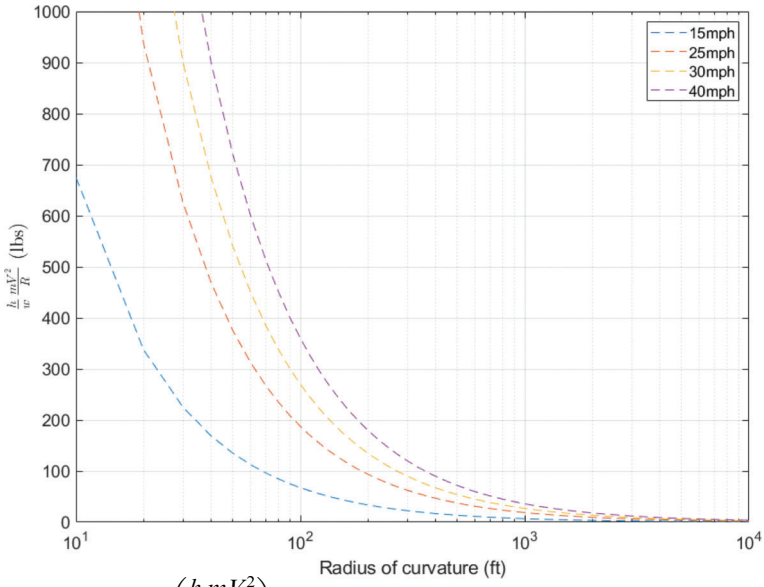

Figure 5.26 Additional tire vertical forces $\left(\frac{h}{w}\frac{mV^2}{R}\right)$.

With lateral inclination, the left and right tires behave differently when making left and right turns. The outboard tire is more sensitive with speed and less sensitive to the impact added by lateral inclination denoted as term $\left(\frac{c}{c+d}\right)\frac{mV_s^2}{2R}e \pm \frac{h}{w}\left(\frac{mV_s^2}{R} - mge\right)$ in Equation 5.9. The force transducer is equipped on the left smooth tire of our experimental vehicle tester. Thus, the test tire is observed more sensitive to this impact with speed when making right turns (Figure 5.27). Term $mge\frac{h}{w}$ for the experimental vehicle is estimated 35.9-lbs for an 8% superelevation rate, while term $\left(\frac{c}{c+d}\right)\frac{mV^2}{2R}e$ is more complex as it varies with both the superelevation rate and radius of curvature.

The quantitative analysis in terms of curvature impact on tire forces only works for the LWST used in our experiments without further calibration. Limited combinations of test speed, radius of curvature, and superelevation rate are implemented in the field friction tests due to lacking in test fields. Simulation tests using finite element modeling introduced later can extend the applicability of the investigation based on field implementations.

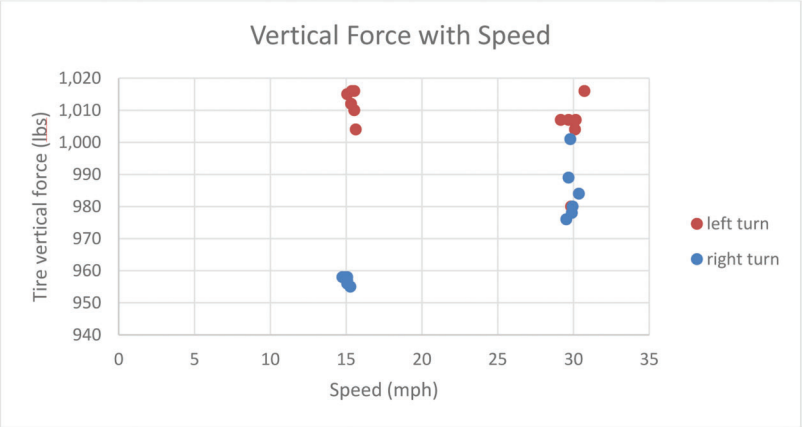

Figure 5.27 Test tire vertical forces.

6. CHAPTER 6. MODELING OF TIRE-PAVEMENT FRICTIONAL INTERACTION WITH FINITE ELEMENT ANALYSIS AND MACHINE LEARNING

6.1 Tire Friction Model Setup

The tire-pavement frictional interaction analysis was conducted using the ABAQUS–3D SIMULIA (Dassault Systèmes, 2014) finite element analysis (FEA) platform. The process involves the creation of a three-dimensional (3D) tire model derived from the rim mounting and inflation analysis of a two-dimensional (2D) axisymmetric tire model. Various analyses, including footprint analysis, steady state analysis, and cornering analysis, were systematically performed to examine the distribution of contact force and friction force on roads.

The components of the model include the following.

1. *2D Axisymmetric Tire Modeling:* Initial representation of the tire in a two-dimensional axisymmetric form.
2. *Rim Mounting Analysis on 2D Tire Model:* Evaluation of the tire's interaction with the rim within the 2D model.
3. *Inflation Analysis on 2D Tire Model:* Examination of tire inflation dynamics within the 2D model.
4. *2D to 3D Conversion of Tire Model:* Transformation of the 2D model into a comprehensive three-dimensional representation.
5. *Footprint Analysis on 3D Tire Model:* Investigation into the tire's contact with the road surface in three dimensions.
6. *Steady State Analysis on 3D Tire Model:* Study of tire deformation and free rolling solution in steady-state conditions.
7. *Cornering Analysis on 3D Model with Different Slip Angles:* Evaluation of tire performance during cornering with varying slip angles.
8. *Effect of Different Values of Camber Angle on Footprint Results and Cornering Forces:* Examination of the impact of different camber angles (or superelevation or lateral inclination) on footprint and cornering forces.

The workflow for tire performance simulation in ABAQUS is depicted in Figure 6.1, illustrating the sequential steps involved in the comprehensive analysis.

The process initiates with the establishment of a 2D axisymmetric tire model within the static structural system. Figure 6.2 illustrates the assembly of components constituting the 2D axisymmetric tire, encompassing rubber, sidewall, tread, interlinear, and bead. This 2D model forms the foundation for subsequent analyses, providing a representation of the essential elements influencing tire behavior.

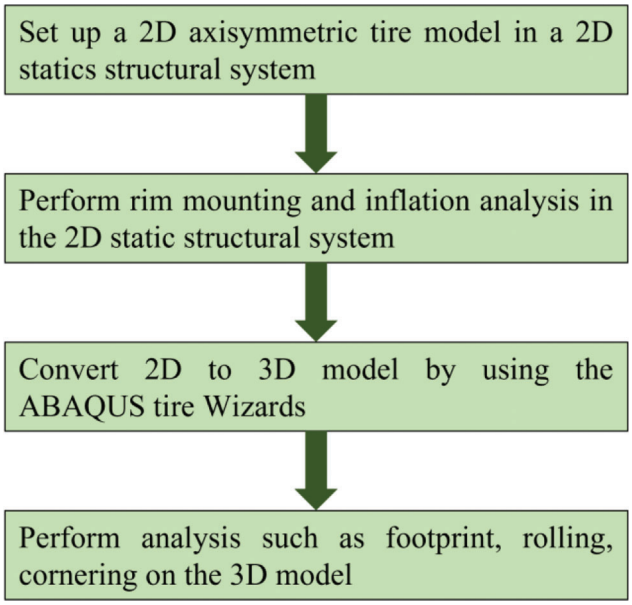

Figure 6.1 Workflow of the tire-pavement frictional interaction simulation.

Following the establishment of the 2D tire model, the subsequent steps involve rim mounting and inflation analysis within the 2D static structural system. This process serves to transition the 2D model into a 3D representation. Leveraging the ABAQUS Tire Wizards plug-in tool, the 2D components are swept and symmetrized, yielding a comprehensive 3D tire model. Notably, the rib tire model in the toolbox is adaptable to achieve a smooth tire profile aligning with the specifications set by INDOT. Figure 6.3 visually delineates the transformation from the 2D tire model to the 3D tire model for both rib and smooth tire configurations.

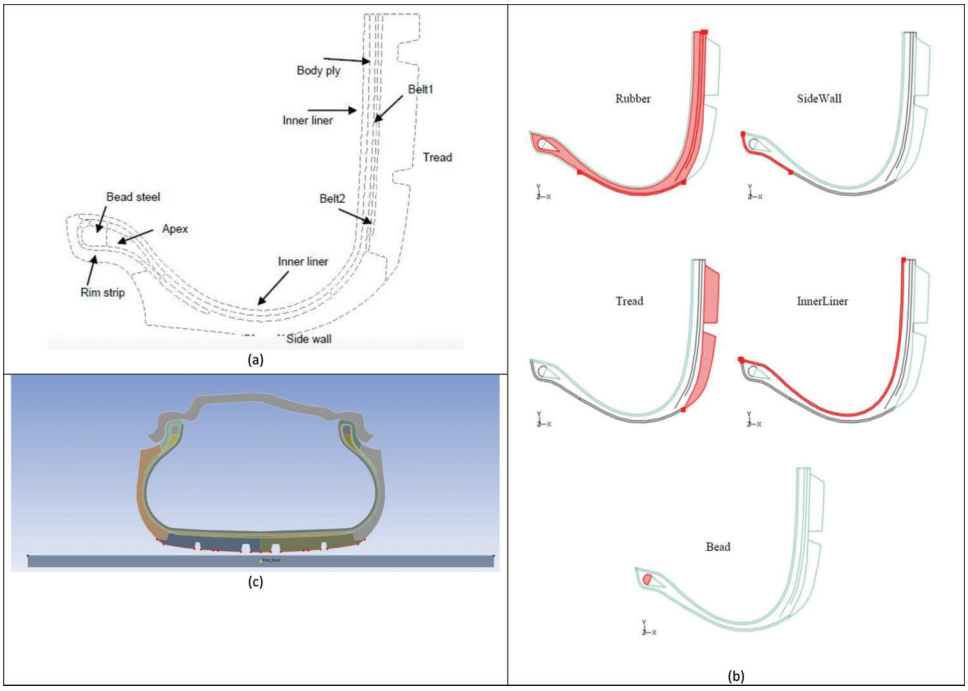

Figure 6.2 2D model of tire: (a) radial structure of tire, (b) 2D tire components, and (c) tire-pavement friction area.

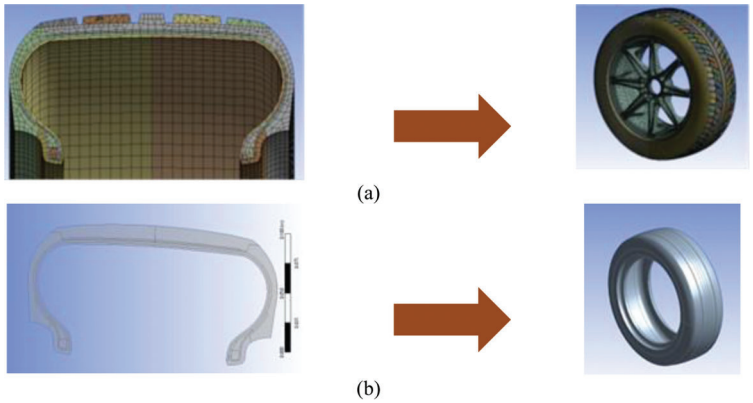

Figure 6.3 Map 2D to 3D tire model for (a) rib tire, and (b) smooth tire.

6.2 Tire Model Analysis

6.2.1 3D Tire-Pavement Footprint Analysis

Upon the creation of the 3D tire model, subsequent analyses were conducted in ABAQUS to predict the distribution of contact force and friction force between the tire and the road. This process involves footprint and brake analyses performed in two or three load steps. In the initial load step, contact between the road and the tire is established by applying a small displacement or force value on the remote point of the tire-pavement connection, thereby moving the rigid road surface towards the tire. The second load step involves applying the vehicle load on the tire via the same remote point, with loading occurring only in the negative global X-axis direction. An optional third load step can be introduced to apply a non-zero camber value to the tire via the same remote point.

For the 3D FEA tire model, vertical force and inter-tire pressure are predefined before the analysis, inducing tire vertical deflection and geometry changes during the pressurized stage. During the full brake stage, a relative speed between the tire and the road, along with a friction coefficient, is assigned. Subsequently, the contact pressure between the tire and road, along with general von Mises stress, is recorded from the 3D tire analysis. Figure 6.4 illustrates the results of the footprint analysis between the 3D tire and road.

6.2.2 3D Rolling Analysis and Cornering Analysis

Following the footprint analysis, the steady-state rolling analysis is conducted by specifying the spin and ground velocities. The coefficient of friction for the tire-pavement contact pair can be adjusted based on the road type and temperature within the model.

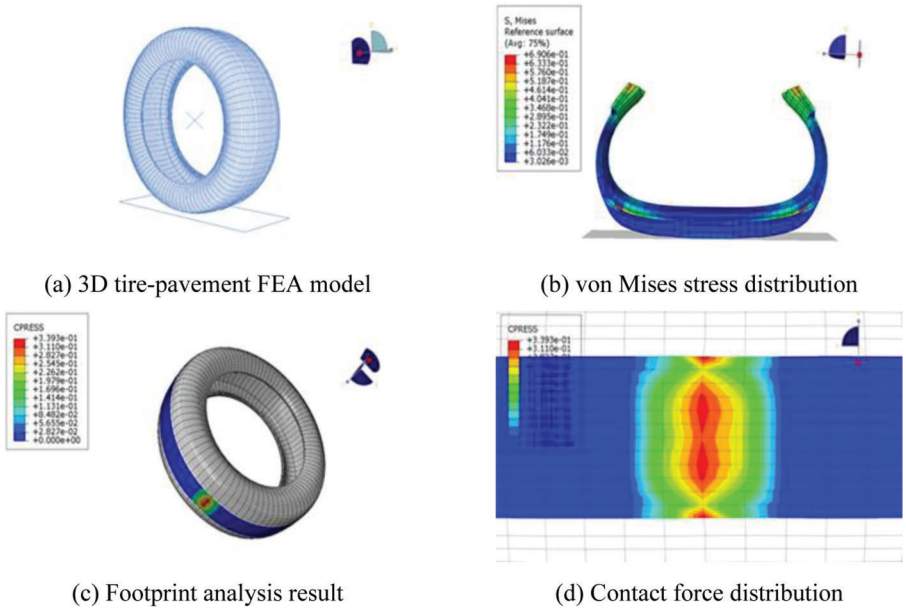

(a) 3D tire-pavement FEA model

(b) von Mises stress distribution

(c) Footprint analysis result

(d) Contact force distribution

Figure 6.4 Footprint analysis results.

Subsequent to the steady state rolling analysis, free rolling analysis and cornering analysis can be introduced. Free rolling analysis predicts the spin when the vehicle is freely rolling, while cornering analysis estimates friction forces when the vehicle undergoes a turn, or the road has an inclination. In cornering analysis, the slip angle, depicted in Figure 6.5(a), represents the angle between a rolling tire's actual direction of travel and the direction toward which it is pointing. Figure 6.5(b) illustrates the camber angle, denoting road inclination.

6.2.3 Forces in Vehicle Dynamics

To comprehend the relationships among slip angle, curve radius, camber angle and friction force, the fundamentals of vehicle dynamics (Gillespie, 2021) are introduced as follows.

6.2.3.1 Lateral slip. In Figure 6.6, force analysis is presented with and without a turn. The longitudinal force F_x represents the force component acting on the tire by the road, parallel to the intersection of the wheel plane with the road plane. The lateral force F_y is the force component acting on the tire by the road, normal to the intersection of the wheel plane with the road plane. The normal force F_z is the force component acting on the tire by the road, perpendicular to the road plane. The slip angle α is the angle between the direction of wheel heading and the direction of travel.

The connection between the lateral force F_y and the slip angle is expressed in Equation 6.1 (Gillespie, 2021).

$$F_y = F_f \sin\alpha = \mu_s F_z \sin\alpha \qquad \text{(Eq. 6.1)}$$

where μ_s is sliding coefficient of friction, F_z is the verticle load, and α is the slip angle.

6.2.3.2 Lateral inclination. Figure 6.7 illustrates the force analysis with and without road inclination. In this depiction, the camber angle γ represents the inclination angle of the road surface. The weight on the tire is denoted as W. The lateral force F_y is the component of the force acting on the tire by the road in the plane of the road and normal to the intersection of the wheel plane with the road plane. Simultaneously, the normal force F_z is the component of the force acting on the tire by the road, which is normal to the plane of the road.

The relationship between the lateral force F_y and the camber angle is expressed in Equation 6.2 (Gillespie, 2021):

$$\frac{F_y}{W} = \sin\gamma \qquad \text{(Eq. 6.2)}$$

where F_y is the lateral force, W is the weight on the tire, and γ is camber angle.

6.3 Validation of the 3D Tire-Pavement FEA Results with the Field Test Results

The validation of the finite element analysis results for the 3D tire-pavement model is conducted by comparing them with field testing results on highways sections and on Purdue airport runways, considering both straight and curved roads. The input parameters for the FEA model include vehicle speed, vertical force, slip angle, and friction number (FN), while the output predicted by the FEA model is the horizontal force. The field experiments and results can be found in Chapter 5.

6.3.1 Straight Road Analysis

Tire friction testing was carried out on the INDOT friction test track, incorporating three distinct pavement surfaces: bituminous, tined concrete and slick

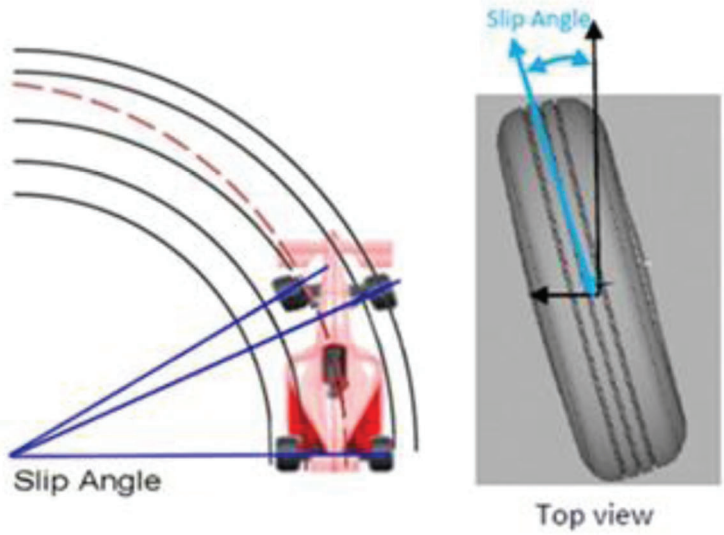

(a) Slip angle from the lateral slip of the tire

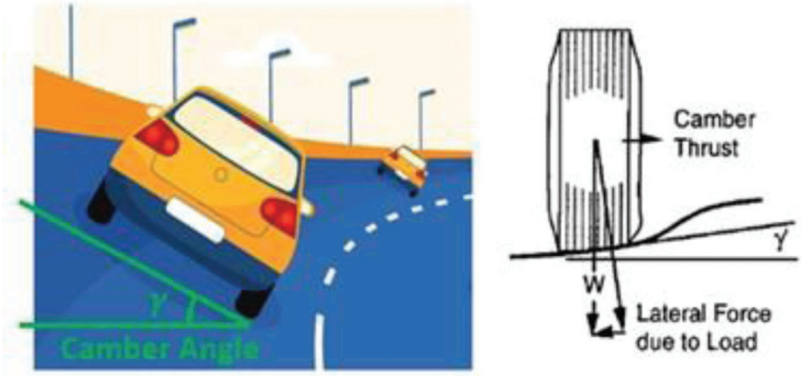

(b) Camber angle from the lateral inclination

Figure 6.5 Cornering analysis angles.

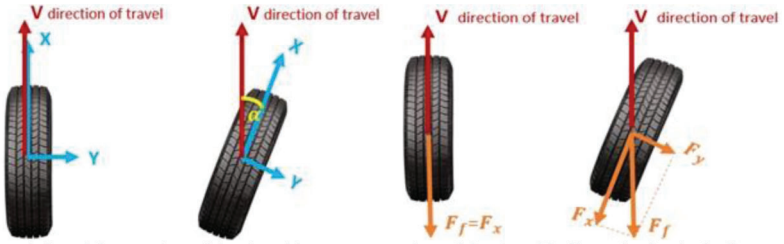

From left to right: top view of the tire with no turn; top view of the tire with slip angle; free body diagram for the tire with no turn; and free body diagram for the tire with turn.

Figure 6.6 Force analysis.

concrete. The 3D tire-pavement model was constructed using information derived from the INDOT smooth test tire and test track data. The results of the 3D tire finite element analysis were successfully validated against eight physical test results, as outlined in Table 6.1. The disparities between the FEA model and physical testing results ranged from -3.0% to 5.8%. Additionally, the FEA model was validated with five physical testing results obtained on a straight segment of a real-world road, namely SR-37. Figure 6.8 illustrates the FEA results on different straight roads. The FEA model demonstrates a comparable level of accuracy, with relative differences falling within the 0% to 1.67% range, as depicted in Table 6.2. These validation results affirm the accuracy and reliability of the FEA model in reproducing real-world tire friction behavior.

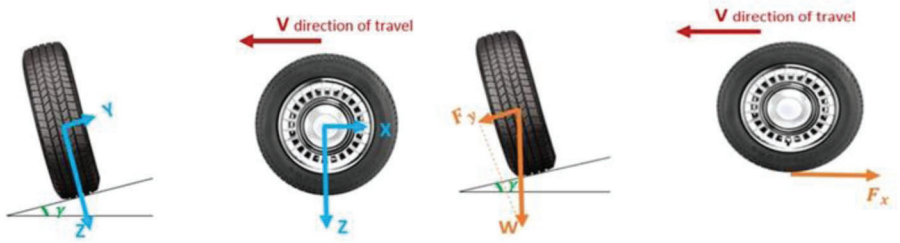

(a) Tire on an inclined road (b) Free body diagram of tire with inclination angle

Figure 6.7 Tire lateral inclination.

TABLE 6.1
FEA Validation with Field Testing on INDOT Friction Test Track (05/2023)

No.	Surface	Speed (mph)	Vertical Force (lbs)	Horizontal Force (lbs)	FEA Horizontal Force (lbs)	Difference (%)
1	Bituminous	29.75	1,010	505	506.7	-0.337
2	Bituminous	29.69	1,015	472	474.0	0.428
3	Bituminous	30.11	1,017	458	460.3	0.499
4	Bituminous	15.24	984	703	704.0	0.141
5	Bituminous	15.55	988	702	703.3	0.180
6	Tined concrete	29.54	980	679	681.1	0.317
7	Tined concrete	29.59	977	643	645.2	0.336
8	Slick concrete	29.6	1,063	232	225.8	0.356

6.3.2 Curved Road Analysis

In addition to straight road segment analysis, a curved road analysis was conducted to examine changes in friction during turns, incorporating slip angle as a crucial variable for understanding tire behavior under different turning conditions. This updated configuration includes four key elements: (1) the incorporation of slip angle to consider varying slip conditions; (2) simulation of tire-pavement contact dynamics for accurate replication of real-world interactions; (3) application of the appropriate vehicle load to account for weight and forces acting on the tire; and (4) simulation of the full braking process to facilitate an in-depth analysis of tire performance under braking conditions. Figure 6.9 illustrates the 3D FEA model for the tire with slip angle.

Two field friction measurements on curved runways at Purdue University Airport were conducted in April and October 2023 to validate the FEA tire-pavement friction model, encompassing six field testing results across a speed range from 15.24 mph to 40.15 mph. Figure 6.10 presents the FEA results on different horizontal curves at Purdue airport. This analysis demonstrated the FEA model's capability to provide highly precise horizontal force results, with a minimal deviation from field testing data. The difference ranges from -0.136% to 0.377%, indicating a reasonable alignment between the FEA predictions and the physical testing data, as shown in Table 6.3 and Table 6.4.

6.4 Friction Analysis on Straight and Curved Roads

6.4.1 Sensitivity Analysis

The correlation map, also known as a heatmap, serves as a graphical representation of two-dimensional data, utilizing colors to depict various factors. This visual aid is invaluable for quickly conveying statistical or data-driven information. In this study, a heatmap is employed to illustrate the sensitivity of different parameters in the friction analysis, streamlining the visualization by eliminating unnecessary factors in the system. The purpose is to provide a clear, visual representation of how various elements interconnect, aiding in understanding, planning, and decision-making within a given context.

The friction analysis for the tire-pavement system focuses on the longitudinal frictional number (see Chapter 5), speed, vertical force, slip angle, and curving radius. The longitudinal frictional number is intricately linked to both vertical force and longitudinal horizontal force, establishing a notable dependence between the friction number and horizontal force. To simplify the experimental system and remove unnecessary variables, the correlation map excludes the independent inclusion of horizontal force.

An additional consideration is the curve radius. Given that the new field testing data from Purdue Airport in October 2023 encompasses both left and right turns, the sign of the slip angle is recorded accordingly.

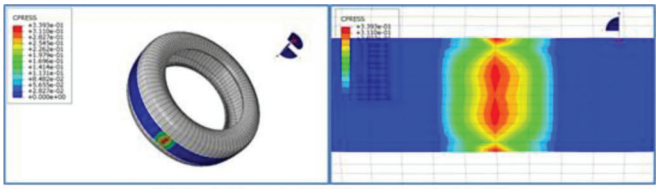

(a) Straight road - INDOT test track data #7

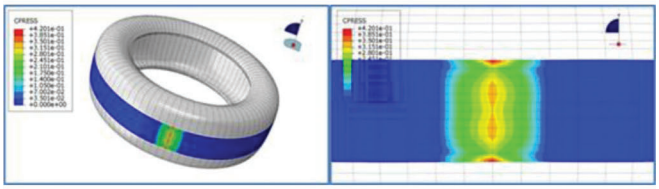

(b) Straight road – SR-37 data #1

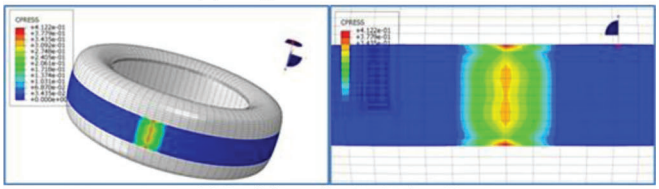

(c) Straight road – SR-37 data #2

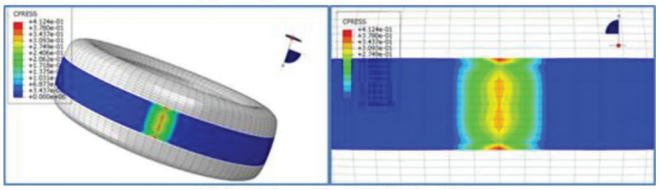

(d) Straight road – SR-37 data #3

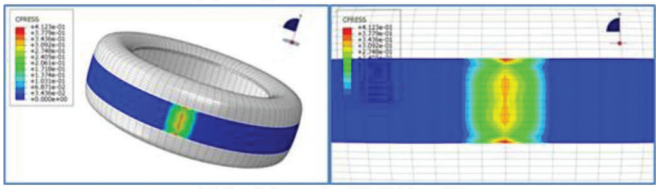

(e) Straight road – SR-37 data #4

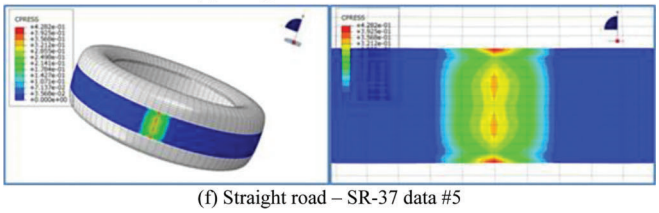

(f) Straight road – SR-37 data #5

Figure 6.8 Straight road FEA results on INDOT friction test track and SR-37.

TABLE 6.2
FEA Validation with Field Testing on Real-World SR-37

No.	Speed (mph)	Friction Number	Vertical Force (lbs)	Horizontal Force (lbs)	FEA Horizontal Force (lbs)	Difference (%)
1	50.14	10.8	1,084	117	118.0	0.038
2	49.92	13	1,075	140	140	0.00
3	49.27	19.6	1,071	209	196.5	0.255
4	50.57	15.7	1,075	169	170	0.59
5	50.07	17.5	1,093	191	191.2	0.125

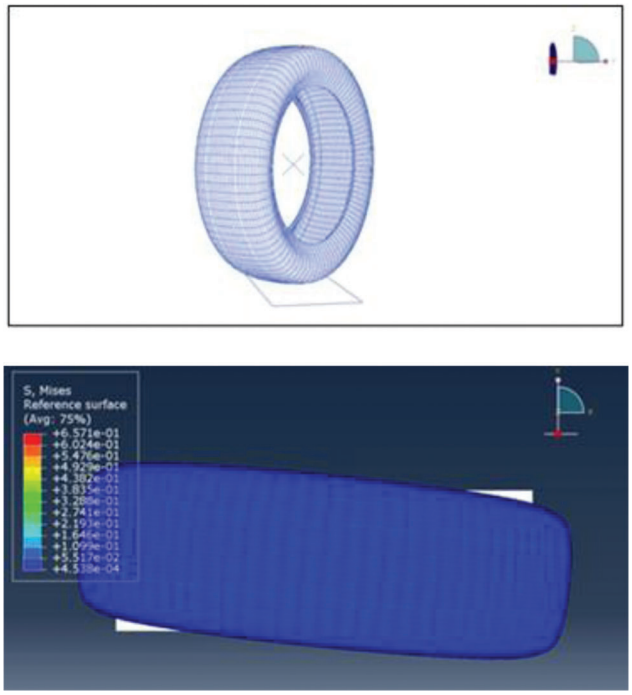

Figure 6.9 3D tire with slip angle.

As the sensor is fixed on one side of the tire, the vertical force records for left and right turns are influenced by the shift in gravity. To address this, a correlation map is compiled using data from straight and curved roads along with the slip angle separately. Figure 6.11 illustrates the correlation maps with the field testing data at Purdue Airport.

The central variable in this correlation analysis is the longitudinal friction number, a pivotal parameter in the study. The correlation map highlights a robust negative correlation between the longitudinal friction coefficient and speed (-0.96), and a somewhat weaker negative correlation with vertical force (-0.68), as evidenced in the straight road friction test. Similarly, the data from the curved road friction test reveals a -0.87 correlation value between longitudinal friction and speed and a -0.34 correlation between longitudinal friction and vertical force. This implies that as the vehicle's speed increases, the longitudinal frictional number decreases accordingly (Gillespie, 2021).

Another important independent variable in the Airport dataset is the curving radius, with three distinct radii measured at 165 feet, 136 feet, and 146 feet. Different curving radii can result in varied vertical forces, especially during right turns when the vehicle's

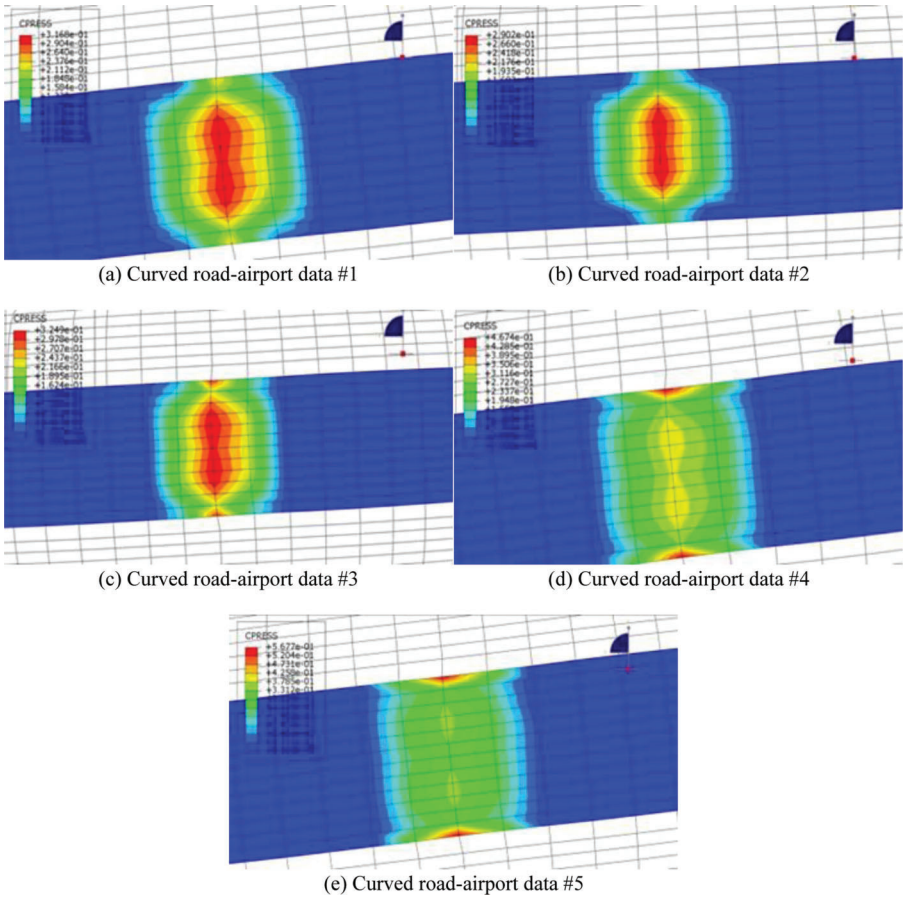

Figure 6.10 FEA results on curved runways.

TABLE 6.3
FEA Validation with Field Testing on Curved Runways (04/2023)

No.	Speed (mph)	Friction Number	Vertical Force (lbs)	Horizontal Force (lbs)	α	Camper	FEA Horizontal Force (lbs)	Differences (%)
1	15.24	0.817	892	729	5.75151	0	730	0.136
2	40.15	0.568	696	395	2.9057	0	396.5	0.370
3	15.08	0.809	974	788	8.404	0	789.8	0.233
4	25.58	0.728	1,154	840	6.33014	0	842.3	0.279
5	40.04	0.446	1,257	560	6.22784	0	562.1	0.377

TABLE 6.4
FEA Validation with Field Testing on Straight and Curved Runways (10/2023)

No.	Speed (mph)	Friction Number	Vertical Force (lbs)	Horizontal Force (lbs)	α	Camper	FEA Horizontal Force (lbs)	Differences (%)
1	39.89	0.748	941	704	0	0	703.99	0.128
2	20.54	0.893	921	822	0	0	824.3	0.274
3	15.03	0.867	931	807	0	0	808.1	0.141
4	24.28	0.803	832	668	–5.78590	0	669.2	0.182
5	22.41	0.831	826	686	–5.69534	0	687.9	0.279
6	20.33	0.792	840	665	-5.8548	0	666.1	0.310
7	25.38	0.799	1,132	905	4.929	0	907.3	0.25
8	14.56	0.892	993	886	7.164	0	887.7	0.2

center of gravity shifts, influencing the measured vertical force on the left-side tires. Consequently, this variation affects the alpha value, representing the slip angle, demonstrating a correlation of -0.54.

It's essential to emphasize that the curving radius contributes to correlation with speed or the longitudinal frictional number, as indicated by the correlation map. Comparing the correlation maps from the straight road data with those of the curved road data reveals a significant change in the relationship between the longitudinal friction number and other variables. While in straight road analysis, the correlation was predominantly influenced by speed and vertical force, the curved road data from both April and October necessitates considering the contributions of slip angle and curve radius. This points to a noteworthy variation in the impact of slip angle on the longitudinal friction number.

6.4.2 Friction Force Analysis with Machine Learning Algorithm

Gaussian process regression (GPR) was employed to analyze the variation in friction force as tires navigate curved roads. The analysis is based on the longitudinal friction force F_x obtained from the test fields and the theoretical lateral force F_y, calculated by dividing F_x by the real-time sideslip angle αs measured by the camera. The resultant forces F_x and F_y together form the friction force F_f for curved roads, as depicted in Figure 6.12. Equations 6.3 through 6.6 outline the calculations for the corrected friction number on curved roads, where N is the ground reaction force perpendicular to the surface of the pavement.

$$F_y = F_x \times \tan \alpha_s \qquad \text{(Eq. 6.3)}$$

$$F_f = \frac{F_x}{\cos \alpha_s} \qquad \text{(Eq. 6.4)}$$

$$FN_{longitudinal} = \frac{F_x}{N} \qquad \text{(Eq. 6.5)}$$

$$FN_{curve} = \frac{F_x}{N \times \cos \alpha_s} \qquad \text{(Eq. 6.6)}$$

Because of the negative correlation between curve radius and vertical force, the curve radius consequently influences the FN during cornering. Figure 6.13 illustrates the FN plotted against curve radius from field experiments in Chapter 5, demonstrating that as the curve radius decreases, leading to an increased slip angle, the friction number also decreases. This is attributed to an increase in the vertical force at the inner curve side as the curve radius increases, while the longitudinal friction force remains consistent. As a result, the FN decreases.

Additionally, Figure 6.14 depicts that the FN under pure sideslip cornering conditions is slightly higher than the longitudinal FN under the same external loads. Their relationship displays a linear function. It is important to note that this linearity is due to the small slip angles considered in the study, less than 8 degrees,

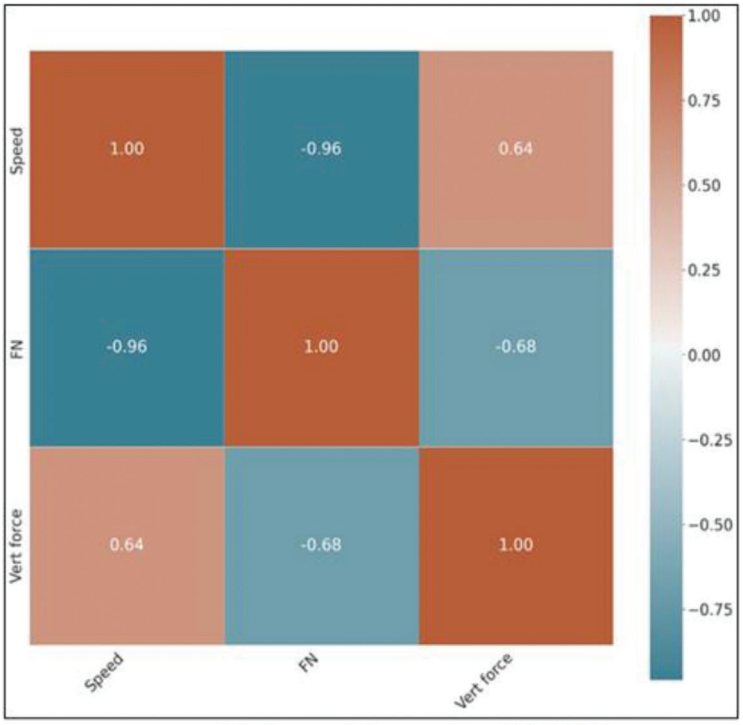

(a) On straight runway (10/2023)

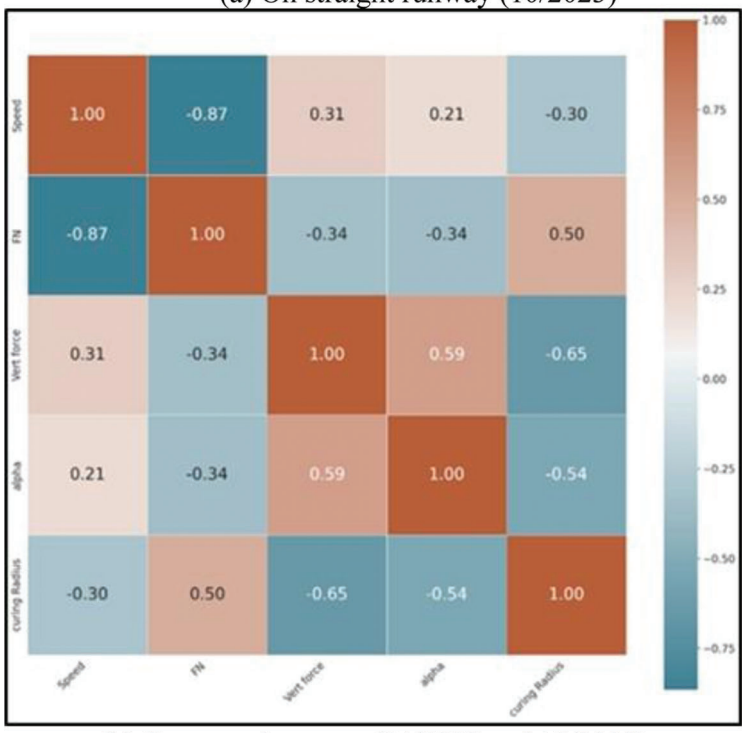

(b) On curved runway (04/2023 and 10/2023)

Figure 6.11 Correlation map from field-testing data.

where the cosine value is close to 1, and thus, a cosine basis function is not prominently manifested. Considering the available data limitations, 75% of the experimental dataset is allocated for training, incorporating parameters like speed, vertical load, and slip angle. The remaining 25% is dedicated to testing, specifically for predicting the FN. The prediction results are visualized in Figure 6.15.

The cross-validated loss estimation indicates a value of 3.1693. Given the model's validity and the constraints of the experimental data, the subsequent GPR analysis relies on training with 100% of the available

experimental data for a more accurate estimation. Figure 6.16 represents the predicted FN, demonstrating a decrease with increasing speed, aligning with trends suggested by Gillespie (2021). In accordance with Equations 6.3–6.6, the correction coefficient between friction number and friction force from longitudinal to curve can be calculated as $1/\cos\alpha$. Figure 6.17 illustrates that the vertical force remains constant when the vehicle is on a straight road. Additionally, it emphasizes the correlation between the vertical force and the direction of vehicle movement. For instance, the vertical force increases with speed during right turns and decreases during left turns. Furthermore, the vehicle's proceeding direction is identified as an influencing factor of friction numbers. The relationship between friction numbers and proceeding speed is depicted in Figure 6.18, where friction values are close when the vehicle proceeds at a low speed (15 mph).

Figure 6.12 Top view of the tire under pure sideslip cornering conditions.

However, the friction differences become more pronounced as the vehicle accelerates. These findings align well with outcomes from Gillespie (2021), who observed that the friction coefficient decreases with velocity. Figure 6.19 illustrates the relationship between longitudinal friction force and speed. It is evident that at the same speeds, the longitudinal force remains consistent whether the vehicle is on a straight or curved road. This discovery aids in examining the actual friction force experienced when the vehicle undergoes pure sideslip cornering conditions.

Figure 6.20 presents the GPR prediction results with the true values of friction numbers corresponding to the April 2023 measurements. The figure shows that the GPR predictions are very close to the true friction numbers, demonstrating the accuracy of this model. The cross-validated loss is calculated to be 0.2772. In October 2023, an additional friction testing was performed, the GPR predictions and the measured friction numbers, including both friction measurements in April and October, are shown in Figure 6.21. The GPR predictions with added data points are also of high accuracy.

6.4.3 Finite Element Model Validation for GPR Prediction

A validation of the accuracy of GPR learning outcomes was conducted through an extensive set of FEA models. The GPR model, trained on data from prior physical experiments, demonstrates its capability in predicting vertical force as a machine learning output, utilizing parameters such as velocity, slip angle,

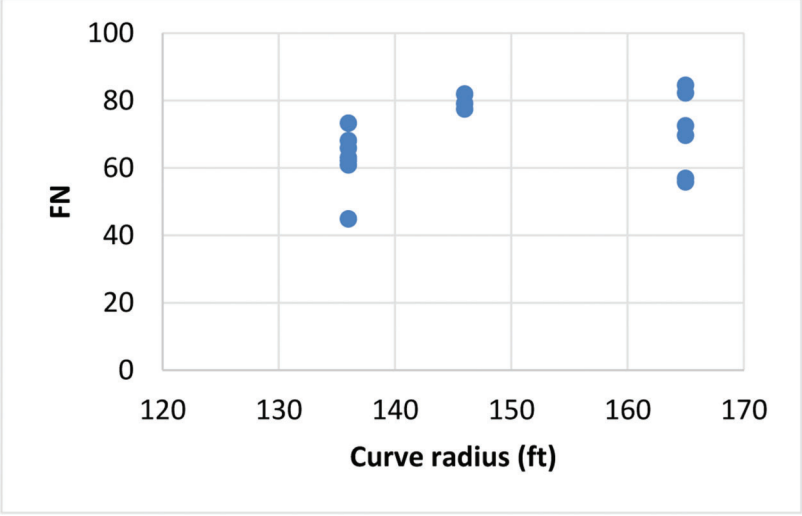

Figure 6.13 Estimated friction numbers under pure sideslip cornering conditions.

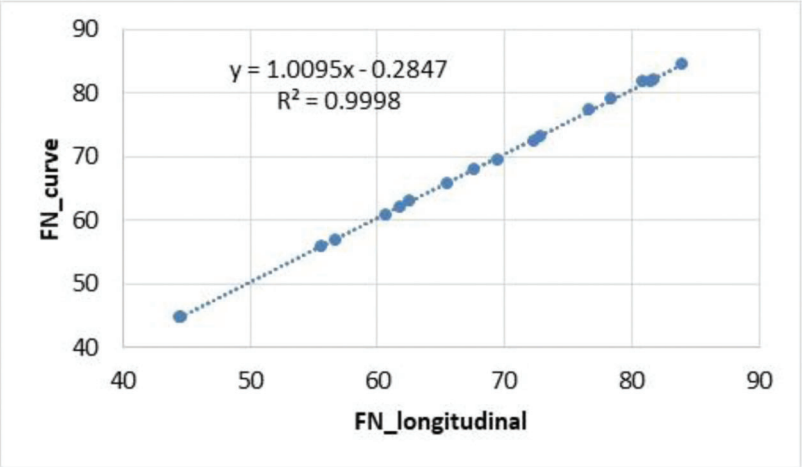

Figure 6.14 Estimated friction numbers on curved and straight roads.

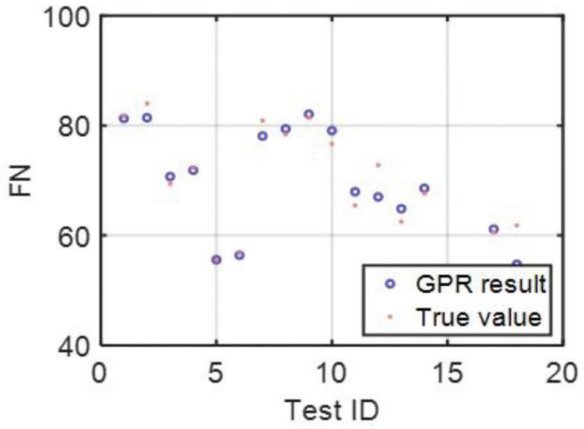

Figure 6.15 GPR predicted vs. actual measured friction numbers.

and curve radius. The objective involves the construction of a dataset of 500 predictions. Subsequently, corresponding FEA models are executed to derive the longitudinal horizontal force. This horizontal force, determined from the FEA, represents the actual value, and takes into account factors such as velocity, slip angle, vertical force, and tangential friction number, as detailed in Equation 6.7.

$$INPUT(Velocity, slip\ angle, vertical\ force, tangential\ longitudinal\ FN) = FEA(OUTPUT) \quad \text{(Eq. 6.7)}$$

The inputs for the FEA comprise a dataset of 500 data points, evenly distributed across a spectrum of velocity and slip angle values. Furthermore, the vertical force data, predicted with precision by a GPR machine learning model, serves as an additional critical input for the FEA. It is imperative to note that these inputs are aligned with the same range employed in the experimental testing phase. Figure 6.22 shows the input distributions for velocity, slip angle, and vertical force in the FEA model.

The outcomes of the FEA in terms of longitudinal horizontal force are compared to the "true" horizontal force. The predicted horizontal force is computed using Equation 6.8, incorporating the FN. The difference between these values is obtained using Equation 6.9.

$$F_x(Prediction) = F_y \times longitudinal\ FN \quad \text{(Eq. 6.8)}$$

$$Difference\ (\%) = \frac{F_x(FEA) - F_x(GPR)}{F_x(GPR)} * 100\% \quad \text{(Eq. 6.9)}$$

The differences, as illustrated in Figure 6.23, reveal that the disparities in longitudinal horizontal force (F_x) values between the FEA runs and GPR predictions are minimal, ranging from 0.110% to 0.375%. Figure 6.24 presents a box plot illustrating the distribution of differences between GPR and FEA produced F_x values. The average difference across the dataset is 0.242%, with the maximum and minimum recorded differences being 0.378% and 0.124%, respectively. This plot provides a comprehensive overview of the distribution of differences, further emphasizing the consistency and reliability of the predictive capabilities of the GPR model in estimating F_x values.

6.4.4 Derived True Friction on Curved Road Through Machine Learning

This study investigates the intricate dynamics of tire-pavement interactions on horizontal roadway curves, focusing on a locked wheel skid tester (LWST) and employing a mechanistic-empirical approach. Through an analysis of various vehicle operational characteristics in different configurations, the study scrutinizes slip angles recorded by cameras installed on the friction tester. These slip angles serve as a basis for determining both vertical and horizontal forces at the points of tire-pavement contact. To establish true friction values on curved roads, the study leverages FEA and machine learning. The results of FEA simulations, coupled with GPR predictions, are consolidated in Appendix C for

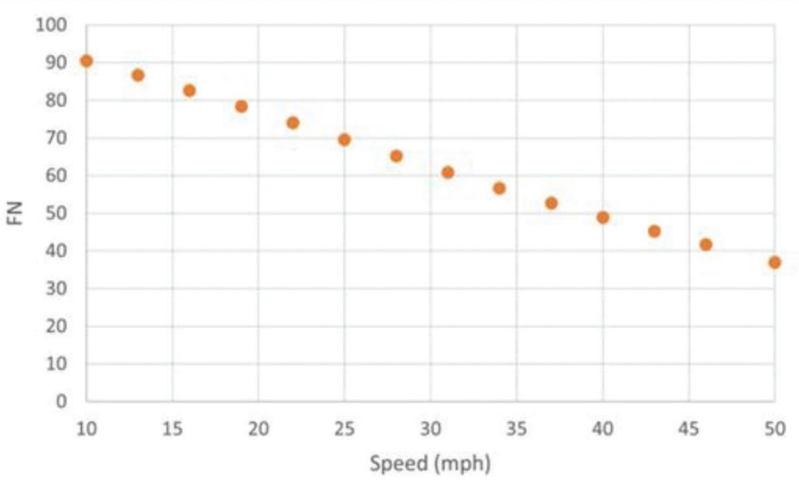

Figure 6.16 Estimated friction numbers on curved road at various speeds.

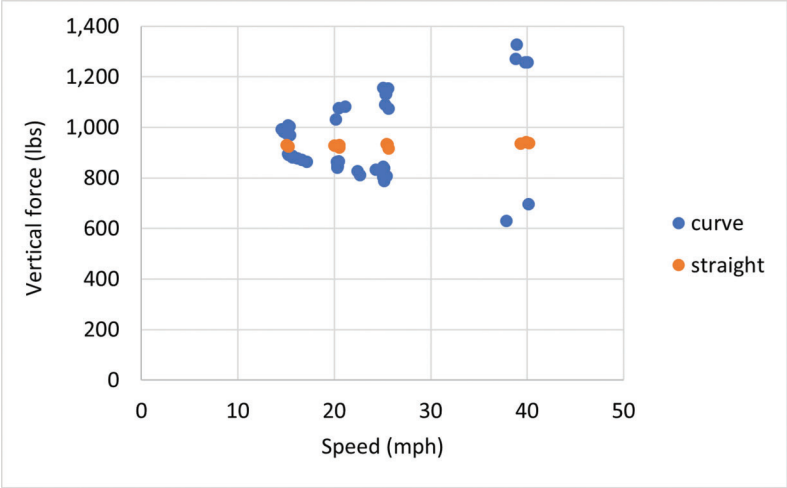

Figure 6.17 Locked wheel smooth tire vertical forces.

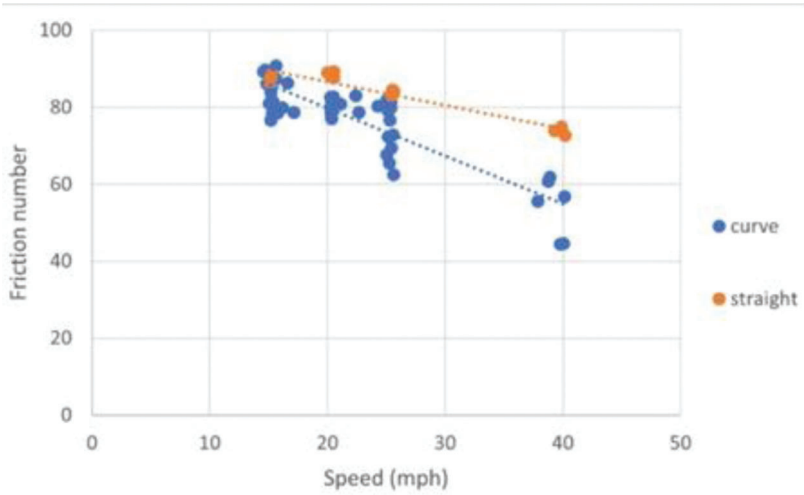

Figure 6.18 Locked wheel smooth tire friction numbers.

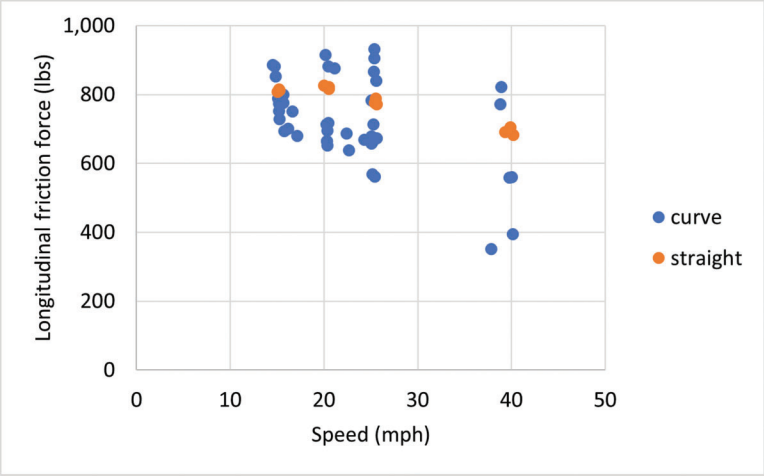

Figure 6.19 Locked wheel smooth tire longitudinal friction forces.

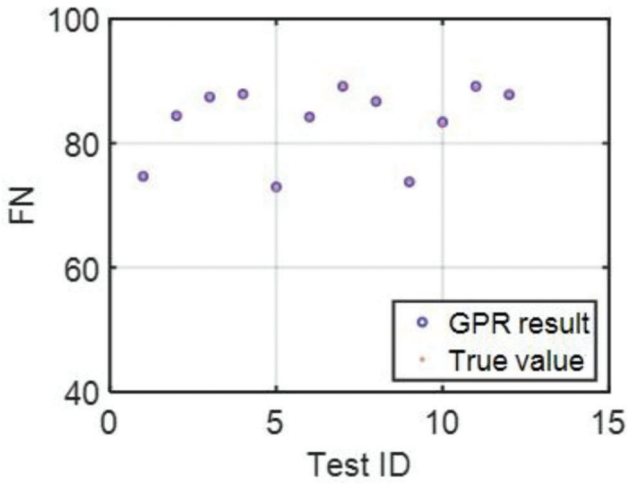

Figure 6.20 GPR predicted vs. measured friction (04/2023).

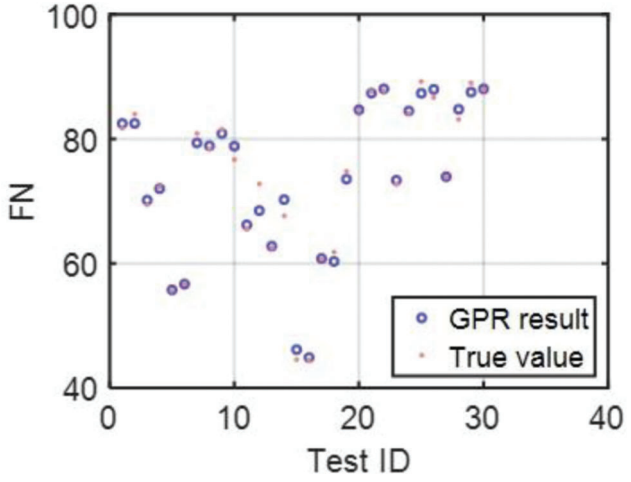

Figure 6.21 GPR predicted vs. measured friction (04/2023 and 10/2023).

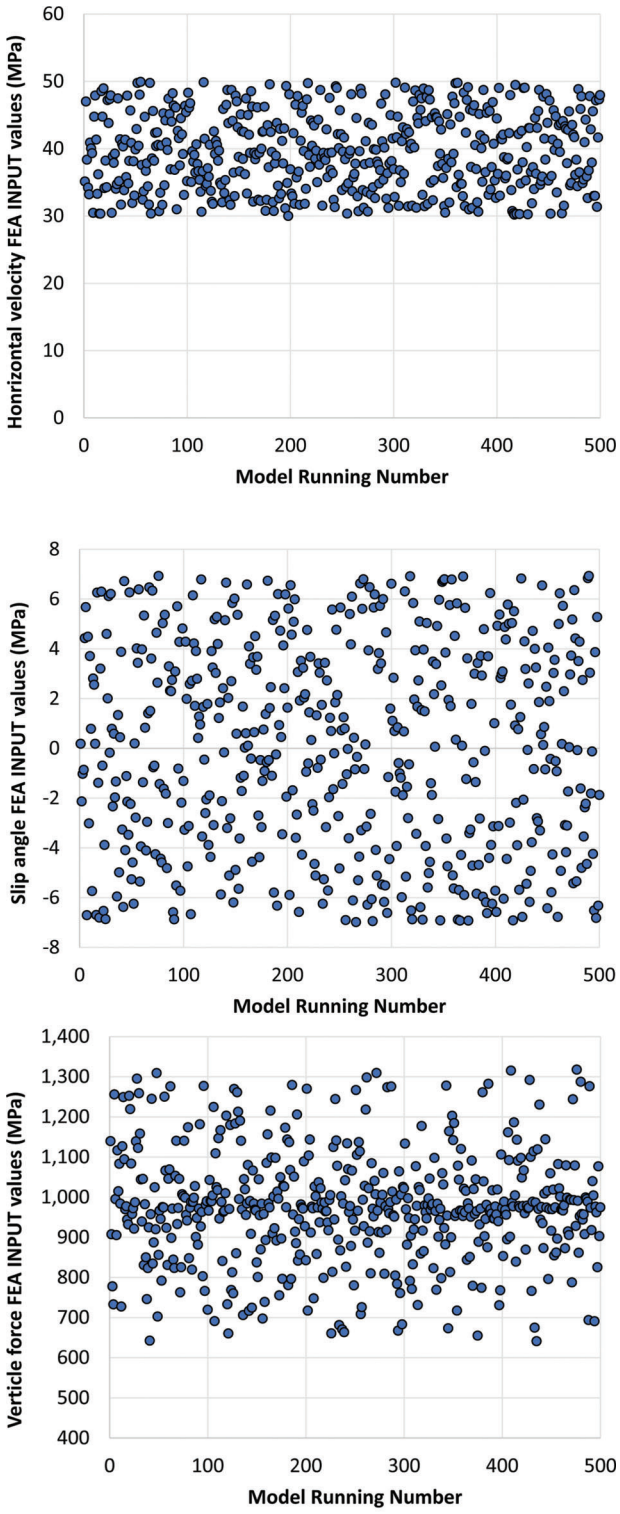

Figure 6.22 Plot of 500 runs of FEA inputs.

comprehensive reference. This table summarizes true friction numbers, providing a representation of the actual frictions between the tires of the test vehicle and the pavement on horizontal roadway curves. These numbers are derived from the vertical and horizontal forces acting on the LWST tire during its traversal of horizontal roadway curves. Consequently, Appendix C offers a practical tool for obtaining true friction numbers by directly referencing the values alongside the geometric characteristics of the curves.

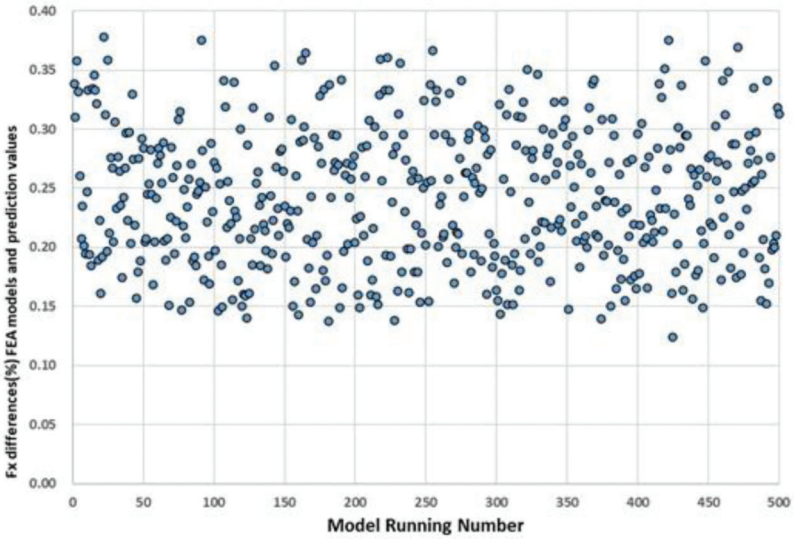

Figure 6.23 Differences between GPR and FEA calculated Fx values.

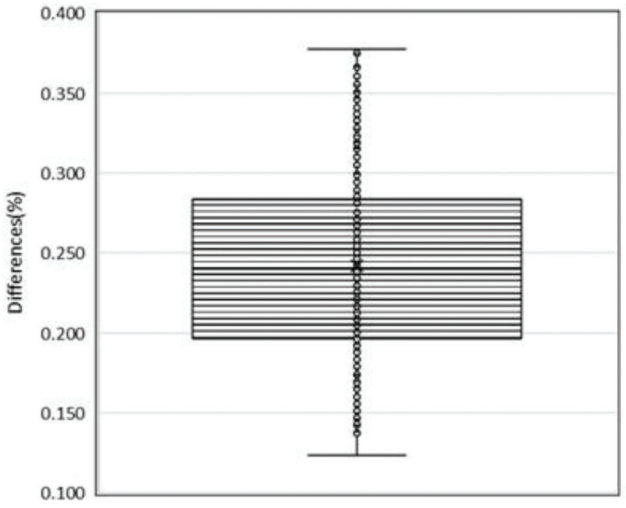

Figure 6.24 The box plot of differences of GPR and FEA results.

The following steps may be used to use Appendix C.

- Get information on the speed of the vehicle (mph), slip angle (degree), and camber angle (degree) of the horizontal roadway curves. The camber angle could be calculated from road inclination.
- Go to Table C.1 and find the true friction number by using the information of the three items in Step 1. The first 500 rows of Table C.1 represent horizontal roadway curves with slip angle only. The last 500 rows of Table C.2 represent horizontal roadway curves with inclinations.
- The true friction numbers are predicted by machine learning algorithms through the training of experimental data and validated by physical modeling through finite element analysis. The ranges of the vehicle speed, slip angle, and camber angle are feasible based on INDOT standards and practices. If larger ranges of the three items are suggested, the friction number can also be predicted through the machine learning tool presented in the report.

7. CHAPTER 7. CONCLUSIONS

This project has investigated the intricate realm of pavement friction, aiming to achieve seamless coverage and a comprehensive understanding of the associated issues, including pavement markings, aggregates, color surface treatment (CST), and locked wheel skid trailer (LWST) testing on horizontal curves. Major findings and conclusions are drawn as follows.

Pavement Markings

- *Wet and Dry Surface:* For new markings without polishing, the British Pendulum Number (BPN) in dry conditions is 44% higher than in wet conditions on average.
- *Waterborne and Non-Waterborne Markings:* For new markings without polishing, waterborne makings exhibit BPN values 27% greater than non-waterborne markings on average when the same type of beads, application rate, and thickness are applied. Most waterborne markings can withstand no more than 1,500 polishing cycles. However, waterborne markings with Type 1 beads and a thickness of 20 mils or more exhibit better durability, i.e., up to 5,000 polishing cycles.
- *Pavement Marking Thickness:* Increasing the thickness of pavement marking can significantly enhances its durability but does not substantially increase friction.
- *Bead Size and Application Rate:* For glass beads, an increase in bead size contributes to initial mean profile depth (MPD) but doesn't necessarily result in higher initial friction. Also, larger beads, particularly Type 4, may lead to a decrease in durability. Nevertheless, smaller beads consistently exhibit higher durability and friction. A higher bead application rate also leads to an increase in MPD, particularly for waterborne markings.
- *Ceramic Particles:* Adding ceramic particles tends to increase both MPD and friction significantly, especially under wet conditions, but compromise the durability.
- *Friction Metrics:* In addition to macrotexture features, additional microtexture features should be considered to fully define the correlation between texture and friction. There also are discrepancies between BPN and DF40.

TABLE 7.1
Recommended Chemical Requirements

Property	Test Method	Dolomite (%)	Limestone (%)	Gravel (%)	Steel Slag (%)	Bauxite (%)
Al_2O_3, %	ASTM C25	≥0.03	≥0.61	≥2.9	≥5.00	≥86.5
TiO_2, %	ASTM C25	≥0.01	≥0.04	≥0.11	≥0.33	–
MgO, %	ASTM C25	≤21.2	≤17.9	≤7.9	≤10.3	–
CaO, %	ASTM C25	≤31.0	≤36.0	≤33.5	≤38.5	–

TABLE 7.2
Recommended Physical and Mechanical Requirements

Attribute	Method	Dolomite (%)	Limestone (%)	Gravel (%)	Steel Slag (%)	Bauxite (%)
Los Angeles Abrasion (LAA)	AASHTO T96	≤29.6	≤26.2	≤23.4	≤15.1	≤12.5
Micro-Deval Abrasion (MDA)	AASHTO T327	≤12.3	≤16.3	≤11.2	≤6.7	≤5.5[1]
Polished Stone Value (PSV-10)	AASHTO T278/T279	≥26.0	≥30.0	≥27.0	≥26.0	≥35.0
Bulk Specific Gravity (BSG)	AASHTO T85	≥2.60	≥2.50	≥2.60	≥3.40	ASG ≥ 3.3[2]
Water Absorption (WA)	AASHTO T85	≤2.3	≤2.3	≤1.7	≤1.5	≤3.0

[1]Grading of 4.75-9.5 mm.
[2]Apparent specific gravity.

- *Friction Performance and Requirements:* Most new markings exhibit friction performance with BPN ranging from 30 to 65. A tentative minimum requirement of BPN = 40~45 is recommended. If a minimum BPN of 40 is required, only new thermoplastic (intermixed beads) markings, new epoxy markings, and waterborne markings in the later stage of their service life may not meet this requirement. However, this can be addressed by either adding ceramic particles or by combining the addition of ceramic particles with an increase in the marking thickness. The mixing ratio of glass beads and ceramic particles can usually refer to the vendor's recommendation.

Aggregates

- *Physical Properties vs. Mechanical Properties:* Bulk specific gravity (BSG) has a more significant impact on the mechanical properties than water absorption (WA) and soundness. The correlation between LAA and PSV-10 is weak or very weak, regardless of the type of aggregate. MDA and PSV-10 exhibit mixed correlations, depending on the type of aggregate.
- *Chemical Compositions vs. Mechanical Properties:* The chemical contents of Al_2O_3 and TiO_2 have strong positive correlations with hardness and the contents of MgO and CaO have strong negative correlations with hardness. However, the chemical components, including Al_2O_3 and TiO_2, exhibit greater variabilities, regardless of aggregate types, including dolomite, limestone, and gravel. To ensure the consistent aggregate quality (particularly mechanical properties), it is advisable to specify the chemical requirements for aggregates as shown in Table 7.1.
- *Mg Content for Dolomite:* The current requirement for minimum Mg content in dolomite is 10.3% that is lower than the Mg contents of both most dolomite samples and some limestone samples. It is recommended to revise the current requirement to 12.0% to help ensure consistent engineering properties and performance characteristics of the dolomite aggregate.
- *Physical and Mechanical Properties:* Aligned with the recommended chemical requirements, the suggested criteria for aggregate physical and mechanical properties, are presented in Table 7.2.
- When assessing the frictional performance of aggregates, including dolomite, limestone, gravel, steel slag, and calcined bauxite, they may be ranked in terms of abrasion resistance (LAA and MDA), resistance to polishing (PSV-10), and/or Mohs hardness in descending order as follows.

  Calcined bauxite → Steel slag → Gravel → Dolomite → Limestone

Color Surface Treatment

- *Green Bike Lane:* The current color surface treatment (CST) with bauxite aggregate of size 6 × 16 can maintain durable surface integrity and friction performance (BPN equal to or greater than 60, measured with a 6 × 25 × 76 mm slider; and MPD not less than 1.00 mm) for over 3 years.
- *Red Bus Lane:* The current CST may perform satisfactorily for up to 3 years depending on the surface condition of underlying pavement. However, the current CST, featuring bauxite aggregate of size 6 × 16, showed an MPD of 0.22 mm~0.23 mm after 3 years in service. Furthermore, it exhibited an MPD of 0.78 mm~0.85 mm and a friction number (FN) of 32~36 (measured with the standard smooth tire at 40 mph) after six months in service. Both the MPD and friction number are markedly lower than those of HFST. The two key takeaways are: first, the surface of the red bus lane undergoes severe polishing, necessitating the use of high polish-resistant aggregates, especially calcined bauxite; and second, to enhance the surface frictional properties of the red bus lane, consideration can be given to appropriately increasing the size of the bauxite aggregate.

Friction Test with Locked Wheel Skid Trailer on Horizontal Curves

- Tire cornering stiffness is dependent on numerous tire properties, including the material, size, vertical load, inflation pressure, and tread pattern, and can be estimated with the longitudinal friction force and the vertical force measured for a test tire in the case of pure side slip.
- The effect of the speed discrepancies between the vehicle and trailer on the friction coefficient measurement is negligible for locked wheel skid trailer (LWST) test on actual highway horizontal curves as long as a test failure due to trailer fishtailing is avoided.
- To limit the cornering impact on test tire vertical load (<100-lb), a radius of curvature greater than $0.3V^2$ is suggested for cornering tests in pure sideslip condition. If a selected superelevation rate of 4%, 6%, or 8% is added, a minimum curve radius of 445.92-ft, 432.576-ft, or 420.92-ft is suggested for realiable measurements at 40 mph, respectively.

Tire Friction Modeling with Finite Element Analysis and Machine Learning

- The adaptability of the Finite Element Analysis (FEA) model and the efficiency of machine learning techniques offer an effective avenue for comprehending the intricate dynamics between tires and varying roadway conditions.
- Through FEA simulations, coupled with Gaussian process regression (GPR) predictions, true friction numbers on horizontal roadway curves can be derived from the testing results with locked wheel skid tester (LWST).
- A comprehensive reference table is developed to provide a practical tool for obtaining true friction numbers by directly referencing the measured friction values alongside the geometric characteristics of the roadway curves.

REFERENCES

3M. (n.d.). *3M connected roads all weather elements* [Webpage]. https://www.3m.com/3M/en_US/p/d/b5005047004/

3M. (2020, April). *3M all weather thermoplastic*. https://multimedia.3m.com/mws/media/504580O/pb-3m-all-weather-thermoplastic.pdf

3M. (2022). *3M Stamark high performance pavement marking tape series 380AW*. https://www.3m.com/3M/en_US/p/d/b5005178004/

AASHTO. (2018). *AASHTO M 247-13: Standard specification for glass beads used in pavement markings*. American Association of State Highway and Transportation Officials.

AASHTO. (2021). *AASHTO T 278-90: Surface frictional properties using the British pendulum tester*. American Association of State Highway and Transportation Officials.

AASHTO. (2022a). *AASHTO T 327-22: Standard method of test for resistance of coarse aggregate to degradation by abrasion in the micro-deval apparatus*. American Association of State Highway and Transportation Officials.

AASHTO. (2022b). *AASHTO T 279-18: Standard method of test for accelerated polishing of aggregates using the British wheel*. American Association of State Highway and Transportation Officials.

AASHTO. (2022c). *AASHTO T 85-22: Standard method of test for specific gravity and absorption of coarse aggregate*. American Association of State Highway and Transportation Officials.

AASHTO. (2022d). *AASHTO T 96-22: Standard method of test for resistance to degradation of small-size coarse aggregate by abrasion and impact in the Los Angeles machine*. American Association of State and Highway Transportation Officials.

Ababsa, F., & Mallem, M. (2004, June 16). Robust camera pose estimation using 2d fiducials tracking for real-time augmented reality systems. *Proceedings of the 2004 ACM SIGGRAPH International Conference on Virtual Reality Continuum and Its Applications in Industry* (pp. 431–435). https://doi.org/10.1145/1044588.1044682

Ahammed, M. A., & Tighe, S. L. (2012). Asphalt pavements surface texture and skid resistance–exploring the reality. *Canadian Journal of Civil Engineering*, *39*(1), 1–9.

Ajalloeian, R., & Kamani, M. (2019). An investigation of the relationship between Los Angeles abrasion loss and rock texture for carbonate aggregates. *Bulletin of Engineering Geology and the Environment*, *78*(3), 1555–1563.

Albin, R. B., Brinkly, V., Cheung, J., Julian, F., Satterfield, C., Stein, W. J., Donnell, E. T., McGee, H. W., Holzem, A., Albee, M., Wood, J., & Hanscom, F. R. (2016). *Low-cost treatments for horizontal curve safety 2016* (Report No. FHWA-SA-15-084). Pennsylvania State University.

Alhasan, A., Smadi, O., Bou-Saab, G., Hernandez, N., & Cochran, E. (2018). Pavement friction modeling using texture measurements and pendulum skid tester. *Transportation Research Record: Journal of the Transportation Research Board*, *2672*(40), 440–451.

Ames Engineering. (n.d.). *Laser texture scanner 9400/9400HD*. https://amesengineering.com/products/laser-texture-scanner-model-9400/

Anderson, D., & Henry, J. (1980). Wet-pavement friction of pavement-marking materials. *Transportation Research Record*, *777*, 58–62.

Anderson, D. A., Henry, J. J., & Hayhoe, G. F. (1982). Prediction and significance of wet skid resistance of pavement marking materials. *Transportation Research Record*, *893*, 27–32.

Asdrubali, F., Buratti, C., Moretti, E., D'Alessandro, F., & Schiavoni, S. (2013). Assessment of the performance of road markings in urban areas: The Outcomes of the CIVITAS RENAISSANCE Project. *The Open Transportation Journal*, *7*, 7–19.

Asi, I. M. (2007). Evaluating skid resistance of different asphalt concrete mixes. *Building and Environment*, *42*(1), 325–329.

ASTM. (2015a). *ASTM E1845-15: Standard practice for calculating pavement macrotexture mean profile depth*. American Society for Testing and Materials.

ASTM. (2015b). *ASTM E1960-07: Standard practice for calculating international friction index of a pavement surface*. American Society for Testing and Materials.

ASTM. (2019a). *ASTM E1911-19: Standard test method for measuring surface frictional properties using the dynamic friction tester*. American Society for Testing and Materials.

ASTM. (2019b). *ASTM E2157-15: Standard test method for measuring pavement macrotexture properties using the circular track meter*. American Society for Testing and Materials.

ASTM. (2019b). *ASTM C25-19: Standard test methods for chemical analysis of limestone, quicklime, and hydrated lime*. American Society for Testing and Materials.

ASTM. (2020a). *ASTM E274/E274M-15: Standard test method for skid resistance of paved surfaces using a full-scale tire*. American Society for Testing and Materials.

ASTM. (2020b). *ASTM C1895-20: Standard test method for determination of Mohs scratch hardness*. American Society for Testing and Materials.

ASTM. (2020c). *ASTM E524-08: Standard specification for standard smooth tire for pavement skid-resistance tests*. American Society for Testing and Materials.

Atkinson, J., Clark, J., & Ercisli, S. (2016). *High friction surface treatment curve selection and installation guide* (Report No. FHWA-SA-16-034). Federal Highway.

Aytekin, B., & Mardani-Aghabaglou, A. (2022). Sustainable Materials: A review of recycled concrete aggregate utilization as pavement material. *Transportation Research Record: Journal of the Transportation Research Board*, *2676*(3), 468–491.

Babić, D., Burghardt, T. E., & Babić, D. (2015). Application and characteristics of waterborne road marking paint. *International Journal of Traffic and Transport Engineering*, *5*(2), 150–169.

Bagot, K. (1996, July). *Follow-up friction testing of retro-reflective glass beads* (Report No. DOT/FAA/AR-TN96/74). Federal Aviation Administration.

Bao, J., Jiang, Y., & Li, S. (2023). Determination of safety-oriented pavement-friction performance ratings at network level using a hybrid clustering algorithm. *Lubricants*, *11*(7), 275.

Bektas, B. A., Gkritza, K., & Smadi, O. (2016). Pavement marking retroreflectivity and crash frequency: Segmentation, line type, and imputation effects. *Journal of Transportation Engineering*, *142*(8).

Bergman, W., & Beauregard, C. (1974). *Transient tire properties* (SAE Technical Paper 740068). https://doi.org/10.4271/740068

Botha, T. R., & Els, P. S. (2014). Tire longitudinal slip-ratio measurement using a camera. In *International Design Engineering Technical Conferences & Computers and Information in Engineering Conference*. The American Society of Mechanical Engineers.

Botha, T. R., & Els, P. S. (2015). Digital image correlation techniques for measuring tyre-road interface parameters: Part 1 – Side-slip angle measurement on rough terrain. *Journal of Terramechanics*, *61*, 87–100.

BSI. (2018). *Road marking materials–Road marking performance for road users and test methods* (British Standards Publication BS EN 1436). British Standard Institute.

Cairney, P., & Styles, E. (2005, February). *A pilot study of the relationship between macrotexture and crash occurrence* (No. CR 223). ARRB Transport Research.

Carlson, P., Park, E.-S., Pike, A., Porter, R. J., Miles, J., Boulanger, B., Smadi, O., Hawkins, N., Chalmers, S., Darmiento, F., Burde, A., Kuhn, B., & Ealding, W. (2013, November). *Pavement marking demonstration Projects: State of Alaska and State of Tennessee* (Report No. FHWA-HRT-12-048). Texas Transportation Institute.

Caroux, J., Lamy, C., Basset, M., & Gissinger, G.-L. (2007). Sideslip angle measurement, experimental characterization and evaluation of three different principles. *IFAC Proceedings Volumes*, *40*(15), 505–510. https://doi.org/10.3182/20070903-3-FR-2921.00086

Carry, W., Donnell, E., Rado, Z., Hartman, M., & Scalici, S. (2012, February). *Red bus lane treatment evaluation*. New York City Department of Transportation and the Pennsylvania State University. https://www.nctcog.org/getmedia/826d3748-201e-4ca3-b707-0755d3158383/RedBusLaneTreatmentEval.pdf

Caup, L., Salmen, J., Muharemovic, I., & Houben, S. (2013). Video-based trailer detection and articulation estimation. *2013 IEEE Intelligent Vehicles Symposium (IV)* (pp. 1179–1184). https://doi.org/10.1109/IVS.2013.6629626

Chan, R., Santana, M. A., Oda, A. M., Paniguel, R. C., Vieira, L. B., Figueiredo, A. D., & Galobardes, I. (2019). Analysis of potential use of fibre reinforced recycled aggregate concrete for sustainable pavements. *Journal of Cleaner Production*, *218*, 183–191.

Chu, L., Fang, Y., Shang, M., Guo, J., & Zhou, F. (2010). Estimation of articulation angle for tractor semi-trailer based on State observer. *2010 International Conference on Measuring Technology and Mechatronics Automation*, *2*, 158–163. https://doi.org/10.1109/ICMTMA.2010.342

Coves-Campos, A., Bañón, L., Coves-García, J., & Ivorra, S. (2018). In situ study of road marking durability using glass microbeads and antiskid aggregates as drop-on materials. *Coating*, *8*(10), 371.

Dassault Systèmes. (2014). *Abaqus/CAE user's guide* (Software 6.14). https://62.108.178.35:2080/v6.14/books/usi/default.htm

De Saxe, C., & Cebon, D. (2021, August). Camera-based articulation angle sensing for heavy goods vehicles. *IEEE Transactions on Vehicular Technology*, *70*(8), 7522–7535. https://doi.org/10.1109/TVT.2021.3091759

De Saxe, C., Berman, R. J., Clarke, A., & Reinecke, D. (2019, July 8–11). *Camera-based side-slip measurement for tyre testing* [Conference session]. 38th Southern African Transport Conference (SATC), Pretoria, South Africa. https://repository.up.ac.za/bitstream/handle/2263/74267/2C_DeSaxe_Camera_2019.pdf

Donnell, E. T., Chehab, G. R., Tang, X., & Schall, D. (2009). Exploratory analysis of accelerated wear testing to evaluate the performance of pavement markings. *Transportation Research Board: Journal of Transportation Research Board*, *2107*, 76–84.

Doumiati, M., Victorino, A. C., Charara, A., & Lechner, D. (2011). Onboard real-time estimation of vehicle lateral tire–road forces and sideslip angle. *IEEE/ASME Transactions on Mechatronics*, *16*(4), 601–614. https://doi.org/10.1109/TMECH.2010.2048118

Dravitzki, V. K., Wood, C., Charara, A., & Lechner, D. (1997). *Assessing road surface friction with the British pendulum tester in New Zealand*. Transfund New Zealan.

Dugoff, H., Fancher, P. S., & Segel, L. (1970). *An analysis of tire traction properties and their influence on vehicle dynamic performance* (SAE Technical Paper 700377). https://doi.org/10.4271/700377

Ehlgen, T., Pajdla, T., & Ammon, D. (2008, December). Eliminating blind spots for assisted driving. *IEEE Transactions on Intelligent Transportation Systems*, *9*(4), 657–665. https://doi.org/10.1109/TITS.2008.2006815

FHWA. (n.d.). *Roundabouts & rural highways*. https://safety.fhwa.dot.gov/intersection/roundabouts/fhwasa14097.pdf

FHWA. (2011, April 15). *Manual on uniform traffic control devices: Interim approval for optional use of green colored pavement for bike lanes* [Memorandum]. Federal Highway Administration.

FHWA. (2020). National standards for traffic control devices: Manual on uniform traffic control devices for streets and highways; Revision. *Federal Register*, *85*(240), 80898–8097.

FHWA. (2023, December). *Manual on uniform traffic control devices for streets and highways* (11th Edition). Federal

Highway Administration. https://mutcd.fhwa.dot.gov/pdfs/11th_Edition/mutcd11thedition.pdf

Figueroa, A., & Colucci, B. (2007, May 14). *Motorcycle crashes and its implications to local roads* [Conference session]. Southeast Local Roads Conference (SELRC), Orange Beach, Alabama.

Fischler, M., & Bolles, R. (1981). Random sample consensus: A paradigm for model fitting with applications to image analysis and automated cartography. *Communications of the ACM*, *24*(6), 381–395.

Flintsch, G. W., de León Izeppi, E., McGhee, K. K., & Najafi, S. (2010). Speed adjustment factors for locked-wheel skid trailer measurements. *Transportation Research Record: Journal of the Transportation Research Board*, *2155*(1), 117–123. https://doi.org/10.3141/2155-13

Fowler, D. W., & Rached, M. (2012, December). Polishing resistance of fine aggregates in Portland cement concrete pavements. *Transportation Research Record: Journal of the Transportation Research Board*, *2267*(1), 29–36.

Fuchs, C., Neuhaus, F., & Paulus, D. (2015). Advanced 3-D trailer pose estimation for articulated vehicles. *2015 IEEE Intelligent Vehicles Symposium (IV)* (pp. 211–216). IEEE. https://doi.org/10.1109/IVS.2015.7225688

Gates, T. J., Hawkins, G., Jr., & Rose, E. R. (2003). *Effective pavement marking materials and applications for Portland cement concrete roadways* (Texas Transportation Institute Publication No. FHWA/TX-03/4150-2). Texas Transportation Institute.

Giles, C., Sabey, B. E., & Cardew, K. (1965). Development and performance for the portable skid resistance tester. *Rubber Chemistry and Technology*, *38*(4), 840–862.

Gillespie, T. D. (2021). *Fundamentals of vehicle dynamics*. SAE International.

Goodyear. (n.d.). *Tire size chart* [Webpage]. Retrieved January 18, 2024, from https://www.goodyear.com/en_US/learn/choosing-your-tires/tire-size-chart.html

Goodyear. (2018). Commercial tires and retreads-engineering data book. https://stg.goodyeartrucktires.com/pdf/resources/publications/2018_goodyear_commercial_tires_engineering_databook.pdf

Hajj, R., Filonzi, A., Smit, A., & Bhasin, A. (2019, May). Design and performance of mixes for use as ultrathin overlay. *Journal of Transportation Engineering, Part B: Pavements*, *145*(3).

Hall, J. W., Smith, K. L., Titus-Glover, L., Wambold, J. C., Yager, T. J., & Rado, Y. Z. (2009, February). *Guide for pavement friction* (Final Report for NCHRP Project 01-43). National Cooperative Highway Research Program.

Hanna, A. N. (2003). Aggregate tests for Portland cement concrete pavements: Review and recommendations. *NCHRP Research Results Digest*, (281), 1–28. National Cooperative Highway Research Program.

Harlow, A. (2005). *Skid resistance and pavement marking materials*. Transit New Zealand.

Harris, M. (2013). *Application of computer vision systems to heavy goods vehicles: Visual sensing of articulation angle* [Master's thesis, University of Cambridge].

Heitzman, M., & Erukulla, S. (2011, September 14–16). *Accelerated laboratory testing protocol to measure asphalt mixture friction characteristics* [Conference presentation]. 3rd International Conference on Road Safety and Simulation, Indianapolis, Indiana.

Heitzman, M., Turner, P., & Greer, M. (2015). *High friction surface treatment alternative aggregates study* (NCAT Report 15-04). National Center for Asphalt Technology.

Henry, J. J. (2000). *Evaluation of pavement friction characteristics* (NCHRP Synthesis of Highway Practice 291). Transportation Research Board.

Hibbs, B. O., & Larson, R. M. (1996, May). *Tire pavement noise and safety performance* (Report No. FHWA-SA-96-068). Pavement Division, Office of Engineering, Federal Highway Administration. https://www.fhwa.dot.gov/pavement/pubs/013169.pdf

INDOT. (2013/2022). Section 502: Traffic design. In *2013 Indiana Design Manual*. Indiana Department of Transportation. https://www.in.gov/dot/div/contracts/design/Part%205/Chapter%20502%20-%20Traffic%20Design.pdf

INDOT. (2016). *Acceptance procedures for polish resistant aggregates* (ITM No. 214-16). Indiana Department of Transportation.

INDOT. (2018). *Acceptance procedures for HMA surface mixture coarse aggregates for ESAL <10,000* (ITM No. 221-18). Indiana Department of Transportation.

INDOT. (2022). *2022 Standard specifications* [Webpage]. Indiana Department of Transportation.

Jeong, D., Ko, G., & Choi, S. B. (2022). Estimation of sideslip angle and cornering stiffness of an articulated vehicle using a constrained lateral dynamics model. *Mechatronics*, *85*, 102810. https://doi.org/10.1016/j.mechatronics.2022.102810

Jiang, Y. (2008). *Durability and retroreflectivity of pavement markings (synthesis study)* (Joint Transportation Research Program Publication No. FHWA/IN/JTRP-2007/11). West Lafayette, IN: Purdue University. https://doi.org/10.5703/1288284313356

Johnson, E. N., Izevbekhai, B. I., & Olson, R. C. (2009). Thermoplastic inlay pavement markings: Field performance and effect on hot-mix asphalt. *Transportation Research Record: Journal of the Transportation Research Board*, *2107*(1), 85–91.

Johnson, R. W. (2001, May). An introduction to the Bootstrap. *Teaching Statistics*, *23*(2), 49–54.

Kassem, E., Awed, A., Masad, E. A., & Little, D. N. (2013). Development of the prediction model of the skid loss of asphalt pavements. *Transportation Research Record: Journal of the Transportation Research Board*, *2372*(1), 83–96.

Kassem, E., Lowry, M., Fanijo, E., & Mohamed, M. (2021, February). Deterioration of green conflict paint for bicycle facilities (No. 2018-S-UI-2). *Pacific Northwest Transportation Consortium*.

Kogbara, R. B., Masad, E. A., Kassem, E., Scarpas, A., & Anupam, K. (2016). A state-of-the-art review of parameters influencing measurement and modeling of skid resistance of asphalt pavement. *Construction and Building Materials*, *114*, 602–617.

Komaragiri, S., Amirkhanian, A., & Bhasin, A. (2020). Friction and texture retention of concrete pavements. *Transportation Research Record: Journal of the Transportation Research Record*, *2674*(6), 457–465.

Kummer, H. W. (1966). *Unified theory of rubber and tire friction* (Engineering Research Bulletin B-94). The Pennsylvania State University.

Kutner, M. H., Nachtsheim, C. J., Neter, J., & Li, W. (2013). *Applied linear statistical models* (Fifth Edition). McGraw-Hill Irwin.

Li, S., Noureldin, S., & Zhu, K. (2005). Considerations in developing a network pavement inventory friction test program for a state highway agency. *Journal of Testing and Evaluation*, *33*(5), 287–294.

Li, S., Zhu, K., & Noureldin, S. (2007). Evaluation of friction performance of coarse aggregates and hot-mix asphalt pavements. *Journal of Testing and Evaluation*, *35*(6), 571–577.

Li, S., Harris, D., & Wells, T. (2016). Surface texture and friction characteristics of diamond-ground concrete and asphalt pavements. *Journal of Traffic and Transportation Engineering (English Edition)*, *3*(5), 475–482.

Li, S., Noureldin, S., & Zhu, K. (2010). *Safety enhancement of the INDOT network pavement friction testing program: Macrotexture and microtexture testing using laser sensors* (Joint Transportation Research Program Publication No. FHWA/IN/JTRP-2010/25). West Lafayette, IN: Purdue University. https://doi.org/10.5703/1288284314248

Li, S., Xiong, R., Yu, D., Zhao, G., Cong, P., & Jiang, Y. (2017). *Friction surface treatment selection: Aggregate properties, surface characteristics, alternative treatments, and safety effects* (Joint Transportation Research Program Publication No. FHWA/IN/JTRP-2017/09). West Lafayette, IN: Purdue University. https://doi.org/10.5703/1288284316509

Liu, J., Guan, B., Chen, H., Liu, K., Xiong, R., & Xie, C. (2020). Dynamic model of polished stone value attenuation in coarse aggregate. *Materials*, *13*(8), 1875.

Lorenz, B., Oh, Y. R., Nam, S. K., Jeon, S. H., & Persson, B. N. J. (2015). Rubber friction on road surfaces: Experiment and theory for low sliding speed. *The Journal of Chemical Physics*, *142*(19), 194701.

Lucas, B. D., & Kanade, T. (1981, April). An iterative image registration technique with an application to stereo vision. *Proceedings of Imaging Understanding Workshop* (pp. 121–130).

Ma, Y. (2020). Modeling of wheel–soil interaction and dynamics of wheeled unmanned ground vehicle in three-dimensional space. In *Dynamics and Advanced Motion Control of Off-Road UGVs* (pp. 119–141). https://doi.org/10.1016/B978-0-12-818799-9.00005-0

Mahmoud, E., & Masad, E. (2007). Experimental methods for the evaluation of aggregate resistance to polishing, abrasion, and breakage. *Journal of Materials in Civil Engineering*, *19*(11), 977–985.

Mastrad. (2001). *S885 Mastrad Skid Tester operating instructions*.

Merritt, D., Himes, S., & Porter, R. J. (2021, October). *High friction surface treatment site selection and installation guide* (Report No. FHWA-SA-21-093). Federal Highway Administration Office of Safety.

Miller, T. R. (1993). Benefit-cost analysis of lane marking. *Public Roads*, *56*(4), 153–163.

Mohamed, M., Abdel-Rahim, A., Kassem, E., Chang, K., & McDonald, A. (2020). Laboratory-based evaluation of pavement marking characteristics. *Journal of Transportation Engineering, Part B: Pavements*, *146*(2).

Mohamed, M., Skinner, A., Abdel-Rahim, A., Kassem, E., & Change, K. (2019). Deterioration characteristics of waterborne pavement markings subjected to different operating conditions. *Journal of Transportation Engineering, Part B: Pavements*, *145*(2), 04019003.

NACTO. (2013). *Urban street design guide* [Webpage]. National Association of City Transportation Officials (NACTO). https://nacto.org/publication/urban-street-design-guide/

NACTO. (2020). *Colored pavement material guidance* [National Association of City Transportation Officials]. https://nacto.org/publication/urban-bikeway-design-guide/bikeway-signing-marking/colored-pavement-material-guidance/

NCUTCD. (2019). *Approved changes to the manual on uniform traffic control devices*. National Committee on Uniform Traffic Control Devices. https://ncutcd.org/approved-changes/

NYC DOT. (2024, January 3). *Color surface treatment for pavements (CST)*. New York City Department of Transportation. https://www.nyc.gov/html/dot/downloads/pdf/pavement-marking-specs-mma-cst.pdf

Papagiannakis, A. T., & Masad, E. A. (2008). *Pavement design and materials*. John Wiley & Sons.

Park, G., Choi, S. B., Hyun, D., & Lee, J. (2018). Integrated observer approach using in-vehicle sensors and GPS for vehicle state estimation. *Mechatronics*, *50*, 134–147.

Pasetto, M., & Barbati, S. D. (2011). Definition and validation of a new methodological approach for friction evaluations of dropped-on products for road markings. *Proceeding in 3rd International Surface Friction Conference*.

Pauwelussen, J. P. (2015). *Essentials of vehicle dynamics*. Elsevier.

PIARC. (1987, September 13-19). *Technical committee report on surface characteristics*. PIARC XVIII World Road Congress, Brussels, Belgium.

Pike, A. M., Barrette, T. P., & Carlson, P. J. (2019). *Evaluation of the effects of pavement marking width on detectability by machine vision: 4-inch vs. 6-in markings*. American Traffic Safety Services Association.

Rajamani, R. (2012). *Vehicle dynamics and control* (2nd ed.). Springer.

Richard, C. (1975). *Skid testing of pavement markings* (Report No. TSD-277-75). Michigan Department of State Highways and Transportation. https://mdotjboss.state.mi.us/SpecProv/getDocumentById.htm?docGuid=ad658229-ae27-4b10-8b68-e95d9da7ba42

Rodin, H., III., Nassiri, S., & Yekkalar, M. (2018). *Evaluation of motorcyclists' and bikers' safety on wet pavement markings*. PacTrans.

Saghafi, A., Abdallah, I. N., & Nazarian, S. (2022). Practical specimen preparation and testing protocol for evaluation of the friction performance of asphalt pavement aggregates with three-wheel polishing device. *Journal of Materials in Civil Engineering*, *34*(1).

Saito, K., Horiguchi, T., Kasahara, A., Abe, H., & Henry, J. J. (1996). Development of portable tester for measuring skid resistance and its speed dependency on pavement surfaces. *Transportation Research Record*, *1536*(1), 45–51.

Scalici, S. P., Carry, W., Sr., Donnel, E., Rado, Z., & Hartmann, M. R. (2014). Red bus lane treatment evaluation. *Proceedings of the T&DI Congress 2014: Planes, Trains, and Automobiles*, (pp. 132–141). https://doi.org/10.1061/9780784413586.01

Schmidt, B. (2000). *Laser texture measurements of asphalt concrete*. Nordic Road and Transport Research, No. 1, Danish Road Directorate.

Shi, J., & Tomasi. (1994). Good features to track. *Proceedings of IEEE Conference on Computer Vision and Pattern Recognition* (pp. 593–600). https://doi.org/10.1109/CVPR.1994.323794

Siyahi, A., Kavussi, A., & Boroujerdian, A. M. (2015). Enhancing the skid resistance of two-component road marking paint using material and recycled materials. *International Journal of Transportation Engineering*, *3*(3), 195–206.

Su, Y.-M., Chen, J.-H., Cheng, J.-Y., Hsu, Y.-T., & Huang, M.-C. (2022). Rough-set based association rules toward

performance of high-friction road markings. *Journal of Transportation Engineering, Part B: Pavements*, *148*(2). American Society of Civil Engineers.

Tan, P.-N., Steinbach, M., & Kumar, V. (2006). *Introduction to data mining*. Pearson.

Teymen, A. (2019). Estimation of Los Angeles abrasion resistance of igneous rocks from mechanical aggregate properties. *Bulletin of Engineering Geology and the Environment*, *78*(2), 837–846.

Transpo Industries. (n.d.). *COLOR-SAFE® MMA colored pavement marking*. https://transpo.com/wp-content/uploads/Color-Safe-Technical-Data-Sheet.pdf

van Ginkel, J. (2014, July 8). *Estimating the tire-road friction coefficient based on tire force measurements* [Master of Science]. Delft University of Technology.

Wei, F., Wang, C., Tian, X., Li, S., & Shan, J. (2021). *Investigation of durability and performance of high friction surface treatment* (Joint Transportation Research Program Publication No. FHWA/IN/JTRP-2021/02). West Lafayette, IN: Purdue University. https://doi.org/10.5703/1288284317281

Xiong, R., Zong, Y., Lv, H., Sheng, Y., Guan, B., Niu, D., & Wang, H. (2021). Investigation on the anti-skid performance of asphalt mixture composed of calcined bauxite and limestone aggregate. *Construction and Building Materials*, *306*(2), 124932.

Xu, X., Luo, Y., Sreeram, A., Wu, Q., Chen, G., Cheng, S., Chen, Z., & Chen, X. (2022). Potential use of recycled concrete aggregate (RCA) for sustainable asphalt pavements of the future: A state-of-the-art review. *Journal of Cleaner Production*, *344*, 130893.

Yoon, J.-H., & Peng, H. (2014). Robust vehicle sideslip angle estimation through a disturbance rejection filter that integrates a magnetometer with GPS. *IEEE Transactions on Intelligent Transportation Systems*, *15*(1), 191–204.

Yu, D., Xiong, R., Li, S., Cong, P., Shah, A., & Jiang, Y. (2019). Laboratory evaluation of critical properties and attributes of calcined bauxite and steel slag aggregates for pavement friction surfacing. *Journal of Materials in Civil Engineering*, *31*(8), 04019155.

Zhan, Y., Li, J. Q., Liu, C., Wang, K. C. P., Pittenger, D. M., & Musharraf, Z. (2021). Effect of aggregate properties on asphalt pavement friction based on random forest analysis. *Construction and Building Materials*, *292*, 123467.

Zhao, G., Li, S., Jiang, Y., & Lee, J. (2018). *Quality assurance procedures for chip seal operations using macrotexture metrics* (Joint Transportation Research Program Publication No. FHWA/IN/JTRP2018/12). West Lafayette, IN: Purdue University. https://doi.org/10.5703/1288284316779

Zhao, H., Wei, F., Wang, C., Li, S., & Shan, J. (2021). Determination of friction performance of high friction surface treatment based on alternative macrotexture metric. *Materials*, *14*(22), 6895.

Zhang, Z. (2000). A flexible new technique for camera calibration. *IEEE Transactions on Pattern Analysis and Machine Intelligence*, *22*(11), 1330–1334.

Zong, Y., Li, S., Zhang, J., Zhai, J., Li, C., Ji, K., Feng, B., Zhao, H., Guan, B., & Xiong, R. (2021). Effect of aggregate type and polishing level on the long-term skid resistance of thin friction course. *Construction and Building Materials*, *282*, 122730.

APPENDICES

Appendix A. Pavement Markings Laboratory Test Results and Photos

Appendix B. Locked Wheel Skid Trailer In-situ Test Results

Appendix C. Friction Simulation Results

APPENDIX A. PAVEMENT MARKINGS LABORATORY TEST RESULTS AND PHOTOS

Table A.1 MPD measurements by LST before polishing

Group No.	MPD (mm)				
	Specimen 1	**Specimen 2**	**Specimen 3**	**Specimen 4**	**Avg.**
Group 1	0.33	0.37	0.29	0.25	0.31
Group 2	0.35	0.46	–	–	0.40
Group 3	0.38	0.36	–	–	0.37
Group 4	0.43	0.49	–	–	0.46
Group 5	0.77	0.54	–	–	0.65
Group 6	1.23	1.21	–	–	1.22
Group 7	1.26	1.26	–	–	1.26
Group 8	0.92	0.66	–	–	0.79
Group 9	1.31	1.21	–	–	1.26
Group 10	1.13	1.04	1.18	0.96	1.08
Group 11	0.46	0.39	–	–	0.42
Group 12	0.87	0.63	–	–	0.75
Group 13	0.93	0.65	–	–	0.79
Group 14	1.52	1.59	–	–	1.55
Group 15	0.37	0.36	–	–	0.37
Group 16	0.38	0.31	–	–	0.34
Group 17	0.30	0.21	–	–	0.25
Group 18	0.28	0.22	–	–	0.25

Table A.2 Dry BPN measurements before polishing

Group No.	BPN					
	Specimen 1	**Specimen 2**	**Specimen 3**	**Specimen 4**	**S.D**	**Avg.**
Group 1	71.4	71.2	80.0	78.0	4.78	75.33
Group 2	86.0	87.0	–	–	0.71	86.50
Group 3	87.0	84.0	–	–	2.12	85.50
Group 4	84.0	84.0	–	–	0.00	84.00
Group 5	85.0	90.0	–	–	3.54	87.50
Group 6	85.0	95.0	–	–	7.07	90.00
Group 7	90.0	85.0	–	–	3.54	87.50
Group 8	86.0	90.0	–	–	2.83	88.00
Group 9	81.0	80.0	–	–	0.71	80.50
Group 10	80.0	80.0	80.0	80.0	0.00	80.00
Group 11	78.0	68.0	–	–	7.07	73.00
Group 12	83.0	80.0	–	–	1.84	81.30
Group 13	75.0	85.0	–	–	7.07	80.00
Group 14	75.0	77.0	–	–	1.41	76.00
Group 15	87.0	85.0	–	–	1.41	86.00
Group 16	80.0	80.0	–	–	0.00	80.00
Group 17	80.0	80.0	–	–	0.00	80.00
Group 18	80.0	80.0	–	–	0.00	80.00

Table A.3 Wet BPN measurements before polishing

Group No.	BPN					
	Specimen 1	**Specimen 2**	**Specimen 3**	**Specimen 4**	**S.D.**	**Avg.**
Group 1	60.0	50.0	51.8	55.0	3.80	54.20
Group 2	56.0	55.0	–	–	0.71	55.50
Group 3	50.0	50.0	–	–	0.00	50.00
Group 4	50.0	55.0	–	–	3.54	52.50
Group 5	55.0	50.0	–	–	3.54	52.50
Group 6	60.0	65.0	–	–	3.54	62.50
Group 7	65.0	59.0	–	–	4.24	62.00
Group 8	45.0	35.0	–	–	7.07	40.00
Group 9	50.0	50.0	–	–	0.00	50.00
Group 10	40.0	41.0	40.0	42.0	0.96	40.75
Group 11	37.0	34.0	–	–	1.98	35.50
Group 12	32.0	36.0	–	–	3.11	33.80
Group 13	33.0	35.0	–	–	1.41	34.00
Group 14	50.0	60.0	–	–	7.07	55.00
Group 15	40.0	45.0	–	–	3.54	42.50
Group 16	50.0	45.0	–	–	3.54	47.50
Group 17	31.0	30.0	–	–	0.71	30.50
Group 18	35.0	30.0	–	–	3.54	32.50

Table A.4 MPD measurements by CTM before and after polishing

Group No.	Polishing Cycles	MPD (mm)				
		Specimen 1	Specimen 2	Specimen 3	Specimen 4	Avg.
Group 1	0	0.36	0.36	0.37	0.32	0.35
	500	0.29	0.21	0.21	0.19	0.22
	1,500	0.29	0.20	0.24	0.17	0.22
Group 2	0	0.43	0.61	–	–	0.52
	500	0.17	0.20	–	–	0.18
	1,500	0.11	0.14	–	–	0.12
Group 3	0	0.42	0.40	–	–	0.41
	500	0.07	0.19	–	–	0.13
	1,500	0.08	0.09	–	–	0.08
Group 4	0	0.55	0.45	–	–	0.50
	500	0.33	0.31	–	–	0.32
	1,500	0.29	0.28	–	–	0.28
	5,000	0.22	0.24	–	–	0.23
Group 5	0	0.84	0.78	–	–	0.81
	500	0.39	0.22	–	–	0.31
	1,500	0.31	0.21	–	–	0.29
	5,000	0.28	0.13	–	–	0.20
Group 6	0	1.20	1.25	–	–	1.23
	500	0.11	0.09	–	–	0.10
Group 7	0	1.17	1.32	–	–	1.24
	500	0.27	0.21	–	–	0.24
	1,500	0.18	0.08	–	–	0.13
Group 8	0	0.95	0.54	–	–	0.74
	500	0.15	0.15	–	–	0.15
Group 9	0	1.40	1.49	–	–	1.44
	500	0.09	0.08	–	–	0.08

Table A.4 MPD measurements by CTM before and after polishing (contd.)

Group No.	Polishing Cycles	MPD (mm)				
		Specimen 1	Specimen 2	Specimen 3	Specimen 4	Avg.
Group 10	0	1.07	1.00	1.12	1.07	1.06
	500	1.07	1.02	1.06	1.02	1.04
	1,500	1.01	–	1.04	–	1.02
	2,000	–	1.02	–	1.02	1.02
	4,500	1.00	–	1.03	–	1.01
	5,000	–	1.00	–	1.01	1.01
	10,000	1.02	0.98	1.00	0.52	0.88
	12,500	–	1.00	–	0.22	0.61
	15,000	–	1.01	–	0.19	0.60
	17,500	–	0.99	–	–	0.99
	20,000	1.06	1.03	0.27	–	0.78
	50,000	0.39		–	–	0.39
Group 11	0	0.59	0.42	–	–	0.50
	500	0.51	0.43	–	–	0.47
	2,000	0.48	0.47	–	–	0.47
	5,000	0.50	0.43	–	–	0.46
	10,000	0.48	0.41	–	–	0.45
	15,000	0.51	0.43	–	–	0.47
	25,000	0.48	0.42	–	–	0.45
	40,000	0.46	0.42	–	–	0.44
	60,000	0.48	0.45	–	–	0.46
Group 12	0	0.72	0.64	–	–	0.68
	500	0.59	0.63	–	–	0.61
	1,500	0.57	0.60	–	–	0.58
	5,000	0.55	0.62	–	–	0.58
	10,000	0.59	0.56	–	–	0.57
	20,000	0.57	0.60	–	–	0.58
Group 13	0	0.93	0.66	–	–	0.79
	500	0.68	0.58	–	–	0.63
	1,500	0.69	0.57	–	–	0.63
	5,000	0.68	0.56	–	–	0.62
	10,000	0.65	0.58	–	–	0.61
	20,000	0.71	0.56	–	–	0.64
	30,000	0.69	0.54	–	–	0.61
	50,000	0.67	0.57	–	–	0.62
Group 14	0	1.44	1.75	–	–	1.59
	500	0.68	0.96	–	–	0.82
	1,500	0.67	0.84	–	–	0.75
	5,000	0.65	0.82	–	–	0.73
	10,000	0.70	0.78	–	–	0.74

Table A.4 MPD measurements by CTM before and after polishing (contd.)

Group No.	Polishing Cycles	Specimen 1	Specimen 2	Specimen 3	Specimen 4	Average MPD
Group 15	0	0.61	0.39	–	–	0.50
	500	0.52	0.42	–	–	0.47
	1,500	0.50	0.41	–	–	0.45
	5,000	0.51	0.39	–	–	0.45
	10,000	0.50	0.45	–	–	0.47
	20,000	0.52	0.40	–	–	0.46
	40,000	0.51	0.41	–	–	0.46
	70,000	0.51	0.40	–	–	0.45
	100,000	0.49	0.41	–	–	0.45
Group 16	0	0.73	0.40	–	–	0.56
	500	0.71	0.37	–	–	0.54
	1,500	0.69	0.37	–	–	0.53
	5,000	0.65	0.39	–	–	0.52
	10,000	0.65	0.37	–	–	0.51
	20,000	0.63	0.39	–	–	0.51
	40,000	0.65	0.35	–	–	0.50
	60,000	0.64	0.37	–	–	0.50
	80,000	0.65	0.38	–	–	0.52
	100,000	0.66	0.35	–	–	0.50
Group 17	0	0.30	0.29	–	–	0.29
	500	0.32	0.29	–	–	0.30
	1,500	0.33	–	–	–	0.33
	2,000	–	0.29	–	–	0.29
	5,000	0.33	–	–	–	0.33
	7,000	–	0.30	–	–	0.30
	10,000	0.35	0.29	–	–	0.32
	30,000	0.31	0.29	–	–	0.30
	50,000	0.37	0.30	–	–	0.34
	75,000	0.39	0.28	–	–	0.33
	100,000	0.35	0.31	–	–	0.33
Group 18	0	0.36	0.32	–	–	0.34
	500	0.33	0.33	–	–	0.33
	1,500	0.34	–	–	–	0.34
	2,000	–	0.30	–	–	0.30
	5,000	0.38	–	–	–	0.38
	7,000	–	0.30	–	–	0.30
	10,000	0.36	0.29	–	–	0.33
	30,000	0.38	0.35	–	–	0.36
	50,000	0.44	0.33	–	–	0.38
	75,000	0.47	0.28	–	–	0.37
	100,000	0.46	0.28	–	–	0.37

Table A.5 DF20 measurements before and after polishing

Group No.	Polishing Cycles	DF20				
		Specimen 1	Specimen 2	Specimen 3	Specimen 4	Avg.
Group 1	0	0.32	0.39	0.34	0.36	0.35
	500	0.28	0.31	0.17	0.20	0.24
	1,500	0.25	0.26	0.23	0.25	0.25
Group 2	0	0.30	0.32	–	–	0.31
	500	0.28	0.27	–	–	0.28
	1,500	0.26	0.26	–	–	0.26
Group 3	0	0.28	0.30	–	–	0.29
	500	0.34	0.25	–	–	0.29
	1,500	0.37	0.39	–	–	0.38
Group 4	0	0.31	0.33	–	–	0.32
	500	0.24	0.23	–	–	0.23
	1,500	0.22	0.23	–	–	0.22
	5,000	0.21	0.22	–	–	0.22
Group 5	0	0.33	0.31	–	–	0.32
	500	0.16	0.12	–	–	0.14
	1,500	0.07	0.07	–	–	0.07
	5,000	0.11	0.14	–	–	0.13
Group 6	0		0.65	–	–	0.65
	500	0.30	0.40	–	–	0.35
Group 7	0	0.49	0.45	–	–	0.47
	500	0.17	0.19	–	–	0.18
	1,500	0.16	0.20	–	–	0.18
Group 8	0	0.15	0.13	–	–	0.14
	500	0.20	0.20	–	–	0.20
Group 9	0	0.46	0.44	–	–	0.45
	500	0.23	0.25	–	–	0.24
Group 10	0	0.42	0.45	0.47	0.47	0.45
	500	0.42	0.45	0.49	0.47	0.46
	1,500	0.41	–	0.49	–	0.45
	2,000	–	0.44	–	0.48	0.46
	4,500	0.41	–	0.49	–	0.45
	5,000		0.44		0.50	0.47
	10,000	0.41	0.45	0.51	0.41	0.44
	12,500		0.48		0.32	0.40
	15,000		0.48		0.30	0.39
	17,500		0.50			0.50
	20,000	0.42	0.47	0.31		0.40
	50,000	0.36				0.36

Table A.5 DF20 measurements before and after polishing (contd.)

Group No.	Polishing Cycles	DF20				
		Specimen 1	Specimen 2	Specimen 3	Specimen 4	Avg.
Group 11	0	0.38	0.35	–	–	0.36
	500	0.34	0.31	–	–	0.33
	2,000	0.33	0.30	–	–	0.31
	5,000	0.33	0.29	–	–	0.31
	10,000	0.26	0.22	–	–	0.24
	15,000	0.22	0.24	–	–	0.23
	25,000	0.28	0.22	–	–	0.25
	40,000	0.25	0.19	–	–	0.22
	60,000	0.29	0.24	–	–	0.26
Group 12	0	0.18	0.23	–	–	0.21
	500	0.18	0.25	–	–	0.21
	1,500	0.10	0.21	–	–	0.15
	5,000	0.11	0.19	–	–	0.16
	10,000	0.14	0.19	–	–	0.16
	20,000	0.07	0.07	–	–	0.07
Group 13	0	0.29	0.24	–	–	0.26
	500	0.28	0.22	–	–	0.25
	1,500	0.30	0.21	–	–	0.25
	5,000	0.32	0.23	–	–	0.27
	10,000	0.33	0.23	–	–	0.28
	20,000	0.32	0.22	–	–	0.27
	30,000	0.31	0.23	–	–	0.27
	50,000	0.34	0.23	–	–	0.28
Group 14	0	0.51	0.53	–	–	0.52
	500	0.38	0.49	–	–	0.43
	1,500	0.36	0.51	–	–	0.44
	5,000	0.31	0.46	–	–	0.39
	10,000	0.34	0.45	–	–	0.39
Group 15	0	0.27	0.30	–	–	0.28
	500	0.28	0.31	–	–	0.29
	1,500	0.28	0.29	–	–	0.29
	5,000	0.37	0.30	–	–	0.34
	10,000	0.30	0.28	–	–	0.29
	20,000	0.29	0.27	–	–	0.28
	40,000	0.30	0.26	–	–	0.28
	70,000	0.28	0.27	–	–	0.27
	100,000	0.27	0.26	–	–	0.26

Table A.5 DF20 measurements before and after polishing (contd.)

Group No.	Polishing Cycles	DF20				
		Specimen 1	Specimen 2	Specimen 3	Specimen 4	Avg.
Group 16	0	0.29	0.25	–	–	0.27
	500	0.30	0.21	–	–	0.25
	1,500	0.33	0.24	–	–	0.29
	5,000	0.36	0.23	–	–	0.30
	10,000	0.36	0.24	–	–	0.30
	20,000	0.38	0.24	–	–	0.31
	40,000	0.38	0.23	–	–	0.31
	60,000	0.38	0.23	–	–	0.31
	80,000	0.40	0.22	–	–	0.29
	100,000	0.39	0.22	–	–	0.29
Group 17	0	0.17	0.13	–	–	0.15
	500	0.16	0.15	–	–	0.16
	1,500	0.18	–	–	–	0.18
	2,000	–	0.15	–	–	0.15
	5,000	0.19	–	–	–	0.19
	7,000	–	0.16	–	–	0.16
	10,000	0.19	0.15	–	–	0.17
	30,000	0.18	0.13	–	–	0.16
	50,000	0.17	0.12	–	–	0.14
	75,000	0.17	0.09	–	–	0.14
	100,000	0.17	0.13	–	–	0.15
Group 18	0	0.13	0.13	–	–	0.13
	500	0.14	0.14	–	–	0.14
	1,500	0.16	–	–	–	0.16
	2,000	–	0.16	–	–	0.16
	5,000	0.15	–	–	–	0.15
	7,000	–	0.15	–	–	0.15
	10,000	0.17	0.14	–	–	0.15
	30,000	0.15	0.13	–	–	0.14
	50,000	0.15	0.14	–	–	0.14
	75,000	0.16	0.13	–	–	0.15
	100,000	0.12	0.14	–	–	0.13

Table A.6 DF40 measurements before and after polishing

Group No.	Polishing Cycles	DF40				
		Specimen 1	Specimen 2	Specimen 3	Specimen 4	Avg.
Group 1	0	0.33	0.35	0.36	0.36	0.35
	500	0.27	0.29	0.25	0.23	0.25
	1,500	0.26	0.27	0.25	0.25	0.25
Group 2	0	0.30	0.32	–	–	0.31
	500	0.25	0.25	–	–	0.25
	1,500	0.22	0.23	–	–	0.22
Group 3	0	0.28	0.29	–	–	0.29
	500	0.26	0.24	–	–	0.25
	1,500	0.31	0.35	–	–	0.33
Group 4	0	0.32	0.34	–	–	0.33
	500	0.25	0.24	–	–	0.24
	1,500	0.22	0.23	–	–	0.22
	5,000	0.21	0.22	–	–	0.21
Group 5	0	0.32	0.31	–	–	0.32
	500	0.18	0.13	–	–	0.15
	1,500	0.09	0.09	–	–	0.09
	5,000	0.11	0.14	–	–	0.13
Group 6	0		0.67	–	–	0.67
	500	0.25	0.37	–	–	0.31
Group 7	0	0.52	0.48	–	–	0.50
	500	0.17	0.17	–	–	0.17
	1,500	0.15	0.13	–	–	0.14
Group 8	0	0.17	0.13	–	–	0.15
	500	0.13	0.16	–	–	0.14
Group 9	0	0.44	0.42	–	–	0.43
	500	0.14	0.16	–	–	0.15
Group 10	0	0.42	0.42	0.45	0.44	0.43
	500	0.41	0.41	0.48	0.43	0.43
	1,500	0.41	–	0.48	–	0.44
	2,000	–	0.42	–	0.45	0.43
	4,500	0.41	–	0.47	–	0.44
	5,000		0.42	–	0.48	0.45
	10,000	0.41	0.43	0.47	0.32	0.40
	12,500	–	0.45	–	0.24	0.34
	15,000	–	0.45	–	0.22	0.33
	17,500	–	0.46	–	–	0.46
	20,000	0.43	0.44	0.22	–	0.37
	50,000	0.26	–	–	–	0.26

Table A.6 DF40 Measurements before and after Polishing (contd.)

Group No.	Polishing Cycles	DF40				
		Specimen 1	Specimen 2	Specimen 3	Specimen 4	Avg.
Group 11	0	0.39	0.36	–	–	0.37
	500	0.35	0.32	–	–	0.33
	2,000	0.33	0.30	–	–	0.32
	5,000	0.33	0.30	–	–	0.32
	10,000	0.30	0.28	–	–	0.29
	15,000	0.29	0.28	–	–	0.28
	25,000	0.29	0.26	–	–	0.27
	40,000	0.30	0.26	–	–	0.28
	60,000	0.29	0.22	–	–	0.25
Group 12	0	0.23	0.27	–	–	0.20
	500	0.22	0.26	–	–	0.25
	1,500	0.20	0.24	–	–	0.17
	5,000	0.21	0.23	–	–	0.22
	10,000	0.22	0.22	–	–	0.24
	20,000	0.18	0.16	–	–	0.17
Group 13	0	0.31	0.24	–	–	0.28
	500	0.29	0.23	–	–	0.26
	1,500	0.29	0.21	–	–	0.25
	5,000	0.30	0.23	–	–	0.27
	10,000	0.32	0.23	–	–	0.27
	20,000	0.30	0.22	–	–	0.26
	30,000	0.29	0.23	–	–	0.26
	50,000	0.32	0.24	–	–	0.28
Group 14	0	0.48	0.50	–	–	0.49
	500	0.33	0.42	–	–	0.37
	1,500	0.29	0.43	–	–	0.36
	5,000	0.27	0.39	–	–	0.33
	10,000	0.28	0.37	–	–	0.32
Group 15	0	0.28	0.30	–	–	0.29
	500	0.29	0.29	–	–	0.29
	1,500	0.28	0.28	–	–	0.28
	5,000	0.31	0.29	–	–	0.30
	10,000	0.23	0.25	–	–	0.24
	20,000	0.24	0.26	–	–	0.25
	40,000	0.24	0.23	–	–	0.24
	70,000	0.24	0.25	–	–	0.24
	100,000	0.22	0.24	–	–	0.23

Table A.6 DF40 Measurements before and after Polishing (contd.)

Group No.	Polishing Cycles	DF40				
		Specimen 1	Specimen 2	Specimen 3	Specimen 4	Avg.
Group 16	0	0.30	0.26	–	–	0.28
	500	0.29	0.22	–	–	0.26
	1,500	0.32	0.24	–	–	0.28
	5,000	0.35	0.24	–	–	0.29
	10,000	0.34	0.23	–	–	0.29
	20,000	0.36	0.23	–	–	0.29
	40,000	0.36	0.23	–	–	0.29
	60,000	0.36	0.23	–	–	0.29
	80,000	0.38	0.23	–	–	0.29
	100,000	0.37	0.22	–	–	0.28
Group 17	0	0.15	0.14	–	–	0.15
	500	0.16	0.16	–	–	0.16
	1,500	0.18	–	–	–	0.18
	2,000	–	0.16	–	–	0.16
	5,000	0.17	–	–	–	0.17
	7,000	–	0.16	–	–	0.16
	10,000	0.17	0.16	–	–	0.17
	30,000	0.17	0.14	–	–	0.16
	50,000	0.17	0.12	–	–	0.15
	75,000	0.17	0.10	–	–	0.14
	100,000	0.18	0.09	–	–	0.14
Group 18	0	0.13	0.14	–	–	0.13
	500	0.12	0.16	–	–	0.14
	1,500	0.17	–	–	–	0.17
	2,000	–	0.18	–	–	0.18
	5,000	0.17	–	–	–	0.17
	7,000	–	0.17	–	–	0.17
	10,000	0.19	0.15	–	–	0.17
	30,000	0.16	0.14	–	–	0.15
	50,000	0.16	0.14	–	–	0.15
	75,000	0.15	0.11	–	–	0.14
	100,000	0.14	0.12	–	–	0.13

Table A.7 F60 values before and after polishing

Group No.	Polishing Cycles	F60
Group 1	0	0.19
	500	0.14
	1,500	0.14
Group 2	0	0.20
	500	0.13
	1,500	0.11
Group 3	0	0.18
	500	0.12
	1,500	0.12
Group 4	0	0.20
	500	0.15
	1,500	0.14
	5,000	0.13
Group 5	0	0.23
	500	0.12
	1,500	0.11
	5000	0.11
Group 6	0	0.44
	500	0.12
Group 7	0	0.35
	500	0.12
	1,500	0.10
Group 8	0	0.15
	500	0.11
Group 9	0	0.32
	500	0.10
Group 10	0	0.30
	500	0.30
	1,500	0.30
	2,000	0.30
	4,500	0.30
	5,000	0.31
	10,000	0.27
	12,500	0.22
	15,000	0.22
	17,500	0.31
	20,000	0.25
	50,000	0.17

Table A.7 F60 values before and after polishing (contd.)

Group No.	Polishing Cycles	F60
Group 11	0	0.22
	500	0.20
	2,000	0.20
	5,000	0.19
	10,000	0.18
	15,000	0.18
	25,000	0.18
	40,000	0.18
	60,000	0.17
Group 12	0	0.19
	500	0.18
	1,500	0.17
	5,000	0.17
	10,000	0.17
	20,000	0.15
Group 13	0	0.21
	500	0.19
	1,500	0.19
	5,000	0.19
	10,000	0.19
	20,000	0.19
	30,000	0.19
	50,000	0.21
Group 14	0	0.36
	500	0.25
	1,500	0.24
	5,000	0.23
	10,000	0.23
Group 15	0	0.19
	500	0.19
	1,500	0.18
	5,000	0.19
	10,000	0.17
	20,000	0.17
	40,000	0.17
	70,000	0.17
	100,000	0.16

Table A.7 F60 values before and after polishing (contd.)

Group No.	Polishing Cycles	F60
Group 16	0	0.19
	500	0.18
	1,500	0.19
	5,000	0.19
	10,000	0.19
	20,000	0.19
	40,000	0.19
	60,000	0.19
	80,000	0.19
	100,000	0.19
Group 17	0	0.12
	500	0.12
	1,500	0.13
	2,000	0.12
	5,000	0.13
	7,000	0.12
	10,000	0.13
	30,000	0.12
	50,000	0.12
	75,000	0.12
	100,000	0.12
Group 18	0	0.12
	500	0.12
	1,500	0.13
	2,000	0.13
	5,000	0.14
	7,000	0.13
	10,000	0.13
	30,000	0.13
	50,000	0.13
	75,000	0.12
	100,000	0.12

Table A.8 Closeups of marking specimens before and after polishing

Group No.	Before	At the End of Polishing
1 (Waterborne)		
2 (Waterborne)		
3 (Waterborne)		
4 (Waterborne)		

Table A.8 Closeups of marking specimens before and after polishing (contd.)

Group No.	Before	At the End of Polishing
5 (Waterborne)		
6 (Waterborne)		
7 (Waterborne)		
8 (Waterborne)		

Table A.8 Closeups of marking specimens before and after polishing (contd.)

Group No.	Before	At the End of Polishing
9 (Waterborne)		
10 (Preformed Tape)		
11 (Epoxy)		
12 (Epoxy)	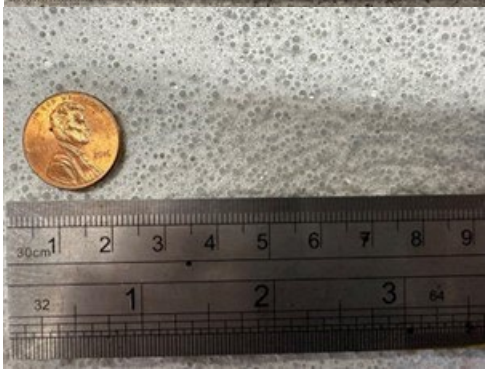	

Table A.8 Closeups of marking specimens before and after polishing (contd.)

Group No.	Before	At the End of Polishing
13 (Polyurea)	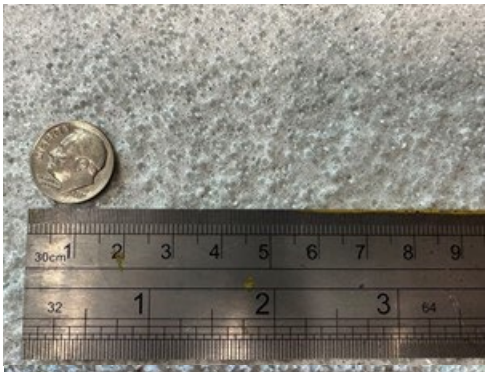	
14 (Polyurea)		
15 (Polyurea)		
16 (MMA)		

Table A.8 Closeups of marking specimens before and after polishing (contd.)

Group No.	Before	At the End of Polishing
17 (Thermoplastic)		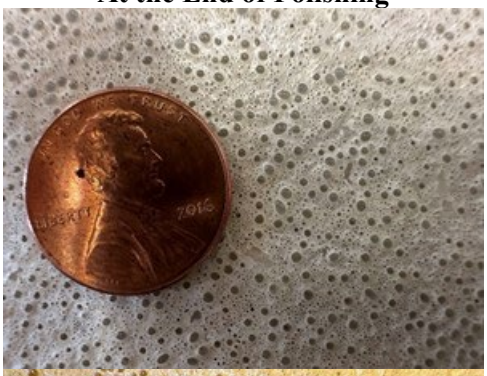
18 (Thermoplastic)		

APPENDIX B. LOCKED WHEEL SKID TRAILER IN-SITU TEST RESULTS

Table B.1 Data measurements from airport friction tests

Vertical Force F_Z (lbs)	Longitudinal Friction Force F_x (lbs)	Curvature Radius (ft)	Tire Speed (mph)	Test Tire Slip Angle (°)	Vehicle Articulation Angle (°)
892	729	165.13	13.66230	-5.751517852	5.2928181
895	752	165.13	13.74729	-5.726146019	4.599217996
808	561	165.13	23.02924	-3.666031082	2.703258334
787	569	165.13	23.62321	-5.745144632	2.959999527
631	351	165.13	34.44051	-3.85982	1.754519653
696	395	165.13	36.1126	-2.90578	5.137543164
974	788	146	12.59475	8.404424813	-4.867974419
1,005	788	136.48	12.02413	7.241279617	-6.950920275
969	790	146	12.72534	5.442504961	-4.33522109
1,008	773	136.48	12.17057	7.628625305	-5.991552728
1,089	713	146	20.93595	5.781367789	-4.238160526
1,154	840	136.48	19.51254	6.330145978	-6.365301812
1,075	672	146	20.71231	6.679737144	-4.224539388
1,156	782	136.48	18.40004	6.063244609	-5.693386612
1,257	560	146	30.55440	6.227848857	-2.440121793
1,257	559	146	31.67547	6.829862364	-2.872285621
1,271	771	136.48	27.66835	3.924644506	-0.350547025
1,328	821	136.48	28.16540	5.773564137	-0.831041917
941	704	infinity	39.83058	0.015058672	–
932	788	infinity	25.65141	-0.121037025	–
931	816	infinity	20.51910	0.093597293	–
925	812	infinity	14.54373	-0.607053664	–
938	682	infinity	39.94888	0.170594042	–
916	771	infinity	25.89180	-0.180506747	–
921	822	infinity	20.47434	0.212469698	–
931	807	infinity	14.72801	0.008509310	–
935	691	infinity	40.18021	-0.069424100	–
933	776	infinity	25.59718	0.116934659	–
928	826	infinity	20.66238	0.389093921	–
926	814	infinity	15.23819	-0.196714668	–
832	668	165.13	23.06859	-5.785903121	3.892268776
811	638	165.13	21.86412	-5.169643943	3.384584009
845	678	165.13	24.16971	-6.018679188	0.550418401

Table B.1 Data measurements from airport friction tests (contd.)

Vertical Force F_Z (lbs)	Longitudinal Friction Force F_x (lbs)	Curvature Radius (ft)	Tire Speed (mph)	Test Tire Slip Angle (°)	Vehicle Articulation Angle (°)
826	686	165.13	21.54012	-5.695343150	2.600247724
838	661	165.13	23.63146	-5.543233566	0.282279422
803	657	165.13	23.64312	-5.307909347	2.840125115
863	713	165.13	19.89829	-7.353181167	2.988668725
846	652	165.13	20.40975	-6.858642264	3.130534248
866	717	165.13	20.22881	-6.317005515	3.273073784
848	664	165.13	20.51237	-6.327960379	4.430516782
859	695	165.13	20.26141	-6.495695877	2.793164560
840	665	165.13	20.62991	-5.854898154	2.835494664
882	800	165.13	15.35101	-7.560528367	2.232561978
882	693	165.13	15.24876	-7.243853288	3.483546143
888	776	165.13	15.59926	-7.217522041	2.239600760
877	700	165.13	16.32777	-6.477944556	3.544947623
871	751	165.13	16.94923	-7.187550632	1.716512831
864	680	165.13	16.97430	-6.434215155	3.494911301
1,132	905	165.13	22.56135	4.929394313	-6.145475214
1,145	932	165.13	22.30079	4.554600981	-6.368956485
1,130	866	165.13	23.19811	4.432694349	-5.861274600
1,076	882	165.13	18.66951	4.997697087	-6.535332991
1,083	876	165.13	19.51077	4.991446685	-6.176366622
1,031	915	165.13	18.86636	5.438873886	-5.908810866
983	882	165.13	14.19641	7.128058162	-5.930055383
993	886	165.13	14.61059	7.164015896	-6.042474646
989	852	165.13	13.70036	7.190030794	-5.928043811

Table B.2 Data measurements from SR-26 friction tests

Vertical Force F_Z (lbs)	Friction Force F_f (lbs)	Curvature Radius (ft)	Tire Speed (mph)	Test Tire Slip Angle (°)	Vehicle Articulation Angle (°)
971	585	infinity	29.32223	0.00556	-0.03564
970	577	infinity	29.65789	0.01731	-0.06461
960	636	infinity	15.00631	0.05974	-0.11380
969	583	infinity	15.62535	0.11502	-0.08665
964	611	infinity	14.74244	0.08726	-0.10043
953	623	infinity	40.13993	0.07784	-0.04373
965	533	infinity	39.69890	0.04444	-0.07421
1,001	452	2,348	29.94574	2.99520	-0.53674
989	513	2,348	30.08078	3.44900	-0.69473
980	594	2,348	30.17151	-3.23930	1.01492
1,004	564	2,348	29.83766	-3.33020	0.97565
958	557	2,348	14.93938	1.86060	-0.66798
955	513	2,348	14.96021	2.00360	-0.68043
978	598	infinity	15.22523	0.06777	0.15600
1,012	647	2,348	14.74003	-1.76170	0.98463
1,004	665	2,348	14.85150	-2.19650	0.84431
947	727	infinity	14.98606	-0.00559	0.07802
968	569	infinity	40.85553	0.04102	-0.00176
960	647	infinity	30.08515	0.03727	-0.06896
978	535	infinity	28.27379	0.00357	-0.06871
980	481	2,348	28.75471	3.31270	-0.63336
984	488	2,348	28.81379	3.40120	-0.52222
1,007	558	2,348	28.74320	-3.12950	1.07141
1,016	548	2,348	29.18659	-2.99130	0.96256
958	549	2,348	15.04770	1.56742	-1.14089
957	550	2,348	15.25551	1.99080	-1.26840
974	608	infinity	14.79671	0.00752	0.13194
1,016	634	2,348	14.77189	-1.67165	0.47997
1,015	612	2,348	14.18153	-1.60001	0.39071
965	701	infinity	14.95686	-0.00306	-0.05554
957	632	infinity	29.18635	-0.04594	0.01034
965	611	infinity	29.64864	-0.01077	-0.00322
965	563	infinity	29.41965	0.02627	-0.01153

Table B.2 Data Measurements from SR-26 Friction Tests (contd.)

Vertical Force F_Z (lbs)	Friction Force F_f (lbs)	Curvature Radius (ft)	Tire Speed (mph)	Test Tire Slip Angle (°)	Vehicle Articulation Angle (°)
980	578	infinity	39.59928	0.01665	-0.00012
984	521	infinity	39.10395	0.01733	0.00494
976	533	2,348	29.35742	2.82660	-0.71302
978	517	2,348	29.39508	3.36960	-0.82328
1,007	582	2,348	28.72242	-3.17950	0.55886
1,007	573	2,348	29.91297	-3.28300	0.65475
956	572	2,348	15.03217	2.00310	-0.54262
958	521	2,348	15.03110	1.73640	-0.85200
980	606	infinity	15.32027	0.10946	0.11629
1,016	660	2,348	15.28421	-1.94558	0.79707
1,010	695	2,348	15.30922	-2.18195	0.21759
951	725	2,348	15.37218	-0.35940	0.18130
951	662	infinity	30.42320	0.00325	0.01659
977	591	infinity	28.81360	-0.00233	0.01648
967	577	infinity	28.29820	-0.00184	0.01486

APPENDIX C. FRICTION SIMULATION RESULTS

Table C.1 Friction numbers by speed, radius and camber angle

Speed (mph)	Curve Radius (ft)	Camber Angle (degree)	Slip Angle (degree)	Vertical Force (lbs)	Longitudinal FN	Ideal Longitudinal Force (lbs)	FEA Longitudinal Force (lbs)	Ideal Lateral Force (lbs)	Ideal Friction Force (lbs)	True FN (%)	FEA Lateral Force (lbs)	FEA Friction Force (lbs)	FEA True FN
24.14	158.94	0.00	-0.87	1,023.86	74.18	759.47	760.92	-11.55	759.55	74.19	-11.57	761.01	74.33
24.47	158.91	0.00	-1.93	1,119.32	73.79	825.99	828.85	-27.88	826.46	73.84	-27.97	829.32	74.09
16.75	150.38	0.00	0.68	856.21	76.98	659.08	660.55	7.79	659.13	76.98	7.81	660.60	77.15
22.91	152.51	0.00	-4.00	1,158.34	73.33	849.40	851.15	-59.29	851.47	73.51	-59.41	853.21	73.66
24.98	161.68	0.00	-1.01	985.19	72.94	718.55	721.00	-12.63	718.66	72.95	-12.67	721.11	73.20
17.83	148.75	0.00	3.65	1,028.49	77.68	798.94	801.26	50.90	800.56	77.84	51.05	802.88	78.06
22.47	148.95	0.00	6.98	814.90	76.10	620.18	620.92	75.32	624.73	76.66	75.41	625.47	76.75
24.10	136.20	0.00	-6.44	870.58	73.05	636.00	637.03	-71.29	639.98	73.51	-71.41	641.01	73.63
22.37	163.76	0.00	-4.86	832.83	77.73	647.37	648.64	-54.90	649.69	78.01	-55.00	650.96	78.16
24.37	142.11	0.00	-2.98	884.41	72.95	645.18	647.26	-33.54	646.06	73.05	-33.65	648.13	73.28
19.02	135.27	0.00	6.67	1,023.82	68.32	699.47	701.38	81.21	704.17	68.78	81.44	706.07	68.96
15.39	149.44	0.00	-0.30	1,113.13	74.03	824.01	826.67	-4.25	824.03	74.03	-4.26	826.69	74.27
24.39	150.28	0.00	-5.75	810.22	75.32	610.25	611.55	-61.14	613.31	75.70	-61.27	614.60	75.86
16.27	150.51	0.00	-5.99	805.86	74.40	599.57	600.50	-62.54	602.83	74.80	-62.64	603.75	74.92
16.89	156.00	0.00	-5.26	1,011.25	79.03	799.20	801.22	-73.25	802.54	79.36	-73.43	804.56	79.56
21.00	162.38	0.00	-0.85	1,160.21	73.80	856.27	859.36	-12.69	856.37	73.81	-12.73	859.45	74.08
20.77	137.52	0.00	2.23	970.31	70.98	688.77	689.89	26.81	689.29	71.04	26.85	690.41	71.15
24.36	159.45	0.00	-1.64	987.48	73.48	725.58	728.00	-20.77	725.88	73.51	-20.83	728.29	73.75
18.90	140.08	0.00	-3.38	1,150.43	72.77	837.11	839.10	-49.41	838.57	72.89	-49.52	840.55	73.06
17.11	155.75	0.00	-5.82	997.70	79.53	793.48	795.86	-80.50	797.56	79.94	-80.74	799.92	80.18
19.32	138.57	0.00	5.16	1,139.48	69.16	788.08	789.96	70.85	791.25	69.44	71.02	793.13	69.60
23.37	155.35	0.00	4.89	1,049.73	78.23	821.17	822.94	69.93	824.15	78.51	70.08	825.91	78.68
20.02	148.55	0.00	3.32	798.31	75.87	605.69	607.56	35.07	606.70	76.00	35.18	608.58	76.23
17.87	143.46	0.00	0.78	821.40	75.69	621.70	623.07	8.50	621.76	75.70	8.52	623.12	75.86
21.27	164.82	0.00	4.02	973.87	85.28	830.52	832.26	58.23	832.56	85.49	58.35	834.30	85.67
20.58	140.15	0.00	2.87	909.66	74.13	674.37	675.39	33.74	675.21	74.23	33.79	676.23	74.34
15.32	158.65	0.00	5.39	924.00	87.43	807.88	809.84	75.95	811.44	87.82	76.14	813.40	88.03
21.17	160.41	0.00	-0.83	764.06	69.59	531.68	533.40	-7.74	531.73	69.59	-7.76	533.46	69.82
23.11	154.95	0.00	-0.29	930.88	73.71	686.16	688.60	-3.47	686.16	73.71	-3.48	688.61	73.97
24.04	136.81	0.00	1.63	813.73	72.65	591.15	592.23	16.81	591.39	72.68	16.84	592.47	72.81
22.40	151.93	0.00	-3.61	992.54	74.48	739.19	741.33	-46.55	740.66	74.62	-46.69	742.79	74.84
17.48	135.32	0.00	2.85	1,029.55	71.26	733.68	736.05	36.43	734.59	71.35	36.55	736.95	71.58
19.83	145.63	0.00	3.01	777.29	75.22	584.70	586.66	30.66	585.51	75.33	30.76	587.46	75.58
15.06	149.83	0.00	1.51	1,168.49	72.81	850.78	853.06	22.38	851.07	72.83	22.44	853.36	73.03
21.05	159.08	0.00	4.51	1,186.45	75.61	897.09	898.91	70.48	899.86	75.84	70.62	901.67	76.00

Table C.1 Friction numbers by speed, radius and camber angle (Contd.)

Speed (mph)	Curve Radius (ft)	Camber Angle (degree)	Slip Angle (degree)	Vertical Force (lbs)	Longitudinal FN	Ideal Longitudinal Force (lbs)	FEA Longitudinal Force (lbs)	Ideal Lateral Force (lbs)	Ideal Friction Force (lbs)	True FN (%)	FEA Lateral Force (lbs)	FEA Friction Force (lbs)	FEA True FN
19.72	161.72	0.00	-4.17	1,136.01	74.60	847.41	849.96	-61.63	849.65	74.79	-61.82	852.19	75.02
15.23	140.38	0.00	4.29	1,119.32	71.25	797.47	799.08	59.66	799.70	71.44	59.79	801.31	71.59
20.73	154.95	0.00	-2.59	1,162.34	73.38	852.96	855.68	-38.50	853.83	73.46	-38.62	856.55	73.69
21.50	153.32	0.00	6.67	1,152.50	74.61	859.84	862.64	99.80	865.61	75.11	100.13	868.40	75.35
19.67	137.17	0.00	1.69	1,036.22	70.46	730.12	732.59	21.55	730.44	70.49	21.62	732.91	70.73
19.99	138.19	0.00	-5.23	879.06	73.31	644.40	646.05	-58.73	647.07	73.61	-58.88	648.71	73.80
22.21	152.45	0.00	-2.41	851.82	73.04	622.16	624.14	-26.14	622.71	73.10	-26.23	624.69	73.34
18.99	141.57	0.00	-4.28	972.65	73.72	717.06	718.59	-53.56	719.06	73.93	-53.68	720.59	74.08
24.45	147.05	0.00	5.87	843.80	74.21	626.22	627.60	64.08	629.49	74.60	64.22	630.86	74.76
24.98	141.06	0.00	1.57	745.52	72.90	543.47	545.26	14.87	543.68	72.93	14.92	545.46	73.17
18.83	138.10	0.00	4.15	935.61	74.16	693.82	695.23	50.25	695.64	74.35	50.35	697.04	74.50
21.79	142.37	0.00	-3.18	1,096.04	72.70	796.82	799.04	-44.26	798.05	72.81	-44.38	800.26	73.01
15.95	141.00	0.00	-5.46	1,034.94	73.62	761.87	763.93	-72.46	765.31	73.95	-72.65	767.36	74.15
17.91	160.06	0.00	2.52	1,075.32	79.77	857.73	860.33	37.72	858.56	79.84	37.83	861.15	80.08
15.75	139.69	0.00	0.39	1,176.49	72.21	849.52	851.67	5.84	849.54	72.21	5.86	851.69	72.39
17.16	151.91	0.00	6.19	898.30	84.61	760.10	762.34	81.90	764.49	85.10	82.14	766.72	85.35
23.37	146.10	0.00	-6.77	862.79	74.32	641.22	642.64	-75.61	645.66	74.83	-75.77	647.07	75.00
17.85	153.05	0.00	-2.10	1,061.99	75.45	801.30	802.73	-29.39	801.84	75.50	-29.44	803.27	75.64
19.17	135.66	0.00	-2.79	790.54	73.30	579.47	580.67	-28.20	580.16	73.39	-28.26	581.36	73.54
15.04	157.81	0.00	5.24	817.08	79.59	650.33	652.10	59.41	653.03	79.92	59.57	654.80	80.14
16.31	151.17	0.00	5.64	836.26	81.38	680.56	681.85	66.85	683.83	81.77	66.97	685.12	81.93
24.14	151.79	0.00	-0.45	843.85	71.56	603.83	604.77	-4.72	603.84	71.56	-4.72	604.79	71.67
18.19	159.48	0.00	4.89	910.94	86.43	787.32	789.14	67.10	790.17	86.74	67.26	791.99	86.94
16.03	135.85	0.00	3.61	1,151.63	70.88	816.33	818.86	51.41	817.95	71.03	51.57	820.47	71.24
20.86	151.40	0.00	0.55	904.56	75.76	685.30	687.56	6.60	685.33	75.76	6.62	687.59	76.01
15.85	135.42	0.00	-3.71	895.71	73.57	659.01	660.92	-42.59	660.39	73.73	-42.71	662.29	73.94
21.30	147.93	0.00	-4.37	1,038.58	73.91	767.64	769.55	-58.50	769.87	74.13	-58.65	771.77	74.31
18.53	159.68	0.00	6.88	990.16	89.05	881.74	882.91	105.55	888.03	89.69	105.69	889.20	89.80
19.35	150.30	0.00	-5.03	1,045.35	74.93	783.25	785.46	-68.71	786.25	75.21	-68.90	788.46	75.42
20.19	163.63	0.00	-5.69	901.75	80.28	723.90	725.15	-71.71	727.45	80.67	-71.83	728.68	80.81
19.78	139.96	0.00	5.27	1,071.40	68.44	733.31	734.85	67.33	736.40	68.73	67.47	737.93	68.88
15.85	140.64	0.00	-3.24	979.08	74.22	726.69	728.55	-41.03	727.84	74.34	-41.13	729.70	74.53
22.28	154.85	0.00	2.52	804.76	72.51	583.51	584.58	25.67	584.07	72.58	25.71	585.14	72.71
23.20	147.49	0.00	-1.97	1,191.87	73.13	871.67	873.62	-30.01	872.19	73.18	-30.08	874.14	73.34
16.03	139.97	0.00	-1.80	1,043.28	73.68	768.71	770.12	-24.15	769.09	73.72	-24.20	770.50	73.85
23.91	136.00	0.00	5.58	700.88	73.11	512.39	513.38	49.86	514.81	73.45	49.96	515.80	73.59
24.76	147.13	0.00	3.43	1,168.71	73.10	854.31	855.72	51.15	855.84	73.23	51.24	857.24	73.35
18.99	143.58	0.00	1.34	954.59	75.94	724.87	726.95	16.98	725.07	75.96	17.03	727.15	76.17
16.07	137.82	0.00	-1.71	928.13	74.42	690.75	692.03	-20.61	691.05	74.46	-20.65	692.33	74.59
15.87	145.70	0.00	5.30	847.85	81.12	687.75	689.18	63.55	690.68	81.46	63.68	692.10	81.63
19.38	163.29	0.00	2.03	874.56	77.29	675.99	678.43	23.93	676.41	77.34	24.01	678.85	77.62
20.39	155.74	0.00	-1.73	1,044.06	75.48	788.02	790.50	-23.82	788.38	75.51	-23.89	790.86	75.75
16.40	154.51	0.00	-2.09	808.64	72.88	589.33	591.18	-21.52	589.73	72.93	-21.58	591.57	73.16

Table C.1 Friction numbers by speed, radius and camber angle (Contd.)

Speed (mph)	Curve Radius (ft)	Camber Angle (degree)	Slip Angle (degree)	Vertical Force (lbs)	Longitudinal FN	Ideal Longitudinal Force (lbs)	FEA Longitudinal Force (lbs)	Ideal Lateral Force (lbs)	Ideal Friction Force (lbs)	True FN (%)	FEA Lateral Force (lbs)	FEA Friction Force (lbs)	FEA True FN
17.70	161.50	0.00	-4.52	972.48	80.51	782.96	785.24	-61.66	785.38	80.76	-61.84	787.66	81.00
18.05	148.84	0.00	-3.01	808.87	73.57	595.06	596.80	-31.26	595.88	73.67	-31.35	597.62	73.88
23.81	160.10	0.00	-2.01	787.73	69.94	550.92	551.96	-19.31	551.26	69.98	-19.35	552.30	70.11
16.83	164.13	0.00	-3.10	755.77	71.00	536.60	538.11	-28.99	537.38	71.10	-29.07	538.89	71.30
21.25	155.57	0.00	2.48	805.12	73.15	588.94	590.75	25.45	589.49	73.22	25.53	591.29	73.44
17.19	140.90	0.00	-1.62	926.15	74.87	693.45	695.46	-19.65	693.73	74.90	-19.71	695.73	75.12
19.25	144.53	0.00	1.73	957.50	76.25	730.09	732.74	21.99	730.42	76.28	22.07	733.07	76.56
17.57	157.92	0.00	-5.72	996.93	80.48	802.29	804.61	-79.97	806.27	80.88	-80.20	808.58	81.11
19.85	151.15	0.00	4.57	907.41	81.26	737.32	739.15	58.70	739.65	81.51	58.85	741.47	81.71
21.02	155.14	0.00	-5.35	1,018.40	76.39	777.94	780.20	-72.58	781.32	76.72	-72.80	783.57	76.94
22.29	142.82	0.00	1.52	905.50	73.61	666.52	667.48	17.66	666.75	73.63	17.69	667.72	73.74
24.35	157.06	0.00	3.58	720.27	70.12	505.07	506.20	31.54	506.06	70.26	31.61	507.18	70.41
16.09	159.45	0.00	-3.75	752.66	71.86	540.83	542.58	-35.42	541.99	72.01	-35.53	543.74	72.24
19.90	142.84	0.00	-2.49	972.84	73.87	718.59	720.27	-31.22	719.27	73.93	-31.30	720.95	74.11
19.29	152.54	0.00	4.25	1,108.81	75.09	832.62	834.34	61.64	834.90	75.30	61.77	836.61	75.45
16.85	154.62	0.00	2.86	1,159.28	73.68	854.16	855.50	42.62	855.22	73.77	42.69	856.56	73.89
21.38	155.66	0.00	-5.03	1,034.21	75.92	785.17	787.52	-68.91	788.19	76.21	-69.11	790.53	76.44
19.03	141.67	0.00	-0.93	1,025.46	73.35	752.19	754.91	-12.27	752.29	73.36	-12.32	755.01	73.63
18.82	144.97	0.00	-6.07	876.77	74.10	649.73	651.84	-68.68	653.35	74.52	-68.90	655.45	74.76
24.28	163.79	0.00	-3.21	731.30	73.01	533.92	535.63	-29.87	534.76	73.12	-29.96	536.46	73.36
21.14	140.12	0.00	-0.02	1,040.55	71.43	743.26	746.09	-0.28	743.26	71.43	-0.28	746.09	71.70
15.65	164.79	0.00	0.32	1,037.82	80.06	830.84	833.06	4.71	830.86	80.06	4.72	833.07	80.27
23.74	136.34	0.00	4.73	971.98	66.01	641.63	643.19	52.96	643.81	66.24	53.09	645.37	66.40
15.89	141.97	0.00	5.03	955.37	79.02	754.88	756.45	66.14	757.78	79.32	66.28	759.33	79.48
19.17	155.27	0.00	-6.46	1,071.41	76.48	819.43	822.03	-92.24	824.60	76.96	-92.53	827.18	77.21
18.62	154.90	0.00	0.36	757.45	72.07	545.93	547.07	3.45	545.94	72.08	3.46	547.08	72.23
15.95	152.19	0.00	4.10	1,001.15	82.46	825.51	827.71	59.00	827.62	82.67	59.15	829.81	82.89
19.83	136.70	0.00	6.56	741.36	74.08	549.17	550.33	62.77	552.74	74.56	62.90	553.90	74.71
17.94	157.88	0.00	2.24	740.65	72.42	536.35	537.89	20.94	536.76	72.47	21.00	538.30	72.68
20.14	141.21	0.00	-0.17	887.15	74.44	660.38	661.32	-2.00	660.38	74.44	-2.00	661.33	74.55
23.06	144.93	0.00	4.48	848.57	74.59	632.98	634.30	49.44	634.91	74.82	49.55	636.23	74.98
24.88	164.95	0.00	-2.30	1,047.19	73.79	772.77	774.94	-30.97	773.39	73.85	-31.06	775.56	74.06
15.50	141.50	0.00	6.25	884.09	80.49	711.63	713.73	77.48	715.83	80.97	77.71	717.92	81.20
17.32	136.28	0.00	6.14	908.73	75.51	686.17	688.37	73.41	690.09	75.94	73.64	692.27	76.18
16.05	147.77	0.00	3.91	976.80	81.03	791.47	793.63	54.01	793.31	81.22	54.16	795.46	81.44
16.38	141.19	0.00	5.31	1,112.43	70.62	785.62	787.46	72.74	788.99	70.92	72.91	790.81	71.09
20.90	147.89	0.00	0.38	867.45	74.92	649.88	652.27	4.29	649.89	74.92	4.31	652.28	75.20
23.71	159.73	0.00	-2.55	1,061.47	74.18	787.42	789.07	-35.00	788.20	74.26	-35.08	789.84	74.41
24.25	142.08	0.00	-6.48	760.76	73.50	559.15	560.46	-63.07	562.70	73.96	-63.21	564.00	74.14
22.28	135.62	0.00	-0.99	954.88	71.74	685.07	686.76	-11.87	685.17	71.75	-11.90	686.86	71.93
17.90	147.18	0.00	-2.25	948.32	75.48	715.79	717.17	-28.08	716.34	75.54	-28.13	717.72	75.68
19.10	141.28	0.00	5.46	812.69	76.70	623.32	625.02	59.33	626.13	77.05	59.50	627.83	77.25
19.91	146.84	0.00	-3.62	972.92	74.43	724.19	726.40	-45.69	725.63	74.58	-45.83	727.83	74.81

Table C.1 Friction numbers by speed, radius and camber angle (Contd.)

Speed (mph)	Curve Radius (ft)	Camber Angle (degree)	Slip Angle (degree)	Vertical Force (lbs)	Longitudinal FN	Ideal Longitudinal Force (lbs)	FEA Longitudinal Force (lbs)	Ideal Lateral Force (lbs)	Ideal Friction Force (lbs)	True FN (%)	FEA Lateral Force (lbs)	FEA Friction Force (lbs)	FEA True FN
16.02	159.21	0.00	0.26	767.38	71.76	550.69	551.66	2.49	550.70	71.76	2.49	551.67	71.89
19.44	164.27	0.00	-5.87	909.70	81.17	738.40	740.52	-75.48	742.25	81.59	-75.69	744.36	81.82
16.00	143.47	0.00	1.79	730.43	74.43	543.64	545.01	17.01	543.91	74.46	17.06	545.28	74.65
15.21	136.05	0.00	-4.61	852.90	73.42	626.21	627.69	-50.30	628.22	73.66	-50.41	629.70	73.83
22.33	137.94	0.00	-3.40	706.30	73.09	516.23	517.84	-30.60	517.14	73.22	-30.70	518.74	73.45
19.61	136.39	0.00	-1.99	758.99	73.29	556.29	557.11	-19.28	556.62	73.34	-19.31	557.44	73.45
23.28	147.75	0.00	-5.64	872.63	74.40	649.26	651.23	-63.80	652.38	74.76	-63.99	654.35	74.99
16.91	146.14	0.00	3.91	855.58	80.20	686.21	687.43	46.83	687.81	80.39	46.92	689.02	80.53
21.42	149.94	0.00	0.50	1,075.26	73.74	792.87	795.41	6.94	792.90	73.74	6.96	795.44	73.98
15.78	140.18	0.00	-0.59	1,122.20	72.67	815.54	817.11	-8.44	815.59	72.68	-8.46	817.16	72.82
20.71	150.26	0.00	4.75	747.70	74.49	556.94	558.38	46.10	558.85	74.74	46.22	560.28	74.93
20.97	140.36	0.00	3.05	872.07	74.53	649.97	651.16	34.59	650.89	74.64	34.65	652.07	74.77
22.92	158.65	0.00	-6.48	755.71	80.01	604.67	606.63	-68.26	608.51	80.52	-68.49	610.46	80.78
17.26	145.30	0.00	-5.90	835.61	73.92	617.69	619.65	-63.47	620.95	74.31	-63.67	622.89	74.54
15.03	164.96	0.00	2.86	736.93	72.81	536.59	537.50	26.79	537.26	72.91	26.84	538.17	73.03
17.66	159.26	0.00	-3.12	898.81	76.10	683.98	685.43	-37.25	685.00	76.21	-37.33	686.44	76.37
18.35	142.74	0.00	-3.41	1,147.59	72.93	836.93	839.58	-49.79	838.41	73.06	-49.95	841.05	73.29
18.06	154.77	0.00	4.66	820.45	78.94	647.64	649.19	52.65	649.78	79.20	52.77	651.32	79.39
21.60	163.44	0.00	4.08	776.91	72.03	559.60	561.03	39.80	561.01	72.21	39.90	562.44	72.39
16.85	151.83	0.00	-5.22	810.28	74.25	601.66	603.15	-54.78	604.15	74.56	-54.91	605.63	74.74
20.00	147.68	0.00	2.32	1,008.73	75.83	764.97	766.93	30.93	765.59	75.90	31.01	767.56	76.09
17.98	148.51	0.00	-6.20	1,090.53	74.25	809.71	811.06	-87.47	814.43	74.68	-87.62	815.77	74.80
22.19	144.20	0.00	-0.92	1,058.93	72.34	766.02	767.56	-12.34	766.12	72.35	-12.36	767.65	72.49
22.84	135.34	0.00	-2.18	1,148.71	72.38	831.42	833.98	-31.64	832.02	72.43	-31.73	834.58	72.65
24.70	151.62	0.00	-5.12	1,059.75	73.73	781.36	783.29	-69.76	784.47	74.02	-69.94	786.39	74.21
20.36	141.41	0.00	-2.57	823.80	73.60	606.30	608.30	-27.13	606.91	73.67	-27.22	608.91	73.91
16.07	159.64	0.00	-2.12	791.79	71.45	565.75	567.01	-20.92	566.14	71.50	-20.97	567.39	71.66
15.12	162.54	0.00	6.35	763.59	76.19	581.77	583.42	64.33	585.31	76.65	64.52	586.96	76.87
19.59	137.05	0.00	3.63	754.49	74.09	559.01	560.57	35.41	560.13	74.24	35.51	561.69	74.45
17.80	161.35	0.00	-3.66	955.28	79.02	754.82	756.95	-48.18	756.36	79.18	-48.32	758.48	79.40
23.17	160.53	0.00	2.37	1,165.26	76.04	886.10	888.75	36.69	886.86	76.11	36.80	889.51	76.34
15.17	148.47	0.00	2.13	942.04	80.68	760.04	761.98	28.28	760.56	80.74	28.35	762.51	80.94
17.41	143.08	0.00	1.95	802.00	76.09	610.23	612.46	20.82	610.58	76.13	20.89	612.81	76.41
17.54	158.41	0.00	1.26	876.11	77.62	680.07	682.52	14.94	680.23	77.64	15.00	682.68	77.92
24.55	160.62	0.00	2.66	1,159.76	76.88	891.63	892.95	41.34	892.59	76.96	41.40	893.91	77.08
20.68	136.85	0.00	5.40	842.69	73.94	623.11	624.82	58.65	625.86	74.27	58.81	627.57	74.47
15.35	139.42	0.00	6.57	1,001.67	75.25	753.76	756.33	86.20	758.67	75.74	86.50	761.23	76.00
15.11	143.08	0.00	-6.43	1,186.04	73.11	867.14	870.03	-97.12	872.57	73.57	-97.44	875.44	73.81
17.83	137.77	0.00	-2.33	1,156.57	72.57	839.27	840.81	-34.06	839.96	72.63	-34.12	841.50	72.76
20.17	155.16	0.00	6.81	1,156.22	75.12	868.54	869.74	102.97	874.62	75.64	103.11	875.81	75.75
22.00	143.87	0.00	-5.09	743.02	73.48	545.99	547.38	-48.41	548.13	73.77	-48.54	549.51	73.96
16.15	156.16	0.00	-5.40	877.62	77.98	684.36	685.85	-64.46	687.39	78.32	-64.60	688.87	78.49
24.53	139.46	0.00	2.82	729.78	73.05	533.09	533.86	26.20	533.73	73.14	26.24	534.51	73.24

Table C.1 Friction numbers by speed, radius and camber angle (Contd.)

Speed (mph)	Curve Radius (ft)	Camber Angle (degree)	Slip Angle (degree)	Vertical Force (lbs)	Longitudinal FN	Ideal Longitudinal Force (lbs)	FEA Longitudinal Force (lbs)	Ideal Lateral Force (lbs)	Ideal Friction Force (lbs)	True FN (%)	FEA Lateral Force (lbs)	FEA Friction Force (lbs)	FEA True FN
18.80	155.41	0.00	-2.78	1,150.06	73.68	847.41	849.94	-41.13	848.41	73.77	-41.25	850.93	73.99
23.49	156.34	0.00	-5.29	1,108.74	74.08	821.36	823.86	-75.66	824.84	74.39	-75.89	827.33	74.62
23.11	144.94	0.00	-0.94	1,082.78	72.24	782.23	784.71	-12.82	782.33	72.25	-12.86	784.81	72.48
16.56	153.61	0.00	-0.58	1,015.18	77.72	788.99	790.95	-7.98	789.03	77.72	-8.00	790.99	77.92
23.60	149.42	0.00	-4.42	1,090.61	73.37	800.22	802.66	-61.61	802.59	73.59	-61.79	805.02	73.81
16.49	142.17	0.00	6.59	1,094.07	70.96	776.34	777.41	89.13	781.44	71.43	89.26	782.51	71.52
17.49	157.16	0.00	-2.07	1,072.53	76.13	816.56	818.06	-29.51	817.10	76.18	-29.56	818.59	76.32
17.49	146.76	0.00	0.78	1,099.17	73.48	807.67	810.55	11.02	807.75	73.49	11.06	810.63	73.75
18.64	153.17	0.00	-3.06	809.60	73.12	592.01	593.83	-31.65	592.85	73.23	-31.75	594.67	73.45
17.02	158.16	0.00	-5.47	733.23	73.61	539.72	541.31	-51.45	542.16	73.94	-51.60	543.75	74.16
17.84	156.26	0.00	2.43	722.57	72.66	525.03	526.81	22.27	525.50	72.73	22.34	527.28	72.97
20.47	154.76	0.00	0.31	908.11	75.89	689.18	690.38	3.68	689.19	75.89	3.68	690.39	76.03
18.74	161.35	0.00	3.17	931.03	84.57	787.40	788.63	43.52	788.60	84.70	43.59	789.83	84.83
21.13	145.22	0.00	-5.82	783.45	73.79	578.09	579.87	-58.62	581.05	74.17	-58.80	582.82	74.39
22.81	163.09	0.00	4.92	1,128.94	79.21	894.18	896.44	76.65	897.46	79.50	76.84	899.71	79.70
23.98	151.70	0.00	6.96	714.10	73.21	522.81	523.74	63.35	526.64	73.75	63.47	527.56	73.88
19.49	140.59	0.00	-0.69	802.82	74.01	594.16	595.63	-7.13	594.20	74.01	-7.14	595.67	74.20
23.72	139.82	0.00	1.24	1,001.14	69.58	696.62	698.41	15.02	696.78	69.60	15.06	698.57	69.78
15.56	159.38	0.00	-3.89	950.37	80.09	761.14	762.88	-51.69	762.89	80.27	-51.80	764.63	80.46
20.91	141.71	0.00	0.99	1,157.73	71.66	829.62	832.22	14.39	829.75	71.67	14.43	832.35	71.89
21.38	159.87	0.00	-5.33	1,132.33	74.52	843.86	846.43	-78.42	847.50	74.85	-78.66	850.06	75.07
24.73	150.18	0.00	-5.24	724.19	74.65	540.59	541.99	-49.38	542.84	74.96	-49.51	544.24	75.15
22.50	161.33	0.00	-6.35	765.29	80.77	618.13	619.97	-68.40	621.90	81.26	-68.60	623.73	81.50
22.21	141.80	0.00	-4.22	1,125.98	72.84	820.15	822.42	-60.36	822.37	73.04	-60.53	824.63	73.24
24.63	148.68	0.00	5.37	908.93	74.38	676.03	677.88	63.27	678.98	74.70	63.44	680.83	74.90
20.89	162.17	0.00	0.06	900.22	74.28	668.73	671.24	0.71	668.73	74.28	0.71	671.24	74.56
24.81	135.66	0.00	2.25	801.99	72.47	581.18	582.31	22.84	581.62	72.52	22.89	582.76	72.66
21.07	142.07	0.00	4.61	1,025.94	69.85	716.64	718.15	57.57	718.95	70.08	57.69	720.45	70.22
19.46	151.46	0.00	5.48	889.19	81.99	729.03	730.73	69.65	732.35	82.36	69.81	734.04	82.55
24.68	145.19	0.00	6.28	1,108.90	69.80	774.04	775.75	84.71	778.66	70.22	84.90	780.36	70.37
24.91	147.60	0.00	4.57	1,124.23	71.97	809.07	810.74	64.43	811.63	72.19	64.56	813.29	72.34
23.36	137.01	0.00	-2.18	960.27	72.07	692.02	693.23	-26.31	692.52	72.12	-26.35	693.73	72.24
22.87	151.51	0.00	-5.70	1,193.03	73.24	873.82	876.57	-86.73	878.11	73.60	-87.01	880.85	73.83
18.00	151.16	0.00	-6.22	898.82	76.43	687.00	688.12	-74.38	691.01	76.88	-74.50	692.13	77.00
21.21	152.22	0.00	-3.45	731.62	73.42	537.16	538.15	-32.30	538.13	73.55	-32.36	539.12	73.69
22.68	145.61	0.00	3.90	721.74	73.42	529.92	530.93	36.05	531.14	73.59	36.12	532.16	73.73
17.61	160.21	0.00	0.95	1,154.58	74.13	855.93	858.62	14.12	856.04	74.14	14.16	858.73	74.38
17.64	161.02	0.00	-5.90	1,152.04	75.16	865.87	868.22	-89.08	870.44	75.56	-89.32	872.78	75.76
19.82	155.20	0.00	6.14	957.82	85.24	816.43	818.14	87.35	821.09	85.72	87.53	822.79	85.90
18.73	148.82	0.00	3.09	821.66	77.40	635.99	636.96	34.28	636.91	77.52	34.33	637.88	77.63
24.36	154.64	0.00	-3.32	727.82	73.25	533.09	534.73	-30.91	533.99	73.37	-31.01	535.62	73.59
23.18	146.10	0.00	1.56	1,098.56	71.69	787.58	790.62	21.49	787.87	71.72	21.58	790.92	72.00
16.11	152.90	0.00	-4.60	1,002.87	77.42	776.40	778.69	-62.22	778.89	77.67	-62.41	781.17	77.89

Table C.1 Friction numbers by speed, radius and camber angle (Contd.)

Speed (mph)	Curve Radius (ft)	Camber Angle (degree)	Slip Angle (degree)	Vertical Force (lbs)	Longitudinal FN	Ideal Longitudinal Force (lbs)	FEA Longitudinal Force (lbs)	Ideal Lateral Force (lbs)	Ideal Friction Force (lbs)	True FN (%)	FEA Lateral Force (lbs)	FEA Friction Force (lbs)	FEA True FN
16.66	145.02	0.00	3.79	1,115.76	72.07	804.09	805.77	53.16	805.84	72.22	53.27	807.52	72.37
21.69	144.35	0.00	4.41	903.76	75.42	681.65	683.31	52.36	683.65	75.65	52.49	685.31	75.83
24.62	148.85	0.00	1.28	1,026.14	72.62	745.22	746.65	16.61	745.41	72.64	16.65	746.83	72.78
22.92	156.91	0.00	6.71	1,151.82	76.95	886.28	888.51	103.54	892.30	77.47	103.80	894.52	77.66
19.56	155.75	0.00	0.23	1,101.99	74.90	825.44	827.66	3.28	825.45	74.91	3.29	827.67	75.11
15.34	161.35	0.00	1.04	1,052.27	79.97	841.49	844.58	15.29	841.63	79.98	15.34	844.72	80.28
18.94	148.04	0.00	2.77	961.89	78.86	758.51	759.82	36.68	759.40	78.95	36.74	760.70	79.08
16.86	141.26	0.00	4.10	798.32	76.93	614.14	615.37	43.94	615.71	77.13	44.03	616.93	77.28
21.11	145.65	0.00	0.43	959.92	74.57	715.77	718.51	5.40	715.79	74.57	5.42	718.53	74.85
15.26	156.53	0.00	-0.24	1,120.42	74.90	839.24	842.31	-3.50	839.25	74.90	-3.51	842.32	75.18
24.42	162.45	0.00	1.90	725.05	67.11	486.57	487.22	16.14	486.84	67.15	16.16	487.49	67.24
23.12	158.56	0.00	4.28	1,001.64	81.30	814.36	816.03	60.82	816.63	81.53	60.95	818.29	81.70
17.97	153.14	0.00	0.15	1,017.38	77.64	789.93	791.28	2.11	789.93	77.64	2.12	791.29	77.78
23.38	138.85	0.00	1.83	1,124.13	70.13	788.30	791.28	25.24	788.71	70.16	25.34	791.69	70.43
24.04	151.61	0.00	2.39	726.27	71.44	518.84	520.01	21.62	519.29	71.50	21.66	520.46	71.66
24.49	136.77	0.00	3.83	1,125.36	68.81	774.35	775.99	51.75	776.08	68.96	51.86	777.71	69.11
21.82	154.08	0.00	3.22	1,120.72	74.95	839.93	842.65	47.12	841.25	75.06	47.28	843.97	75.31
24.63	139.37	0.00	-5.44	975.06	72.90	710.80	712.65	-67.37	713.99	73.23	-67.55	715.83	73.41
22.86	159.16	0.00	-0.87	752.35	69.24	520.95	522.92	-7.90	521.01	69.25	-7.93	522.98	69.51
20.05	147.07	0.00	4.82	1,178.67	71.82	846.52	848.51	71.18	849.50	72.07	71.34	851.49	72.24
19.06	138.48	0.00	6.50	788.31	75.42	594.58	596.29	67.28	598.37	75.91	67.48	600.07	76.12
18.94	159.55	0.00	-1.60	1,056.42	76.55	808.66	811.40	-22.59	808.97	76.58	-22.67	811.71	76.84
22.71	154.64	0.00	1.42	934.15	75.74	707.48	708.86	17.50	707.70	75.76	17.54	709.08	75.91
17.69	159.46	0.00	-4.21	1,125.90	75.23	846.98	849.45	-62.24	849.26	75.43	-62.42	851.73	75.65
21.01	147.00	0.00	-4.94	976.18	74.24	724.71	726.57	-62.46	727.40	74.52	-62.62	729.25	74.70
19.94	145.40	0.00	1.68	711.02	73.51	522.65	523.89	15.34	522.87	73.54	15.37	524.12	73.71
21.25	162.79	0.00	-5.08	738.70	77.11	569.63	571.19	-50.42	571.86	77.41	-50.56	573.42	77.63
19.52	142.24	0.00	3.64	704.05	73.91	520.35	521.70	33.06	521.39	74.06	33.15	522.75	74.25
17.51	159.83	0.00	0.79	959.23	80.90	776.03	778.61	10.66	776.10	80.91	10.70	778.69	81.18
19.69	152.70	0.00	-0.34	946.85	76.62	725.52	726.99	-4.25	725.54	76.63	-4.26	727.00	76.78
22.02	135.15	0.00	-6.63	853.84	73.08	624.00	624.87	-72.10	628.15	73.57	-72.20	629.02	73.67
21.00	158.30	0.00	3.82	1,195.33	74.99	896.41	898.05	59.67	898.39	75.16	59.78	900.03	75.30
15.06	144.74	0.00	3.85	1,041.52	75.97	791.21	792.57	53.08	792.99	76.14	53.17	794.34	76.27
21.86	138.35	0.00	-3.88	807.12	73.20	590.80	592.65	-40.01	592.15	73.37	-40.13	594.00	73.59
16.22	156.26	0.00	-3.92	1,014.12	78.41	795.21	797.64	-54.35	797.07	78.60	-54.52	799.49	78.84
17.14	145.71	0.00	-2.90	1,148.24	73.13	839.73	841.58	-42.42	840.80	73.23	-42.51	842.65	73.39
23.16	142.49	0.00	-3.55	718.30	73.17	525.60	526.58	-32.50	526.60	73.31	-32.56	527.59	73.45
17.90	162.24	0.00	-3.15	1,062.06	77.42	822.19	824.45	-45.24	823.44	77.53	-45.36	825.69	77.74
24.91	146.87	0.00	2.64	901.76	72.81	656.54	657.93	30.25	657.23	72.88	30.32	658.63	73.04
18.38	137.53	0.00	-0.40	987.90	73.19	723.03	724.35	-5.00	723.04	73.19	-5.01	724.36	73.32
23.56	149.40	0.00	-4.22	998.13	73.83	736.90	739.09	-54.25	738.89	74.03	-54.41	741.08	74.25
21.44	164.42	0.00	-1.25	794.12	69.27	550.05	551.22	-12.00	550.18	69.28	-12.03	551.36	69.43
18.26	164.43	0.00	0.42	1,010.72	80.31	811.68	812.84	5.98	811.71	80.31	5.99	812.86	80.42

Table C.1 Friction Numbers by Speed, Radius and Camber Angle (Contd.)

Speed (mph)	Curve Radius (ft)	Camber Angle (degree)	Slip Angle (degree)	Vertical Force (lbs)	Longitudinal FN	Ideal Longitudinal Force (lbs)	FEA Longitudinal Force (lbs)	Ideal Lateral Force (lbs)	Ideal Friction Force (lbs)	True FN (%)	FEA Lateral Force (lbs)	FEA Friction Force (lbs)	FEA True FN
18.81	138.99	0.00	-0.61	877.26	74.42	652.84	655.24	-6.93	652.88	74.42	-6.95	655.28	74.70
21.44	143.47	0.00	0.35	756.26	73.46	555.56	557.22	3.38	555.57	73.46	3.39	557.23	73.68
21.18	157.16	0.00	-3.83	987.81	76.26	753.34	754.81	-50.36	755.02	76.43	-50.45	756.48	76.58
24.74	148.14	0.00	6.57	915.80	74.06	678.25	679.68	77.57	682.67	74.54	77.73	684.10	74.70
17.33	143.45	0.00	-3.06	725.50	73.22	531.22	532.17	-28.31	531.97	73.32	-28.36	532.93	73.46
21.48	149.69	0.00	0.85	779.42	72.98	568.82	570.66	8.48	568.88	72.99	8.51	570.72	73.22
18.47	161.93	0.00	-2.14	737.39	70.79	522.02	523.81	-19.52	522.39	70.84	-19.59	524.17	71.08
24.23	156.41	0.00	3.66	971.84	77.90	757.05	759.03	48.29	758.59	78.06	48.42	760.57	78.26
19.97	142.54	0.00	3.28	1,095.68	70.33	770.58	773.15	44.14	771.85	70.44	44.28	774.41	70.68
18.58	150.95	0.00	4.73	739.69	75.02	554.89	556.40	45.74	556.77	75.27	45.86	558.28	75.47
19.58	135.96	0.00	-3.86	1,012.18	72.86	737.46	739.35	-49.71	739.13	73.02	-49.83	741.02	73.21
23.33	164.72	0.00	-6.94	970.59	80.04	776.82	778.47	-93.82	782.46	80.62	-94.02	784.10	80.79
21.88	153.19	0.00	4.29	733.96	72.93	535.28	536.69	40.03	536.77	73.13	40.14	538.18	73.33
24.00	147.76	0.00	4.90	1,056.94	71.48	755.51	757.27	64.56	758.26	71.74	64.71	760.02	71.91
17.46	154.62	0.00	4.31	883.53	83.08	733.99	735.58	55.14	736.06	83.31	55.26	737.65	83.49
18.36	148.55	0.00	-0.56	840.83	74.97	630.33	631.53	-6.16	630.36	74.97	-6.18	631.56	75.11
23.09	137.58	0.00	6.06	961.99	66.83	642.92	645.10	67.87	646.50	67.20	68.10	648.66	67.43
17.30	140.40	0.00	-6.46	766.54	73.22	561.22	562.89	-63.12	564.76	73.68	-63.30	566.41	73.89
16.62	161.01	0.00	-6.45	841.13	79.54	669.05	671.10	-75.12	673.26	80.04	-75.35	675.29	80.28
16.53	140.03	0.00	5.12	724.35	74.78	541.68	543.08	48.30	543.83	75.08	48.43	545.22	75.27
15.36	163.36	0.00	-6.45	1,082.48	80.00	866.00	868.46	-97.32	871.45	80.50	-97.60	873.90	80.73
17.15	145.93	0.00	3.18	1,016.08	76.98	782.15	783.65	43.45	783.35	77.10	43.53	784.86	77.24
17.55	161.33	0.00	2.18	784.30	73.10	573.32	575.38	21.82	573.73	73.15	21.90	575.79	73.42
18.92	150.68	0.00	-2.46	769.71	72.90	561.16	562.79	-24.08	561.67	72.97	-24.15	563.31	73.18
18.63	152.47	0.00	-0.16	875.82	75.70	663.03	664.78	-1.84	663.03	75.70	-1.84	664.78	75.90
22.38	146.93	0.00	-6.12	741.33	74.20	550.10	551.36	-58.65	553.22	74.63	-58.79	554.47	74.79
22.38	157.17	0.00	-3.73	930.80	75.27	700.60	702.59	-45.57	702.08	75.43	-45.70	704.07	75.64
16.79	146.37	0.00	-5.47	894.45	74.67	667.92	669.63	-63.68	670.95	75.01	-63.84	672.65	75.20
19.99	138.85	0.00	5.18	864.43	75.17	649.76	651.23	58.66	652.40	75.47	58.79	653.86	75.64
22.99	144.15	0.00	2.90	1,007.32	70.91	714.30	715.76	36.15	715.21	71.00	36.22	716.67	71.15
24.61	136.06	0.00	-0.96	708.31	73.00	517.04	518.94	-8.66	517.12	73.01	-8.69	519.01	73.27
23.49	135.27	0.00	-3.14	1,104.35	72.29	798.28	799.94	-43.66	799.47	72.39	-43.75	801.14	72.54
21.00	159.31	0.00	-0.67	754.71	69.88	527.39	529.37	-6.17	527.43	69.88	-6.19	529.41	70.15
15.42	153.09	0.00	6.92	853.62	82.98	708.35	710.77	85.33	713.47	83.58	85.62	715.88	83.86
18.57	151.69	0.00	0.55	1,025.93	76.97	789.69	791.07	7.60	789.73	76.98	7.61	791.11	77.11
18.52	145.75	0.00	4.34	941.55	79.50	748.50	750.47	56.64	750.64	79.72	56.79	752.60	79.93
23.04	164.51	0.00	-6.83	859.36	82.70	710.65	712.78	-84.50	715.66	83.28	-84.75	717.77	83.52
18.46	151.25	0.00	6.97	796.79	78.47	625.22	626.05	75.84	629.80	79.04	75.94	630.63	79.15
21.75	156.11	0.00	3.59	829.10	75.05	622.22	624.05	38.98	623.44	75.19	39.09	625.27	75.42
19.10	146.57	0.00	-4.73	736.36	73.38	540.36	541.69	-44.53	542.20	73.63	-44.64	543.52	73.81
22.26	140.89	0.00	-2.47	1,050.61	72.34	760.01	762.52	-32.72	760.71	72.41	-32.83	763.22	72.65
18.12	164.80	0.00	-4.98	757.27	74.08	560.97	562.40	-48.65	563.07	74.36	-48.78	564.50	74.54
22.40	162.07	0.00	5.35	711.31	71.61	509.37	510.64	47.53	511.59	71.92	47.65	512.85	72.10

Table C.1 Friction numbers by speed, radius and camber angle (Contd.)

Speed (mph)	Curve Radius (ft)	Camber Angle (degree)	Slip Angle (degree)	Vertical Force (lbs)	Longitudinal FN	Ideal Longitudinal Force (lbs)	FEA Longitudinal Force (lbs)	Ideal Lateral Force (lbs)	Ideal Friction Force (lbs)	True FN (%)	FEA Lateral Force (lbs)	FEA Friction Force (lbs)	FEA True FN
17.82	159.64	0.00	-6.49	1,172.67	74.52	873.93	875.47	-98.82	879.50	75.00	-98.99	881.02	75.13
16.73	140.52	0.00	-1.14	1,044.94	73.61	769.14	771.88	-15.24	769.29	73.62	-15.29	772.03	73.88
23.32	160.85	0.00	-2.34	1,170.69	73.75	863.42	864.96	-35.23	864.14	73.81	-35.29	865.67	73.95
15.62	163.43	0.00	6.90	1,116.32	80.07	893.80	896.86	107.31	900.21	80.64	107.67	903.26	80.91
15.77	149.49	0.00	2.81	1,134.73	73.24	831.05	833.80	40.79	832.05	73.33	40.93	834.79	73.57
23.43	159.70	0.00	3.52	1,110.47	77.68	862.64	864.95	52.99	864.27	77.83	53.14	866.57	78.04
17.53	162.22	0.00	-5.36	867.24	78.71	682.60	684.61	-63.72	685.56	79.05	-63.91	687.57	79.28
22.64	162.75	0.00	0.02	710.98	68.68	488.27	489.75	0.15	488.27	68.68	0.15	489.75	68.88
17.07	156.63	0.00	-5.78	1,103.71	76.25	841.62	844.25	-84.83	845.89	76.64	-85.09	848.50	76.88
24.25	153.36	0.00	3.47	1,004.75	76.06	764.19	766.07	46.30	765.59	76.20	46.41	767.46	76.38
24.68	140.65	0.00	1.75	827.51	72.64	601.11	602.20	18.39	601.39	72.67	18.42	602.48	72.81
17.50	140.51	0.00	-6.60	767.40	73.22	561.92	563.28	-64.57	565.61	73.70	-64.72	566.97	73.88
21.85	159.34	0.00	-4.62	977.37	77.13	753.85	756.16	-60.73	756.29	77.38	-60.91	758.59	77.62
21.59	150.56	0.00	-3.77	1,123.08	73.43	824.69	826.86	-54.17	826.46	73.59	-54.32	828.63	73.78
16.58	144.75	0.00	0.64	1,162.42	72.39	841.46	842.81	9.43	841.51	72.39	9.44	842.86	72.51
18.78	141.33	0.00	0.19	821.33	74.80	614.32	616.18	2.00	614.32	74.80	2.00	616.18	75.02
22.85	150.18	0.00	-5.26	866.93	74.88	649.20	650.94	-59.51	651.92	75.20	-59.67	653.66	75.40
16.04	160.17	0.00	1.93	836.32	76.49	639.68	641.26	21.55	640.04	76.53	21.61	641.62	76.72
20.44	160.54	0.00	-1.41	787.90	70.24	553.43	555.20	-13.61	553.60	70.26	-13.65	555.37	70.49
17.09	139.77	0.00	1.89	954.47	75.80	723.51	725.45	23.88	723.90	75.84	23.95	725.84	76.05
19.87	139.96	0.00	-1.28	822.72	73.85	607.62	608.53	-13.52	607.77	73.87	-13.54	608.68	73.98
17.90	140.84	0.00	-0.50	924.05	75.17	694.63	695.73	-6.04	694.66	75.18	-6.05	695.76	75.29
15.70	161.37	0.00	-3.94	1,117.42	76.12	850.60	852.84	-58.46	852.61	76.30	-58.61	854.85	76.50
23.54	155.02	0.00	0.59	1,001.23	74.98	750.73	752.74	7.76	750.77	74.98	7.78	752.78	75.19
18.63	159.60	0.00	5.06	825.35	79.18	653.51	655.26	57.59	656.04	79.49	57.75	657.79	79.70
22.59	155.99	0.00	-3.74	1,184.26	73.40	869.26	871.41	-56.71	871.11	73.56	-56.85	873.26	73.74
19.86	150.38	0.00	-5.39	861.18	74.99	645.80	647.57	-60.64	648.64	75.32	-60.81	650.41	75.53
17.66	159.51	0.00	0.15	1,185.79	73.22	868.24	870.42	2.24	868.25	73.22	2.24	870.42	73.40
18.86	151.43	0.00	5.60	907.64	83.18	754.99	757.00	73.73	758.58	83.58	73.92	760.58	83.80
17.23	162.65	0.00	6.49	702.34	73.74	517.88	519.57	58.53	521.17	74.21	58.72	522.86	74.45
21.26	142.41	0.00	2.19	1,156.55	71.30	824.62	827.47	31.55	825.22	71.35	31.66	828.07	71.60
23.91	150.59	0.00	0.70	824.95	71.98	593.82	594.88	7.25	593.86	71.99	7.26	594.93	72.12
22.74	139.21	0.00	-0.98	961.74	72.00	692.45	695.03	-11.79	692.55	72.01	-11.83	695.13	72.28
18.38	150.47	0.00	0.78	705.71	72.92	514.59	515.32	7.02	514.64	72.93	7.03	515.37	73.03
18.33	155.18	0.00	-5.24	764.22	74.16	566.72	567.79	-51.74	569.08	74.47	-51.84	570.14	74.61
19.03	157.13	0.00	1.45	1,010.26	80.21	810.34	812.69	20.48	810.60	80.24	20.54	812.95	80.47
22.52	141.15	0.00	-1.09	933.56	72.83	679.89	682.22	-12.94	680.01	72.84	-12.98	682.34	73.09
23.35	152.96	0.00	6.56	1,169.71	74.90	876.08	878.99	100.02	881.78	75.38	100.36	884.66	75.63
17.38	161.46	0.00	-4.82	757.88	73.36	555.98	557.47	-46.73	557.95	73.62	-46.86	559.42	73.81
23.21	162.40	0.00	5.38	931.78	82.71	770.64	772.53	72.25	774.02	83.07	72.43	775.91	83.27
19.86	145.07	0.00	6.05	808.58	77.27	624.78	626.06	65.89	628.25	77.70	66.02	629.52	77.86
23.86	151.47	0.00	-5.58	803.59	75.65	607.95	609.33	-59.15	610.82	76.01	-59.29	612.20	76.18
17.74	164.62	0.00	-5.54	812.80	76.48	621.62	623.37	-60.06	624.51	76.84	-60.23	626.26	77.05
20.40	142.32	0.00	6.38	1,021.89	70.40	719.39	720.45	79.99	723.83	70.83	80.11	724.88	70.94

Table C.1 Friction numbers by speed, radius and camber angle (Contd.)

Speed (mph)	Curve Radius (ft)	Camber Angle (degree)	Slip Angle (degree)	Vertical Force (lbs)	Longitudinal FN	Ideal Longitudinal Force (lbs)	FEA Longitudinal Force (lbs)	Ideal Lateral Force (lbs)	Ideal Friction Force (lbs)	True FN (%)	FEA Lateral Force (lbs)	FEA Friction Force (lbs)	FEA True FN
20.29	138.03	0.00	1.46	1,019.27	70.72	720.86	721.93	18.36	721.09	70.75	18.39	722.16	70.85
23.93	154.10	0.00	3.36	944.91	76.62	724.00	726.23	42.42	725.24	76.75	42.55	727.47	76.99
22.17	150.51	0.00	6.44	820.24	76.61	628.41	629.43	70.50	632.35	77.09	70.62	633.36	77.22
16.63	143.30	0.00	5.05	1,192.96	71.06	847.77	850.08	74.61	851.05	71.34	74.81	853.35	71.53
22.23	144.39	0.00	2.23	951.52	73.45	698.87	700.11	27.23	699.40	73.50	27.27	700.64	73.63
22.40	161.82	0.00	-3.81	853.59	74.86	638.99	640.77	-42.51	640.40	75.02	-42.63	642.18	75.23
23.39	144.98	0.00	6.13	884.91	74.22	656.82	658.74	70.11	660.55	74.65	70.32	662.46	74.86
21.45	154.72	0.00	5.86	965.74	82.68	798.45	800.49	81.51	802.60	83.11	81.72	804.63	83.32
24.26	147.69	0.00	-0.74	747.42	72.24	539.94	541.16	-6.98	539.98	72.25	-6.99	541.21	72.41
24.99	140.04	0.00	-0.36	993.87	70.68	702.46	705.11	-4.45	702.47	70.68	-4.46	705.13	70.95
18.01	159.23	0.00	-0.12	924.57	77.86	719.87	720.95	-1.49	719.87	77.86	-1.49	720.95	77.98
19.87	137.80	0.00	1.53	1,162.54	71.20	827.75	829.85	22.14	828.05	71.23	22.20	830.15	71.41
19.88	139.96	0.00	3.74	869.02	75.53	656.34	658.21	42.77	657.73	75.69	42.90	659.59	75.90
18.65	146.52	0.00	6.46	874.66	80.85	707.17	708.43	79.55	711.63	81.36	79.69	712.89	81.50
18.09	154.00	0.00	-0.14	704.43	72.11	507.95	508.66	-1.28	507.95	72.11	-1.28	508.66	72.21
19.71	140.36	0.00	3.67	1,109.11	69.48	770.65	773.01	49.35	772.23	69.63	49.50	774.58	69.84
16.01	142.44	0.00	-3.87	701.83	73.11	513.13	514.74	-34.63	514.30	73.28	-34.74	515.90	73.51
23.52	144.42	0.00	-5.76	754.74	73.73	556.46	558.04	-55.89	559.26	74.10	-56.05	560.83	74.31
18.90	158.74	0.00	1.15	1,042.95	79.16	825.59	827.80	16.55	825.76	79.18	16.59	827.97	79.39
23.50	161.34	0.00	5.27	1,019.37	82.96	845.71	847.51	77.69	849.27	83.31	77.85	851.06	83.49
15.91	140.19	0.00	5.05	1,062.09	72.22	767.05	768.64	67.51	770.02	72.50	67.65	771.60	72.65
21.84	139.39	0.00	-2.11	751.58	73.19	550.11	551.16	-20.21	550.48	73.24	-20.25	551.53	73.38
15.33	152.91	0.00	-0.59	1,172.84	73.21	858.61	861.40	-8.82	858.66	73.21	-8.85	861.45	73.45
17.71	164.93	0.00	3.36	922.56	85.03	784.43	786.78	45.97	785.77	85.17	46.11	788.12	85.43
24.58	135.52	0.00	0.20	745.94	72.95	544.13	545.63	1.91	544.14	72.95	1.92	545.64	73.15
22.98	141.80	0.00	-5.54	1,185.11	73.03	865.44	868.05	-83.59	869.46	73.37	-83.84	872.06	73.59
17.47	145.13	0.00	0.76	992.74	76.35	758.00	760.69	10.00	758.06	76.36	10.03	760.75	76.63
17.88	157.08	0.00	-5.92	713.96	74.24	530.07	531.28	-54.71	532.88	74.64	-54.83	534.09	74.81
21.84	147.99	0.00	-6.92	765.52	74.72	571.99	572.75	-68.92	576.13	75.26	-69.01	576.88	75.36
21.27	138.67	0.00	-4.00	783.21	73.21	573.41	574.69	-39.98	574.81	73.39	-40.07	576.08	73.55
24.60	137.05	0.00	0.75	1,165.39	72.30	842.58	844.57	11.08	842.66	72.31	11.10	844.64	72.48
23.84	146.59	0.00	2.99	1,130.97	71.86	812.75	815.40	42.36	813.85	71.96	42.50	816.50	72.19
20.23	164.52	0.00	-3.16	897.72	75.12	674.32	676.49	-37.22	675.35	75.23	-37.34	677.52	75.47
24.67	148.01	0.00	6.16	980.07	72.59	711.47	713.11	76.38	715.55	73.01	76.56	717.19	73.18
22.87	151.33	0.00	3.26	1,068.56	74.45	795.54	796.91	45.27	796.82	74.57	45.34	798.19	74.70
16.94	157.49	0.00	0.34	755.12	71.78	542.05	543.95	3.24	542.06	71.78	3.25	543.96	72.04
22.40	164.54	0.00	-6.55	1,029.14	78.31	805.94	808.27	-92.00	811.18	78.82	-92.26	813.49	79.05
19.42	162.72	0.00	0.94	789.73	70.54	557.06	559.18	9.14	557.14	70.55	9.17	559.25	70.82
20.87	163.15	0.00	0.09	739.98	69.01	510.67	512.63	0.85	510.68	69.01	0.85	512.63	69.28
24.93	140.39	0.00	-1.82	1,143.40	72.59	829.96	832.44	-26.32	830.38	72.62	-26.40	832.85	72.84
22.70	147.72	0.00	1.16	826.98	73.55	608.21	609.54	12.27	608.34	73.56	12.30	609.66	73.72
23.96	150.28	0.00	-0.45	749.34	71.61	536.57	537.34	-4.18	536.58	71.61	-4.19	537.36	71.71
24.57	151.36	0.00	0.57	1,013.62	73.44	744.44	746.25	7.35	744.48	73.45	7.37	746.29	73.63

Table C.1 Friction numbers by speed, radius and camber angle (Contd.)

Speed (mph)	Curve Radius (ft)	Camber Angle (degree)	Slip Angle (degree)	Vertical Force (lbs)	Longitudinal FN	Ideal Longitudinal Force (lbs)	FEA Longitudinal Force (lbs)	Ideal Lateral Force (lbs)	Ideal Friction Force (lbs)	True FN (%)	FEA Lateral Force (lbs)	FEA Friction Force (lbs)	FEA True FN
20.84	157.74	0.00	3.65	883.75	79.68	704.12	705.30	44.86	705.55	79.84	44.94	706.72	79.97
21.80	163.58	0.00	3.87	1,111.34	78.98	877.76	880.20	59.20	879.75	79.16	59.36	882.19	79.38
22.59	148.55	0.00	0.43	957.88	74.26	711.32	713.04	5.29	711.34	74.26	5.30	713.06	74.44
20.84	142.75	0.00	-5.49	796.98	73.48	585.62	587.27	-56.00	588.30	73.82	-56.16	589.94	74.02
18.44	162.72	0.00	2.09	1,081.45	79.20	856.55	857.86	31.29	857.12	79.26	31.34	858.43	79.38
21.68	151.77	0.00	-2.93	1,160.94	73.24	850.25	852.11	-43.40	851.36	73.33	-43.49	853.21	73.49
24.96	156.68	0.00	0.40	1,059.01	74.31	786.98	789.99	5.55	787.00	74.31	5.57	790.01	74.60
20.75	149.36	0.00	0.25	1,182.00	72.87	861.31	863.93	3.80	861.32	72.87	3.81	863.93	73.09
23.03	156.65	0.00	-6.92	779.85	79.75	621.93	623.81	-74.90	626.42	80.33	-75.12	628.29	80.57
15.37	142.17	0.00	-0.67	724.68	73.64	533.64	535.26	-6.22	533.68	73.64	-6.23	535.30	73.87
19.75	141.89	0.00	-3.36	773.87	73.37	567.77	569.27	-33.29	568.75	73.49	-33.38	570.25	73.69
18.12	136.35	0.00	3.24	1,019.10	71.09	724.47	726.59	40.93	725.63	71.20	41.05	727.74	71.41
24.47	142.82	0.00	1.42	864.04	72.62	627.44	628.39	15.57	627.64	72.64	15.60	628.59	72.75
19.18	158.09	0.00	3.25	731.62	72.43	529.89	531.00	30.07	530.74	72.54	30.13	531.85	72.69
23.95	145.19	0.00	1.04	1,098.73	71.53	785.88	787.32	14.31	786.01	71.54	14.33	787.45	71.67
16.79	135.17	0.00	-5.18	743.82	73.10	543.75	545.01	-49.07	545.96	73.40	-49.18	547.22	73.57
24.55	156.83	0.00	0.25	798.96	68.33	545.90	547.36	2.38	545.91	68.33	2.38	547.36	68.51
19.88	156.67	0.00	-3.67	813.37	73.58	598.45	600.26	-38.27	599.67	73.73	-38.38	601.48	73.95
15.18	149.55	0.00	-2.49	1,143.08	73.58	841.09	843.22	-36.47	841.88	73.65	-36.57	844.01	73.84
17.43	144.03	0.00	3.10	835.24	78.07	652.07	653.82	35.28	653.03	78.18	35.37	654.77	78.39
17.36	140.87	0.00	-4.94	972.26	73.79	717.40	719.34	-61.72	720.05	74.06	-61.89	721.98	74.26
21.01	140.59	0.00	4.62	841.03	75.07	631.33	632.64	50.89	633.37	75.31	51.00	634.68	75.46
16.05	154.16	0.00	-0.43	841.03	74.84	629.45	630.34	-4.74	629.47	74.85	-4.75	630.36	74.95
17.77	154.63	0.00	3.56	753.85	74.55	562.00	563.71	34.85	563.08	74.69	34.96	564.79	74.92
21.22	160.56	0.00	-3.05	945.42	75.81	716.70	718.02	-38.11	717.71	75.92	-38.18	719.03	76.05
17.64	151.11	0.00	3.31	953.80	82.14	783.40	785.78	45.25	784.71	82.27	45.39	787.08	82.52
18.54	135.14	0.00	-5.70	1,079.46	72.94	787.38	789.04	-78.17	791.25	73.30	-78.34	792.90	73.45
17.11	157.52	0.00	-0.34	1,149.97	73.85	849.23	852.40	-5.09	849.25	73.85	-5.11	852.41	74.13
17.00	157.04	0.00	-6.38	867.47	79.10	686.18	688.43	-76.20	690.40	79.59	-76.46	692.64	79.85
19.77	154.26	0.00	0.19	881.00	75.33	663.64	665.00	2.23	663.65	75.33	2.24	665.00	75.48
22.88	159.21	0.00	0.22	845.35	69.96	591.38	593.69	2.30	591.38	69.96	2.31	593.69	70.23
15.66	135.07	0.00	1.34	872.94	75.01	654.81	657.05	15.29	654.99	75.03	15.34	657.23	75.29
15.52	163.99	0.00	5.94	799.46	78.14	624.73	626.45	64.61	628.06	78.56	64.79	629.78	78.77
18.87	142.39	0.00	0.72	1,024.73	73.50	753.18	755.40	9.50	753.24	73.51	9.53	755.46	73.72
22.07	149.99	0.00	-3.33	765.55	73.37	561.65	563.47	-32.63	562.59	73.49	-32.73	564.41	73.73
15.88	162.29	0.00	-2.91	811.83	72.22	586.33	587.71	-29.80	587.09	72.32	-29.87	588.46	72.49
20.26	138.29	0.00	-2.23	932.79	73.29	683.66	685.77	-26.56	684.17	73.35	-26.64	686.28	73.57
17.77	143.07	0.00	-1.13	868.63	75.15	652.78	653.85	-12.82	652.91	75.17	-12.85	653.97	75.29
15.18	151.43	0.00	-3.91	759.30	72.93	553.77	554.89	-37.81	555.06	73.10	-37.88	556.18	73.25
24.41	135.45	0.00	-2.23	989.57	71.61	708.66	711.10	-27.52	709.19	71.67	-27.62	711.64	71.91
19.86	164.90	0.00	2.88	1,176.96	75.07	883.49	886.47	44.33	884.60	75.16	44.48	887.58	75.41
18.01	141.92	0.00	-2.23	721.63	73.29	528.86	530.07	-20.58	529.26	73.34	-20.63	530.47	73.51
19.15	139.93	0.00	5.44	772.72	75.37	582.42	583.97	55.26	585.04	75.71	55.41	586.57	75.91

Table C.1 Friction numbers by speed, radius and camber angle (Contd.)

Speed (mph)	Curve Radius (ft)	Camber Angle (degree)	Slip Angle (degree)	Vertical Force (lbs)	Longitudinal FN	Ideal Longitudinal Force (lbs)	FEA Longitudinal Force (lbs)	Ideal Lateral Force (lbs)	Ideal Friction Force (lbs)	True FN (%)	FEA Lateral Force (lbs)	FEA Friction Force (lbs)	FEA True FN
16.94	152.37	0.00	2.52	1,021.73	79.84	815.73	817.12	35.81	816.52	79.92	35.87	817.90	80.05
21.13	156.50	0.00	6.50	1,087.52	79.19	861.19	863.90	97.46	866.68	79.69	97.77	869.38	79.94
23.25	156.64	0.00	6.49	1,188.26	76.44	908.36	911.45	102.72	914.15	76.93	103.07	917.22	77.19
24.17	139.79	0.00	-7.00	1,126.15	73.00	822.14	824.30	-100.17	828.22	73.54	-100.43	830.37	73.73
24.63	145.67	0.00	-0.58	1,083.67	72.10	781.37	784.20	-7.84	781.41	72.11	-7.87	784.24	72.37
24.20	153.18	0.00	2.26	1,071.64	74.53	798.69	800.10	31.51	799.31	74.59	31.56	800.72	74.72
21.27	161.68	0.00	-2.44	784.60	71.30	559.42	560.50	-23.77	559.92	71.36	-23.82	561.01	71.50
20.14	155.66	0.00	-4.42	1,097.82	74.81	821.31	823.65	-63.36	823.75	75.04	-63.54	826.08	75.25
22.48	161.10	0.00	3.95	868.73	77.02	669.09	670.61	46.14	670.68	77.20	46.24	672.20	77.38
15.53	145.97	0.00	4.46	780.35	77.50	604.79	606.09	47.04	606.61	77.74	47.14	607.91	77.90
23.41	149.70	0.00	2.39	1,195.53	73.69	881.02	884.19	36.77	881.79	73.76	36.90	884.96	74.02
16.04	160.17	0.00	2.82	924.36	84.19	778.21	780.45	38.31	779.15	84.29	38.42	781.39	84.53
18.29	136.00	0.00	6.75	881.71	75.05	661.69	662.65	77.74	666.24	75.56	77.85	667.19	75.67
16.72	136.72	0.00	3.53	1,020.37	72.36	738.39	739.74	45.45	739.79	72.50	45.53	741.13	72.63
15.38	139.16	0.00	2.87	1,181.35	71.52	844.88	847.19	42.35	845.94	71.61	42.47	848.25	71.80
19.90	159.13	0.00	5.78	809.47	77.75	629.38	630.55	63.38	632.57	78.15	63.49	633.73	78.29
19.32	140.37	0.00	0.01	1,191.77	72.24	860.92	863.85	0.11	860.92	72.24	0.11	863.85	72.48
16.41	162.80	0.00	4.35	829.69	79.31	658.02	659.80	49.87	659.90	79.54	50.01	661.68	79.75
16.71	156.56	0.00	4.23	786.05	76.64	602.43	603.82	44.41	604.06	76.85	44.51	605.45	77.02
20.68	162.20	0.00	5.53	783.77	75.01	587.94	589.52	56.63	590.66	75.36	56.78	592.23	75.56
17.35	156.64	0.00	0.13	891.85	76.97	686.48	688.86	1.59	686.48	76.97	1.59	688.86	77.24
18.23	159.60	0.00	-6.58	1,125.40	76.05	855.86	857.34	-98.15	861.47	76.55	-98.32	862.94	76.68
22.57	143.75	0.00	-6.30	1,049.87	73.30	769.52	771.99	-84.38	774.14	73.74	-84.65	776.59	73.97
24.44	164.75	0.00	-1.24	778.34	67.34	524.11	525.95	-11.33	524.23	67.35	-11.37	526.08	67.59
18.60	147.05	0.00	-5.99	883.85	74.61	659.47	661.23	-68.81	663.05	75.02	-68.99	664.80	75.22
20.00	163.99	0.00	-1.80	1,109.08	74.77	829.24	830.85	-25.99	829.64	74.80	-26.04	831.26	74.95
24.38	160.56	0.00	-0.96	815.98	67.77	553.02	554.66	-9.24	553.10	67.78	-9.26	554.74	67.98
23.87	157.42	0.00	-5.18	701.04	76.76	538.11	539.55	-48.54	540.30	77.07	-48.67	541.72	77.27
24.36	164.77	0.00	-6.36	942.18	79.48	748.83	750.78	-82.91	753.41	79.96	-83.13	755.35	80.17
17.35	146.31	0.00	-3.14	797.28	73.61	586.88	587.92	-32.12	587.76	73.72	-32.18	588.80	73.85
24.29	145.48	0.00	-0.21	825.11	72.72	600.05	601.16	-2.17	600.05	72.72	-2.17	601.16	72.86
21.52	163.17	0.00	-4.95	946.23	78.61	743.85	746.05	-64.25	746.62	78.90	-64.44	748.81	79.14
15.37	164.99	0.00	0.44	1,169.40	73.81	863.16	866.40	6.64	863.18	73.81	6.67	866.43	74.09
18.11	147.24	0.00	-1.15	858.48	75.10	644.75	645.84	-12.92	644.88	75.12	-12.94	645.97	75.25
23.20	159.63	0.00	5.42	734.15	71.82	527.27	528.63	49.78	529.61	72.14	49.91	530.97	72.32
18.61	161.05	0.00	-1.91	786.47	70.70	556.04	558.00	-18.55	556.35	70.74	-18.61	558.31	70.99
21.22	138.97	0.00	0.89	1,074.23	70.30	755.17	758.11	11.77	755.27	70.31	11.82	758.21	70.58
21.41	148.23	0.00	2.22	841.52	75.31	633.78	636.07	24.53	634.26	75.37	24.62	636.54	75.64
22.58	150.78	0.00	6.37	1,001.62	76.84	769.67	771.14	85.34	774.38	77.31	85.50	775.85	77.46
16.69	149.01	0.00	-0.07	706.44	73.13	516.63	517.98	-0.67	516.63	73.13	-0.68	517.98	73.32
22.55	147.42	0.00	-0.13	910.10	73.94	672.97	674.76	-1.52	672.97	73.94	-1.52	674.76	74.14
21.26	149.91	0.00	3.70	1,192.29	73.04	870.89	872.84	56.15	872.70	73.19	56.28	874.65	73.36
24.60	154.71	0.00	-2.16	937.12	72.78	682.01	684.33	-25.72	682.49	72.83	-25.81	684.81	73.08

Table C.1 Friction numbers by speed, radius and camber angle (Contd.)

Speed (mph)	Curve Radius (ft)	Camber Angle (degree)	Slip Angle (degree)	Vertical Force (lbs)	Longitudinal FN	Ideal Longitudinal Force (lbs)	FEA Longitudinal Force (lbs)	Ideal Lateral Force (lbs)	Ideal Friction Force (lbs)	True FN (%)	FEA Lateral Force (lbs)	FEA Friction Force (lbs)	FEA True FN
17.68	159.26	0.00	1.65	871.56	77.88	678.80	681.07	19.51	679.08	77.92	19.57	681.35	78.18
23.58	147.16	0.00	6.08	905.24	74.89	677.92	679.43	71.77	681.71	75.31	71.92	683.21	75.47
18.65	151.29	0.00	-2.30	881.93	74.71	658.92	661.12	-26.40	659.45	74.77	-26.49	661.64	75.02
24.33	143.70	0.00	2.63	813.13	73.13	594.62	595.64	27.26	595.25	73.20	27.31	596.27	73.33
19.44	140.14	0.00	0.97	1,097.17	71.19	781.06	784.00	13.26	781.18	71.20	13.31	784.12	71.47
21.67	148.76	0.00	1.47	1,078.64	73.21	789.69	792.02	20.26	789.95	73.24	20.32	792.28	73.45
15.65	145.89	0.00	2.83	880.18	80.24	706.29	708.64	34.86	707.15	80.34	34.97	709.50	80.61
20.14	163.27	0.00	-5.78	767.06	77.64	595.52	596.54	-60.02	598.53	78.03	-60.13	599.56	78.16
22.35	136.86	0.00	-2.21	1,030.95	71.83	740.53	743.04	-28.54	741.08	71.88	-28.64	743.58	72.13
22.64	164.51	0.00	-6.11	1,104.93	75.31	832.12	834.70	-88.54	836.81	75.73	-88.81	839.39	75.97
21.27	138.46	0.00	-5.24	968.42	73.10	707.93	710.01	-64.60	710.87	73.41	-64.79	712.95	73.62
21.64	153.81	0.00	6.66	1,026.20	79.85	819.46	821.77	95.09	824.96	80.39	95.35	827.25	80.61
15.53	164.24	0.00	-6.61	1,162.59	75.49	877.63	879.77	-101.07	883.43	75.99	-101.31	885.55	76.17
15.75	163.46	0.00	0.37	1,039.37	80.04	831.96	833.99	5.32	831.98	80.05	5.33	834.01	80.24
19.45	152.30	0.00	-4.09	1,190.79	73.24	872.19	874.31	-62.16	874.40	73.43	-62.31	876.52	73.61
20.65	145.29	0.00	-4.00	984.43	73.92	727.66	729.32	-50.79	729.44	74.10	-50.90	731.09	74.27
20.63	156.98	0.00	5.83	976.87	85.40	834.29	836.11	84.75	838.58	85.84	84.94	840.39	86.03
19.74	135.05	0.00	-3.61	1,077.28	72.57	781.73	783.93	-49.27	783.28	72.71	-49.41	785.48	72.91
21.70	138.43	0.00	2.16	958.69	70.90	679.73	682.07	25.60	680.22	70.95	25.69	682.55	71.20
15.25	159.43	0.00	5.63	914.15	87.28	797.84	799.98	78.32	801.67	87.70	78.53	803.80	87.93
18.25	154.16	0.00	-1.04	1,072.38	75.47	809.35	810.93	-14.67	809.49	75.48	-14.70	811.06	75.63
24.02	163.25	0.00	-3.79	1,115.67	73.99	825.48	828.10	-54.58	827.28	74.15	-54.75	829.90	74.39
20.58	151.52	0.00	4.18	915.83	80.33	735.65	737.36	53.58	737.60	80.54	53.70	739.30	80.72
20.78	157.73	0.00	4.11	1,092.01	78.59	858.21	859.91	61.54	860.41	78.79	61.66	862.11	78.95
24.36	144.61	0.00	0.50	939.37	72.26	678.82	679.92	5.90	678.85	72.27	5.91	679.94	72.38
17.86	135.34	0.00	5.66	1,089.68	68.79	749.54	751.09	73.90	753.17	69.12	74.06	754.72	69.26
24.52	142.91	0.00	-5.92	1,083.42	73.03	791.17	793.41	-81.62	795.37	73.41	-81.86	797.60	73.62
22.86	158.87	0.00	6.21	737.38	72.80	536.84	538.35	58.08	539.97	73.23	58.24	541.47	73.43
17.35	139.20	0.00	-6.22	784.57	73.22	574.46	576.15	-62.29	577.82	73.65	-62.47	579.51	73.86
16.32	144.79	0.00	-2.31	1,055.01	74.23	783.16	785.51	-31.53	783.79	74.29	-31.62	786.14	74.51
23.79	151.72	0.00	5.12	1,016.36	75.86	771.02	772.65	68.75	774.07	76.16	68.89	775.71	76.32
23.52	161.92	0.00	5.00	1,092.10	80.34	877.44	879.40	76.46	880.77	80.65	76.64	882.72	80.83
22.05	148.35	0.00	-4.21	1,044.14	73.75	770.09	772.45	-56.50	772.16	73.95	-56.67	774.52	74.18
22.20	137.33	0.00	1.08	1,082.73	69.59	753.46	754.53	14.26	753.60	69.60	14.28	754.66	69.70
16.21	N/A	4.09	-1.18	987.35	57.27	564.06	560.42	-11.62	564.17	57.14	-11.54	560.54	56.77
28.21	N/A	4.67	2.85	1,018.61	46.33	470.41	465.32	23.38	470.99	46.24	23.13	465.91	45.74
22.18	N/A	4.36	-0.71	981.24	59.22	579.36	575.50	-7.21	579.41	59.05	-7.16	575.54	58.65
15.90	N/A	4.77	-1.28	1,005.11	63.99	640.99	636.08	-14.37	641.15	63.79	-14.26	636.24	63.30
29.45	N/A	4.76	-2.47	990.86	59.81	590.57	585.69	-25.46	591.11	59.66	-25.25	586.24	59.16
24.53	N/A	4.55	-2.61	967.55	63.03	607.90	604.78	-27.67	608.53	62.89	-27.53	605.42	62.57
23.83	N/A	4.99	0.69	983.44	57.29	561.26	555.86	6.80	561.31	57.08	6.74	555.90	56.53
23.37	N/A	4.48	-1.15	979.10	60.94	594.89	591.04	-11.98	595.01	60.77	-11.91	591.16	60.38
19.96	N/A	4.97	-1.88	1,014.29	60.99	616.27	611.08	-20.18	616.60	60.79	-20.01	611.41	60.28

Table C.1 Friction numbers by speed, radius and camber angle (Contd.)

Speed (mph)	Curve Radius (ft)	Camber Angle (degree)	Slip Angle (degree)	Vertical Force (lbs)	Longitudinal FN	Ideal Longitudinal Force (lbs)	FEA Longitudinal Force (lbs)	Ideal Lateral Force (lbs)	Ideal Friction Force (lbs)	True FN (%)	FEA Lateral Force (lbs)	FEA Friction Force (lbs)	FEA True FN
17.26	N/A	4.05	1.51	952.08	55.60	528.06	526.38	13.87	528.24	55.48	13.83	526.56	55.31
21.15	N/A	4.95	2.23	1,017.60	51.71	524.27	518.23	20.40	524.66	51.56	20.16	518.63	50.97
18.08	N/A	5.00	-2.14	1,002.73	63.03	629.60	624.89	-23.51	630.03	62.83	-23.34	625.33	62.36
15.06	N/A	4.94	0.41	965.67	60.69	583.86	580.56	4.18	583.88	60.46	4.15	580.57	60.12
27.87	N/A	4.53	-0.83	972.77	59.67	578.61	574.40	-8.41	578.67	59.49	-8.35	574.46	59.05
15.62	N/A	4.29	-2.58	982.76	60.28	590.78	586.97	-26.60	591.38	60.18	-26.42	587.57	59.79
24.27	N/A	4.82	0.70	964.39	59.34	570.24	565.48	6.94	570.28	59.13	6.88	565.53	58.64
20.98	N/A	4.52	-1.32	978.92	62.44	609.32	606.68	-14.09	609.48	62.26	-14.03	606.85	61.99
26.05	N/A	4.45	1.57	958.14	56.97	544.24	540.08	14.93	544.45	56.82	14.82	540.29	56.39
15.91	N/A	5.00	2.12	988.18	57.23	563.38	558.97	20.81	563.77	57.05	20.64	559.35	56.60
15.71	N/A	4.65	0.46	961.91	60.51	580.17	576.63	4.64	580.18	60.32	4.61	576.64	59.95
29.27	N/A	4.85	0.19	974.33	57.17	555.00	550.79	1.81	555.00	56.96	1.80	550.79	56.53
25.76	N/A	4.54	-1.15	1,002.02	57.35	572.83	568.36	-11.50	572.95	57.18	-11.41	568.48	56.73
18.57	N/A	4.83	-2.30	989.76	66.21	653.00	649.92	-26.18	653.53	66.03	-26.06	650.45	65.72
20.07	N/A	4.27	-2.46	1,005.13	58.32	584.56	581.20	-25.05	585.09	58.21	-24.91	581.74	57.88
24.80	N/A	4.41	1.82	984.97	55.16	541.70	537.48	17.21	541.97	55.02	17.07	537.76	54.60
23.35	N/A	4.15	2.21	972.68	55.85	541.78	539.06	20.88	542.19	55.74	20.77	539.46	55.46
21.81	N/A	4.66	-2.18	997.27	63.81	634.23	630.16	-24.09	634.69	63.64	-23.94	630.62	63.24
18.37	N/A	4.51	-1.37	974.49	62.76	609.73	606.47	-14.53	609.90	62.59	-14.45	606.65	62.25
22.55	N/A	4.02	1.58	1,016.75	55.55	563.43	559.82	15.50	563.64	55.44	15.40	560.04	55.08
26.13	N/A	4.85	-0.27	1,003.43	55.32	553.08	547.17	-2.58	553.08	55.12	-2.55	547.18	54.53
16.97	N/A	4.95	2.26	962.08	58.38	559.52	554.30	22.11	559.95	58.20	21.90	554.74	57.66
19.99	N/A	4.54	2.89	1,018.93	51.31	521.15	516.18	26.29	521.81	51.21	26.04	516.85	50.72
21.14	N/A	4.21	1.76	986.63	55.97	550.69	547.88	16.94	550.96	55.84	16.85	548.14	55.56
20.13	N/A	4.12	-1.03	980.58	57.44	561.76	558.05	-10.11	561.85	57.30	-10.05	558.15	56.92
23.78	N/A	4.52	-1.25	995.14	59.75	592.71	588.53	-12.90	592.85	59.57	-12.81	588.67	59.15
20.23	N/A	4.18	-1.84	991.24	58.05	573.86	570.87	-18.41	574.15	57.92	-18.32	571.17	57.62
29.96	N/A	4.76	-2.55	980.93	60.52	591.63	587.92	-26.30	592.21	60.37	-26.13	588.51	60.00
21.63	N/A	4.79	-2.40	1,019.51	61.29	622.65	618.04	-26.10	623.20	61.13	-25.91	618.60	60.68
26.96	N/A	4.28	0.74	1,008.46	53.88	541.86	539.04	7.03	541.91	53.74	6.99	539.09	53.46
24.43	N/A	4.01	-1.30	985.62	56.80	558.43	555.79	-12.67	558.57	56.67	-12.61	555.93	56.40
20.59	N/A	4.68	2.02	971.35	57.65	558.13	553.45	19.72	558.48	57.50	19.55	553.80	57.01
25.36	N/A	4.91	1.95	993.75	52.73	522.09	518.06	17.74	522.39	52.57	17.60	518.36	52.16
26.61	N/A	4.19	1.27	973.35	56.35	547.04	543.46	12.15	547.17	56.22	12.07	543.60	55.85
28.47	N/A	4.15	0.19	992.33	55.94	553.65	550.54	1.88	553.66	55.79	1.87	550.55	55.48
24.44	N/A	4.16	0.12	996.41	56.13	557.81	554.33	1.13	557.81	55.98	1.12	554.33	55.63
16.02	N/A	4.71	1.20	950.20	58.89	557.70	553.45	11.71	557.83	58.71	11.62	553.58	58.26
23.05	N/A	4.61	2.76	1,009.18	50.03	503.23	497.75	24.27	503.81	49.92	24.00	498.34	49.38
22.04	N/A	4.74	2.25	958.76	57.93	553.54	549.03	21.69	553.96	57.78	21.51	549.45	57.31
19.59	N/A	4.17	1.37	962.00	56.03	537.61	535.32	12.86	537.76	55.90	12.81	535.47	55.66
18.96	N/A	4.56	-0.32	988.18	61.18	602.62	600.32	-3.39	602.63	60.98	-3.37	600.33	60.75
25.64	N/A	4.40	2.10	984.99	54.70	537.17	533.47	19.70	537.53	54.57	19.56	533.84	54.20
23.86	N/A	4.56	2.77	990.57	52.79	521.27	516.78	25.19	521.88	52.68	24.97	517.39	52.23

Table C.1 Friction numbers by speed, radius and camber angle (Contd.)

Speed (mph)	Curve Radius (ft)	Camber Angle (degree)	Slip Angle (degree)	Vertical Force (lbs)	Longitudinal FN	Ideal Longitudinal Force (lbs)	FEA Longitudinal Force (lbs)	Ideal Lateral Force (lbs)	Ideal Friction Force (lbs)	True FN (%)	FEA Lateral Force (lbs)	FEA Friction Force (lbs)	FEA True FN
23.28	N/A	4.06	0.08	1,012.72	55.58	561.42	558.42	0.76	561.42	55.44	0.76	558.42	55.14
20.24	N/A	4.23	-1.89	971.50	58.98	571.38	568.49	-18.83	571.69	58.85	-18.73	568.81	58.55
25.91	N/A	4.79	1.11	992.84	53.81	532.39	526.84	10.33	532.49	53.63	10.22	526.95	53.07
20.66	N/A	4.87	-0.32	1,015.41	57.31	579.82	574.99	-3.20	579.83	57.10	-3.18	575.00	56.63
24.10	N/A	4.33	-2.93	1,014.08	57.00	576.35	572.77	-29.49	577.11	56.91	-29.31	573.53	56.56
16.49	N/A	5.00	2.14	988.27	57.04	561.59	555.60	20.99	561.98	56.86	20.77	556.00	56.26
17.22	N/A	4.40	-1.20	972.53	60.77	589.26	586.47	-12.32	589.38	60.60	-12.26	586.60	60.32
19.38	N/A	4.41	-1.01	958.10	59.67	569.96	566.64	-10.06	570.05	59.50	-10.00	566.73	59.15
17.95	N/A	4.94	1.37	962.78	59.31	568.90	564.12	13.59	569.06	59.11	13.48	564.28	58.61
26.92	N/A	4.25	1.54	954.72	56.34	536.39	533.30	14.39	536.59	56.20	14.30	533.49	55.88
20.16	N/A	4.50	1.34	1,011.26	54.11	545.51	540.73	12.73	545.65	53.96	12.62	540.88	53.49
20.86	N/A	4.99	0.16	959.10	59.78	571.16	566.87	1.59	571.16	59.55	1.58	566.87	59.10
26.46	N/A	4.34	0.39	987.81	56.30	554.57	550.77	3.80	554.58	56.14	3.77	550.78	55.76
21.82	N/A	4.99	2.80	965.84	57.03	548.73	543.69	26.78	549.39	56.88	26.54	544.35	56.36
29.66	N/A	4.14	0.65	996.06	55.44	550.81	547.22	6.22	550.85	55.30	6.18	547.25	54.94
19.43	N/A	4.79	1.50	960.88	59.31	567.93	564.50	14.83	568.12	59.13	14.74	564.70	58.77
23.10	N/A	4.06	0.03	1,000.43	56.09	559.76	557.34	0.31	559.76	55.95	0.31	557.34	55.71
28.75	N/A	4.75	2.35	985.83	51.66	507.49	502.50	20.84	507.92	51.52	20.63	502.93	51.02
15.22	N/A	4.31	1.93	997.15	56.31	559.86	556.68	18.84	560.17	56.18	18.73	556.99	55.86
28.23	N/A	4.55	-2.48	967.99	61.76	595.91	593.14	-25.79	596.47	61.62	-25.67	593.70	61.33
28.45	N/A	4.88	2.48	964.85	56.00	538.35	532.93	23.30	538.85	55.85	23.07	533.44	55.29
28.98	N/A	4.79	1.21	984.36	53.75	527.29	523.54	11.14	527.40	53.58	11.06	523.65	53.20
15.75	N/A	4.94	-0.05	995.92	60.94	604.68	599.85	-0.50	604.68	60.72	-0.50	599.85	60.23
27.96	N/A	4.33	-1.33	1,019.21	53.75	546.22	541.76	-12.68	546.37	53.61	-12.57	541.90	53.17
29.77	N/A	4.98	-1.55	1,002.08	56.32	562.26	556.69	-15.25	562.47	56.13	-15.10	556.90	55.57
19.39	N/A	4.21	-0.88	1,016.98	56.13	569.28	565.90	-8.71	569.34	55.98	-8.66	565.97	55.65
17.42	N/A	4.79	-2.28	1,004.83	65.74	658.30	653.92	-26.24	658.82	65.57	-26.07	654.44	65.13
22.11	N/A	4.50	-2.11	964.54	62.44	600.39	597.03	-22.11	600.80	62.29	-21.99	597.44	61.94
22.56	N/A	4.33	-2.36	956.07	59.85	570.59	567.69	-23.47	571.07	59.73	-23.35	568.17	59.43
19.28	N/A	4.65	-1.00	954.42	61.57	585.71	582.35	-10.26	585.80	61.38	-10.20	582.44	61.03
15.36	N/A	4.86	1.30	987.58	59.31	583.66	580.58	13.29	583.82	59.12	13.22	580.73	58.80
20.20	N/A	4.74	0.33	994.86	59.04	585.33	580.35	3.39	585.34	58.84	3.36	580.36	58.34
20.23	N/A	4.42	2.85	988.44	54.80	540.04	535.92	26.86	540.70	54.70	26.66	536.59	54.29
27.13	N/A	4.05	-1.23	953.00	57.11	542.86	540.21	-11.65	542.98	56.98	-11.59	540.33	56.70
23.91	N/A	4.19	-1.98	974.11	58.58	569.08	565.76	-19.68	569.42	58.46	-19.56	566.11	58.12
23.55	N/A	4.95	2.92	990.75	52.99	523.05	518.25	26.66	523.72	52.86	26.42	518.94	52.38
17.53	N/A	4.05	-1.51	1,001.91	56.74	567.05	563.52	-14.90	567.24	56.62	-14.80	563.72	56.26
17.97	N/A	4.67	2.18	989.45	56.34	555.60	551.41	21.10	556.00	56.19	20.95	551.82	55.77
25.88	N/A	4.47	-0.44	978.16	59.02	575.57	571.60	-4.40	575.59	58.84	-4.37	571.62	58.44
16.96	N/A	4.19	-1.05	980.95	58.09	568.28	566.19	-10.37	568.37	57.94	-10.34	566.28	57.73
24.21	N/A	4.15	-2.40	1,008.31	56.30	566.22	562.97	-23.66	566.71	56.20	-23.53	563.47	55.88
27.11	N/A	4.80	2.68	972.21	54.84	531.29	527.09	24.82	531.87	54.71	24.62	527.68	54.28
18.19	N/A	4.82	-1.62	990.71	65.23	643.98	639.84	-18.26	644.24	65.03	-18.14	640.10	64.61

Table C.1 Friction numbers by speed, radius and camber angle (Contd.)

Speed (mph)	Curve Radius (ft)	Camber Angle (degree)	Slip Angle (degree)	Vertical Force (lbs)	Longitudinal FN	Ideal Longitudinal Force (lbs)	FEA Longitudinal Force (lbs)	Ideal Lateral Force (lbs)	Ideal Friction Force (lbs)	True FN (%)	FEA Lateral Force (lbs)	FEA Friction Force (lbs)	FEA True FN
28.11	N/A	4.58	1.11	1,017.82	49.10	498.15	492.44	9.64	498.24	48.95	9.53	492.53	48.39
24.48	N/A	4.56	-1.40	999.75	59.20	589.99	586.47	-14.45	590.16	59.03	-14.37	586.65	58.68
19.00	N/A	4.40	0.23	980.02	58.88	575.32	573.17	2.26	575.32	58.70	2.25	573.17	58.49
20.54	N/A	4.29	0.01	973.49	58.02	563.26	559.83	0.08	563.26	57.86	0.08	559.83	57.51
20.25	N/A	4.92	-2.32	1,003.85	63.59	636.04	631.90	-25.74	636.56	63.41	-25.57	632.42	63.00
23.16	N/A	4.02	-2.21	970.77	57.34	555.27	552.28	-21.42	555.68	57.24	-21.30	552.70	56.93
22.96	N/A	4.95	0.27	998.88	56.74	564.67	560.16	2.62	564.67	56.53	2.60	560.17	56.08
19.39	N/A	4.22	0.06	967.17	57.31	552.78	550.33	0.56	552.78	57.15	0.55	550.33	56.90
28.00	N/A	4.53	-0.21	995.35	55.34	549.08	543.96	-2.03	549.08	55.16	-2.01	543.96	54.65
15.80	N/A	4.50	2.10	1,012.47	54.81	553.18	550.14	20.26	553.55	54.67	20.15	550.52	54.37
29.23	N/A	4.46	-2.28	969.44	60.73	586.96	583.11	-23.36	587.42	60.59	-23.20	583.57	60.20
28.06	N/A	4.12	0.11	965.66	56.98	548.78	545.36	1.04	548.79	56.83	1.04	545.36	56.48
20.14	N/A	4.08	2.64	962.73	55.56	533.55	530.54	24.61	534.12	55.48	24.47	531.11	55.17
22.86	N/A	4.01	1.14	1,012.94	55.64	562.26	559.40	11.16	562.37	55.52	11.10	559.51	55.24
27.28	N/A	4.99	-0.23	972.58	58.23	564.16	559.57	-2.30	564.17	58.01	-2.29	559.58	57.54
27.16	N/A	4.49	2.85	971.64	54.83	531.13	527.43	26.38	531.79	54.73	26.20	528.09	54.35
20.37	N/A	4.65	0.25	950.18	59.67	565.08	560.63	2.42	565.09	59.47	2.40	560.63	59.00
20.28	N/A	4.08	1.01	987.23	56.32	554.56	550.53	9.79	554.65	56.18	9.72	550.62	55.77
25.87	N/A	4.98	-0.93	951.69	59.42	563.39	558.09	-9.19	563.46	59.21	-9.11	558.16	58.65
28.05	N/A	4.35	-2.24	985.63	58.99	579.73	576.83	-22.62	580.17	58.86	-22.50	577.27	58.57
26.44	N/A	4.65	-2.91	1,010.59	59.59	600.28	596.91	-30.51	601.05	59.48	-30.34	597.69	59.14
19.12	N/A	4.18	-2.02	961.96	58.15	557.89	555.04	-19.62	558.23	58.03	-19.52	555.39	57.74
16.38	N/A	4.57	0.96	977.57	59.57	580.53	575.75	9.77	580.62	59.39	9.69	575.83	58.90
18.00	N/A	4.86	2.27	1,007.28	53.83	540.31	534.97	21.37	540.74	53.68	21.16	535.39	53.15
22.57	N/A	4.38	-0.36	995.73	57.59	571.81	568.30	-3.56	571.82	57.43	-3.54	568.31	57.07
23.26	N/A	4.72	-1.37	993.92	61.75	611.70	607.53	-14.64	611.88	61.56	-14.54	607.70	61.14
26.96	N/A	4.53	-0.12	1,017.11	52.17	528.92	525.62	-1.15	528.92	52.00	-1.14	525.63	51.68
22.93	N/A	4.32	-0.78	984.55	58.60	575.32	572.43	-7.80	575.37	58.44	-7.76	572.49	58.15
21.94	N/A	4.06	0.07	961.54	56.57	542.62	539.01	0.64	542.62	56.43	0.63	539.01	56.06
21.45	N/A	4.23	-0.50	965.22	57.82	556.54	553.28	-4.84	556.56	57.66	-4.81	553.30	57.32
18.20	N/A	4.57	0.09	1,015.97	56.91	576.39	571.17	0.91	576.39	56.73	0.90	571.17	56.22
25.07	N/A	4.43	-0.09	1,004.76	55.09	551.90	548.48	-0.83	551.90	54.93	-0.82	548.48	54.59
22.58	N/A	4.41	1.24	956.90	57.06	544.40	540.47	11.82	544.52	56.91	11.74	540.59	56.49
29.24	N/A	4.59	-1.68	1,009.21	55.14	554.67	549.72	-16.27	554.91	54.98	-16.12	549.96	54.49
22.27	N/A	4.39	0.44	997.71	56.37	560.74	556.53	4.34	560.76	56.20	4.30	556.55	55.78
25.19	N/A	4.20	2.92	1,015.26	54.11	547.84	544.06	27.95	548.55	54.03	27.76	544.78	53.66
28.29	N/A	4.26	-1.32	1,006.71	55.21	554.22	551.18	-12.81	554.37	55.07	-12.74	551.33	54.77
29.82	N/A	4.06	-2.75	981.96	57.24	560.67	558.18	-26.94	561.32	57.16	-26.82	558.83	56.91
20.49	N/A	4.16	0.50	965.83	56.67	545.89	542.08	4.81	545.92	56.52	4.78	542.10	56.13
29.03	N/A	4.35	-0.69	963.79	58.68	563.89	561.15	-6.76	563.93	58.51	-6.72	561.19	58.23
25.66	N/A	4.17	0.53	994.24	55.91	554.43	550.80	5.11	554.45	55.77	5.08	550.83	55.40
17.83	N/A	4.72	-1.98	969.91	65.19	630.13	625.79	-21.73	630.50	65.01	-21.58	626.17	64.56
23.72	N/A	4.88	0.13	977.28	59.41	578.49	573.71	1.32	578.49	59.19	1.31	573.72	58.71

Table C.1 Friction numbers by speed, radius and camber angle (Contd.)

Speed (mph)	Curve Radius (ft)	Camber Angle (degree)	Slip Angle (degree)	Vertical Force (lbs)	Longitudinal FN	Ideal Longitudinal Force (lbs)	FEA Longitudinal Force (lbs)	Ideal Lateral Force (lbs)	Ideal Friction Force (lbs)	True FN (%)	FEA Lateral Force (lbs)	FEA Friction Force (lbs)	FEA True FN
28.47	N/A	4.05	-0.66	960.84	57.06	546.86	544.55	-6.33	546.90	56.92	-6.30	544.59	56.68
16.18	N/A	4.05	-0.94	992.77	56.91	563.55	559.81	-9.28	563.63	56.77	-9.21	559.88	56.40
23.49	N/A	4.00	0.76	1,008.10	55.77	560.82	557.81	7.47	560.87	55.64	7.43	557.86	55.34
23.93	N/A	4.90	-1.06	1,009.36	58.02	583.53	578.25	-10.81	583.63	57.82	-10.71	578.36	57.30
22.09	N/A	4.08	-2.85	999.90	56.95	568.04	564.98	-28.23	568.74	56.88	-28.08	565.68	56.57
21.27	N/A	4.39	2.17	951.44	55.88	530.09	526.91	20.04	530.47	55.75	19.92	527.29	55.42
24.84	N/A	4.78	-0.20	954.29	60.33	573.75	570.22	-1.97	573.75	60.12	-1.96	570.22	59.75
16.79	N/A	4.49	1.13	963.91	58.16	558.87	554.74	11.02	558.98	57.99	10.94	554.85	57.56
18.88	N/A	4.38	2.63	954.11	55.43	527.32	523.11	24.23	527.88	55.33	24.04	523.67	54.89
19.80	N/A	4.88	-0.17	965.17	61.42	590.64	585.83	-1.79	590.64	61.20	-1.78	585.83	60.70
22.46	N/A	4.29	2.65	1,009.48	53.82	541.75	537.53	25.04	542.32	53.72	24.84	538.12	53.31
16.60	N/A	4.97	-1.55	987.32	63.60	625.55	621.95	-16.94	625.78	63.38	-16.85	622.18	63.02
22.19	N/A	4.17	2.74	992.93	55.35	548.14	544.60	26.24	548.77	55.27	26.07	545.24	54.91
29.63	N/A	4.07	1.44	955.35	56.30	536.53	533.62	13.49	536.70	56.18	13.42	533.79	55.87
16.86	N/A	4.22	-2.77	970.86	59.11	572.36	569.74	-27.65	573.03	59.02	-27.52	570.41	58.75
28.68	N/A	4.89	-1.87	960.00	60.14	575.26	571.59	-18.82	575.56	59.95	-18.70	571.90	59.57
26.76	N/A	4.16	1.70	963.32	56.17	539.71	536.36	15.97	539.95	56.05	15.87	536.60	55.70
27.11	N/A	4.17	-2.80	1,000.98	56.65	565.61	562.25	-27.68	566.28	56.57	-27.51	562.93	56.24
18.85	N/A	4.89	2.72	963.43	57.83	555.15	550.06	26.38	555.78	57.69	26.14	550.69	57.16
22.50	N/A	4.60	-1.10	963.80	62.07	596.29	592.99	-11.44	596.40	61.88	-11.38	593.10	61.54
20.57	N/A	4.26	-1.14	1,000.75	57.64	575.22	572.56	-11.44	575.33	57.49	-11.39	572.68	57.22
26.79	N/A	4.34	-0.76	1,001.91	55.73	556.75	553.88	-7.35	556.80	55.57	-7.31	553.93	55.29
20.58	N/A	4.67	-0.89	1,007.05	60.06	602.86	599.22	-9.38	602.93	59.87	-9.32	599.30	59.51
28.82	N/A	4.55	-1.03	956.53	60.07	572.77	570.08	-10.34	572.87	59.89	-10.29	570.17	59.61
29.77	N/A	4.59	0.93	965.04	57.34	551.60	547.15	8.91	551.67	57.17	8.84	547.22	56.70
18.06	N/A	4.17	-2.15	973.61	58.42	567.24	563.94	-21.29	567.64	58.30	-21.16	564.34	57.96
17.72	N/A	4.68	2.64	1,016.04	52.19	528.47	523.90	24.34	529.03	52.07	24.13	524.46	51.62
24.11	N/A	4.61	1.26	992.61	54.70	541.24	536.27	11.88	541.37	54.54	11.77	536.41	54.04
20.91	N/A	4.16	0.17	952.52	56.45	536.24	534.15	1.59	536.24	56.30	1.58	534.15	56.08
28.48	N/A	4.55	-0.49	972.38	59.05	572.33	569.29	-4.93	572.35	58.86	-4.91	569.31	58.55
27.24	N/A	4.91	0.74	993.51	54.06	535.16	531.07	6.90	535.20	53.87	6.84	531.11	53.46
27.37	N/A	4.62	1.64	969.12	56.51	545.82	542.81	15.59	546.04	56.34	15.50	543.04	56.03
20.59	N/A	4.42	-2.21	958.97	61.03	583.50	580.82	-22.51	583.93	60.89	-22.41	581.26	60.61
18.56	N/A	4.46	0.78	952.71	57.60	547.10	542.66	7.40	547.15	57.43	7.34	542.71	56.96
23.68	N/A	4.41	-1.88	990.26	60.24	594.80	590.96	-19.52	595.12	60.10	-19.39	591.29	59.71
23.45	N/A	4.45	2.92	978.04	54.78	534.20	530.37	27.26	534.90	54.69	27.06	531.07	54.30
23.12	N/A	4.98	-2.00	1,002.96	60.83	607.84	603.23	-21.23	608.21	60.64	-21.07	603.60	60.18
15.62	N/A	4.50	1.22	999.03	57.55	573.21	570.48	12.22	573.34	57.39	12.16	570.61	57.12
19.46	N/A	4.80	-1.20	967.75	63.55	612.80	608.64	-12.79	612.93	63.34	-12.70	608.78	62.91
28.33	N/A	4.34	0.26	977.35	57.09	556.32	552.46	2.55	556.33	56.92	2.53	552.47	56.53
18.67	N/A	4.84	1.03	980.01	59.59	581.91	576.87	10.49	582.00	59.39	10.40	576.96	58.87
24.79	N/A	4.06	-2.18	956.63	57.49	548.54	545.96	-20.91	548.94	57.38	-20.81	546.36	57.11
21.12	N/A	4.49	1.37	960.62	57.68	552.35	549.24	13.17	552.51	57.52	13.10	549.40	57.19

Table C.1 Friction numbers by speed, radius and camber angle (Contd.)

Speed (mph)	Curve Radius (ft)	Camber Angle (degree)	Slip Angle (degree)	Vertical Force (lbs)	Longitudinal FN	Ideal Longitudinal Force (lbs)	FEA Longitudinal Force (lbs)	Ideal Lateral Force (lbs)	Ideal Friction Force (lbs)	True FN (%)	FEA Lateral Force (lbs)	FEA Friction Force (lbs)	FEA True FN
26.35	N/A	4.65	2.96	1,010.20	47.65	479.81	473.89	24.80	480.45	47.56	24.49	474.54	46.98
15.63	N/A	4.37	2.02	972.18	56.58	548.43	546.04	19.29	548.77	56.45	19.20	546.38	56.20
20.36	N/A	4.07	-2.38	979.49	57.62	562.91	560.49	-23.36	563.40	57.52	-23.26	560.98	57.27
16.64	N/A	4.53	-2.36	1,016.93	61.67	625.20	622.32	-25.72	625.73	61.53	-25.60	622.85	61.25
20.43	N/A	4.68	-1.70	982.87	64.76	634.42	631.46	-18.81	634.70	64.58	-18.72	631.74	64.27
20.39	N/A	4.74	1.68	950.63	58.67	555.79	551.11	16.30	556.03	58.49	16.16	551.35	58.00
26.75	N/A	4.40	0.20	1,008.98	53.48	538.04	534.93	1.90	538.05	53.33	1.89	534.93	53.02
15.57	N/A	4.34	-0.26	987.32	59.08	581.59	578.44	-2.67	581.59	58.91	-2.65	578.44	58.59
25.62	N/A	4.93	1.03	952.18	58.63	556.24	551.72	10.03	556.33	58.43	9.95	551.81	57.95
16.16	N/A	4.10	-1.17	955.58	56.76	540.99	537.30	-11.03	541.11	56.63	-10.96	537.41	56.24
21.26	N/A	4.15	2.39	968.56	55.71	538.13	535.38	22.42	538.60	55.61	22.30	535.85	55.32
22.84	N/A	4.81	-1.14	959.06	61.91	591.70	587.97	-11.77	591.82	61.71	-11.70	588.09	61.32
29.92	N/A	4.99	0.16	959.78	57.84	553.03	547.59	1.53	553.03	57.62	1.51	547.59	57.05
18.84	N/A	4.93	0.28	994.31	59.46	589.00	584.75	2.91	589.01	59.24	2.89	584.76	58.81
27.65	N/A	4.60	2.87	1,000.69	49.10	489.80	485.45	24.55	490.42	49.01	24.33	486.07	48.57
16.25	N/A	4.11	0.16	960.34	56.36	539.83	535.87	1.48	539.83	56.21	1.47	535.87	55.80
16.99	N/A	4.53	1.12	983.90	58.73	576.01	572.68	11.22	576.12	58.55	11.15	572.79	58.22
17.70	N/A	4.49	0.60	1,007.34	57.00	572.40	568.67	6.01	572.43	56.83	5.97	568.70	56.46
22.16	N/A	4.67	2.08	991.44	54.19	535.50	530.36	19.41	535.85	54.05	19.22	530.71	53.53
24.55	N/A	4.82	2.70	950.67	57.71	546.72	541.50	25.80	547.33	57.57	25.55	542.11	57.02
19.06	N/A	4.01	2.50	1,019.41	55.76	567.01	563.96	24.69	567.55	55.67	24.56	564.50	55.37
16.10	N/A	4.05	0.39	992.54	56.52	559.57	555.92	3.84	559.58	56.38	3.81	555.93	56.01
22.74	N/A	4.35	2.97	979.97	54.97	537.12	533.08	27.80	537.84	54.88	27.59	533.80	54.47
15.79	N/A	4.10	1.31	990.47	56.37	556.85	554.22	12.76	557.00	56.24	12.70	554.36	55.97
21.08	N/A	4.97	2.92	1,004.90	52.26	523.20	516.83	26.63	523.87	52.13	26.31	517.51	51.50
15.97	N/A	4.19	1.72	983.87	56.33	552.77	549.78	16.58	553.02	56.21	16.49	550.03	55.90
24.06	N/A	4.54	2.02	986.94	54.41	535.33	530.54	18.91	535.67	54.28	18.74	530.87	53.79
26.84	N/A	4.14	2.50	959.09	55.80	533.77	530.24	23.32	534.28	55.71	23.17	530.75	55.34
19.94	N/A	4.26	-2.90	968.54	59.85	578.07	574.88	-29.20	578.80	59.76	-29.04	575.62	59.43
21.03	N/A	4.13	2.85	989.50	55.61	548.80	545.39	27.30	549.48	55.53	27.13	546.07	55.19
21.41	N/A	4.24	-0.21	964.20	57.60	553.83	550.75	-2.03	553.84	57.44	-2.02	550.75	57.12
26.92	N/A	4.74	1.57	995.38	51.66	512.45	508.05	14.08	512.64	51.50	13.96	508.25	51.06
26.85	N/A	4.82	-1.82	991.30	60.32	595.83	592.15	-18.91	596.13	60.14	-18.79	592.45	59.77
27.78	N/A	4.69	2.66	996.35	49.35	490.10	485.15	22.77	490.63	49.24	22.54	485.68	48.75
17.04	N/A	4.93	2.22	994.65	56.14	556.30	550.96	21.52	556.71	55.97	21.31	551.38	55.43
25.56	N/A	4.72	1.61	990.23	53.45	527.46	523.41	14.83	527.67	53.29	14.71	523.62	52.88
22.66	N/A	4.47	1.53	981.79	56.37	551.79	547.58	14.71	551.99	56.22	14.60	547.78	55.79
20.12	N/A	4.76	1.63	979.96	57.89	565.30	560.50	16.05	565.52	57.71	15.91	560.73	57.22
24.69	N/A	4.56	-0.56	975.83	60.32	586.77	583.49	-5.75	586.80	60.13	-5.72	583.52	59.80
17.57	N/A	4.12	2.25	966.75	55.69	537.02	535.17	21.08	537.43	55.59	21.01	535.59	55.40
20.56	N/A	4.97	-1.91	1,018.65	60.18	610.69	605.98	-20.31	611.02	59.98	-20.15	606.32	59.52
26.11	N/A	4.11	0.92	1,018.83	54.71	555.93	552.09	8.95	556.00	54.57	8.88	552.16	54.20
29.07	N/A	4.47	-2.56	1,012.04	55.71	562.09	557.49	-25.10	562.65	55.60	-24.90	558.06	55.14

Table C.1 Friction numbers by speed, radius and camber angle (Contd.)

Speed (mph)	Curve Radius (ft)	Camber Angle (degree)	Slip Angle (degree)	Vertical Force (lbs)	Longitudinal FN	Ideal Longitudinal Force (lbs)	FEA Longitudinal Force (lbs)	Ideal Lateral Force (lbs)	Ideal Friction Force (lbs)	True FN (%)	FEA Lateral Force (lbs)	FEA Friction Force (lbs)	FEA True FN
16.89	N/A	4.89	2.75	966.38	57.90	557.48	552.19	26.78	558.13	57.75	26.53	552.84	57.21
23.96	N/A	4.29	0.50	973.97	57.35	556.99	553.25	4.82	557.01	57.19	4.79	553.27	56.81
18.07	N/A	4.18	1.61	976.18	56.24	547.51	544.06	15.36	547.72	56.11	15.26	544.28	55.76
23.93	N/A	4.45	2.99	966.62	55.43	534.20	530.11	27.85	534.93	55.34	27.64	530.85	54.92
24.02	N/A	4.81	0.04	1,002.73	56.04	559.92	554.42	0.36	559.92	55.84	0.36	554.42	55.29
27.15	N/A	4.57	0.84	952.48	58.36	554.09	551.14	8.12	554.14	58.18	8.07	551.20	57.87
19.50	N/A	4.95	-0.97	996.59	61.54	611.00	606.11	-10.32	611.09	61.32	-10.24	606.20	60.83
18.88	N/A	4.97	-1.93	966.79	62.48	601.77	598.05	-20.24	602.11	62.28	-20.11	598.39	61.89
25.34	N/A	4.65	1.42	972.72	57.03	552.92	549.28	13.66	553.09	56.86	13.57	549.45	56.49
23.72	N/A	4.74	2.29	1,018.28	48.77	494.91	490.17	19.81	495.30	48.64	19.62	490.57	48.18
20.55	N/A	4.50	2.67	959.36	56.22	537.67	533.30	25.05	538.25	56.11	24.84	533.89	55.65
27.05	N/A	4.93	-0.23	977.68	58.21	566.97	563.23	-2.32	566.98	57.99	-2.30	563.23	57.61
17.08	N/A	4.85	-1.77	979.00	65.34	637.42	634.08	-19.69	637.73	65.14	-19.59	634.38	64.80
17.12	N/A	4.45	0.74	994.65	58.07	575.85	573.56	7.48	575.90	57.90	7.45	573.61	57.67
23.00	N/A	4.12	-0.14	1,017.04	55.28	560.80	557.96	-1.36	560.80	55.14	-1.36	557.96	54.86
24.62	N/A	4.77	-2.15	970.97	63.32	612.74	609.32	-22.94	613.16	63.15	-22.82	609.75	62.80
20.17	N/A	4.87	2.54	989.94	54.81	540.64	535.25	23.97	541.17	54.67	23.73	535.79	54.12
18.86	N/A	4.03	-2.53	957.79	57.13	545.84	543.45	-24.09	546.37	57.04	-23.99	543.98	56.80
25.55	N/A	4.41	-1.27	998.63	57.55	573.01	569.02	-12.73	573.15	57.39	-12.64	569.16	56.99
22.82	N/A	4.90	-0.09	1,013.38	55.72	562.54	557.97	-0.93	562.54	55.51	-0.92	557.97	55.06
21.30	N/A	4.58	2.81	1,003.69	51.83	518.53	513.61	25.45	519.15	51.72	25.21	514.24	51.23
25.68	N/A	4.05	2.93	995.88	55.57	551.99	549.02	28.22	552.71	55.50	28.07	549.74	55.20
26.36	N/A	4.95	1.29	993.07	53.68	531.06	524.76	11.97	531.19	53.49	11.83	524.89	52.86
18.44	N/A	4.98	1.91	975.80	57.95	563.33	557.74	18.74	563.64	57.76	18.55	558.06	57.19
25.24	N/A	4.33	-1.95	961.74	59.82	573.67	570.26	-19.54	574.00	59.68	-19.42	570.60	59.33
16.78	N/A	4.38	0.74	987.96	58.00	571.34	567.65	7.39	571.38	57.83	7.34	567.69	57.46
23.65	N/A	4.65	-0.29	1,009.97	55.69	560.61	555.88	-2.86	560.61	55.51	-2.84	555.89	55.04
17.73	N/A	4.63	2.36	1,002.79	54.32	542.99	539.21	22.32	543.45	54.19	22.16	539.67	53.82
20.14	N/A	4.79	1.80	995.33	55.26	548.11	542.87	17.25	548.38	55.09	17.09	543.15	54.57
19.52	N/A	4.54	2.60	955.18	56.51	538.04	534.83	24.45	538.59	56.39	24.30	535.39	56.05
22.01	N/A	4.22	0.75	1,003.15	55.67	556.98	553.04	7.31	557.03	55.53	7.26	553.09	55.13
22.64	N/A	4.28	-0.52	956.95	57.98	553.30	550.43	-4.99	553.33	57.82	-4.96	550.46	57.52
18.50	N/A	4.17	-2.38	1,017.74	56.66	575.12	572.44	-23.84	575.62	56.56	-23.73	572.93	56.29
20.93	N/A	4.98	2.44	981.90	55.99	547.72	542.16	23.36	548.22	55.83	23.12	542.66	55.27
19.94	N/A	4.14	-2.73	972.47	58.41	566.57	563.44	-26.97	567.21	58.33	-26.82	564.08	58.01
21.23	N/A	4.19	2.03	1,006.26	55.18	553.78	550.99	19.58	554.13	55.07	19.48	551.33	54.79
28.93	N/A	4.58	1.11	1,012.33	49.30	497.46	493.51	9.61	497.56	49.15	9.53	493.60	48.76
24.78	N/A	4.88	2.48	961.38	57.22	548.13	542.77	23.74	548.64	57.07	23.51	543.29	56.51
29.75	N/A	4.50	-1.50	956.43	60.12	573.24	569.17	-15.04	573.43	59.96	-14.94	569.36	59.53
23.93	N/A	4.16	-2.44	1,018.34	55.61	564.81	561.29	-24.01	565.32	55.51	-23.86	561.80	55.17
28.44	N/A	4.93	-1.48	953.08	59.54	565.39	561.88	-14.64	565.58	59.34	-14.54	562.07	58.97
15.31	N/A	4.01	-1.57	983.43	56.91	558.35	555.84	-15.34	558.56	56.80	-15.27	556.05	56.54
21.56	N/A	4.70	2.30	1,014.46	50.47	510.28	505.12	20.44	510.69	50.34	20.23	505.54	49.83

Table C.1 Friction numbers by speed, radius and camber angle (Contd.)

Speed (mph)	Curve Radius (ft)	Camber Angle (degree)	Slip Angle (degree)	Vertical Force (lbs)	Longitudinal FN	Ideal Longitudinal Force (lbs)	FEA Longitudinal Force (lbs)	Ideal Lateral Force (lbs)	Ideal Friction Force (lbs)	True FN (%)	FEA Lateral Force (lbs)	FEA Friction Force (lbs)	FEA True FN
16.98	N/A	4.45	2.15	960.73	56.51	541.23	537.13	20.29	541.61	56.37	20.14	537.51	55.95
26.05	N/A	4.03	-0.78	985.05	56.71	557.22	553.98	-7.57	557.27	56.57	-7.53	554.03	56.24
25.92	N/A	4.12	-0.14	1,003.71	55.63	556.93	553.30	-1.34	556.94	55.49	-1.33	553.31	55.13
15.97	N/A	4.85	-0.29	996.61	62.17	617.33	612.22	-3.09	617.34	61.94	-3.06	612.22	61.43
16.09	N/A	4.24	-2.45	1,013.23	57.88	584.90	581.51	-24.97	585.43	57.78	-24.82	582.05	57.44
21.00	N/A	4.09	-1.20	990.43	57.11	564.21	562.04	-11.79	564.33	56.98	-11.75	562.16	56.76
27.67	N/A	4.50	2.64	968.86	55.26	533.74	530.64	24.56	534.30	55.15	24.42	531.21	54.83
20.96	N/A	4.53	0.26	973.18	59.81	580.20	577.45	2.60	580.21	59.62	2.59	577.46	59.34
20.22	N/A	4.86	-2.53	950.02	61.64	583.47	579.38	-25.81	584.04	61.48	-25.62	579.96	61.05
16.22	N/A	4.23	0.28	965.82	57.04	549.38	545.17	2.70	549.38	56.88	2.68	545.18	56.45
22.89	N/A	4.39	-1.17	963.90	60.01	576.70	573.86	-11.73	576.82	59.84	-11.67	573.98	59.55
27.49	N/A	4.25	0.68	1,009.01	54.03	543.68	540.15	6.45	543.72	53.89	6.40	540.19	53.54
28.21	N/A	4.78	-1.13	983.76	59.01	578.44	574.32	-11.36	578.56	58.81	-11.28	574.43	58.39
17.64	N/A	4.47	2.98	1,015.31	53.16	538.09	534.53	27.98	538.82	53.07	27.79	535.26	52.72
20.66	N/A	4.66	-1.73	957.85	62.76	599.14	596.18	-18.11	599.42	62.58	-18.03	596.46	62.27
22.19	N/A	4.02	0.33	960.96	56.39	540.51	536.97	3.10	540.52	56.25	3.08	536.98	55.88
20.98	N/A	4.41	-1.76	1,006.23	59.08	592.75	589.59	-18.23	593.03	58.94	-18.13	589.87	58.62
25.65	N/A	4.09	-2.40	1,019.08	55.34	562.47	559.02	-23.55	562.96	55.24	-23.40	559.51	54.90
21.18	N/A	4.39	-2.87	998.05	60.98	606.80	603.26	-30.40	607.56	60.87	-30.22	604.03	60.52
23.84	N/A	4.58	-1.21	1,001.46	59.09	589.84	585.53	-12.43	589.97	58.91	-12.33	585.66	58.48
29.75	N/A	4.86	-1.46	961.60	59.76	572.59	567.61	-14.55	572.78	59.57	-14.42	567.80	59.05
19.13	N/A	4.08	0.47	973.15	56.55	548.87	547.38	4.46	548.89	56.40	4.45	547.40	56.25
27.44	N/A	4.78	-1.39	989.99	59.26	584.65	579.75	-14.16	584.83	59.07	-14.04	579.92	58.58
26.34	N/A	4.17	-0.65	970.68	57.61	557.74	554.72	-6.36	557.77	57.46	-6.33	554.76	57.15
24.37	N/A	4.48	0.60	991.89	56.15	555.21	550.82	5.80	555.24	55.98	5.75	550.85	55.54
23.59	N/A	4.70	1.30	987.75	55.71	548.42	543.75	12.48	548.56	55.54	12.37	543.89	55.06
25.01	N/A	4.87	2.89	991.84	51.66	510.50	505.05	25.71	511.15	51.53	25.44	505.71	50.99
24.86	N/A	4.06	-0.57	950.99	56.73	538.15	535.65	-5.38	538.18	56.59	-5.36	535.68	56.33
19.02	N/A	4.44	-1.73	985.21	62.04	609.36	606.66	-18.35	609.63	61.88	-18.26	606.94	61.61
19.80	N/A	4.15	0.03	954.39	56.51	537.93	534.29	0.24	537.93	56.36	0.23	534.29	55.98
15.16	N/A	4.81	-1.43	976.92	65.16	634.36	631.24	-15.80	634.56	64.95	-15.72	631.44	64.64
29.47	N/A	4.64	2.25	1,005.44	47.89	479.89	475.59	18.85	480.26	47.77	18.68	475.96	47.34
26.23	N/A	4.57	0.77	992.27	54.74	541.41	536.23	7.30	541.46	54.57	7.23	536.28	54.05
29.64	N/A	4.24	-1.05	992.48	56.41	558.36	554.09	-10.24	558.46	56.27	-10.16	554.19	55.84
16.40	N/A	4.84	-0.81	975.74	63.83	620.58	616.24	-8.76	620.64	63.61	-8.70	616.31	63.16
16.00	N/A	4.66	1.77	1,007.98	55.58	558.42	554.07	17.20	558.68	55.43	17.07	554.33	54.99
16.19	N/A	4.12	-2.10	961.72	57.51	551.65	548.65	-20.20	552.02	57.40	-20.09	549.02	57.09
29.80	N/A	4.43	2.44	966.10	55.59	535.41	532.10	22.84	535.90	55.47	22.70	532.59	55.13
20.01	N/A	4.97	2.85	974.77	56.58	549.47	544.27	27.28	550.15	56.44	27.02	544.95	55.91
17.12	N/A	4.55	2.90	955.83	56.34	536.86	532.64	27.20	537.55	56.24	26.98	533.33	55.80
23.71	N/A	4.63	-1.00	959.92	61.58	589.16	585.03	-10.33	589.25	61.39	-10.26	585.12	60.96
22.54	N/A	4.23	1.07	1,001.19	55.48	553.92	550.00	10.38	554.02	55.34	10.31	550.10	54.94
20.44	N/A	4.56	-0.72	997.52	60.44	600.99	597.29	-7.51	601.04	60.25	-7.46	597.34	59.88

Table C.1 Friction numbers by speed, radius and camber angle (Contd.)

Speed (mph)	Curve Radius (ft)	Camber Angle (degree)	Slip Angle (degree)	Vertical Force (lbs)	Longitudinal FN	Ideal Longitudinal Force (lbs)	FEA Longitudinal Force (lbs)	Ideal Lateral Force (lbs)	Ideal Friction Force (lbs)	True FN (%)	FEA Lateral Force (lbs)	FEA Friction Force (lbs)	FEA True FN
29.09	N/A	4.51	2.48	994.66	51.02	505.88	502.06	21.85	506.35	50.91	21.68	502.53	50.52
27.32	N/A	4.38	-0.09	960.39	58.41	559.32	556.06	-0.84	559.33	58.24	-0.83	556.06	57.90
27.13	N/A	4.40	-1.22	974.73	59.51	578.36	575.27	-12.33	578.49	59.35	-12.26	575.40	59.03
26.05	N/A	4.65	-2.83	962.71	62.90	603.53	600.30	-29.79	604.26	62.77	-29.63	601.04	62.43
18.23	N/A	4.24	-2.47	950.29	58.11	550.75	547.86	-23.78	551.26	58.01	-23.66	548.38	57.71
17.85	N/A	4.16	0.83	953.20	55.91	531.49	528.24	7.73	531.54	55.76	7.69	528.30	55.42
20.73	N/A	4.49	-0.17	976.46	60.19	585.92	583.05	-1.75	585.92	60.01	-1.74	583.06	59.71
19.73	N/A	4.55	-2.32	1,012.32	61.58	621.43	617.19	-25.11	621.94	61.44	-24.93	617.70	61.02
19.92	N/A	4.45	2.12	996.23	54.95	545.78	541.75	20.18	546.15	54.82	20.03	542.13	54.42
15.56	N/A	4.64	2.49	967.42	57.67	556.05	553.16	24.18	556.58	57.53	24.06	553.69	57.23
19.51	N/A	4.47	2.70	987.12	55.14	542.67	539.33	25.54	543.27	55.04	25.38	539.93	54.70
21.99	N/A	4.69	0.96	950.57	59.15	560.35	555.99	9.36	560.43	58.96	9.29	556.06	58.50
17.92	N/A	4.07	1.45	1,000.87	56.08	559.88	557.00	14.16	560.06	55.96	14.09	557.18	55.67
22.80	N/A	4.82	0.02	1,012.38	55.40	558.85	554.38	0.15	558.85	55.20	0.15	554.38	54.76
25.23	N/A	4.05	2.21	988.82	55.80	550.41	547.74	21.24	550.82	55.70	21.14	548.16	55.44
16.31	N/A	4.42	2.12	999.88	55.81	556.38	552.07	20.56	556.76	55.68	20.40	552.46	55.25
26.33	N/A	4.48	-1.87	999.95	58.35	581.68	578.54	-18.94	581.98	58.20	-18.84	578.85	57.89
27.94	N/A	4.49	2.58	989.45	52.42	517.09	512.94	23.26	517.61	52.31	23.08	513.47	51.89
17.98	N/A	4.30	1.35	1,002.26	56.03	560.03	556.26	13.23	560.19	55.89	13.14	556.41	55.52
20.66	N/A	4.78	-0.09	995.57	59.84	593.64	589.45	-0.91	593.64	59.63	-0.91	589.45	59.21
28.92	N/A	4.61	-2.44	951.48	60.93	577.90	574.34	-24.63	578.42	60.79	-24.48	574.87	60.42
19.98	N/A	4.03	-0.84	1,005.89	56.28	564.75	560.82	-8.25	564.81	56.15	-8.19	560.89	55.76
25.93	N/A	4.56	1.59	1,005.58	51.07	511.95	506.78	14.18	512.14	50.93	14.04	506.98	50.42
25.77	N/A	4.88	-1.25	968.56	60.99	588.62	583.89	-12.83	588.76	60.79	-12.72	584.03	60.30
23.32	N/A	4.91	2.33	965.44	57.29	551.12	546.65	22.43	551.57	57.13	22.24	547.10	56.67
25.70	N/A	4.91	-1.91	960.47	61.05	584.22	579.52	-19.51	584.54	60.86	-19.35	579.85	60.37
20.75	N/A	4.30	0.54	972.34	57.53	557.84	554.62	5.26	557.86	57.37	5.23	554.65	57.04
20.41	N/A	4.84	-1.09	990.69	62.88	620.74	616.76	-11.78	620.85	62.67	-11.70	616.87	62.27
27.98	N/A	4.38	2.94	961.38	55.55	532.53	529.06	27.32	533.23	55.47	27.14	529.76	55.10
27.59	N/A	4.15	-2.71	1,005.79	56.06	562.32	558.95	-26.61	562.95	55.97	-26.45	559.59	55.64
19.61	N/A	4.00	-2.49	984.49	57.12	560.92	557.38	-24.36	561.45	57.03	-24.21	557.91	56.67
17.98	N/A	4.98	-0.94	1,019.23	59.16	600.67	594.81	-9.89	600.75	58.94	-9.79	594.89	58.37
28.70	N/A	4.07	2.15	1,017.86	54.85	556.86	553.11	20.91	557.25	54.75	20.77	553.50	54.38
23.54	N/A	4.24	-0.47	1,015.05	55.10	557.78	553.78	-4.54	557.80	54.95	-4.51	553.80	54.56
26.75	N/A	4.94	-1.93	986.81	60.22	592.04	588.18	-19.95	592.38	60.03	-19.82	588.52	59.64
17.96	N/A	4.74	1.91	980.02	58.05	566.92	562.72	18.88	567.24	57.88	18.74	563.04	57.45
29.46	N/A	4.25	-1.53	982.44	57.82	566.47	562.53	-15.17	566.67	57.68	-15.06	562.74	57.28
28.48	N/A	4.23	-1.99	964.40	58.82	565.75	563.45	-19.65	566.09	58.70	-19.57	563.79	58.46
16.27	N/A	4.84	-0.30	988.80	62.75	618.30	613.15	-3.24	618.31	62.53	-3.22	613.16	62.01
16.12	N/A	4.38	-1.96	990.09	61.49	607.02	603.52	-20.79	607.38	61.35	-20.67	603.88	60.99
23.23	N/A	4.02	-2.38	1,001.24	56.51	564.42	561.18	-23.44	564.91	56.42	-23.30	561.67	56.10
25.49	N/A	4.65	-0.58	987.91	59.00	580.97	576.83	-5.84	581.00	58.81	-5.80	576.86	58.39
19.51	N/A	4.86	2.53	960.07	58.09	555.67	551.74	24.57	556.21	57.93	24.40	552.29	57.53

Table C.1 Friction numbers by speed, radius and camber angle (Contd.)

Speed (mph)	Curve Radius (ft)	Camber Angle (degree)	Slip Angle (degree)	Vertical Force (lbs)	Longitudinal FN	Ideal Longitudinal Force (lbs)	FEA Longitudinal Force (lbs)	Ideal Lateral Force (lbs)	Ideal Friction Force (lbs)	True FN (%)	FEA Lateral Force (lbs)	FEA Friction Force (lbs)	FEA True FN
15.66	N/A	4.24	-0.72	958.75	57.39	548.77	545.33	-6.92	548.81	57.24	-6.88	545.38	56.88
18.76	N/A	4.52	-2.41	998.70	63.63	633.49	630.79	-26.61	634.04	63.49	-26.50	631.35	63.22
20.73	N/A	4.29	-0.53	965.57	58.40	562.31	559.95	-5.24	562.34	58.24	-5.22	559.97	57.99
19.50	N/A	4.04	0.84	1,009.72	55.93	563.28	561.27	8.28	563.34	55.79	8.25	561.34	55.59
24.38	N/A	4.64	-2.45	951.56	61.87	586.78	583.36	-25.13	587.31	61.72	-24.99	583.90	61.36
19.33	N/A	4.05	0.09	977.39	56.64	552.25	550.41	0.86	552.25	56.50	0.86	550.41	56.31
23.92	N/A	4.31	1.54	1,012.39	53.64	541.51	537.19	14.58	541.71	53.51	14.47	537.38	53.08
19.69	N/A	4.80	-0.84	975.89	63.38	616.36	611.85	-9.07	616.43	63.17	-9.00	611.91	62.70
19.10	N/A	4.52	0.63	971.31	59.38	574.99	572.62	6.37	575.03	59.20	6.34	572.65	58.96
22.38	N/A	4.77	-0.13	967.14	61.23	590.16	585.77	-1.37	590.16	61.02	-1.36	585.77	60.57
16.08	N/A	4.09	-0.57	991.42	56.98	563.46	559.52	-5.65	563.49	56.84	-5.61	559.55	56.44
16.73	N/A	4.02	-1.16	1,003.84	56.57	566.45	564.38	-11.45	566.56	56.44	-11.41	564.50	56.23
15.48	N/A	4.46	1.83	1,006.05	55.91	560.83	558.16	17.87	561.11	55.77	17.79	558.45	55.51
19.57	N/A	4.36	-0.01	960.83	58.19	557.46	554.10	-0.09	557.46	58.02	-0.09	554.10	57.67
29.90	N/A	4.32	1.17	979.58	55.79	544.96	540.80	11.16	545.08	55.64	11.07	540.91	55.22
25.73	N/A	4.71	1.60	987.86	53.88	530.43	525.86	14.80	530.64	53.72	14.67	526.07	53.25
24.39	N/A	4.67	-1.08	1,003.29	58.53	585.30	581.32	-11.05	585.40	58.35	-10.98	581.43	57.95
26.15	N/A	4.09	2.58	1,003.05	55.24	552.72	549.10	24.91	553.28	55.16	24.75	549.66	54.80
25.86	N/A	4.14	1.18	1,007.98	54.97	552.67	548.92	11.34	552.79	54.84	11.26	549.03	54.47
21.01	N/A	4.63	0.47	983.50	59.44	582.69	579.49	4.77	582.71	59.25	4.74	579.51	58.92
24.77	N/A	4.61	-1.61	991.04	61.14	603.96	600.64	-16.95	604.20	60.97	-16.86	600.88	60.63
17.47	N/A	4.39	0.45	990.98	58.29	575.98	573.44	4.49	576.00	58.12	4.47	573.45	57.87
29.21	N/A	4.77	-0.11	963.58	58.92	565.83	562.11	-1.10	565.83	58.72	-1.09	562.11	58.34
27.08	N/A	4.55	-0.33	974.55	59.08	573.97	570.80	-3.28	573.98	58.90	-3.26	570.81	58.57
29.59	N/A	4.17	0.44	984.72	56.21	552.02	548.53	4.23	552.04	56.06	4.21	548.55	55.71
16.53	N/A	4.43	-1.02	973.61	61.07	592.78	589.66	-10.52	592.88	60.89	-10.46	589.76	60.57
22.13	N/A	4.28	0.61	1,013.95	54.81	554.17	549.92	5.88	554.20	54.66	5.84	549.96	54.24
19.61	N/A	4.65	-0.39	998.79	60.57	602.95	598.68	-4.14	602.97	60.37	-4.11	598.69	59.94
18.02	N/A	4.92	-1.38	993.23	63.55	628.83	623.79	-15.16	629.02	63.33	-15.04	623.98	62.82
20.84	N/A	4.92	-1.41	975.92	62.82	610.85	607.14	-15.08	611.04	62.61	-14.99	607.33	62.23
19.23	N/A	4.99	-0.92	993.43	61.33	606.96	602.62	-9.78	607.04	61.11	-9.71	602.70	60.67
17.41	N/A	4.33	0.85	967.87	57.35	553.52	551.53	8.19	553.58	57.20	8.16	551.59	56.99
15.01	N/A	4.61	-0.37	973.36	62.48	606.15	603.58	-3.93	606.17	62.28	-3.92	603.59	62.01
23.52	N/A	4.87	-0.33	1,018.83	55.09	559.25	554.02	-3.18	559.26	54.89	-3.15	554.02	54.38
20.35	N/A	4.89	-1.49	1,016.09	60.33	610.74	606.11	-15.93	610.95	60.13	-15.81	606.31	59.67
19.79	N/A	4.44	0.29	981.76	58.96	577.10	573.08	2.87	577.11	58.78	2.85	573.08	58.37
15.30	N/A	4.52	-1.73	1,002.13	63.07	630.04	626.89	-19.06	630.33	62.90	-18.97	627.18	62.58
27.06	N/A	4.94	0.26	1,016.48	52.31	529.78	525.20	2.37	529.78	52.12	2.35	525.20	51.67
15.85	N/A	4.01	1.19	1,006.55	56.16	563.88	561.14	11.66	564.00	56.03	11.61	561.26	55.76
26.66	N/A	4.21	-0.58	1,006.40	55.28	554.84	552.07	-5.62	554.87	55.13	-5.59	552.10	54.86
29.04	N/A	4.74	-2.20	964.17	61.27	588.72	584.58	-22.63	589.15	61.10	-22.47	585.02	60.68
26.57	N/A	4.29	1.71	956.48	56.30	537.02	533.10	16.00	537.26	56.17	15.89	533.34	55.76
19.34	N/A	4.68	1.35	954.47	58.93	560.56	557.52	13.24	560.72	58.75	13.17	557.68	58.43

Table C.1 Friction numbers by speed, radius and camber angle (Contd.)

Speed (mph)	Curve Radius (ft)	Camber Angle (degree)	Slip Angle (degree)	Vertical Force (lbs)	Longitudinal FN	Ideal Longitudinal Force (lbs)	FEA Longitudinal Force (lbs)	Ideal Lateral Force (lbs)	Ideal Friction Force (lbs)	True FN (%)	FEA Lateral Force (lbs)	FEA Friction Force (lbs)	FEA True FN
18.33	N/A	4.23	2.61	982.77	55.73	546.23	542.49	24.89	546.80	55.64	24.72	543.06	55.26
17.87	N/A	4.58	-2.18	1,008.52	63.24	635.75	631.44	-24.22	636.21	63.08	-24.05	631.90	62.66
20.95	N/A	4.69	1.67	971.09	58.20	563.30	559.20	16.42	563.54	58.03	16.30	559.44	57.61
19.75	N/A	4.45	-0.61	960.30	59.82	572.68	568.60	-6.13	572.71	59.64	-6.08	568.63	59.21
21.82	N/A	4.05	0.27	964.22	56.49	543.34	539.95	2.60	543.34	56.35	2.58	539.96	56.00
27.61	N/A	4.45	-1.00	970.10	59.71	577.54	573.69	-10.09	577.63	59.54	-10.02	573.78	59.15
26.66	N/A	4.47	2.51	991.08	52.71	520.79	515.82	22.82	521.29	52.60	22.60	516.32	52.10
28.78	N/A	4.16	0.88	950.59	56.56	536.28	533.83	8.20	536.35	56.42	8.17	533.89	56.16
29.63	N/A	4.85	1.69	960.46	56.99	545.39	541.09	16.08	545.62	56.81	15.96	541.33	56.36
23.05	N/A	4.33	-1.10	1,018.21	55.39	562.36	558.68	-10.79	562.46	55.24	-10.72	558.78	54.88
28.53	N/A	4.56	-1.06	997.25	56.39	560.55	557.48	-10.36	560.65	56.22	-10.30	557.58	55.91
18.72	N/A	4.87	-2.24	992.60	65.63	649.15	645.93	-25.34	649.64	65.45	-25.22	646.43	65.12
21.83	N/A	4.34	-2.04	984.53	60.43	593.23	589.54	-21.15	593.60	60.29	-21.02	589.92	59.92
29.32	N/A	4.94	2.16	1,018.31	48.27	489.68	484.92	18.46	490.03	48.12	18.28	485.27	47.65
22.41	N/A	4.21	1.21	961.66	56.34	540.31	536.59	11.42	540.43	56.20	11.34	536.71	55.81
27.98	N/A	4.36	2.70	975.47	54.92	534.21	530.53	25.16	534.80	54.83	24.99	531.13	54.45
27.65	N/A	4.96	-0.32	984.01	57.26	561.32	555.58	-3.16	561.33	57.05	-3.13	555.59	56.46
24.47	N/A	4.21	-0.07	1,016.58	54.70	554.55	550.86	-0.68	554.55	54.55	-0.68	550.86	54.19
27.67	N/A	4.70	2.30	964.58	56.25	540.78	537.27	21.68	541.21	56.11	21.54	537.71	55.75
27.67	N/A	4.34	-2.24	980.64	59.49	581.69	578.24	-22.73	582.13	59.36	-22.60	578.69	59.01
16.29	N/A	4.14	0.97	953.12	55.74	529.93	525.96	9.00	530.00	55.61	8.94	526.03	55.19
25.63	N/A	4.43	0.99	994.62	54.75	542.90	538.84	9.35	542.98	54.59	9.28	538.92	54.18
27.29	N/A	4.37	2.47	962.19	55.84	535.70	532.76	23.13	536.20	55.73	23.00	533.27	55.42
21.10	N/A	4.08	2.83	987.54	55.74	549.06	545.99	27.13	549.73	55.67	26.98	546.66	55.36
27.00	N/A	4.70	0.58	976.02	57.46	558.89	555.76	5.71	558.92	57.26	5.67	555.79	56.94
15.03	N/A	4.69	0.97	959.69	59.84	572.31	568.84	9.72	572.39	59.64	9.66	568.92	59.28
29.21	N/A	4.82	2.17	955.46	57.19	544.46	541.31	20.65	544.85	57.02	20.53	541.70	56.70
25.30	N/A	4.14	0.53	975.00	56.70	551.34	548.29	5.14	551.37	56.55	5.11	548.32	56.24
26.25	N/A	4.16	-1.45	952.30	57.76	548.63	545.79	-13.91	548.81	57.63	-13.84	545.97	57.33
18.41	N/A	4.54	0.25	961.64	59.81	573.35	568.85	2.54	573.36	59.62	2.52	568.85	59.15
19.42	N/A	4.82	2.78	1,000.37	53.04	528.72	523.67	25.63	529.34	52.91	25.39	524.30	52.41
15.01	N/A	4.68	-2.66	993.35	67.51	668.41	665.49	-30.99	669.12	67.36	-30.86	666.21	67.07
26.11	N/A	4.06	1.10	997.42	55.74	554.60	551.14	10.64	554.70	55.61	10.57	551.24	55.27
29.76	N/A	4.09	1.87	1,001.01	55.17	550.82	547.63	18.02	551.12	55.06	17.91	547.93	54.74
28.86	N/A	4.26	2.77	1,000.97	53.59	534.95	531.08	25.84	535.58	53.51	25.66	531.71	53.12
17.25	N/A	4.41	-1.16	973.54	60.84	590.58	587.74	-11.91	590.70	60.68	-11.85	587.86	60.38
19.26	N/A	4.94	-2.52	959.44	62.31	595.62	591.11	-26.21	596.20	62.14	-26.01	591.70	61.67
21.55	N/A	5.00	2.06	972.40	57.25	554.54	549.59	19.94	554.89	57.06	19.76	549.95	56.56
17.55	N/A	4.75	0.66	1,019.82	55.75	566.56	562.32	6.48	566.60	55.56	6.43	562.36	55.14
24.61	N/A	4.43	0.33	956.57	58.27	555.76	552.20	3.24	555.77	58.10	3.22	552.21	57.73
29.22	N/A	4.36	2.33	953.72	56.16	534.08	531.73	21.71	534.52	56.05	21.61	532.18	55.80
23.45	N/A	4.77	-2.58	1,000.14	63.48	632.72	628.43	-28.51	633.36	63.33	-28.32	629.08	62.90
15.49	N/A	4.64	1.72	980.70	58.64	573.23	570.51	17.21	573.48	58.48	17.13	570.77	58.20

Table C.1 Friction numbers by speed, radius and camber angle (Contd.)

Speed (mph)	Curve Radius (ft)	Camber Angle (degree)	Slip Angle (degree)	Vertical Force (lbs)	Longitudinal FN	Ideal Longitudinal Force (lbs)	FEA Longitudinal Force (lbs)	Ideal Lateral Force (lbs)	Ideal Friction Force (lbs)	True FN (%)	FEA Lateral Force (lbs)	FEA Friction Force (lbs)	FEA True FN
25.62	N/A	4.38	1.51	1,011.41	52.51	529.54	525.49	13.95	529.72	52.37	13.84	525.68	51.97
24.31	N/A	4.81	0.13	961.94	60.17	576.74	572.17	1.32	576.74	59.96	1.31	572.17	59.48
21.12	N/A	4.78	2.78	988.40	54.05	532.41	527.33	25.79	533.04	53.93	25.54	527.96	53.42
18.08	N/A	4.54	0.86	982.00	59.11	578.63	574.18	8.72	578.70	58.93	8.66	574.25	58.48
28.86	N/A	4.60	-1.03	965.07	60.19	578.98	576.11	-10.36	579.07	60.00	-10.31	576.21	59.71
23.28	N/A	4.31	2.45	1,014.47	53.22	538.38	534.54	23.01	538.87	53.12	22.84	535.03	52.74
23.55	N/A	4.23	2.36	1,004.51	54.52	546.19	542.74	22.52	546.65	54.42	22.37	543.21	54.08
25.86	N/A	4.48	-0.20	987.54	57.58	566.85	562.64	-1.96	566.85	57.40	-1.94	562.64	56.97
21.32	N/A	4.75	2.93	969.68	56.48	545.80	541.40	27.90	546.51	56.36	27.67	542.11	55.91
28.38	N/A	4.76	1.32	952.67	58.21	552.66	547.73	12.78	552.81	58.03	12.66	547.88	57.51
29.79	N/A	4.12	-1.86	960.46	57.83	554.03	550.96	-17.98	554.32	57.71	-17.88	551.26	57.39
21.39	N/A	4.77	-0.86	955.76	61.73	587.92	583.78	-8.85	587.99	61.52	-8.79	583.84	61.09
26.12	N/A	4.48	0.68	988.20	55.84	550.10	545.42	6.54	550.14	55.67	6.48	545.46	55.20
23.32	N/A	4.64	-1.46	1,014.00	58.24	588.63	584.17	-15.04	588.82	58.07	-14.93	584.36	57.63
20.10	N/A	4.93	1.28	1,005.81	55.07	551.80	546.07	12.36	551.94	54.88	12.23	546.21	54.31
26.47	N/A	4.75	2.44	951.30	57.57	545.75	540.68	23.20	546.25	57.42	22.98	541.17	56.89
17.94	N/A	4.74	0.20	1,006.84	58.79	589.88	584.80	2.09	589.89	58.59	2.07	584.80	58.08
15.45	N/A	4.71	1.96	999.86	56.54	563.37	560.17	19.24	563.70	56.38	19.13	560.50	56.06
19.13	N/A	4.14	-1.06	978.63	57.65	562.72	560.50	-10.45	562.82	57.51	-10.41	560.60	57.28
24.58	N/A	4.87	-2.87	1,013.00	61.12	616.96	613.12	-30.93	617.73	60.98	-30.74	613.90	60.60
16.34	N/A	4.49	-2.19	997.88	63.42	630.89	627.96	-24.14	631.35	63.27	-24.02	628.43	62.98
19.09	N/A	4.25	-1.28	999.89	57.98	578.14	575.59	-12.94	578.28	57.83	-12.88	575.73	57.58
16.01	N/A	4.76	2.99	1,004.29	53.87	539.11	534.90	28.17	539.84	53.75	27.95	535.64	53.34
23.48	N/A	4.22	2.15	1,000.58	54.90	547.85	544.55	20.55	548.24	54.79	20.43	544.94	54.46
21.06	N/A	4.18	-1.50	964.24	58.11	558.80	556.22	-14.63	558.99	57.97	-14.56	556.42	57.70
18.86	N/A	4.92	0.29	1,001.89	58.54	584.34	580.01	2.93	584.35	58.32	2.91	580.01	57.89
15.44	N/A	4.49	-0.11	996.07	60.27	598.48	595.55	-1.12	598.48	60.08	-1.12	595.55	59.79
25.86	N/A	4.89	1.85	961.69	57.57	551.63	546.90	17.79	551.92	57.39	17.63	547.19	56.90
21.55	N/A	4.40	1.46	966.24	56.99	549.03	545.81	14.02	549.21	56.84	13.94	545.99	56.51
26.92	N/A	4.18	-2.21	950.49	58.14	551.14	548.50	-21.30	551.55	58.03	-21.19	548.91	57.75
29.89	N/A	4.41	-0.60	995.17	55.43	550.00	545.19	-5.77	550.03	55.27	-5.72	545.22	54.79
22.65	N/A	4.86	1.07	966.12	59.11	569.04	564.30	10.59	569.13	58.91	10.50	564.40	58.42
18.60	N/A	4.56	-1.94	1,006.63	62.61	628.28	625.48	-21.22	628.64	62.45	-21.13	625.84	62.17
25.71	N/A	4.81	1.46	955.59	58.45	556.57	552.17	14.22	556.75	58.26	14.11	552.35	57.80
20.76	N/A	4.99	-1.58	983.52	62.16	609.01	604.88	-16.79	609.25	61.95	-16.67	605.11	61.52
27.33	N/A	4.55	0.39	1,016.00	51.08	517.29	512.98	3.56	517.30	50.92	3.53	512.99	50.49
22.19	N/A	4.16	-2.48	1,019.17	55.90	568.22	564.83	-24.57	568.75	55.81	-24.43	565.37	55.47
15.64	N/A	4.89	-1.29	974.74	64.10	622.51	617.94	-14.03	622.67	63.88	-13.93	618.10	63.41
18.77	N/A	4.17	0.19	988.11	57.02	561.94	559.24	1.90	561.94	56.87	1.89	559.25	56.60
29.28	N/A	4.52	-0.93	985.37	57.75	567.30	563.19	-9.18	567.37	57.58	-9.12	563.27	57.16
17.48	N/A	4.99	-1.06	1,017.66	59.69	605.12	600.01	-11.15	605.23	59.47	-11.05	600.11	58.97
21.28	N/A	4.07	1.45	982.26	56.17	550.34	548.32	13.92	550.51	56.05	13.87	548.49	55.84
15.11	N/A	4.09	0.54	1,017.08	56.11	569.25	567.10	5.40	569.28	55.97	5.38	567.13	55.76

Table C.1 Friction numbers by speed, radius and camber angle (Contd.)

Speed (mph)	Curve Radius (ft)	Camber Angle (degree)	Slip Angle (degree)	Vertical Force (lbs)	Longitudinal FN	Ideal Longitudinal Force (lbs)	FEA Longitudinal Force (lbs)	Ideal Lateral Force (lbs)	Ideal Friction Force (lbs)	True FN (%)	FEA Lateral Force (lbs)	FEA Friction Force (lbs)	FEA True FN
26.06	N/A	4.46	0.80	974.56	57.27	556.49	552.24	7.74	556.54	57.11	7.68	552.29	56.67
21.52	N/A	4.21	1.36	981.15	56.33	551.15	548.42	13.10	551.31	56.19	13.04	548.57	55.91
26.16	N/A	4.16	1.01	999.58	55.32	551.51	547.65	9.70	551.59	55.18	9.64	547.74	54.80
16.86	N/A	4.84	0.96	968.93	60.46	583.68	579.41	9.78	583.76	60.25	9.71	579.49	59.81
28.84	N/A	4.52	2.84	968.19	55.00	530.83	526.64	26.29	531.48	54.89	26.08	527.30	54.46
25.63	N/A	4.26	-0.03	1,017.39	54.05	548.33	544.36	-0.31	548.33	53.90	-0.31	544.36	53.51
15.66	N/A	4.91	2.80	1,017.83	53.27	540.18	535.54	26.41	540.82	53.14	26.18	536.20	52.68
15.38	N/A	4.01	-0.63	955.17	56.29	536.31	533.98	-5.86	536.34	56.15	-5.83	534.01	55.91
29.47	N/A	4.64	-0.50	1,009.54	52.40	527.27	521.99	-4.56	527.28	52.23	-4.51	522.01	51.71
19.49	N/A	4.95	2.10	958.77	58.38	557.65	553.45	20.46	558.02	58.20	20.31	553.83	57.76
25.58	N/A	4.65	2.82	962.22	56.26	539.56	535.79	26.53	540.21	56.14	26.35	536.45	55.75
23.22	N/A	4.90	0.09	999.33	56.98	567.30	562.71	0.91	567.30	56.77	0.91	562.71	56.31
22.20	N/A	4.25	0.33	1,009.36	55.40	557.64	553.55	3.19	557.65	55.25	3.17	553.56	54.84
17.52	N/A	4.87	-0.42	1,002.43	61.12	610.52	606.19	-4.43	610.53	60.91	-4.39	606.21	60.47
24.42	N/A	4.50	0.00	957.32	59.24	565.40	561.66	0.04	565.40	59.06	0.04	561.66	58.67
27.74	N/A	4.87	0.68	1,018.78	50.28	510.37	504.36	6.09	510.41	50.10	6.02	504.39	49.51
22.75	N/A	4.69	-0.95	985.62	61.95	608.54	605.08	-10.07	608.63	61.75	-10.01	605.16	61.40

Note: All results with Curve Radius labeled as N/A are generated corresponding to the field experiment on SR-26 with a radius of 2,348 ft.

About the Joint Transportation Research Program (JTRP)

On March 11, 1937, the Indiana Legislature passed an act which authorized the Indiana State Highway Commission to cooperate with and assist Purdue University in developing the best methods of improving and maintaining the highways of the state and the respective counties thereof. That collaborative effort was called the Joint Highway Research Project (JHRP). In 1997 the collaborative venture was renamed as the Joint Transportation Research Program (JTRP) to reflect the state and national efforts to integrate the management and operation of various transportation modes.

The first studies of JHRP were concerned with Test Road No. 1—evaluation of the weathering characteristics of stabilized materials. After World War II, the JHRP program grew substantially and was regularly producing technical reports. Over 1,600 technical reports are now available, published as part of the JHRP and subsequently JTRP collaborative venture between Purdue University and what is now the Indiana Department of Transportation.

Free online access to all reports is provided through a unique collaboration between JTRP and Purdue Libraries. These are available at http://docs.lib.purdue.edu/jtrp.

Further information about JTRP and its current research program is available at http://www.purdue.edu/jtrp.

About This Report

An open access version of this publication is available online. See the URL in the citation below.

Bao, J., Hu, X., Peng, C., Duan, J., Lin, Y., Tao, C., Jiang, Y., & Li, S. (2024). *Advancing INDOT's friction test program for seamless coverage of system: Pavement markings, typical aggregates, color surface treatment, and horizontal curves* (Joint Transportation Research Program Publication No. FHWA/IN/JTRP-2024/09). West Lafayette, IN: Purdue University. https://doi.org/10.5703/1288284317734